Development and evaluation of unmanned aerial vehicles for high throughput phenotyping of field-based wheat trials

Holman, Fenner

Awarding institution:
King's College London

Development and Evaluation of Unmanned Aerial Vehicles for High Throughput Phenotyping of Field-based Wheat Trials.

Fenner Holman

1332874

A thesis submitted for the degree of Doctor of Philosophy (PhD).

Department of Geography, King's College London.

25th October 2019.

Abstract

Growing demands for increased global yields are driving researchers to develop improved crops, capable of securing higher yields in the face of significant challenges including climate change and competition for resources. However, abilities to measure favourable physical characteristics (phenotypes) of key crops in response to these challenges is limited. For crop breeders and researchers, current abilities to phenotype field-based experiments with sufficient precision, resolution and throughput is restricting any meaningful advances in crop development. This PhD thesis presents work focused on the development and evaluation of Unmanned Aerial Vehicles (UAVs) in combination with remote sensing technologies as a solution for improved phenotyping of field-based crop experiments. **Chapter 2** presents first, a review of specific target phenotypic traits within the categories of crop morphology and spectral reflectance, together with critical review of current standard measurement protocols. After reviewing phenotypic traits, focus turns to UAVs and UAV specific technologies suitable for the application of crop phenotyping, including critical evaluation of both the strengths and current limitations associated with UAV methods and technologies, highlighting specific areas for improvement. **Chapter 3** presents a published paper successfully developing and evaluating Structure from Motion photogrammetry for accurate ($R^2 \geq 0.93$, RMSE ≤ 0.077m, and Bias ≤ -0.064m) and temporally consistent 3D reconstructions of wheat plot heights. The superior throughput achieved further facilitated measures of crop growth rate through the season; whilst very high spatial resolutions highlighted both the inter- and intra-plot variability in crop heights,

something unachievable with the traditional manual ruler methods. **Chapter 4** presents published work developing and evaluating modified Commercial 'Off the Shelf' (COTS) cameras for obtaining radiometrically calibrated imagery of canopy spectral reflectance. Specifically, development focussed on improving application of these cameras under variable illumination conditions, via application of camera exposure, vignetting, and irradiance corrections. Validation of UAV derived Normalised Difference Vegetation Index (NDVI) against a ground spectrometer from the COTS cameras ($0.94 \leq R^2 \geq 0.88$) indicated successful calibration and correction of the cameras. The higher spatial resolution obtained from the COTS cameras, facilitated the assessment of the impact of background soil reflectance on derived mean Normalised Difference Vegetation Index (NDVI) measures of experimental plots, highlighting the impact of incomplete canopy on derived indices. **Chapter 5** utilises the developed methods and cameras from **Chapter 4** to assess the impact of nitrogen fertiliser application on the formation and senescence dynamics of canopy traits over multiple growing seasons. Quantification of changes in canopy reflectance, via NDVI, through three select trends in the wheat growth cycle were used to assess any impact of nitrogen on these periods of growth. Results showed consistent impact of zero nitrogen application on crop canopies within all three development phases. Additional results found statistically significant positive correlations between quantified phases and harvest metrics (e.g. final yield), with greatest correlations occurring within the second (Full Canopy) and third (Senescence) phases. **Chapter 6** focusses on evaluation of the financial costs and throughput associated with UAVs; with specific focus on comparison to conventional methods in a real-world phenotyping scenario. A 'cost throughput' analysis based on real-world

experiments at Rothasmted Research, provided quantitative assessment demonstrating both the financial savings (£4.11 per plot savings) and superior throughput obtained (229% faster) from implementing a UAV based phenotyping strategy to long term phenotyping of field-based experiments. Overall the methods and tools developed in this PhD thesis demonstrate UAVs combined with appropriate remote sensing tools can replicate and even surpass the precision, accuracy, cost and throughput of current strategies.

Acknowledgements

I thank my supervisors, Professor Martin Wooster and Professor Malcolm Hawkesford, whose expertise, guidance, feedback and encouragement have been invaluable throughout this project.

Thanks to Bayer Crop Sciences, Dr Michael Schlemmer, Dr Wolfgang Thierlet and Dr Elisa Liras for your inputs into this PhD project. Thank you also to the Biotechnology and Biological Sciences Research Council (BBSRC) for the funding of this PhD (award BB/L016516/1).

I thank the various members of Rothamsted Research whose inputs throughout this PhD have been invaluable. In particular, thanks go to Andrew Riche for his guidance, advice and ever-reliable responses to emails regardless of the question. Thanks to March Castle, without whom I would have had a fraction of the data I have been able to utilise. A shout out to other members of Malcolm's lab, including all the student volunteers, whom reliably collected the necessary ground data to validate my work.

Thank you to King's College London and the Department of Geography. Thank you go to Dr Francis O'Shea and Dr Bruce Main for all the advice, chats and technical help along the way. To all members of the King's College London/NCEO Wildfire Research Team, past and present, a huge shout out for everything. Specific thanks to Jake, Mark (v1 and v2), Big T, Mary, Hannah, and Tom. Special thanks as well to all my fellow PhDs including Rory, El, Lara, Smedley, Tubs, Nat B, Randa, and Claudia.

A shout-out also to NTX, a special group of people who helped me to escape the stresses of PhD life.

To my family, the biggest thank you. To Huw and AJ for not really understanding or particularly caring about what I do, but supporting me regardless. Finally, to my parents, Helen and Bruce, you are the greatest support crew I could have asked for. Your unwavering support and guidance are unparalleled, and I will forever be eternally grateful for it, thank you.

Table of Contents

List of Figures

List of Tables

Chapter 1: Introduction

The Food and Agriculture Organisation (FAO) of the United Nations (UN) predicts that an increase of at least 50% in the yield potential of key cereal crops (*e.g.* rice, barley, wheat) is needed by 2050 (Food and Agriculture Organization of the United Nations, 2017). This is required to meet demands of a growing World population, forecasted to reach 10 billion by the same year (United Nations, 2015). Furthermore, securing increases in yield potential must be achieved in the face of significant challenges posed by climate change (Altieri and Nicholls, 2017; Hunter et al., 2017), biotic and abiotic stresses (Ashraf and Harris, 2005), and increasing competition for natural resources and arable land (Oerke, 2006; Rathmann et al., 2010; Valentine et al., 2012). Though past improvements in crop varieties, technologies and agricultural practices have more than tripled yields in key cereal crops in the last 50 years, these varieties and strategies are no longer delivering the required gains in yield potential (Evenson and Gollin, 2003; Pingali, 2012). Therefore, pursuit of new sustainable, integrated, and multidisciplinary approaches is concentrating on achieving meaningful gains in potential yield of major agricultural crop types in the face of modern challenges (Lobos et al., 2017; Parry and Hawkesford, 2010; Tanger et al., 2017). Important to these approaches will be the utilisation of genetics and natural genetic variation within key crop species to develop new, better adapted crops and achieve the ultimate goal of improved yield potentials. Advances in genotyping techniques, including high-throughput DNA sequencing, bioinformatics and genetic technologies have vastly improved the ability to analyse and dissect genetic variation, producing significantly

greater quality and quantity of genetic information (Araus and Cairns, 2014a). However, in order to harness this wealth of new information, careful and comprehensive understanding, or phenotyping, of the association, interaction and impression of genetics (genotypes) on target physical characteristics (phenotypes) such as yield and stress tolerance is required (Furbank and Tester, 2011a).

Phenotyping is the application of methods, technologies and protocols used to measure a specific observable trait or set of traits related to plant structures or functions at a range of scales from cellular to whole-plant levels (Fiorani and Schurr, 2013a; Ghanem et al., 2015). Successful phenotyping facilitates the understanding of these traits as a result of the plant's genotype and growing environment, including interactions between the two over time and space (Gaudin et al., 2013; Yang et al., 2015). The challenge or difficulty of phenotyping relates to the plasticity and dynamic nature of phenotypes over both temporal and spatial scales, as plants grow through their life cycle and adapt to their growing environment (Houle et al., 2010; Pieruschka and Schurr, 2019). Many current methods for phenotyping lack adequate detail, precision and speed of throughput to facilitate sufficient exploitation of new genetic material and technologies to their maxima (Virlet et al., 2016). This is especially the case for phenotyping of field-based experiments, where conventional techniques are considered labour intensive, limited in throughput, economically inefficient, often subjective due to the reliance on visual scoring, and frequently lack any measures of spatial variation (Furbank and Tester, 2011a; Jones et al., 2003). This is despite the known superiority of results of field experiments over alternative controlled environments such as growth chambers and greenhouses, where translation of results into real-world yield gains have

suffered from lack of true environmental conditions (Araus and Cairns, 2014a; Passioura, 2006; Poorter et al., 2012; Reynolds et al., 2012; White et al., 2012a). Therefore, only by making significant improvements in the methods, technologies and protocols available for phenotyping plants in field-based experiments, can the wealth of new genetic material and tools be exploited and the challenges of improving crop yield potentials be met.

Remote sensing (RS) is a prime candidate for improved phenotyping methods and technologies due to its rapid and non-invasive data capture, and proven application to temporal and spatial monitoring tasks (Tattaris et al., 2016). RS sensors and methods are already employed for phenotyping applications in numerous growth chambers and glass houses around the World (e.g. European Plant Phenotyping Network (European Plant Phenotyping Network, 2019), and the Australian Plant Phenomics Facility (Australian Plant Phenomics Facility, 2019). Techniques such as multispectral, hyperspectral, and thermal infrared imaging, along with laser scanning, are providing researchers with a suite of new methods for collecting valuable phenotypic information. Importantly, these methods provide fast, non-destructive measures of target phenotypes, allowing researchers to observe the continuous, dynamic development of plants in response to environmental conditions (Araus and Kefauver, 2018) However, adoption of these technologies and methods to field-based experiments, sufficient to overcome the bottleneck in phenotyping, remains to be achieved (Araus and Cairns, 2014a; Cobb et al., 2013; White et al., 2012b).

Several RS options for phenotyping in the field are available, however limitations restrict their widespread application. Data from satellite and high-altitude aerial remote

sensing (*e.g.* from helicopters and planes) is widely used in vegetation monitoring (Berni et al., 2012, 2009b, 2009a) . However, the generally low spatial resolution and challenge of obtaining cloud-free images at regular return intervals from satellites, as well as the high costs associated with aerial imaging campaigns, make these options largely unsuitable for most phenotyping field experiments (Gago et al., 2015; Mahlein, 2015). Ground based RS options provide far more options for repeated measurements at frequent intervals, and detail at a spatial scale, and these include handheld devices, vehicles and fixed platforms. The simplest of these options are handheld devices, including spectrometers or imagers, manually walked through experiments (Pietragalla et al., 2012). These low-cost devices require little to no training; however, data collection is labour intensive, and the low throughput makes them inefficient overall unless significant amounts of manual labour is available. Improved throughput, and increased automation can be achieved via the mounting of sensors to vehicles (*e.g.* Tractors) or fixed platforms (e.g. Lemnatec Field Scanalyzer (Lemnatec, Aachen, Germany)) (Virlet et al., 2016). Automation and the carrying of multiple sensors allows for high throughput, reduced labour requirements, and simultaneous measurements of multiple phenotypes (Deery et al., 2014; Liebisch et al., 2015; White et al., 2012b). However, limitations with field access in poor weather conditions, as well as the impact of heavy vehicles on soil structure make vehicles an unpopular option for many situations (Liebisch et al., 2015), whilst limited plot coverage of fixed platforms combined with high investment costs makes this option prohibitive. A potentially viable alternative to these, gaining popularity and recognition over the course of the period that this thesis research was undertaken, is the use of low-altitude Unmanned Aerial Vehicles (UAVs).

UAVs, also referred to as Drones, Unmanned Aerial Systems (UAS), or Remotely Piloted Aerial Systems (RPAS) are defined as any aircraft whose pilot is not on-board (CAA, 2019). Initially developed by the military for photographic monitoring as early as 1955 (Rango et al., 2009), rapid advances in the accuracy, economic efficiency and miniaturisation of many technologies including Global Navigation Satellite Systems (GNSS) such as Global Positioning Systems (GPS), cameras and microprocessors has promoted UAV systems from military tools to cost effective, innovative and commercially available remote sensing platforms for use in a wide variety of applications – including research activities and agriculture (Pajares, 2015; Yao et al., 2019). UAV platforms have the ability to offer high spatial and temporal resolution data at high throughputs, filling a gap in current phenotyping options (Chapman et al., 2014). However, UAVs do suffer from several recognised limitations such as payload size, flight endurance, and risk of damage - which means they do not currently provide a single, 'out of the box' solution to overcome all limitations of alternative field phenotyping platforms. The limited payload does restrict the size and number of RS sensors available for use with UAVs (Sankaran et al., 2015), whilst the endurance restricts the area able to be covered per flight, though this is still comparable to that of ground based vehicles and platforms (Anderson and Gaston, 2013; Dandois and Ellis, 2013).

The need for new field phenotyping technologies and methods is apparent. Remote sensing from UAVs is one viable candidate for providing phenotypic data at sufficient temporal and spatial resolutions to overcome some of the current phenotyping bottlenecks. However, the success of any new phenotyping system will depend on (i)

the quality of the phenotypic information provided; (ii) the affordability; (iii) data management; and (iv) validation of its high throughput abilities (Araus et al., 2018). In respect of this, the broad aims of this thesis are to (i) investigate the use of UAV based remote sensing technologies, data capture methods, and processing methodologies for providing high throughput data collection of phenotypic traits in the field; (ii) validate derived phenotypic measurements against current standard measurement techniques; (iii) prove integration and application of developed methods to phenotyping of on-going field-based wheat crop experiments, (iv) assess affordability and high throughput abilities.

1.1 Outline of Thesis Structure

This thesis is comprised of this Introductory chapter, along with a Background, four chapters reporting empirical research (of which two culminated in published articles presented herein in their published format) and a Summary and Conclusion chapter. Due to the inclusions of these publications, readers may notice some parts of repetition between chapters. The structure of this thesis, as well as details of each chapter is as follows:

Chapter 2: Background and Specific Objectives

This chapter provides an overview of specific phenotypic traits typically measured in the field, along with critical evaluation of existing methods, highlighting the target phenotypes for this thesis research. The chapter also discusses and reviews UAVs as a remote sensing platform. From the review of phenotypic traits and UAVs, a review of suitable RS technologies and methodologies applicable to UAV phenotyping

of targets traits is then provided. Finally, the chapter concludes with an outline of the specific research objectives addressed in subsequent chapters.

Chapter 3: High Throughput Field Phenotyping of Wheat Plant Height and Growth Rate in Field Plot Trials Using UAV Based Remote Sensing

This chapter comprises work conducted developing and testing a methodology for measuring 3D crop structure, specifically plant height, of field trial plots. The work for this chapter culminated in a publication in the international journal *Remote Sensing:*

Holman, F.H.; Riche, A.B.; Michalski, A.; Castle, M.; Wooster, M.J.; Hawkesford, M.J. High Throughput Field Phenotyping of Wheat Plant Height and Growth Rate in Field Plot Trials Using UAV Based Remote Sensing. Remote Sens. **2016**, 8, 1031.

Alongside the published article, additional work investigating Digital Elevation Model (DEM) processing, and Digital Surface Model (DSM) normalising procedures is presented.

Chapter 4: Radiometric Calibration of Commercial 'Off the Shelf' Cameras for UAV-based High-Resolution Crop Phenotyping of Reflectance and NDVI

This chapter comprises work conducted developing a methodology for capturing radiometrically calibrated imagery of canopy reflectance. The work for this chapter culminated in a publication in the international journal *Remote Sensing:*

Holman, F.H.; Riche, A.B.; Castle, M.; Wooster, M.J.; Hawkesford, M.J. Radiometric Calibration of 'Commercial off the Shelf' Cameras for UAV-Based High-Resolution Temporal Crop Phenotyping of Reflectance and NDVI. Remote Sens. **2019**, 11, 1657.

Alongside the published article, a more detailed description of the procedure used for determining spectral responses of the cameras is presented.

Chapter 5: Dynamic Quantifying of Canopy Trait Response of Modern Wheat Cultivars to Varied Nitrogen Applications

This chapter presents further validation of UAV methods into a longer-term field-based wheat experiment. The chapter focuses on the utilisation of high temporal resolution data from UAVs to assess the impact of nitrogen fertiliser treatments on canopy formation and maturation.

Chapter 6: 'Cost-throughput' Analysis of UAVs for Long Term Phenotyping of Field-based Crop Trial Experiments

This chapter presents a cost benefit analysis of UAVs for field-based phenotyping compared to traditional manual methods. The focus of this chapter is on the assessment on the financial and measurement throughput benefits/drawbacks of UAVs in comparison to alternative conventional methods.

Chapter 7: Summary of Findings, Conclusions and Future Work

The final chapter collates together the major findings of this thesis and assesses the extent to which the proposed research aims and objectives were met. Recommendations for future work are also discussed.

Chapter 2: Background and Specific Objectives

2.1 Introduction

The aim of this chapter is to critically assess current standard field phenotyping methods, as well as identify suitable UAV based remote sensing alternatives to facilitate high throughput field phenotyping in the future.

Firstly, the importance of field-based phenotyping is discussed in relation to key target crop characteristics of interest to crop breeders and researchers. Within this discussion, the specific phenotypes selected for focus within this PhD are identified, with focus on their relevance to field phenotyping, as well as known limitations of current standard field phenotyping. The second section introduces and discusses UAVs as low-cost remote sensing platforms, with a focus on their use in high throughput phenotyping. This section also provides a critical review of UAV relevant sensors and methodologies, with a focus on identifying shortcomings and opportunities for improvement. Finally, from these reviews of phenotypes and UAV methods, the third section will summarise the main points from Chapter 2 and present the specific research questions, aims and objectives for the remaining chapters of this thesis.

2.2 Phenotypes and Phenotyping

Phenotyping is the application of methods, technologies and protocols to measure a specific observable trait or traits related to plant structure or function. It is considered a vital step in the development of new cultivars, as measurement and

monitoring of target traits can provide a quantifiable expression of the interaction between a crop's genotype and its growing environment (Walter et al., 2015). Phenotypes are widely used by breeders and scientists looking to develop new cultivars with favourable characteristics such as enhanced nutrient and water use efficiency, better drought and heat tolerance, resistance to diseases and pests, photosynthetic capacity, and improved yield quality and quantity. With yield used as an example target trait, a wide range of phenotypes have been assessed and applied to generating direct or indirect measures of predicted final crop yield. Traits such as in-season biomass, date of anthesis (flowering), early vigour, canopy morphology, growth rates, root structures, spectral reflective properties of canopies, in-season damage and leaf area index have all been utilised to understand and predict final yields during the life cycle of crops pre-harvest (Reynolds et al., 2012).For drought and heat tolerance, traits of interest include canopy temperature, stomatal conductance, leaf water potential, and root structures (Pask et al., 2012).

There is a wide range of phenotypic traits available and applicable to breeding and development of new superior crops. However, these phenotypes are diverse and occur at a range of scales from cellular to whole-plant levels, such that many phenotypes are not suitable for targeted monitoring via UAV based remote sensing techniques (Walter et al., 2015). Therefore, careful selection of phenotypes is required to ensure the developed methods are applicable to real-world end-users, such as breeders. For example, though root structure is of interest in relation to water use efficiency and drought tolerance, it is not suitable for monitoring via remote sensing in the field. Similarly, fine scale traits such as anthesis (flowering) will be more challenging to

monitor from UAVs compared to leaf or even whole canopy scale traits. Considering these factors two categories/areas/types of phenotypic traits have been identified for focus within this PhD through discussions with crop breeders (Rothamsted Research and Bayer Crop Sciences). Selection of these phenotypes was driven by both their application in cultivar development, and their suitability for assessment via remote sensing and UAVs. The phenotypes are crop morphology, specifically plant height and growth; and spectral canopy reflectance, with focus on the visible and near infrared regions of the spectrum. The following section will provide both further specific justification for monitoring these traits in their worth to breeders and researchers; and discussion of current standard techniques implemented in the field along with their advantages and disadvantages.

2.2.1 Crop Morphology: Plant Height and Growth

Crop morphology is the study of the physical form and external structure of plants (Evert and Eichhorn, 2013). Plant height is a fundamental morphological phenotype utilised by crop breeders. Typical applications include direct indication of plant growth and development stages if measured temporally (Figure 2.1). In addition to growth status it has been shown to be a strong predictor for in-season biomass, harvest index, and final grain yields (AHDB, 2015; Erten et al., 2016; Pittman et al., 2015; Schirrmann et al., 2016b; Torres and Pietragalla, 2012); as well as a useful indicator for sensitivity to in-season damage such as lodging, a source of yield loss (Blonquist et al., 2009). Plant growth rate, the changes in height over time, have also been shown to provide good indications of plant responses to environmental stresses, e.g. stunted growth due nitrogen deficiency. Plant height is also often used as a key parameter in

numerous computer-based models including those to evaluate water stress and canopy temperatures (Doelling et al., 2018). Beyond crop breeding and cultivar development, plant height is also an essential parameter for site specific management practices and precision agriculture. For example, taller plants offer the advantage of easier mechanical harvesting, however, this is opposed by increased risk of crop damage resulting from lodging (Lati et al., 2013).

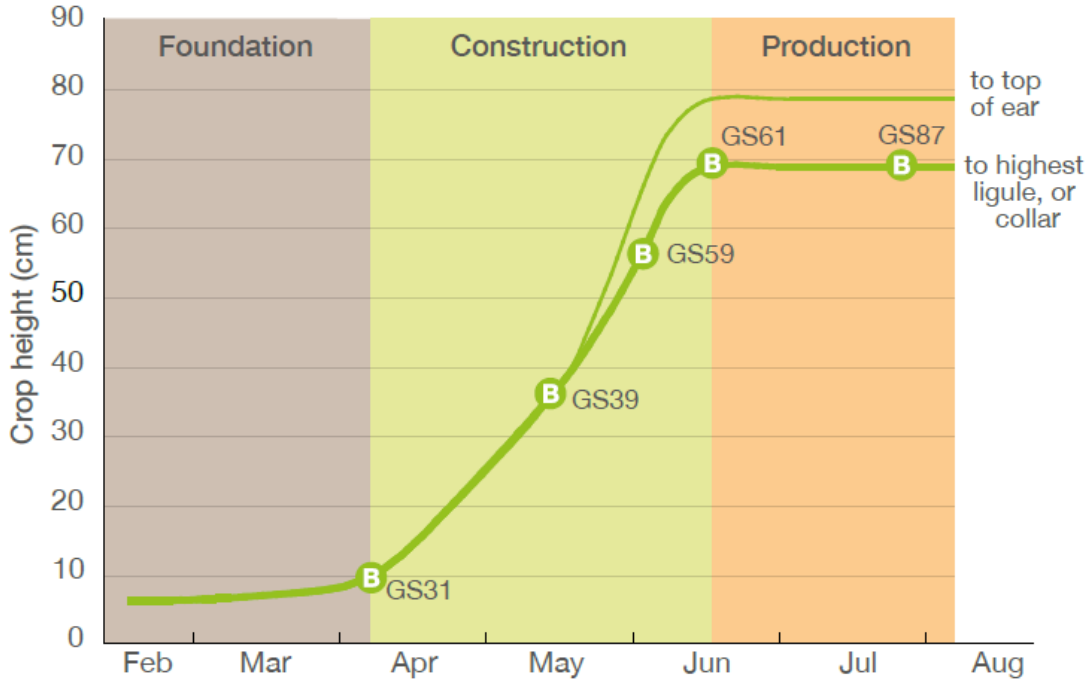

Figure 2.1. Crop height presents a typical temporal trend over the plants life cycle, with the main period of growth occurring between April and June. GS = Growth Stage, and GSXX refers to the specific numbered growth stages as outlined by the Agricultural and Horticultural Development Board (Agriculture and Horticulture Development Board, 2015).

Clearly plant height is a useful phenotype applicable to assessing several important breeding traits such as in-season biomass, risk of lodging and final yields. Yet despite this, current standards for in-field phenotyping of crop height and growth rate are limited. Conventional protocols for field phenotyping of crop height is most commonly performed manually, based simply on use of a meter rule (Torres and Pietragalla, 2012). The method typically involves subsampling of five plants within each experimental plot adjudged to visually represent the average height of the plot. Their heights are measured, and their average defines the plant height for the entire experimental plot. Advantages of this method include its simplicity, minimal training requirements, as well as being a non-destructive assessment. However, several significant limitations are recognised, such that this method is not suitable for large-scale experiments. These include; limited spatially representative sample size, low throughput, labour intensive, and susceptibility to subjectivity and error between measurements (Jiang et al., 2016). The manual, low throughput nature of this method in turn limits the collection of height data to a few time points per season, resulting in a clear loss of dynamic measurements of growth rate through the plant's life cycle (Figure 2.1).

2.2.2 Spectral Reflectance and Absorbance

This section discusses phenotypic traits associated with the spectral reflectance and absorbance of light by above-ground plant structures (e.g. canopy), and their applications in crop breeding programs.

The term 'reflectance' refers to the ratio between the light reflected and light arriving on a target surface (Khan et al., 2018a). Measurement of canopy reflectance is a widely used phenotypic metric for measuring a variety of traits including canopy size, photosynthetic capacity, chlorophyll content, nitrogen status, water status, and biomass (Li et al., 2014). This technique utilises understanding of the interaction of light at different wavelengths of the electromagnetic spectrum with specific constituents within the canopy, in order to produce applicable proxy measures of crop canopies (Pietragalla et al., 2012). Crops exhibit a typical reflectance curve across the electromagnetic spectrum (Figure 2.2), within which sub-domains of the spectrum are related to different typical properties. The visible domain (400-700nm) exhibits high absorption and low reflectance, particularly within the blue (450-490nm) and red (625-700nm) regions caused by foliar pigments of interest such as chlorophyll, carotene and xanthophyll. A sharp increase in reflectance at the red-edge (~700nm) and into the near infrared (NIR) domain (700-1300nm) is related to leaf structure, and in particular the reflective properties of healthy mesophyll structure in the NIR light (Pettorelli et al., 2005). Beyond the NIR, reflectance the short-wave infrared (SWIR) (1300-2500nm) domain is influenced by water content, nitrogen concentration and non-photosynthetic components of the canopy including cellulose and starch (Peña-Barragán et al., 2011). The reflectance curves exhibited by crops within these spectral domains will change in relation to the afore

mentioned canopy components, and how these change through the life cycle of the crops as well ins response to stressors such as drought or nutrient deficiency. Utilising the known relationships between canopy components and reflectance, allows for the development of useful proxy measures for numerous crop health and breeding traits.

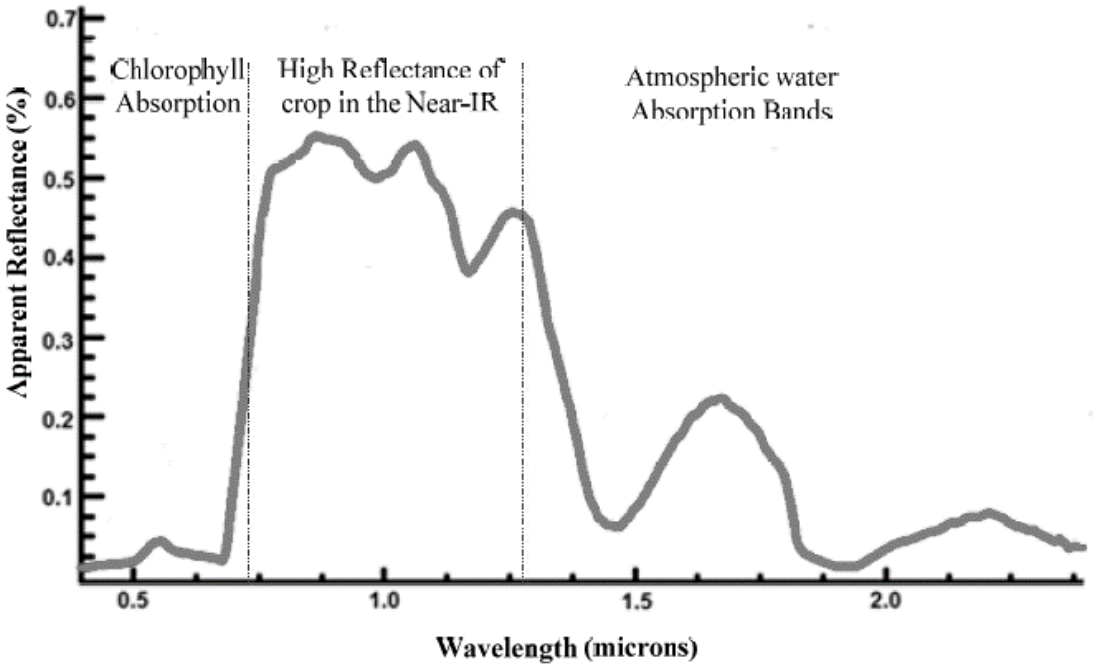

Figure 2.2. Typical trend of reflectance spectra of healthy vegetation in the visible, near infrared and short-wave infrared regions of the electromagnetic spectrum (Li et al., 2014).

Most commonly these measurements of canopy features are achieved through the use of spectral vegetation indices (VIs), formulated to compare reflectance between absorbing and non-absorbing wavelengths (Roberts et al., 2011). Selection of vegetation index is dependent on the canopy component of interest as well as the specific wavelengths available (dictated by monitoring equipment). Table 2.1 provides several examples of previously used VIs applied to vegetation monitoring and crop phenotyping. Most common, these VIs use wavebands in the visible and near infrared regions due to the characteristic photosynthetic response of green vegetation to incident light (Khan et al., 2018b). Of these, the Normalised Difference Vegetation Index (NDVI) is the most commonly used in numerous applications including crop phenotyping. Calculated to relate the difference between reflectance in NIR and red wavebands, NDVI's proven applications include biomass prediction (Bendig et al., 2014; Cabrera-Bosquet et al., 2011), leaf area index and green area index (Ali et al., 2015; Zheng et al., 2009), plant nitrogen status (Muñoz-Huerta et al., 2013), vigour (Khan et al., 2018; Kipp et al., 2014) and final yield prediction (Lopresti et al., 2015).

Table 2.1. Examples of vegetation indices calculated using either visible wavebands, near-infrared wavebands or a combination of both. R = reflectance (%), R_B = reflectance in the Blue waveband, R_G = reflectance in the Green waveband, R_R = reflectance in the Red waveband, R_{NIR} = reflectance in the NIR waveband; L = soil adjustment factor.

Index	Name	Equation	Reference
NDVI	Normalised Difference Vegetation Index	$\frac{R_{NIR} - R_R}{R_{NIR} + R_R}$	(Pettorelli, 2013)
GNDVI	Green Normalised Difference Vegetation Index	$\frac{R_{NIR} - R_G}{R_{NIR} + R_G}$	(Hunt et al., 2008)
SR	Simple Ratio	$\frac{R_{NIR}}{R_R}$	(Slafer, 2012)
PRI	Photochemical Reflectance Index	$\frac{R_{531} - R_{570}}{R_{531} + R_{570}}$	(Berni et al., 2009a)
RGI	Red Green Index	$\frac{R_R}{R_G}$	(Coops et al., 2006)
GRVI	Green Red Vegetation Index	$\frac{R_G - R_R}{R_G + R_R}$	(Motohka et al., 2010)
GLI	Green Leaf Index	$\frac{2 \times (R_G - R_R - R_B)}{2 \times (R_G + R_R + R_B)}$	(Hunt Jr. et al., 2013)
ExG	Excess Green	$2 \times G - R - B$	(Woebbecke et al., 1995)
ExR	Excess Red	$1.4 \times R - G$	(Meyer et al., 1999)
ExGR	Excess Green Red	$ExG - ExR$	(Meyer et al., 2004)
SAVI	Soil Adjusted Vegetation Index	$\left(\frac{R_{NIR} - R_G}{R_{NIR} + R_G + L}\right) \times (1 + L)$	(Huete, 1988)
MSAVI	Modified Soil Adjusted Vegetation Index	$\left(\frac{R_{NIR} - R_R}{R_{NIR} + R_R + L}\right) \times (1 + L)$	(Qi et al., 1994)

Standard methods for measuring canopy reflectance in the field use spectrometers to measure reflectance either over a range of wavebands or at preselected wavebands (*e.g.* red and NIR for NDVI) suitable for calculation of target VIs. Examples include simple hand-held dedicated devices (*e.g.* GreenSeeker (Govaerts and Verhulst, 2010), SPAD meter (Bullock and Anderson, 1998)) which are designed for measuring a single VI quickly and consistently over multiple measurements. Alternatively, multi- or hyperspectral spectrometers provide a more sophisticated technology able to collect measurements at a range of wave bands (e.g. VIS-NIR) from which the user can calculate a wealth of VIs. Advantages of the dedicated hand-held devices is their simplicity, and the automation of data processing, thus requiring minimal expertise or training to collect data. The more complex spectrometers provide greater flexibility and increased phenotypic information by calculating multiple VIs from a single measurement; though, their increased complexity makes training a requirement (Steele et al., 2008).

A common limitation of both these techniques is the lack of spatial resolution and the inability to dissect any trends in spatial variability within the area of measurement (Daughtry et al., 2000). All these devices provide single point measurements from the entire scene contained within the field of view. This poses a significant problem as any measurement of reflectance at the canopy scale will be a measure, not only of the target canopy, but also of the background soil brightness, colour, minerology and canopy architecture (Latorre-Carmona et al., 2014). As such, any derived VIs, and in turn, any measures of specific phenotypes, will be formed from the combination and interaction of these factors into a single measure (Jay et al., 2017a). For example, a crop presenting of low canopy cover, but high vegetation vigour may present

the same VI measurement as a crop expressing high canopy cover but lower vegetation vigour. Though the same VI measurement is derived, the causation varies between the two situations, specifically variations in canopy size vs. canopy quality. Such situations can provide false measures of phenotypic traits, and lead to subsequent errors in crop management practices or prediction models (Knyazikhin et al., 2013).

2.2.2.1 Crop Ground Cover

Crop ground cover is used to assess crop establishment, early vigour and the early stages of the plant's life cycle (Mullan and Barcello Garcia, 2012). It represents the percentage of soil surface covered by the crop (Figure 2.3), and is characterised by fast developing leaf area and/or above-ground biomass (Jimenez-Berni et al., 2018). Rapid early formation of canopies is a target trait, as it has the potential to improved crop photosynthesis. The total period a canopy is able to intercept light directly affects photosynthetic ability, biomass production and yield (Parry et al., 2011a; Parry and Hawkesford, 2010). Early establishment of canopies also leads to increased levels of soil shading which in turn reduces soil water loss from evaporation (Mullan and Reynolds, 2010). This relationship between ground cover and soil water loss is of particular interest in water-limited environments, where water use efficiency is a key requirement for crops. For example, a 16% increase in yield has been previously achieved from high ground cover wheat varieties grown in water limited conditions (Zhao et al., 2019). In addition to water use efficiency, the increased shading from early vigour and high ground cover may positively suppress weed growth through reduced light availability at the soil surface (Coleman et al., 2001).

Figure 2.3. Examples of crop ground cover percentages. Top left = 10% cover; top right = 30% cover; bottom left = 50% cover; bottom right = 90% cover. (Li et al., 2014).

Accurate phenotyping of ground cover has typically been achieved by destructive sampling methods in controlled environments (Botwright et al., 2002; Rebetzke and Richards, 1999). In the field, three standard methods exist for measuring crop ground cover, (i) visual scoring, (ii) digital RGB (Red, Green, Blue) photography and image analysis and (iii) spectral indices from spectral scanning or imaging systems (Jimenez-Berni et al., 2018). Visual scoring involves an estimation of the percentage of ground cover, in increments of 10% (Pask and Pietragalla, 2012). As discussed earlier, the subjectivity of visual scoring severely limits the validity or accuracy of the phenotypic data produced, and therefore is not a robust method for generating quantitative measures of crop ground cover. Digital photography has been used to obtain measures of ground cover by counting number of vegetation pixels versus soil

pixels within an image. Utilising contrast between soils and vegetation, often enhanced via vegetation indices, this process can be easily automated and standardised to ensure consistency between images and datasets (Li et al., 2010). Finally, the use of spectral systems such as handheld scanners, and spectral indices (e.g. NDVI) has been shown to exhibit good correlation with crop ground cover (Prabhakara et al., 2015). However, as discussed and described before in relation to canopy reflectance measurements, there is a chance of multiple contrasting spatial ground cover situations producing similar VI values. Comparison of digital imagery and VIs, found that photography performed better when compared to visual assessments (Duan, 2017). The ability of the imagery to mirror visual assessments, specifically to acknowledge and assess spatial variability, compared to single point VI measurements is the likely cause of improved results.

2.2.2.2 Canopy Maturation/Senescence

Canopy maturation or senescence is associated with the final phase of a plant's life cycle, occurring post-anthesis and is characterised by a series of degenerative processes which lead to plant death (Distelfeld et al., 2014). Its initiation, after anthesis, and duration, under optimal growth conditions, is defined by a 'developmentally-regulated, age-dependent process' (Heyneke et al., 2019). During senescence, nutrients are mobilised and moved from sources (e.g. leaves) to sinks for storage (Balazadeh et al., 2014). Senescence of wheat crops overlaps with grain filling, and the synchronisation of these two phases plays a highly important role in determining crop yield (Liang et al., 2018). For crop development, canopy senescence traits are a target, due to their influence on total period of photosynthetically active canopy. 'Stay-green' traits, present in some varieties, delay the onset of senescence and have been shown to lead to increased yields

and improved performance in response to drought stress (Bagherikia et al., 2019; Christopher et al., 2014). Senescence has also been shown to influence grain quality parameters including protein content (Gaju et al., 2016). Despite the importance of senescence on final yield and grain development, phenotyping of this growth stage is often limited and basic. The most common method is to visually score senescence on a scale from 1-10 depending on the percentage of dead leaf area (Figure 2.4) (Magorokosho, 2010; Pask and Pietragalla, 2012). Obvious limitations including subjectivity, slow through-put, and lack of interpretation of spatial variability result in a sub-par measurement of an important phase of crop development (Pask and Pietragalla, 2012).

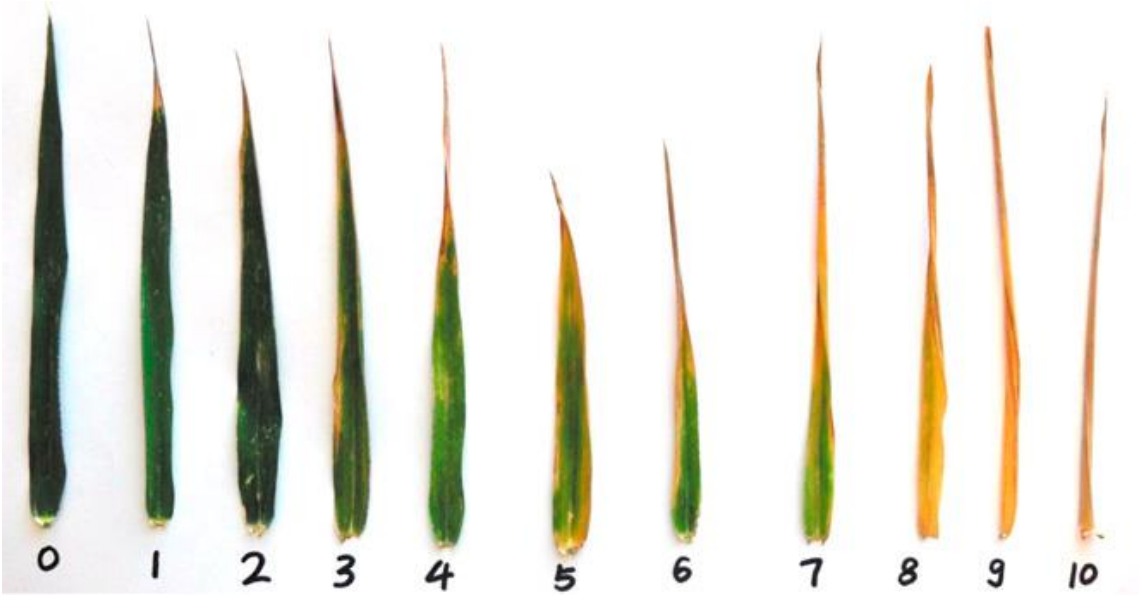

Figure 2.4. Examples of the different stages of wheat leaf senescence, with visual rating scale for each stage indicated (Li et al., 2014).

An alternative has been to use image analysis via digital cameras to analyse the loss of canopy colour during anthesis (Makanza et al., 2018). As with monitoring crop ground cover, quantification of area senesced can be improved through the use of digital images, providing a more robust and less subjective method for measurement.

This review of morphological and spectral reflectance crop traits has highlighted several shortcomings in existing standard conventional field phenotyping methods. These techniques are resulting in a loss of valuable spatial and temporal data, limiting the progress breeders can make via the linking of genotypic and phenotypic measurements. Key limitations common amongst the various traits are the requirement for subjective visual assessments, along with slow throughputs, limited spatial resolution, and costly and laborious methods. Considering these limitations, the need for new techniques capable of high-throughput phenotyping is clear. The next step is to investigate the potential solutions offered by UAV and remote sensing. This will include a critical review of suitable techniques and technologies available for the application of monitoring both crop morphology and canopy reflectance in the visible and near-infrared wavelengths.

2.3 UAVs, Remote Sensing, and Phenotyping.

This next section reviews Unmanned Aerial Vehicles (UAVs) as remote sensing platforms, and covers both their advantages and disadvantages. Focus then moves to sensors and methods applicable to UAV-based phenotyping of morphology and spectral reflectance traits in the field, with attention on improving precision, objectivity and throughput of phenotypic measurements.

2.3.1 Unmanned Aerial Vehicles

Unmanned Aerial Vehicles, sometimes referred to as Drones or Unmanned Aerial Systems (UAS), are a group of technologies rapidly being adopted into both the public and scientific communities, based largely on ideas originally developed for military applications (Rango et al., 2009). Advances in the accuracy, miniaturisation, and cost of key technologies including GNSS (e.g. GPS) and computer processors has enabled UAVs to become a cost effective and innovative aerial platform. High levels of flight automation, user defined spatial and temporal resolutions, and the reduction of risk in certain situations, e.g. in natural hazard monitoring (Niethammer et al., 2012), makes UAVs an attractive option. Furthermore, coupled with a range of different remote sensing devices (Table 2.2. Examples of different UAV specific sensors commercially available.

Type	Examples	Weight (g)	Cost	Resolution	Advantages	Limitations
RGB	DSLR	500-1000	£500-£3000	10-40 MP	Very high resolution, in built storage, easy to integrate with UAVs	Heavy, lack calibration, limited to visible bands

), UAVs have the potential to be used for data acquisition in a range of environmental monitoring applications and disciplines. This includes modelling of the temporal changes in landslide dynamics (Turner et al., 2015); 3D reconstruction of fluvial topography of UK streams (Woodget et al., 2015); monitoring of rangeland (Laliberte and Rango, 2009; Rango et al., 2006) and conservation applications such as surveying of habitats and animal numbers (Koh and Wich, 2012). Alternatively, UAVs have been applied in the documenting of archaeological sites, where the rapid collection of very high-resolution 3D reconstructions from UAV-based methods has proven useful (Fernández-Hernandez et al., 2015). In terms of agriculture, UAVs have been used for the monitoring of water status and drought stresses (Berni et al., 2012); additionally, collecting multispectral and hyperspectral imagery for use in spectral indices (Panda et al., 2010) and even chlorophyll fluorescence (Zarco-Tejada et al., 2013).

Table 2.2. Examples of different UAV specific sensors commercially available.

Type	Examples	Weight (g)	Cost	Resolution	Advantages	Limitations
RGB	DSLR[i]	500-1000	£500-£3000	10-40 MP[ii]	Very high resolution, in built storage, easy to integrate with UAVs	Heavy, lack calibration, limited to visible bands
	Compact	100-1000		10-24 MP		Fixed lenses, lack calibration, limited to visible bands
Multi-spectral	Micasense-MX	230	£4,500 (per camera)	1.2 MP (RGB[iii], RE[iv] + NIR[v] bands)	Small, includes DLS[vi] sensor, Images geo-tagged during capture. Addition of second camera increases number of spectral bands.	Low spatial resolution spectral imagery. No high resolution RGB camera.
	Parrot Sequoia	107	£3,600	1.2 MP spectral bands (RG, RE + NIR) + 16 MP uncalibrated RGB camera	Small, includes DLS sensor, Images geo-tagged during capture. High spatial resolution RGB camera.	Low spatial resolution spectral imagery, no blue spectral band
	Tetracam ADC	90	£4,000	3.2 MP (user-defined bands)	Lightweight.	Limited bands (only G, R, NIR), No DLS
	Adapted RGB cameras		£500-£1000 + filter costs	10-40 MP (RGB + NIR)	Very high resolution, easy to integrate with UAVs.	Wide spectral bands, requires custom radiometric calibration, No included DLS

Hyperspectral	Firefly Rikola	490 700	- £40,000	1 MP 1 MP	High number of bands	Expensive, very low resolution, requires high technical knowledge
Thermal	Flir Duo Pro R	375	£7,500	0.3 MP thermal 12 MP Visible	RGB and thermal combined in single image, Calibrated thermal measurements	Low spatial resolution, High knowledge of calibration and processing required.
	Wiris 640	390	£8,600	0.3MP (RGB, RE + NIR bands)	High thermal resolution (0.05°C), factory calibrated	No visible camera incorporated, low spatial resolution, high knowledge of calibration and processing required.
'Hybrid'	Altum	406	£10,000	3.2 MP (spectral)	Thermal and Spectral (RGB, RE, NIR) imaging combined, small form factor	Low spatial resolution, thermal not calibrated.
LiDAR	Riegel	3000	£50,000-£300,000		High 3d resolution, Offers good canopy structure reconstruction	Complex workflow, Heavy

[i] DSLR – Digital Single-Lens Reflex;
[ii] MP = Megapixels;
[iii] RGB = Red Green Blue;
[iv] RE = Red Edge;
[v] NIR = Near Infrared;
[vi] DLS = Downwelling Light Sensor.

However, despite the advantageous features offered by these aerial platforms, limitations remain. The somewhat low carrying capacity of many UAVs, restricted by reduced take-off weights places limits on the choice of sensors flown. This impacts particularly in the case of larger, more advanced sensors e.g. LiDAR, which are typically larger in volume and mass then standard cameras, for which most UAVs are designed to carry. Short flight times imposed as a result of restricted battery capacity and take-off weight, reduce spatial coverage and leads to the requirement for multiple flights if a large area is being covered. Whilst increasing size or number of batteries is possible to increase fight duration, this comes with increases in mass which will negate some of the gains in flight time. Some of these constraints can be overcome by choice of form factor, though selection of either form factor comes with individual caveats (Table 2.3).

Table 2.3. Discussion of UAV form factors, their advantages and disadvantages (Colomina and Molina, 2014; Nex and Remondino, 2014).

UAV Form factor	Advantages	Disadvantages
Fixed Wing	Increased flight time and area coverage; automated flights	Take-off and landing more complex; Limited sensor carrying capacity. Weather limited
Rotary Wing	Good carrying capacity; ability hover at low altitude over targets; automated flights; Portability	Limited flight time and area coverage. Weather limited
Heli-kites and blimps	High carrying capacity; simple design and set-up	Fixed position, limited spatial coverage; require anchorage.

Sensor choice also limits the application of UAVs and data collected. Depending on data requirements, a range of sensors are available. Miniaturisation of technologies has allowed for UAV specific versions of conventional remote sensing systems to be developed. However, increased miniaturisation results in increased cost, especially if the sensor is designed to deliver data of equal quality and resolution as larger counterparts (Barbedo, 2019; Roy and Miller, 2017). Alternative, low costs sensors exist; however, these come with the caveat of less work focussed on the development and validation of the necessary workflows, calibrations and radiometric corrections required to ensure robust, accurate quantitative measurements (Berni et al., 2009b; Lebourgeois et al., 2008). Finally, with all UAV sensor types, challenges related to processing and storage of high-resolution UAV data remain, adding to the difficulties of generating quantitative information. Though the range of consumer-grade software packages focussed at automatic processing of UAV derived data is increasing to help overcome this problem (Aasen et al., 2018).

The popularity and success of UAVs in remote sensing and mapping applications has been in large part down to their ease of use. The level of technology and automation related to these aerial platforms makes them simple to use. However, limitations remain, particularly related to the sensors and data processing. A current trade-off between high costs or lack of calibration makes sensor choice problematic. In acknowledgement of this, the next two sections focus on available sensor options and methodologies suitable for the measurement of morphology and spectral reflectance.

2.3.2 UAVs, Remote Sensing and 3D Structure

Crop morphology has been previously identified in Section 2.2 as a group of phenotypic traits of interest. Traditional methods for measuring morphological traits such as height, growth rate and lodging have been identified as insufficient in terms of resolution, objectivity and throughput for current phenotyping requirements. Alternative remote sensing methods for determination of crop height exist, including laser rangefinders (LiDAR) (Hoffmeister et al., 2010; Zhang and Grift, 2012), ultrasonic sensors (Scotford and Miller, 2004), and three-dimensional time-of-flight cameras (Andújar et al., 2015; Azzari et al., 2013). Of these, LiDAR is the most common, and its use has been proven for collecting accurate measurements of crop height in the field (Bareth et al., 2016; Hoffmeister et al., 2010). However, all the above systems are typically mounted to ground-based vehicles or fixed platforms, because of the constraints related to weight and power supply. As a result, limitations related to the coverage of multiple locations and access to field sites during bad weather impact on throughput of these systems (Virlet et al., 2017). Furthermore, the cost of UAV specific LiDAR sensors, upwards of £50,000, prohibits the widespread adoption of this option. An alternative UAV suitable technique is Structure from Motion (SfM) photogrammetry which has gained popularity in recent years.

Originally developed for computer vision applications, SfM photogrammetry uses images acquired at multiple viewpoints in order to model the three-dimensional (3D) structure of an object or surface (Fonstad et al., 2013). However, unlike traditional photogrammetry where careful pre-planned and structured image acquisition (e.g. on a

consistent plane or axis) is required; SfM utilises advanced matching algorithms to identify and tag common features between multiple images without any prior information or image processing (Westoby et al., 2012). A detailed review of the exact algorithms utilised in SfM software to achieve this is beyond the scope of this chapter, though readers can refer to Snavely *et al.* (Snavely, 2011; Snavely et al., 2008, 2006) for more detailed descriptions.

Fundamental to the success of SfM processing is its ability to track features between images independent of variations in image scale, resolution, brightness, and view point make them ideal to application with UAV imagery (James et al., 2017). Additionally, SfM processing is able to determine scene geometry and camera position and orientation without inclusion of targets of known 3D position (Snavely, 2011). This allows for much simpler, user-friendly data collection processes, with reduced expertise. Finally, the recent development of both commercial (e.g. Agisoft Photoscan (Agisoft LLC, St. Petersburg, Russia) and Pix4D (Pix4D, Lausanne, Switzerland)) and open-source (e.g. Microsoft ICE (Microsoft, Redmond, USA)) SfM automation software packages, has simplified the required data processing of this method considerably (Woodget et al., 2015). In timely combination with the rise of UAVs for remote sensing, SfM software packages have enhanced the ease of operation of these methods, importantly with minimal training required. However, the use of these relatively user-friendly software packages, does not necessarily promote consideration of the data collection and processing parameters involved, such as the image capture and georeferencing, and their impact on accuracies of the final 3D models (James et al., 2017).

Therefore, consideration of these parameters is needed to ensure consistent and robust data is produced.

In terms of image capture, image resolution has a direct influence on the accuracy of derived elevation models. Higher resolution imagery maintains more fine scale structural detail, which is less susceptible to loss via filtering during SfM processing (Jay et al., 2015; Küng et al., 2011; Willkomm et al., 2016) . As such, sensor selection and UAV flight altitude will be key influencers on final model outputs. Also related to image capture, several studies identified a 'dome-like' distortion towards the edges of 3D models (Smith and Vericat, 2015). Both flying height (Woodget et al., 2015) and nadir viewing imagery (Smith and Vericat, 2015) have been identified as causation factors. Whilst the inclusion of oblique imagery alongside nadir imagery has been identified as a solution offering positive reduction in the distortion (Wackrow and Chandler, 2011).

The other key variable influencing model accuracies relates to the georeferencing of final models. Although SfM processing is able to reconstruct scene geometry and relative camera positions, these models remain within an arbitrary coordinate space. Geo-referencing of 3D models is therefore required in order to transform the model from an arbitrary to an absolute coordinate system (Westoby et al., 2012). This processing step requires the user to provide additional data relating to geographic locations either of the cameras, or of the targets captured within the imagery. Ground Control Points (GCPs) are the simplest and most common technique and have been shown to provide superior accuracy to alternative georeferencing solutions e.g. geo-tagged images (Ruiz et al., 2013). However, poor accuracies from the GPS unit used to locate GCPs, can lead to propagation of error into final models (Bendig et al., 2013a, 2013b).

The use of UAVs and Structure from Motion processing is a fast-moving area of research, that has seen a sharp increase in knowledge development over recent years. The work presented within Chapter 3 of this PhD thesis focussed on the development and validation of these methods for measuring crop heights, and was undertaken and published in 2015/16. Since publication a number of developments and further proof-of-concepts have been achieved. The following section will provide an up-to-date review of the applications of UAVs and SFM for monitoring crop heights, including those developments that have succeeded the work presented in Chapter 3 of this thesis.

Initial investigations into the suitability of SfM processing for measuring crop morphology and height, produced mixed accuracies ($0.22 \leq R^2 \geq 0.71$) for both barley and rice crops at different crop growth stages (Bendig et al., 2013a, 2013b). Subsequent studies produced similar results, with more consistent accuracies ($R^2 \geq 0.7$) (Aasen et al., 2015a; Willkomm et al., 2016). Though accuracies were low, these studies did identify a number of sources of error and key processing steps required to produce crop heights from SfM model outputs. Bendig et al., (2013b) identified sub-optimal accuracies from the GPS (> 1m precision) used for used for GCP measurements as a key source of error present in the final crop height models. The GPS data is required by SfM processing software for geo-referencing of final models, and as such any inaccuracies in these values will be carried through the SfM processing workflow and be incorporated into the final height models. Subsequent studies utilised Differential-GPS (D-GPS) systems, with superior accuracies (≤ 10cm) and found a significant reduction in error of crop height models, and in-turn, increased accuracy of derived crop heights (Aasen and Bolten, 2018; Bareth et al., 2016; Holman et al., 2016). Furthermore, the improper placement and

insufficient spatial coverage of GCPs has been identified as source of doming effects in final models (Woodget et al., 2015). This effect was found to result from using nadir imagery for the SfM processing (Wackrow and Chandler, 2011), and can be minimised through appropriate placement and density of GCPs throughout the target survey area.

In addition to the errors associated with inaccurate GNSS systems, some of the initial studies found SfM derived height models were prone to underestimation, when compared to heights measured by standard rule methods (Aasen et al., 2015a). The authors questioned the suitability of rulers for use as ground validation data, due to known limitations with this method; though this criticism is opposed by the rulers use as the traditional standard method, which the UAV is proposed to replace. An alternative source of validation data is to use high accuracy terrestrial LiDAR scanners to generate high resolution point clouds, from which crop can be determined (Ziliani et al., 2018). Madec et al., (2017) produced a detailed comparison of UAV and LiDAR derived wheat crop heights over a large number of plots (n=1173). Initial accuracy assessments between LiDAR and manual ruler measurements showed high agreements in measured heights (R^2 = 0.9) and no consistent negative bias in results (Bias = 1.4cm). Further comparison of LiDAR and UAV derived heights indicated underestimations of height from the UAV models persisted, ultimately indicating its source is likely from the UAV data or methodology as opposed to poor quality validation data. Suggested reasons for underestimation focussed on the reduced spatial resolution of the UAV models resulting in loss of small plant structures e.g. grain heads. Filtering the plot canopy pixels using percentiles (e.g. 95% or 99%) did improve underestimations of

height, but did not remove the trend all together (Bareth et al., 2016; Voort, 2016), ultimately due to the spatial resolutions filtering out some plant material.

A key component of the SfM workflow highlighted by the initial studies of Bendig et al, (2013a, 2013b), and in turn an influencer on final model accuracies, was the requirement to normalise the final model for underlying topography (Geipel et al., 2014). Without removal of this topography, extraction of crop heights is difficult and prone to error. Two main methods for achieving normalised models, typically referred to as Crop Surface Models (CSMs) do exist, and work via the subtraction of a bare ground topography map or model from SfM derived models. The most common of these, due to practicality and ease of application, is to generate a bare-ground topography model, which is subtracted from the crop SfM models, thus isolating pure crop heights. This method requires the generation of a bare-ground surface model, which is then subtracted from crop models in order to produce normalised CSMs. The alternative method is to filter out soil and vegetation from within models in order to determine crop height from a single flight without requirement for a bare soil map (Tilly et al., 2014; Varela et al., 2017). However, practicality, simplicity and speed of processing has resulted in the subtraction method generally being the preferred solution for generating normalised CSMs. More specific analysis of this technique, found bare ground maps generated for each flight offered marginally superior crop height accuracies compared to bare soil maps generated at the beginning or end of the season (Chapman et al., 2014; Holman et al., 2016). Though the practicality of generating individual, flight specific bare ground maps is often viewed as impractical, compared to the only slight reduction in final height accuracy (RMSE = 0.068m versus RMSE = 0.038m) (Holman et al., 2016).

The above review has outlined the development and validation of SfM photogrammetry methods and techniques for accurate phenotyping of crop height in the field. More recently, as a result of these validations, there has been an increase in the application of SfM derived data for improved phenotyping. Example applications include temporal tracking of plant height, via high-throughput phenotyping though not using a UAV, facilitating the identification of additional quantitative trait loci within wheat, which showed influences on crop height within the tillering stage of growth (Lyra et al., 2020). The ability to utilise multiple timepoints for genetic analysis of crop height greatly increased the available information of growth-stage specific traits; though a trade-off was identified in the increased volume of data required to process in order to utilise this data. Madec et al., (2017) investigated the relationship of wheat crop height with flowering stage, biomass and yield. Maximum plant height and flowering stage were found to be well correlated ($R^2 = 0.7$), whilst biomass and plant height were found to be strongly correlated ($R^2 = 0.91$). Yield was found to be poorly correlated with plant heights ($R^2 = 0.13$). Several studies have also managed to identify the occurrence of lodging within fields from SfM 3D models of plant height. The presence of lodging within fields when measuring crop heights was noted by some, but no attempt to quantify the extent of lodging was attempted (Bendig et al., 2014; Madec et al., 2017). Studies that have quantified lodging from SfM models and UAV imagery, used thresholding to indicate the occurrence of lodging (Chapman et al., 2014; Chu et al., 2017). Comparison of results against standard visual assessments of lodging severity achieved average accuracy ($R^2 = 0.48$). These results show the potential for lodging to be assessed in conjunction with temporal height measurements from UAVs and SfM.

However, the poor accuracy highlights the need to develop improved methods for the identification and quantification of lodging events. More recently, Singh et al., (2019) utilised the high temporal resolutions offered by UAVs to enable genetic dissection of crop lodging in wheat. Comparison with simplistic yet industry standard visual assessments showed both techniques identified the same genome responsible for lodging susceptibility. Ultimately the UAV was proven to provide both the phenotypic accuracy and throughput required for the large-scale assessment of lodging resilience, required by breeders.

This review of the relevant literature has highlighted the key workflow steps required to generate accurate topographic reconstructions from UAV imagery and SfM processing. The literature also highlights the initial sub-optimal results achieved for measurement of crop heights from UAV imagery and SfM processing. A number of data collection and processing variables were identified as probable sources of error, and development of workflows and techniques, including the work presented in Chapter 3 of this thesis, has solved many of these factors. More recently, there has been increased uptake of these methods for temporal monitoring of crop heights, and application of these data into phenotypic studies of commercial crops such as wheat.

2.3.3 UAVs and Spectral Reflectance

Quantitative measurements of the spectral reflectance of plant canopies, particularly in visible and near-infrared wavebands, are an already proven method for phenotyping various phenotypic traits. Though, as highlighted in Section 2.2.2, existing ground-based methods, using hand-held sensors, suffer from poor spatial resolutions and throughput.

Multi- or hyper-spectral imagers are an obvious alternative solution to the lack of spatial resolution found in current methods. Furthermore, the existence of several UAV-based specific spectral imagers (*e.g.* Parrot Sequoia (Parrot, Paris, France), Micasense RedEdge (Micasense, Seattle, USA)), in combination with numerous examples of their application in crop phenotyping, clearly demonstrate their potential fit for UAV-based high-throughput phenotyping. The simplest of application for UAV-sourced imagery, is the quantification of ground cover, of particular interest to breeders during the crop establishment phase. Utilising both RGB and multi-spectral indices, Torres-Sánchez et al., (2014) demonstrated the use of UAVs for large scale mapping of vegetation fraction of field-based wheat crop trials. The authors were able to achieve accuracies up to 92% when flying at a 30m altitude in order to maximise image resolution. Employing the same principles, and similar techniques, UAVs have been used to identify and map weeds within fields, offering data for more targeted herbicide applications (Castro et al., 2012; Gómez-Candón et al., 2014). Similarly, Guo et al., (2018) utilised the high spatial resolutions, in combination with machine learning based image processing, to perform Sorghum head counting. Using simple RGB images, the methods

were found to accurately reproduce manual head counts (R^2 = 0.84). Other example applications include assessing the relationship between canopy reflectance and key breeder traits e.g. crop biomass and yield. Numerous studies have investigated a range of spectral indices, spatial and temporal resolutions for mapping final yields of different crops including wheat (Du and Noguchi, 2017; Guan et al., 2019; Kanning et al., 2018), maize (Maresma et al., 2016; Wahab et al., 2018) and rice (Stroppiana et al., 2015; Yang et al., 2019; Zhou et al., 2017). Common amongst these studies, was the advantageous spatial mapping of yield within field and trail plots, offering greater detail in-to under- or over-performing crops. Monitoring for nitrogen status and uptake has also been investigated via UAV based spectral imaging. Liu et al., (2018) investigated a number of spectral indices for diagnosing nitrogen status of oilseed rape with results varying between the different indices ($0.62 \leq R^2 \geq 0.73$). Similarly, Walsh et al., (2018) utilised UAVs to temporally monitor nitrogen status of wheat via vegetation indices including NDVI and red edge focussed indices. The temporal monitoring facilitated by the UAV based system, allowed for the monitoring of in-season wheat crop nitrogen status, importantly at different growth stages.

The studies discussed above utilised commercially available spectral imagers which have the advantage of pre-determined and automated processing and calibration workflows This makes them attractive options for applying to phenotyping straight out of the box. However, certain limitations remain with regards spatial resolutions. In order to obtain individual spectral bands, these systems use individual sensors to measure each spectral band (Rabatel et al., 2014). This solution for multiple bands, is both costly and limited in resolution due to the need to fit multiple sensors within a small form

factor. Resolution can be increased, either through larger individual sensors or custom built multiband single sensors; though this comes with significant increases in cost pushing the sensors beyond the affordability for many end-users (Rabatel et al., 2011).

In response to the poor spatial resolution and prohibitive costs of existing sensors, some researchers have investigated alternative options, including the potential of Commercial 'Off the Shelf' (COTS) digital cameras (Lebourgeois et al., 2008; Rabatel et al., 2014, 2011). These cameras have the useful feature of natural sensitivity of their internal CMOS (Complementary metal-oxide-semiconductor) or CCD (Charge-coupled device) sensors to both visible and near-infrared light (Verhoeven, 2008). Manufacturers install NIR blocking filters during manufacture to inhibit the NIR sensitivity because it is an unwanted feature for normal everyday use. However, the removal or replacement of these filters with visible blocking filters, reopens this sensitivity to NIR light. This produces a camera in which the combination of visible and NIR light or just NIR light can be measured in all 3 channels (Aber et al., 2010). This sensitivity to visible and NIR light, combined with high resolution sensors, in-built data storage, user-friendly operating interfaces and simple integration with UAVs, makes digital COTS cameras an attractive option for UAV-based spectral reflectance monitoring (Dare, 2008).

Several studies have investigated quantitative measurements of reflectance from COTS cameras (Burud et al., 2017; Kyratzis et al., 2017; Sankaran et al., 2015), though the lack of validation data leaves uncertainties in the translation of results into proof of concept for these cameras (Lebourgeois et al., 2008). More recently, validation of results against ground measured spectral reflectances have indicated that accurate reflectance data can be achieved (Berra et al., 2017). However, instability of results over time

highlights the need for further work to improve the robustness of these methods. The DIY nature of these cameras means complete and proper radiometric calibration and corrections are vital for generating quantitative spectral reflectance data. A number of variables related to the camera including processing workflow and environmental factors impact on the generation of accurate measurements of reflectance (Lebourgeois et al., 2008). Camera related factors include; i) camera exposure settings, ii) vignetting, iii) image file format and conversion.

Exposure settings (aperture, shutter speed, and ISO) work in combination to control the level of light reaching the sensor to maximise the quality of exposure of images. However, where the purpose of the image is to provide a quantitative measure of light, this artificial change in light introduced by the camera is unwanted. Typically, studies have fixed the settings to remove any impact from exposure settings on data (Berra et al., 2017; Gibson-Poole et al., 2017). However, this solution does, present a significant trade-off by narrowing the dynamic range of the camera sensor and increasing the risk of under- or over-exposure in images, which equates to a loss of data (G. L. Ritchie et al., 2008). An alternative approach would be to allow the cameras to adjust exposure settings as required during flights. Proven linear relationships between pixel digital number (DN) and varying ISO, shutter speed and aperture settings (Hiscocks, 2011), indicate normalisation of exposure settings in post-processing to be possible. If confirmed, the use of these linear relationships would allow for an image collected under certain exposure settings to be adjusted in post processing to represent light levels of different exposure settings. Ultimately this would simplify the data collection workflow by using automatic exposure settings on the camera, rather than

user defined and fixed settings. Additionally, the risk of poor image exposure would be minimised, particularly when flights are conducted under variable irradiance conditions.

Vignetting is the darkening, or loss of brightness towards the edges of an image (Conrady, 2013). It is the result of several factors relating to the camera lens and to the geometric nature in which light enters the camera lens falling on the sensor. However, the primary factor behind vignetting is the blocking of light rays by the effective size of the aperture (Yu, 2004; Zheng et al., 2009). Therefore, the level of vignetting distortion in an image is dependent on the lens and aperture used. The impact of vignetting and, in turn, the correction for it has been widely researched in various applications including microscopy, image mosaicking, and digital photography (Bevilacqua et al., 2011; Kim and Pollefeys, 2008; Leong et al., 2003). Typical methods for correcting vignetting involve modelling the vignetting pattern of the camera-lens set-up via a polynomial function, and from this deriving pixel specific correction factors. Alternative solutions include using 8th degree polynomial functions to model the loss in brightness of a flat field image, before application of these models to correct vignetting within individual images (Berra et al., 2017). Though difficulties with illumination and camera angle complicate the ease and ability to produce a perfectly flat field. Alternatively, averaging over an entire image set, such as those collected during UAV campaigns, in combination with 2nd degree polynomials can provide comparable results with a simplified workflow (Lebourgeois et al., 2008; Lelong et al., 2008). For all these methods, correction of vignetting for individual bands and exposure settings separately is used to ensure robust corrections for entire datasets of UAV imagery is achieved. Application

of correction filters or models is also worth noting; should the adjustments brighten the corners, or darken the centre of the image? The most common method is to brighten the corners, in order to avoid a loss of data through saturation of pixels during adjustment (Lelong et al., 2008).

Image file format and conversion plays an important role in maintaining the original, unaffected DN values as measured by the camera sensor. Due to the non-linear response of the human eye to changing light levels, camera manufacturers introduce a non-linear correction to improve the visual appeal of images produced (Bull, 2014). Use of non-raw formats (*e.g.* Joint Photographic Experts Group (JPEG), Portable Network Graphics (PNG)) result in a loss of the linear relationship between light and sensor measurement (Verhoeven, 2010). As quantified measures of reflected light are the intended application of this imagery for crop phenotyping, maintaining this linear trend is vital to ensure the quantitative value of the results generated. Results from previous studies using JPEG imagery, suffered due to the non-linear corrections introduced by the JPEG image file format (Mathews, 2015). The alternative is to use the raw image file format, which stops any post capture processing by the camera to ensure the original pixel values remain unchanged (Lebourgeois et al., 2008). However, raw formats are proprietary, requiring conversion to standard formats (e.g. Tagged Image File Format (TIFF)) to gain compatibility with most post processing software packages such as SfM. Further issues arise from the introduction of this processing step, because the conversion is not performed consistently between conversion software options, with many software packages still introducing non-linear gamma corrections during the conversion process (Gehrke and Greiwe, 2014). As such, the use of the open source

conversion software DCRAW (Coffin, 2007) for conversion is widely recommended and performed as it allows for linear conversions of raw to TIFF format, ensuring the raw pixel DN values are maintained.

Moving away from camera properties, the key environmental factor that requires consideration is the radiometric conversion of the data contained in the imagery from radiances to reflectance. Conversion of measured radiances to spectral reflectance estimates requires a measure of incoming solar irradiance in the same waveband (λ), as per Equation 1.

$$Reflectance(\lambda) = \frac{radiance(\lambda)}{irradiance(\lambda)} \quad (1)$$

A key difficulty with UAV spectral measurement campaigns lies in obtaining temporally relevant measures of spectral irradiance (Miura and Huete, 2009). Solutions previously investigated include the use of ground-based targets of known reflectance to be captured within images (Berra et al., 2017). Inconsistent target capture during UAV flights, limits the success of this method, particularly under variable illumination conditions. Furthermore, the temporal stability of target reflectances if left in the field permanently as is often preferred, can vary by up to 16% over a season as a result of dirt build up, degradation via weathering, or vegetative growth on the surface of the target; thereby impacting on the stability of time series measurements (Anderson and Milton, 2005). An alternative is to utilise a second device to measure incoming solar irradiance simultaneously with collection of UAV imagery, and in the same wavebands of interest. An example of such a sensor is the downwelling light sensor utilised by the Parrot Sequoia (Parrot, Paris, France). Constant temporal measures of total irradiance in conjunction with collection of reflectance imagery, has been proven to provide more

reliable results, with minimal biases compared to single measurements such as those from ground-based targets (Miura and Huete, 2009).

The final area of consideration is the production of georeferenced orthomosaics from the final calibrated images. All previous studies have utilised SfM software to produce reflectance mosaics of UAV captured imagery. Within SfM software, such as Agisoft Photoscan (Agisoft, 2016) three possible methods can be used for the merging of pixels: Mosaic, Average and Disabled. Mosaic utilises custom proprietary algorithms and therefore, potentially alters true pixel values without user knowledge. Average combines all pixels from individual images for a single orthomosaic pixel, and assigns the mean value to it. Disabled uses the value of a single pixel from the single image closest to the nadir. Comparison of these processing settings, has proven that the disabled setting maintains the original quantitative data best (Aasen and Bolten, 2018). The disabled processing methods use of nadir imagery, also ensures a comparable viewing angle to ground-based sensors, such as those already used in phenotyping of field-based experiments.

There is proven application of high-resolution spectral imagery from UAVs for high-throughput phenotyping of several phenotypic traits. However, spatial resolutions or cost have left a gap for development of alternative imaging systems for use with UAVs. The low cost, high resolution, and ease of integration with UAVs of Commercial 'Off the Shelf' (COTS) digital cameras makes them an attractive alternative to commercially available multispectral imagers. Nevertheless, as has been highlighted, the process for obtaining radiometrically calibrated spectral reflectance estimates from the collected imagery is very important, complex, and which at the time of writing remains

incomplete. Further development and validation of temporal stability of these cameras is needed, before their application in UAV phenotyping can be confirmed.

2.4 Summary and Research Objectives

A number of phenotypic traits related to crop morphology and spectral reflectance have been discussed in this chapter. Yet despite their relevance and value to in developing new, improved, high yielding crops capable of adapting to future challenges, the methods for phenotyping them in a field setting remain imperfect and insufficient. Consistent limitations highlighted in Section 2.1, are low spatial resolutions, low throughput and in some cases lack of robust, objective measurements. Alternative UAV-based remote sensing methods exist and are capable of offering improved spatial resolutions, throughput and objective measurements of field-based experiments. Commercial digital cameras have the potential to provide data for both 3D reconstructions, via SfM processing, and spectral reflectance measures, via camera adaptation. Significantly these measurements are offered at lower costs, and better spatial resolutions compared to alternative sensors. However, lack of development and validation of data collection and processing workflows has meant that they ultimately remain as unproven conceptual phenotyping sensors.

Therefore, building on the existing work outlined in this chapter, the specific objectives of this thesis are as follows:

Objective 1: To develop and evaluate use of imagery collected from a UAV-mounted camera in combination with Structure from Motion photogrammetric processing workflows for the spatial and temporal mapping of field-

based wheat crop trials, most specifically focused on derivation of plant height and growth rate (addressed in Chapter 3)

Objective 2: To develop and evaluate the ability to derive radiometrically accurate, high spatial resolution spectral reflectance imagery and vegetation indices of growing crop canopies using UAV-mounted modified Commercial 'Off the Shelf' (COTS) digital cameras (addressed in Chapter 4).

Objective 3: To evaluate the ability of the UAV-based phenotyping methods developed in Chapters 3 and 4 to provide long term phenotyping of nitrogen fertiliser application on canopy development and senescence dynamics of a modern wheat germplasm panel (addressed in Chapter 5).

Objective 4: To assess and quantify the true costs and throughput associated with a UAV-based phenotyping system for long term field experiments (addressed in Chapter 6).

Chapter 3: High Throughput Field Phenotyping of Wheat Plant Height and Growth Rate in Field Plot Trials Using UAV Based Remote Sensing

3.1 Introduction

Crop morphology was previously identified as a key phenotypic trait category, within which crop height is a useful parameter for understanding crop dynamics. However, despite useful applications in the monitoring of crop development and the prediction of final yields and biomass (Torres and Pietragalla, 2012), conventional methods for field measurements are limited. For crop height, these methods are manual, low throughput and subjective, leading to data which is lacking spatial and temporal measurements of crop height in response to environmental stresses. There is a need to improve the efficiency, consistency, throughput and resolution of crop height measurements to assist in overcoming the current bottleneck in the phenotyping of field-based experiments. UAVs and specifically Structure from Motion photogrammetry image processing workflows was identified as an alternative for measuring crop heights and 3D crop morphology. However, incomplete methods and sub-par accuracy assessments indicate further work on developing a complete workflow is required to validate this technique as a viable phenotyping method.

This chapter presents the development and evaluation of Unmanned Aerial Vehicle (UAV) based methods for measuring crop morphology and specifically height of field-based wheat plants within crop phenotyping experiments. The methods are focussed towards the development of improved temporal and spatial resolution data related to plant height, as well as to enhance throughput of measurements. The method is based on standard RGB imagery collected from a UAV mounted Commercial 'Off the Shelf' (COTS) camera, and Structure from Motion (SfM) photogrammetry to process the imagery into 3-dimensional reconstructions. Review of phenotyping plant height, as well as UAV-based SfM photogrammetry can be found in Chapter 2, Section 2.3.2. The work undertaken for this chapter culminated in a published research article in the international journal *Remote Sensing*, for which primary authorship, method development, data processing and analysis was performed by the thesis author. M. Castle assisted in data collection and processing; A. Riche assisted in method development, data collection and manuscript editing; A. Michalski assisted in data processing and analysis; M. Wooster and M. Hawkesford assisted in method development and editing of manuscript. The article is included within this chapter following the requirements of King's College London thesis rules.

In addition to the published article, further work was carried out investigating methods for normalising the digital surface models. This additional work was not fully included within the final article but is provided in Section 3.3 of this chapter.

3.2 Published Article

remote sensing

MDPI

Article

High Throughput Field Phenotyping of Wheat Plant Height and Growth Rate in Field Plot Trials Using UAV Based Remote Sensing

Fenner H. Holman [1,*], Andrew B. Riche [2], Adam Michalski [2], March Castle [2], Martin J. Wooster [1,3] and Malcolm J. Hawkesford [2,*]

1 Department of Geography, King's College London, London WC2R 2LS, UK; martin.wooster@kcl.ac.uk
2 Rothamsted Research, Harpenden, Hertfordshire AL5 2JQ, UK; andrew.riche@rothamsted.ac.uk (A.B.R.); adam.michalski@rothamsted.ac.uk (A.M.); march.castle@rothamsted.ac.uk (M.C.)
3 National Centre for Earth Observation (NCEO), Leicester LE1 7RH, UK
* Correspondence: fenner.holman@kcl.ac.uk (F.H.H.); malcolm.hawkesford@rothamsted.ac.uk (M.J.H.)

Academic Editors: Clement Atzberger and Prasad S. Thenkabail
Received: 20 September 2016; Accepted: 14 December 2016; Published: 18 December 2016

Abstract: There is a growing need to increase global crop yields, whilst minimising use of resources such as land, fertilisers and water. Agricultural researchers use ground-based observations to identify, select and develop crops with favourable genotypes and phenotypes; however, the ability to collect rapid, high quality and high volume phenotypic data in open fields is restricting this. This study develops and assesses a method for deriving crop height and growth rate rapidly from multi-temporal, very high spatial resolution (1 cm/pixel), 3D digital surface models of crop field trials produced via Structure from Motion (SfM) photogrammetry using aerial imagery collected through repeated campaigns flying an Unmanned Aerial Vehicle (UAV) with a mounted Red Green Blue (RGB) camera. We compare UAV SfM modelled crop heights to those derived from terrestrial laser scanner (TLS) and to the standard field measurement of crop height conducted using a 2 m rule. The most accurate UAV-derived surface model and the TLS both achieve a Root Mean Squared Error (RMSE) of 0.03 m compared to the existing manual 2 m rule method. The optimised UAV method was then applied to the growing season of a winter wheat field phenotyping experiment containing 25 different varieties grown in 27 m^2 plots and subject to four different nitrogen fertiliser treatments. Accuracy assessments at different stages of crop growth produced consistently low RMSE values (0.07, 0.02 and 0.03 m for May, June and July, respectively), enabling crop growth rate to be derived from differencing of the multi-temporal surface models. We find growth rates range from −13 mm/day to 17 mm/day. Our results clearly display the impact of variable nitrogen fertiliser rates on crop growth. Digital surface models produced provide a novel spatial mapping of crop height variation both at the field scale and also within individual plots. This study proves UAV based SfM has the potential to become a new standard for high-throughput phenotyping of in-field crop heights.

Keywords: Unmanned Aerial Vehicle; Structure from Motion; photogrammetry; crop height; phenotyping

1. Introduction

1.1. Global Food and Agriculture

There is a need to double output of agricultural systems by 2050 to meet the increasing food demands from a growing global population; forecasted to peak at 9.22 billion by 2050 [1,2]. Wheat continues to provide the sole vital daily nutrition for 35% of the world's population [3] and is therefore a key focus of yield improvement research.

Projects such as the 20:20 Wheat® project at Rothamsted Research, aim to provide the knowledge and tools to increase the UK's wheat yield potential to 20 tonnes of wheat per hectare within 20 years [4], whilst combating the new challenges agriculture is facing such as climate change. These projects focus on developing new improved varieties through methods such as selective breeding.

Key to this is the monitoring of different varieties for favourable genotypes and phenotypes, by providing a continuous stream of data documenting the course of the crops development and responses to environmental conditions [5,6].

1.2. Phenotyping

Phenotyping of crops involves the measurement and assessment of physical observable characteristics [7]. Current phenotyping techniques particularly the capacity to collect quality repeatable phenotypic data in field representative growing conditions is a bottleneck for further advancements in knowledge and development of crop varieties and yield gains [8].

Height may be a useful indicator of yield, carbohydrate storage capacity and susceptibility to lodging [9,10] as well as being an essential parameter for site-specific management practices [11]. Monitoring crop height during development stages is a reflection of cultivar and growing conditions. Crop development stages are often defined by the Zadoks Scale [12,13], and in terms of crop growth and height changes the key period of growth in UK grown wheat occurs between the start of stem elongation in early April, stage GS30, and anthesis in mid-June, stage GS61. Anthesis, or flowering, is the point at which crop height is considered to be at maximum [14]. Whilst exact timings of specific development stages will vary between cultivars, it is an important that any method of measuring crop height is able to accurately measure height during all stages between GS30 and GS61 where vegetative structure can vary.

1.3. Measuring Height

Crop height is classified as the shortest distance between the upper boundary of the main photosynthetic tissues on a plant and the ground level [15,16]. Most commonly height data is collected with a measuring rule [10] which although simple, is both laborious, inefficient and can introduce a level of subjectivity into data collected. Applying this method over large trial fields, totalling upwards of 1000 plots, limits the repeatability of this method.

There is a need for rapid, precise, continuous and in-season acquisition of this data [17] in order to better understand external, environmental influences throughout the crops development cycle. Current methods are not sufficient to meet this need, in particular for use in crop trials where the number of measurements required is large and as such development of new technologies and methods is needed.

Within this paper, we introduce and investigate quantitatively the method of Structure-from-Motion (SfM) photogrammetry using high resolution Unmanned Aerial Vehicle (UAV) imagery to accurately model crop trials, from which generation of crop heights can be calculated.

1.4. UAVs in Research

Unmanned Aerial Vehicles (UAVs), also referred to as Unmanned Aerial Systems (UAS), are a growing technology that is rapidly gaining popularity in both the public and scientific communities. UAVs offer a customisable aerial platform from which a variety of sensors can be mounted and flown to collect aerial imagery with very high spatial and temporal resolutions. Advancements in the accuracy, economic efficiency and miniaturisation of many technologies including GPS and computer processors has pushed UAV systems into a cost effective, innovative remote sensing platform.

Of most significance for research applications is the gap which this technology fills in the remote sensing domain. UAVs overcome the restrictions of resolution and cost that often hamper the use of satellite and airborne remote sensing respectively. The wide variety of sensors which can be

mounted and flown over a predetermined area, means an almost endless list of possible applications for this technology.

A review of the literature highlights the wide range of applications UAVs and mounted sensors have been utilised for. For environmental monitoring, examples include modelling of the temporal changes in landslide dynamics [18]; 3D reconstruction of fluvial topography of UK streams [19]; monitoring of rangeland [20,21] and conservation applications such as surveying of habitats and animal numbers [22]. Alternatively, UAVs have been applied in documenting of archaeological sites, where the rapid collection of very high-resolution 3D reconstructions from UAV based methods has been proven useful [23]. In terms of agriculture, UAVs have been used for the monitoring of water status and drought stresses in fruit trees [24]; additionally, collecting multispectral and hyperspectral imagery for use in spectral indices [25] and even chlorophyll fluorescence [26].

1.5. Structure-from-Motion and Crop Modelling

SfM photogrammetry is an emerging method that offers high resolution 3D topographic or structural reconstruction from overlapping imagery [27,28]. Key to SfM methods is the ability to calculate camera position, orientation and scene geometry purely from the set of overlapping images provided, offering a simple processing workflow compared to alternative photogrammetry techniques [29,30]. The simple and easy workflow of SfM for generating 3D digital reconstructions of landscapes or scenes makes it applicable for use a variety of research fields as well as in agricultural crop monitoring.

A number of studies have applied UAV based SfM to modelling crop heights and/or growth over the growing season. Bendig et al. [31,32] applied UAV based SfM methods to model and calculate heights of barley and rice crops in the field. Results showed room for development in the methods and technologies used; comparisons with ground measured heights of barley produced regression coefficients values of 0.55, 0.22 and 0.71 on three different dates. The authors highlight issues with GPS accuracy as a main source of crop height error, as well as suggesting using higher quality cameras for image collection. Ruiz et al. [33] also found the SfM algorithms suffer from errors present in GPS datasets. Ground-based Control Points (GCP) located within the scene are recommended as best-practice for spatial accuracy and minimisation of model error. Turner et al. [34] found GCPs offered a significant improvement in spatial accuracy compared to directly georeferenced imagery using the UAVs on-board GPS. Aasen et al. [35] used hyperspectral imagery collected from a UAV for vegetation monitoring including height. Results from this study were found to be comparable with others (R^2 = 0.7) with a consistent underestimation of plant height by 0.19 m. The authors highlight the fact that the rule has its own issues when it comes to accuracy and therefore may not offer the best source of ground validation. However, as the standard procedure currently in practice, rule measurements still hold a level of importance when proving the validity of UAV based SfM methods.

Image resolution is particularly important for early season crop modelling where the lack of closed canopies impacts on "Crop Surface Model (CSM)" production [36]. Higher resolutions offer a good level of improvement in model accuracy. Willkomm et al. [37] generated models with spatial resolutions of 0.5 cm, with height reconstructions comparable to the other studies discussed (R^2 = 0.75) and point out a tendency of the UAV models to underestimate heights. Interestingly the authors highlight the inability to isolate singular plant details within the model due plant movement during acquisition, likely due to wind. There is a potential that this crop movement, caused by windy conditions, and subsequent loss of some plant structures may be the cause of the underestimation of the model.

The review of relevant literature has shown UAV based SFM is applicable to modelling of plant heights however accuracy of models achieved in these studies highlights improvements are needed. It is clear that a proof of concept has been achieved, however the development of this concept into a working procedure applicable to real world agricultural research is now the next step.

The aim of this study is to produce a highly accurate and repeatable method for collecting crop heights from UAV based Structure from Motion Photogrammetry models as an alternative to current manual rule based phenotyping methods.

The research will involve accuracy assessments and comparisons with alternative technologies, method development and full season testing of the SfM technique. A full quantitative assessment will address the following research questions:

1. How accurate are the models and crop heights generated, compared to the rule method; the existing industry standard?
2. How replicable is the method over the development cycle of wheat crops, particularly between stages GS30 and GS61 (Zadoks Scale); can growth be monitored?
3. Can these methods be applied in crop research and does it offer a better quality of data compared to the rule method?

2. Materials and Methods

2.1. Field Site

The experiment was performed at Rothamsted Research, UK (51°48′34.56″N, 0°21′22.68″W) as a contribution to the 20:20 Wheat Project, where field trials of a wide range of wheat varieties are ongoing [4]. This study used data collected over the Defra-funded WGIN (Wheat Genetic Improvement Network) Diversity Field Experiment conducted at Rothamsted, which is testing the influence of four different nitrogen fertiliser treatments (0, 100, 200, 350 kg N ha^{-1}) on 25 varieties of wheat, with each treatment having three repetitions [38]. Each repetition consists of a plot of wheat comprising a 9 m × 3 m "main plot", and a 2.5 m × 3 m "sampling plot", used for non-destructive and destructive sampling respectively; all plots are separated by 0.5 m uncropped buffer zones and each treatment strip is separated by 5 m buffers that mostly comprise vehicle tracks. The order of varieties is randomised in each strip. Figure 1 shows an example of one strip containing the 25 wheat varieties subject to one of the four nitrogen treatments. The work used data collected over two growing seasons of the diversity experiment (2014 and 2015), with crop rotation resulting in the location of the plots changing between the years but the experimental set-up remained as shown in Figure 1. The 2014 growing season was used for the pilot project, this included collection and comparison of terrestrial laser scans and UAV SfM photogrammetry against the existing rule method in order to compare methods and determine the performance of the UAV method in crop height estimation. The 2015 main study used the UAV method to derive crop height and growth rate over the entire field as well as to confirm the accuracy levels of height estimation over wider areas and more wheat varieties than the pilot project had included.

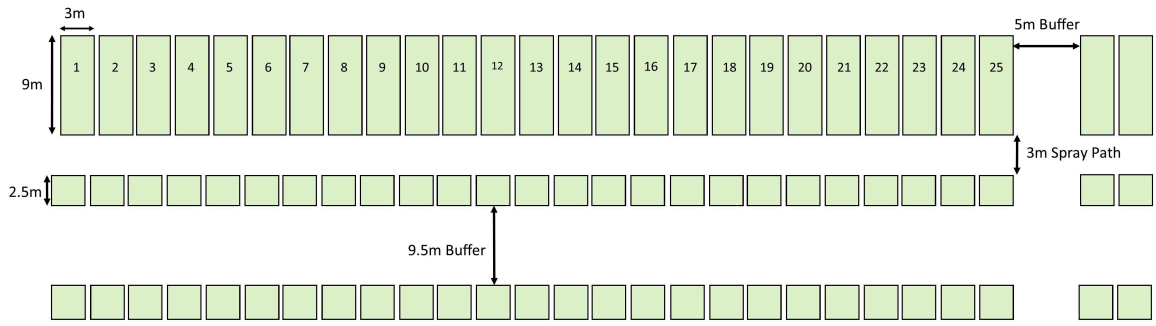

Figure 1. Layout of a single diversity experiment field planting strip, consisting of 25 plots each growing a different wheat cultivar. This layout was repeated 12 times, 3 times for each of the four different nitrogen treatments, and so the field contained 300 plots in total (with each plot consisting of a larger 9 m × 3 m "main plot", and a 2.5 m × 3 m "sampling plot").

For simplicity, N1, N2, N3 and N4 will be used herein to refer to the four different nitrogen fertiliser treatments of 0, 100, 200, 350 kg N ha^{-1} as detailed in Table 1. The 25 different wheat varieties are listed in Table 2 and will from hereon be referred to by the initials codes shown.

Table 1. Details of the four nitrogen fertiliser treatments applied to the diversity field experiment in 2015.

Treatment Code	Total Nitrogen Application (kg N ha^{-1})	Application Dates	Amount of Nitrogen Applied (kg N ha^{-1})
N1	0	-	0
		-	0
		-	0
N2	100	16 March 2015	50
		1 April 2015	50
		30 April 2015	0
N3	200	16 March 2015	50
		1 April 2015	100
		30 April 2015	50
N4	350	16 March 2015	50
		1 April 2015	250
		30 April 2015	50

Table 2. Codes for each cultivar of wheat crop grown in the diversity field experiment.

Cultivar	Code
Avalon	AV
Bonham	BO
Cadenza	CA
Claire	CL
Cocoon	CC
Conqueror	CN
Cordiale	CO
Crusoe	CR
Evoke	EV
Gallant	GA
Hereford	HF
Hereward	HE
Hystar	HY
Istabraq	IS
Malacca	MA
Maris Widgeon	MW
Mercia	ME
Paragon	PA
Riband	RI
Robigus	RO
Skyfall	SY
Stigg	ST
Soissons	SS
Solstice	SL
Xi19	XI

2.2. Pilot Project (2014)

A pilot project in 2014 focused on providing an initial accuracy assessment of UAV based SfM approach to crop height determination, as compared to the alternative method of terrestrial laser scanning (LiDAR). Both were compared to the ground based method currently employed on the diversity experiment and which is standard practice in field phenotyping, i.e., manual measurement using a 2 m rule of five random stems from which the mean plot height is determined. All data were

collected 14–18 July 2014 post-anthesis when the crop were undergoing senescence, so no further crop growth was expected.

2.2.1. UAV SfM Method

To provide data for the UAV SfM approach, a Cinestar Octocopter UAV with a DJI Wookong M flight controller carrying a Sony NEX 7 24.3 megapixel camera was flown over the diversity experiment field at two altitudes (90 m and 40 m), using fixed camera settings and a pre-programmed flight path (Figure 2), and using DJI ground station software. The flight path was designed in order to ensure overlapping imagery of at least 60% side overlap and 80% forward overlap; these values were decided on after consultation of existing literature [32,39,40], as well as the Agisoft Photoscan Software manual [41] (Table 3).

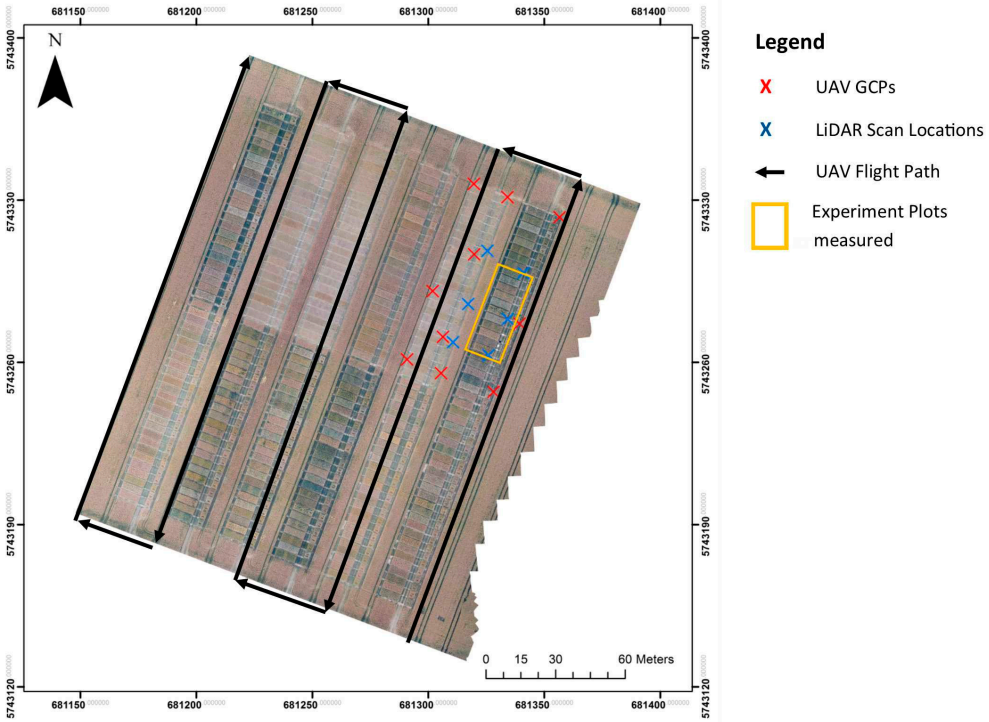

Figure 2. Orthomosaic of the 2014 field, displaying the location of Ground Control Points (GCP), LiDAR scan targets, the UAV flight path and the 10 experimental plots measured for this study. Coordinates are displayed in WGS 1984 Coordinate System.

Table 3. Camera settings and image parameters used for the two data collection flights made during 2014.

Altitude (m)	Aperture	Focal Length	ISO	Shutter Speed	Image Resolution (cm/Pixel)	Image Format
90	f/5.6	14	100	Auto	1.4	JPEG
40	f/4.5	14	100	Auto	0.7	JPEG

The pilot project used only 10 plots of the full diversity field experiment and a set of Ground Control Points (GCPs) consisting of ten 50 cm × 50 cm numbered acrylic panels which were placed evenly across this target area prior to all data collection (Figure 2). The GCP locations were recorded using a differential Global Positioning System (dGPS, Trimble Geo 7, Sunnyvale, CA, USA) to provide sub-centimetre locational precision. Identification of the GCPs in the imagery later allowed for the re-projection of the image mosaic and 3D models into a real-world coordinate system.

Processing of the individual images into an image orthomosaic and Digital Surface Model (DSM) was performed in Agisoft Photoscan Pro (version 1.2.4) [41] (Figure 3), with different models generated using different processing settings and different subsets of the full image database, such as altitude, in order to assess the impact of these on crop height retrieval accuracy. Table 4 provides a summary of the parameters used for the models generated.

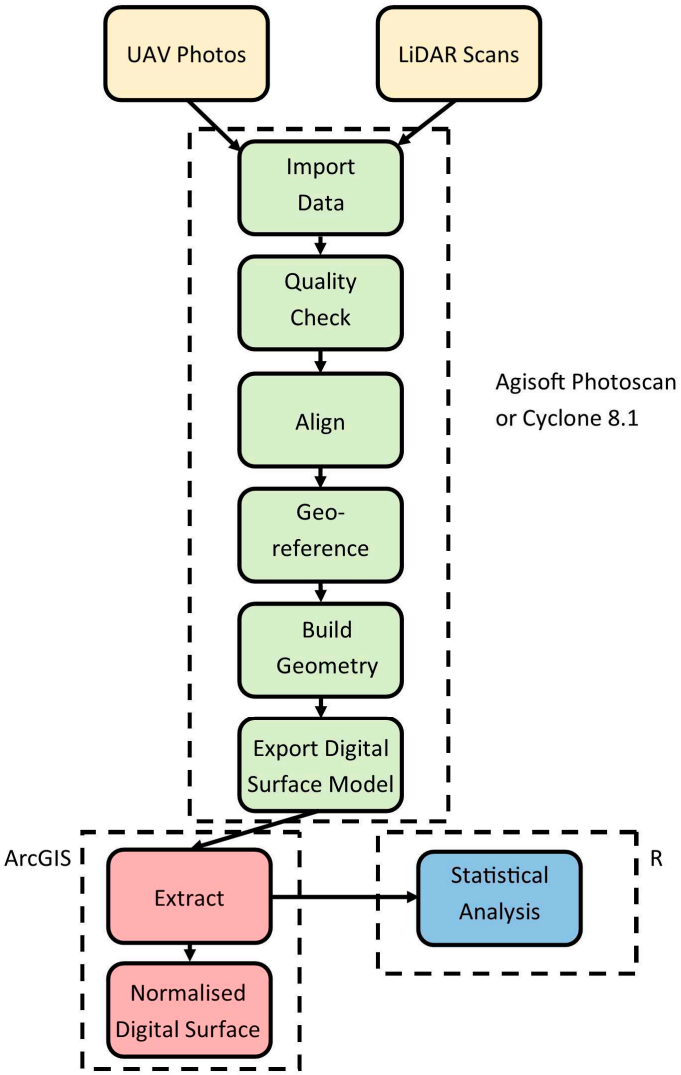

Figure 3. Workflow for processing the collected UAV imagery and Terrestrial LiDAR point clouds into the normalised Digital Surface Model.

Table 4. Parameters of the UAV flights and Agisoft Photoscan processing used in the 2014 Pilot Study. Model resolution is the reported model resolution provide by Agisoft Photoscan.

Model	Altitude (m)	Alignment Accuracy	Dense Cloud Quality	Depth Filtering	Model Resolution (cm/ Pixel)	Model Reference
1	90	High	Medium	Aggressive	2.0	UAV90A
2	90 and 40 combined	High	Medium	Aggressive	1.7	UAV90+40A
3	40	High	Medium	Aggressive	1.0	UAV40A
4	40	High	Medium	Mild	1.0	UAV40M

Review of relevant literature pointed to some disparity in the terminology used to describe the different computed 3D models created in SfM processing. One such example is the use of Crop

Surface Model (CSM), for which Bendig et al. [31,32] describes as the absolute height of crop canopies. Geipel et al. [36], in comparison define a CSM as the difference between the Digital Terrain Model (DTM) and DEM. To prevent confusion and ambiguity, terminology in this article will use definitions as set out by Granshaw [42]. The three model types created within this study, as shown in Figure 4, are Digital Elevation Models (DEM), Digital Surface Models (DSM) and normalised Digital Surface Models (nDSM), definitions are provided in Table 5. It should be noted that the final output from Agisoft Photoscan is what it calls a DEM, this is technically a DSM as it includes both the scene features and underlying topography captured in the imagery although application of depth filtering in processing may remove some top surface features which means use of depth filtering should be acknowledged when assuming a model is a DSM.

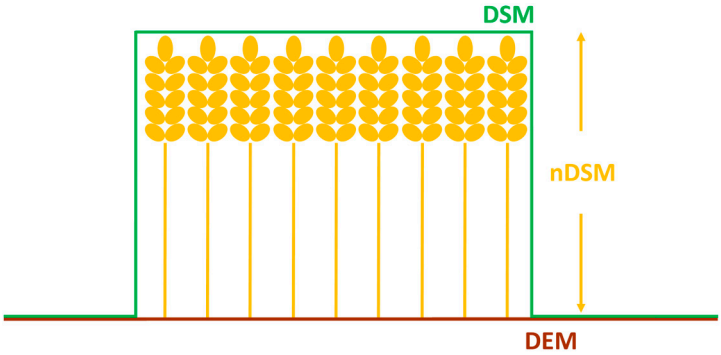

Figure 4. Visual representation of the Digital Surface Model (DSM), normalised Digital Surface Model (nDSM) and Digital Elevation Model (DEM).

Table 5. Definitions of types of models generated in this study, based on definitions offered by Granshaw [42].

Model Name	Abbreviation	Description
Digital Elevation Model	DEM	Model of the underlying field topography without features.
Digital Surface Model	DSM	Combined model of the underlying topography and field features e.g., crops.
Normalised Digital Surface Model	nDSM	Model of field features only (crop heights).

A key step in the production of a final nDSM is the removal of underlying field topography, performed using Equation (1), in order to isolate the pure crop heights.

$$\text{nDSM} = \text{DSM} - \text{DEM} \quad (1)$$

where DSM is the final output model from Agisoft Photoscan Pro and DEM is the underlying field topography, created through extraction of bare ground heights located in the unplanted buffer zones between the plots throughout the field. These bare ground heights were then extrapolated into a DEM. Investigation was also carried out to assess a potentially more universal method for use where large buffer zones are not included in the field layout, such as those in commercial fields. This alternative method involved generating a DEM from the field when no crops were present in order to measure the bare ground.

2.2.2. Terrestrial LiDAR Method

Alongside the UAV data, a Leica HDS6100 Terrestrial LiDAR was used to collect LiDAR point clouds of nine plots, this system providing a very high 5 mm measurement precision but with the disadvantage of a relatively time-consuming measurement procedure compared to the UAV when multiple scans from different directions are required. Here we used six scans from different positions

around the plots (Figure 2) to ensure both a highly dense point cloud and minimal shadowing. Scanner settings are detailed in Table 6, with six Leica "Tip and Turn" targets placed within the scan area whose location was also measured with dGPS and whose record in the scans were used for inter-scan registration and point cloud geo-referencing in the Leica Cyclone 8.1 software [43]. Point clouds were generated from first return pulses and after registration and geo-location, were analysed and crop heights extracted (Figure 3).

Table 6. LiDAR settings used during 2014 study.

Scanner Parameter	Settings Used
Laser Poser	High
Scan Resolution	Super High
Vertical Extent	25°–180°
Horizontal Extent	Manually selected depending on scan.

2.3. Main Study (2015)

The objective of the Main study was to apply the UAV based crop height retrieval method developed in the 2014 Pilot at the full field scale and over the whole growing season—using it to assess the crop growth rate of the different varieties and nitrogen fertiliser application levels of the diversity experiment. During this study, ground-based (rule) measures of the height of all 300 plots were collected on two occasions (18 June 2015 and 17 July 2015) for comparison to the UAV-derived crop height measures; a sub sample of 100 plots was also measured by rule on 22 May 2015.

UAV SfM Method

Image collection flights were conducted over the full diversity experiment field on a regular basis, weather and equipment permitting between March and July 2015. Flight altitude was kept at 45 m on the basis of the findings of the pilot project, and the same flight plan used each time (Figure 5). Camera settings were kept as consistent as possible, though changes were needed occasionally to allow for changing illumination conditions as well as a change in lens due to damage (Table 7). These changes had not detrimental effect on final model resolutions. Between 21 March and 21 April 2015 no flights were conducted due to technical problems with the UAV. Thirty two GCPs were located in the field (Figure 5), evenly spread throughout and with their location measured with dGPS as before. Images were processed using Agisoft Photoscan under the same workflow as Figure 3. There were two changes to processing settings however; investigation of high and ultra-high dense cloud quality settings found DSM quality could be increased when using high quality but ultra-high introduced very high levels of noise, as such all models in the 2015 study were processed with the high setting. The second change was due to updates to the Photoscan software which allowed for depth filtering to be disabled on all models used for monitoring growth. This was done to reduce the smoothing of features such as the tops of the wheat crops in the models. Table 8 details the key model parameters.

Table 7. Camera settings and image parameters for each flight used in the 2015 study.

Date	Focal Length	Aperture	ISO	Shutter Speed	Image Resolution (cm/Pixel)
19 March 2015	20	f/4	Auto	1/1000	0.9
2 April 2015	18	f/4	Auto	1/1600	0.9
14 April 2015	18	f/4	Auto	1/1600	0.9
21 April 2015	15	f/4	Auto	1/1600	0.9
21 May 2015	17	f/4	Auto	1/1600	0.9
4 June 2015	18	f/4	Auto	1/1600	0.9
17 June 2015	20	f/4	Auto	1/1600	0.9
26 June 2015	20	f/4	Auto	1/1600	0.9
6 July 2015	20	f/4	Auto	1/1600	0.9
20 July 2015	20	f/4	Auto	1/1000	0.9

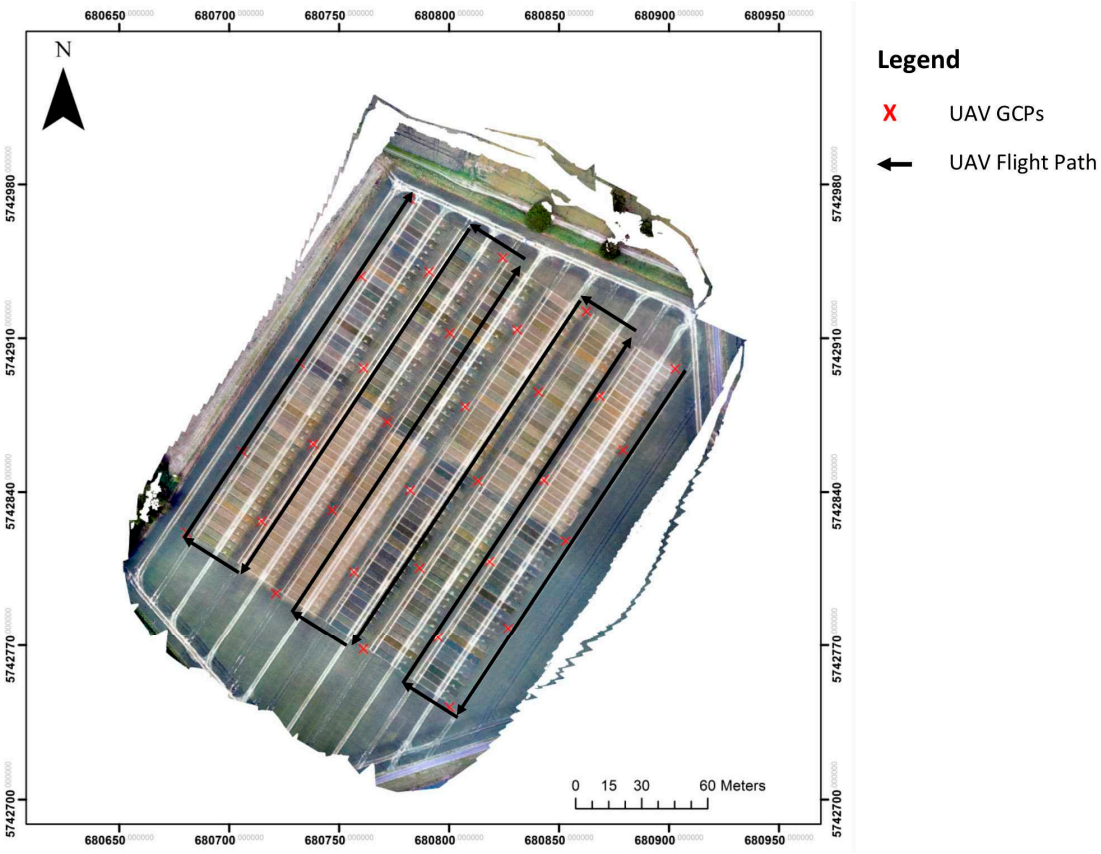

Figure 5. Orthomosaic of the 2015 field, displaying the location of Ground Control Points (GCP) and the UAV flight path used. Coordinates are displayed in WGS 1984 Coordinate System.

Table 8. Agisoft processing parameters used in the 2015 study. The model resolution provided is the resolution reported by Agisoft Photoscan.

Alignment Accuracy	Dense Cloud Quality	Depth Filtering	Model Resolution (cm/Pixel)
High	High	Disabled	1

As a potential alternative to using the heights of the buffer zones as a means to create a bare ground DEM over this much larger area than that used in the 2014 Pilot study, flights were also conducted in 2015 after harvest (but before ploughing) on 25 September 2015 to enable a bare ground DEM to be derived using imagery of the non-cropped field. As this was post-harvest some crop stubble was still remaining in the field.

After creating and normalising the models for field topography, a plot map was created before crop heights for each plot were extracted and mean heights calculated. Plot borders were created in ArcGIS using the experimental layout dimensions (Figure 1). Some actual field plots did not fit the layout plan exactly and so were shifted and rotated manually as necessary to the right position. To prevent plot edge effect influencing calculations, plots were shrunk by 50 cm on each edge using an ArcGIS buffer tool (Figure 6). This value (50 cm) was arbitrarily chosen for this experiment. This approach will require automation in the future for experiments consisting of thousands of plots, where the outlining of individual plots manually is very time consuming.

Initial analyses highlighted an issue with some plots displaying mean heights much lower than the corresponding ground-based measures taken with the measuring rule. Examination of the original imagery indicated that, similar to the findings of [36], a lack of canopy development and stem population density in the unfertilised (N1) plots compared to the fertilised plots was the cause.

The reduced canopy coverage increased the proportion of pixels showing either lower level plant structures or even patches of bare ground between plants (Figure 7). In order to remove this effect, all future mean plot heights were generated from the 99th percentile, rather than the total mean, such that the top height of the plants were reported, as is the case with the current ground-based method. This method was chosen over standard mean or median as it was best at isolating the top photosynthetic tissue of each plant, and avoiding occasional contaminating individual rogue or anomalous plants, which is required in order to obtain true plant height as defined in Section 1.3.

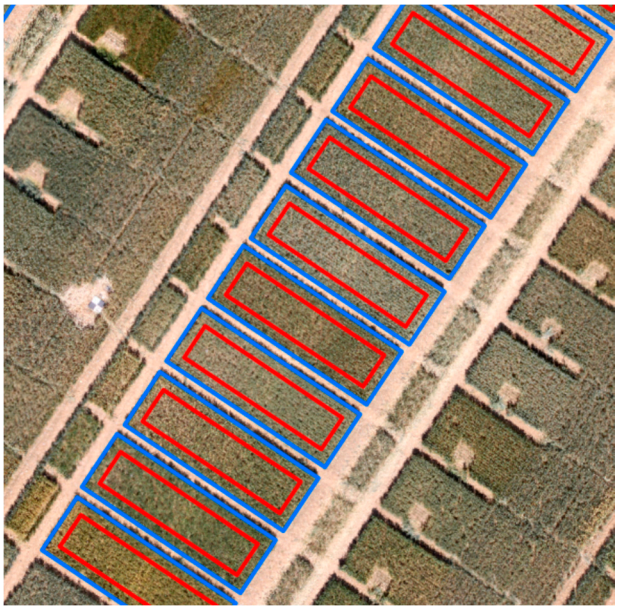

Figure 6. Plot borders before (**blue**) and after (**red**) buffering isolating each plot within the field in order to extract heights.

(**a**) (**b**)

Figure 7. Imagery collected by the UAV flying at 45 m height of an unfertilised (N1) treatment plot (**a**) compared to an N4 (350 kg·ha^{-1} fertiliser application) treatment plot (**b**). Mercia wheat cultivar shown in both cases.

3. Results

3.1. Pilot Project Results

Results from the 2014 Pilot study are focused on a comparison of the different UAV-derived and LiDAR-derived nDSMs with those from the standard ground-based method (Figure 8). All linear best fits between the UAV and LiDAR models and the ground-based measures heights show intercepts close to 0, but with slopes varying from close to 1.0 (LiDAR and UAV40M) to 0.73 (UAV9040A). The LiDAR and lower altitude UAV-derived results also show the highest regression coefficients with the ground-based data (R^2 =0.97 for LiDAR and R^2 = 0.99 for UAV40M). Root Mean Squared Error

(RMSE) statistics indicate both these methods are providing crop height retrievals to within around 3 cm of the ground-based measures. However, there are some biases shown, with all the UAV-derived nDSMs underestimating height to some degree (by 24 mm to 158 mm), with the lowest altitude imagery showing the lowest bias. LiDAR biases are by comparison only 4 mm.

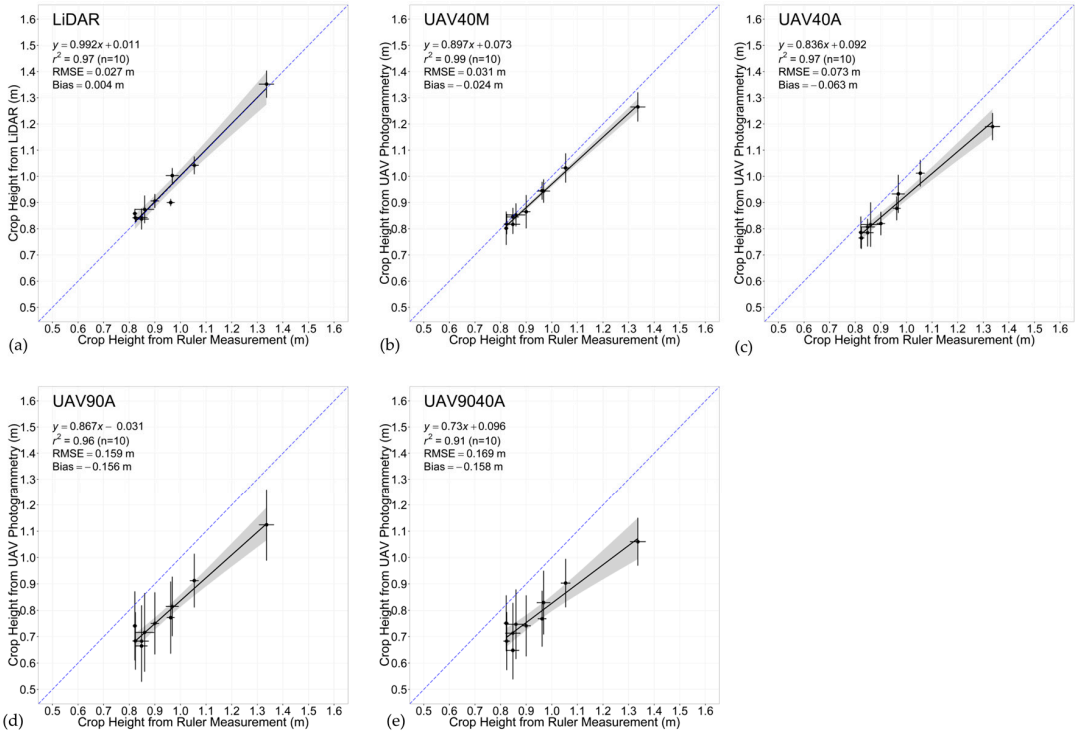

Figure 8. Comparison of crop heights derived from (**a**) LiDAR and (**b**–**e**) the various UAV-based approaches detailed in Table 4 to those from the ground-based (rule) method for each of the ten plots measured during the 2014 Pilot study. Blue dashed line indicates 1:1 slope.

The results show both the LiDAR and UAV based SfM techniques are fully capable of recreating accurate 3D models and subsequent crop heights of wheat crop trials in the field.

For the UAV results, lower altitudes produced significantly more accurate crop heights, due to the higher image ground resolution achieved at the lower altitude. There was a clear advantage to using "mild depth filtering" during processing in order to achieve greater crop height accuracy, likely due to the reduction in "smoothing" of the model allowing for more of the small plant features of interest to remain during the depth filtering step of model processing.

3.2. Main Study Results

3.2.1. "Bare Ground" DEM Selection

Due to its importance in producing the final nDSMs, analysis of two methods for producing the bare ground DEMs was performed. nDSMs were produced using the same "buffer zone height" approach used in the 2014 Pilot, and the alternative "post-harvest DEM" based on a bare ground DEM derived from post-harvest imagery. The resulting maps of crop height were then compared to the corresponding ground-based measures, with both sets of results showing R^2 values of >0.93 (Figure 9). However, the RMSE statistics indicate that use of the DEM based on the buffer zone heights produces crop heights with reduced levels of error compared to that based on the post-harvest imagery. This is likely due to any bias present in the "buffer zone" DEM is also present in the model and crop heights being taken at the same time, therefore this bias is cancelled out, whereas in the case of the post-harvest DEM, any bias present, including the potential impact of the post-harvest stubble will not be cancelled

out when plant heights are extracted. All subsequent nDSMs in this study were generated using the "buffer zone" DEM approach.

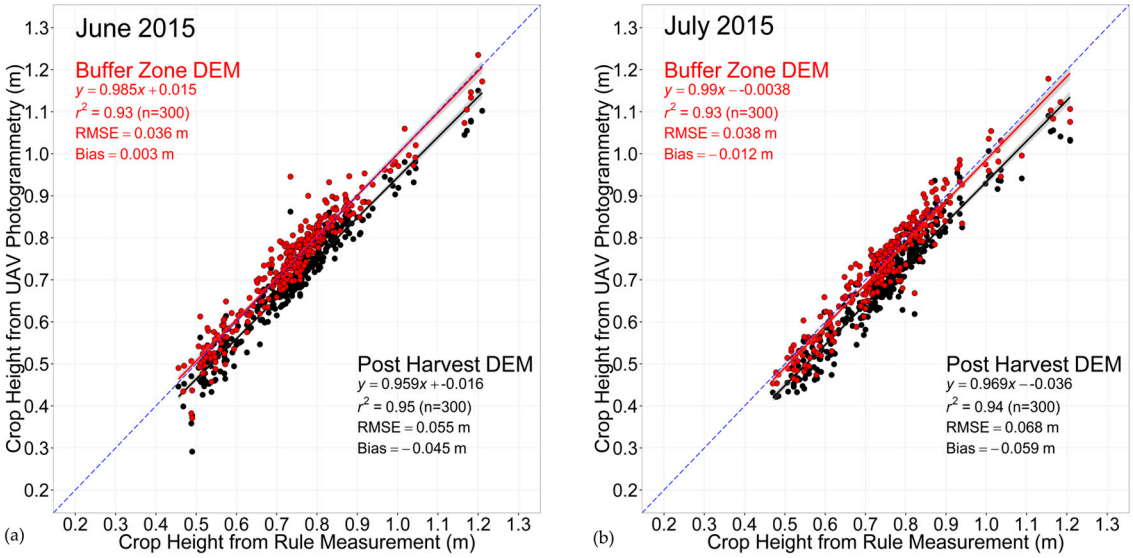

Figure 9. Comparison of "buffer zone" (**red**) and "post-harvest" (**black**) DEM generated crop heights for June (**a**) and July (**b**) 2015. The blue dashed line indicates a 1:1 slope.

3.2.2. Accuracy Assessments

In addition to the accuracy assessment conducted in the Pilot Study during the crop senescent stage, three further similar assessments were conducted in May, June and July of 2015 at different periods during the crop growing cycle (Figure 10). For these accuracy assessments, the mean height of the three replicates measured from the UAV models was compared to the rule measured mean heights.

The comparison between UAV-derived and ground-based crop heights shown in Figure 10 indicates consistently high levels of accuracy, most particularly in the June and July assessments. May aerial measurements show a much more significant underestimation of height compared to July, and June shows some very small overestimation bias (3 mm). The lower accuracy achieved in the May assessment is thought to be caused by the earlier development phase of the varieties where canopies were not fully complete, an influence discussed previously in Section 2.3. Comparison between nitrogen treatments (Table 9) shows the N1 treatment generally has lower accuracy levels, again likely due to the influence of reduced canopy development in these plots.

Table 9. Accuracy Assessment results of three different comparisons of rule measured and UAV measured heights. The results are grouped by the four nitrogen treatments applied within the diversity field experiment.

Model	Treatment	RMSE (m)	BIAS (m)	R2
May	N1 (0 kg·hectare^{-1})	0.094	−0.089	0.76 (n = 25)
	N2 (100 kg·hectare^{-1})	0.099	−0.096	0.85 (n = 25)
	N3 (200 kg·hectare^{-1})	0.063	−0.051	0.52 (n = 25)
	N4 (350 kg·hectare^{-1})	0.026	−0.02	0.91 (n = 25)
June	N1 (0 kg·hectare^{-1})	0.028	−0.007	0.83 (n = 25)
	N2 (100 kg·hectare^{-1})	0.015	0	0.97 (n = 25)
	N3 (200 kg·hectare^{-1})	0.020	0.007	0.99 (n = 25)
	N4 (350 kg·hectare^{-1})	0.024	0.013	0.97 (n = 25)
July	N1 (0 kg·hectare^{-1})	0.033	−0.026	0.89 (n = 25)
	N2 (100 kg·hectare^{-1})	0.022	−0.018	0.98 (n = 25)
	N3 (200 kg·hectare^{-1})	0.021	−0.009	0.98 (n = 25)
	N4 (350 kg·hectare^{-1})	0.020	0.007	0.96 (n = 25)

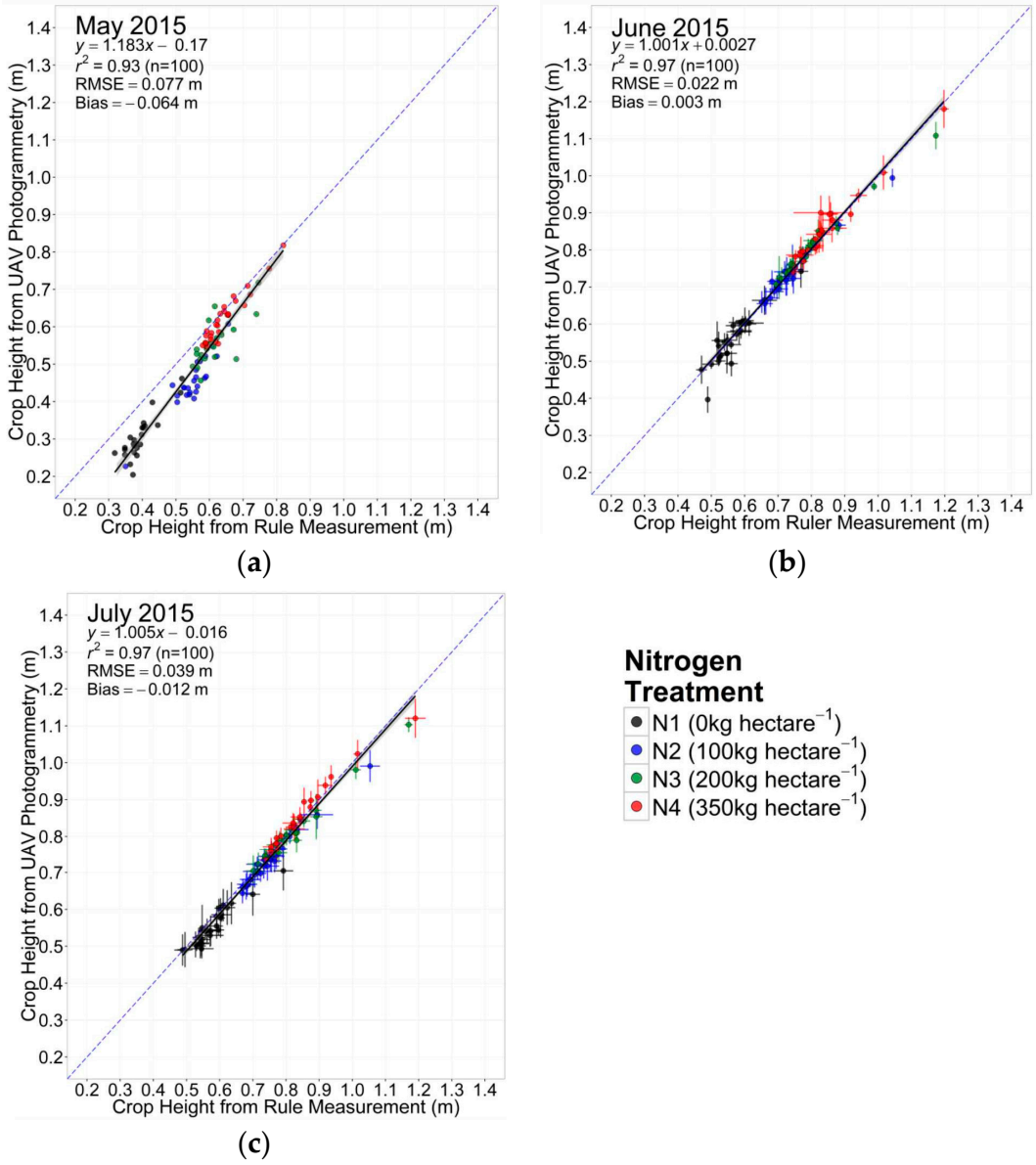

Figure 10. The 2015 accuracy assessments of UAV-derived mean crop heights made against standard ground-based rule measures performed as per Section 2.2). Accuracy assessment covered the four nitrogen treatments in: (**a**) May 2015 where the crops were still growing; and (**b**) June 2015; and (**c**) July 2015 when the crops were post anthesis and no longer expected to grow. The error bars represent the standard deviation of crop height between the three replicates from each cultivar and treatment. The blue dashed line indicates a 1:1 slope.

The replicate standard deviation shown by the error bars show a small amount of variation between replicates as would be expected in a field based experiment such as this, importantly this variation is displayed both in the heights measured by the rule and by the UAV model. The June assessment shows one plot has noticeably larger variation in the rule measured heights compared with the UAV heights for the same plot.

3.2.3. Plant Height

A key objective of the Main Study was to demonstrate the capability to assess crop growth and growth rates over the growing season.

All processed models show consistent patterns with the rule measured heights except for one error in plot 298, Maris Widgeon, in the 4 June 2016 nDSM. On examination this plot showed the presence of noise in the model located above plot 298 resulting in larger than expected heights for this plot. The sources of this noise is unknown and has not impacted on any other plots within this nDSM or other nDSMs. This erroneous plot was omitted from the height and growth rate calculations from this 4 June nDSM, using only data from the other two Maris Widgeon N1 plots.

Figure 11 shows the crop height measures obtained from imagery collected from March 2015 to July 2015, which indicate that the predominant growth in all varieties occurs from mid-April to mid-June. After this point some varieties show a levelling off in crop height suggesting no further growth occurs whilst other varieties and particularly crops grown in the N1 treatment show a decline in height after mid-June.

Overall, there is relatively little variation between the heights of replicates (as depicted by the error bars of Figure 11), similar to the levels seen in the accuracy assessments (Figure 10).

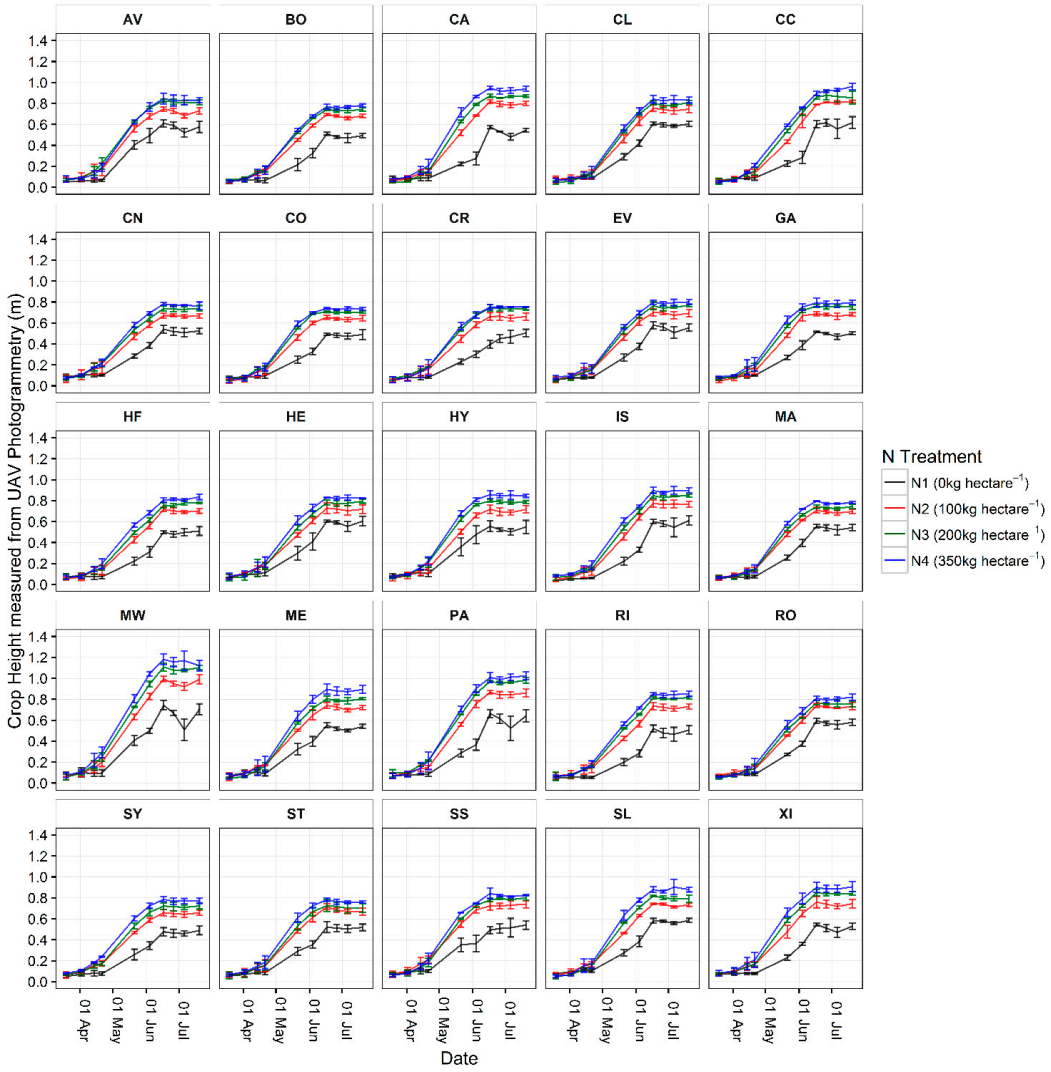

Figure 11. Changes in average crop height of the wheat varieties at the four N treatments. Variation in crop height between replicate plots is displayed by error bars. Crop varieties are referred to by their code as set out in Table 2 and all data are the means of three replicate plots, except Maris Widgeon N1 on the 4 June 2015 which is the mean of two replicates due to plot 298 being omitted because of noise in the model.

3.2.4. Growth Rate

Once the change in crop height was calculated with confidence, crop growth rate was assessed by dividing height change by the date interval to examine how growth rate changes between nitrogen treatments.

Figure 12 presents the growth rate of the different crop varieties and nitrogen treatments. As with crop height data shown in Figure 11, the replicate means and standard deviation of growth for each replicate set is show. Results show a common bell shaped pattern in growth rate between mid-April and mid-June, corresponding to the main period of crop height increase seen in Figure 11. This trend is less apparent in the N1 treatments, which tend to show lower growth rates until June where there is a spike in growth rates displayed by most varieties in the N1 treatments.

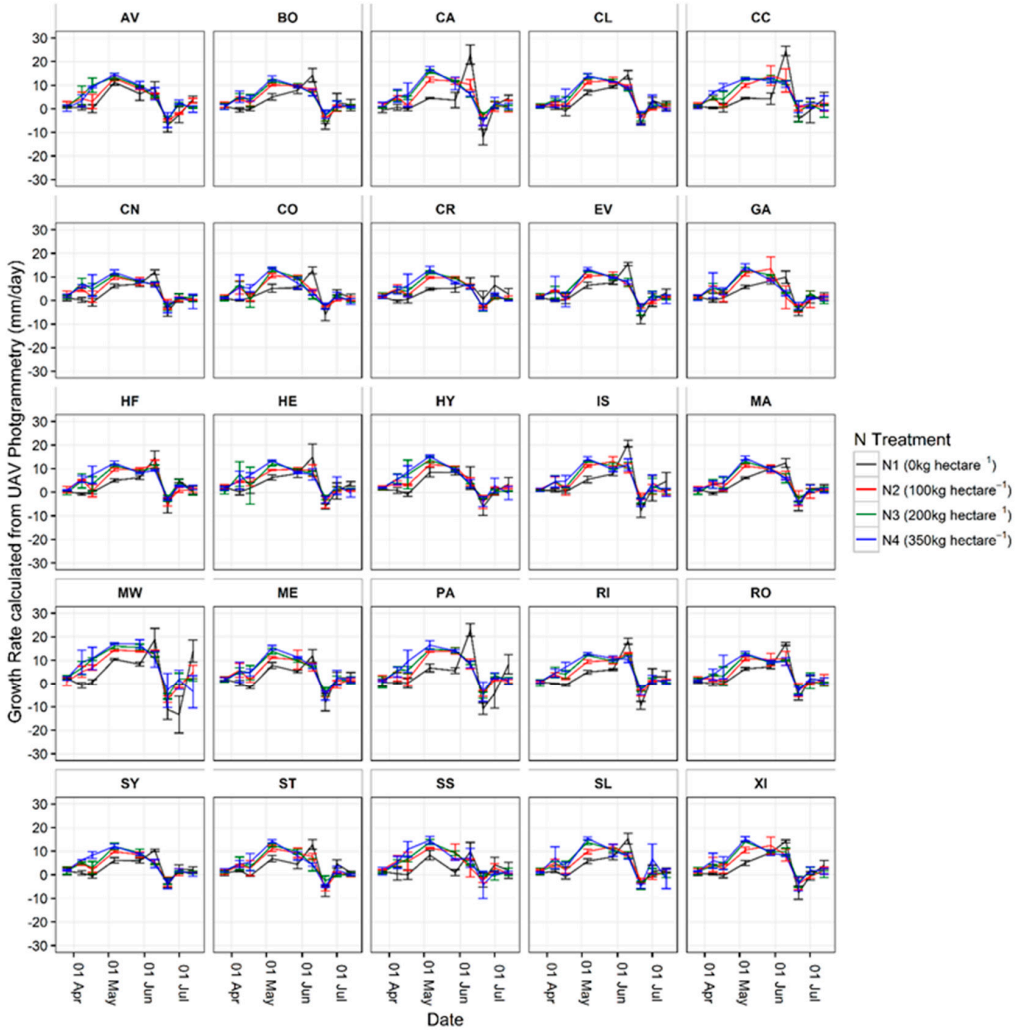

Figure 12. Mean growth rate inferred from height increase of wheat varieties subjected to different nitrogen fertiliser treatments. Growth rate is calculated from the data of Figure 12 and the time interval between the dates of each normalised digital surface model. Crop varieties are referred to by their code as set out in Table 2 and all data are the means of three replicate plots, except Maris Widgeon N1 on the 4 June 2015 which is the mean of two replicates due to plot 298 being omitted because of noise in the model.

All varieties and treatments show a drop into negative growth rates in mid-June. One possible explanation is due to the ears of the plants bending over, sometimes referred to as necking, as the plant matures. Another potential source of the negative growth rate is due to decreasing plant water content

from around 80% when the plants are fully green to <20% at harvest. This decline in water will lead to some level of cell shrinkage and subsequently decreasing plant height after mid-June. It is likely a mix of these two reasons explain the negative growth rate displayed by the crops in mid-June.

3.2.5. Spatial Mapping

The current standard method of using 5 point based rule measures of crop height for each plot offers very little in terms of measuring spatial variability, particularly within individual plots where growing conditions may cause variations in height. The nDSMs produced from the UAV method in this study not only offer measures of height but also visual maps of crop height variability on a field scale (Figure 13), comparing plots side by side throughout crop development. In addition, due to the very high resolution of the models (1cm), variability of crop heights within each plot can be assessed as shown by Figure 14 which even shows areas where the crops have been unable to grow leaving a hole within the plot. This is something unlikely to be noticed from ground based assessments of the fields, particularly when crops are more developed.

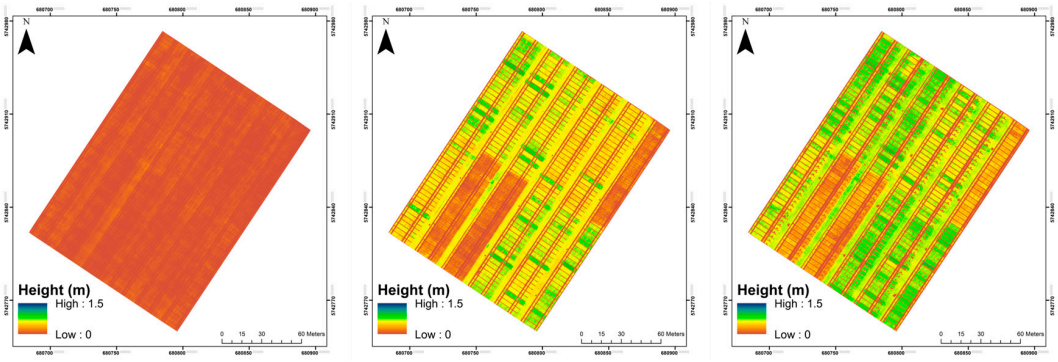

Figure 13. Normalised Digital Surface Models (nDSM) for three different wheat development stages captured on the 14 April 2015, 4 June 2015 and 6 July 2015 respectively. Clearly visible in the middle and right-hand figures are the 0 Kg·hectare^{-1} nitrogen treatment strips where crop height has been noticeably stunted compared to surrounding plots. Coordinates are displayed in WGS 1984 Coordinate System.

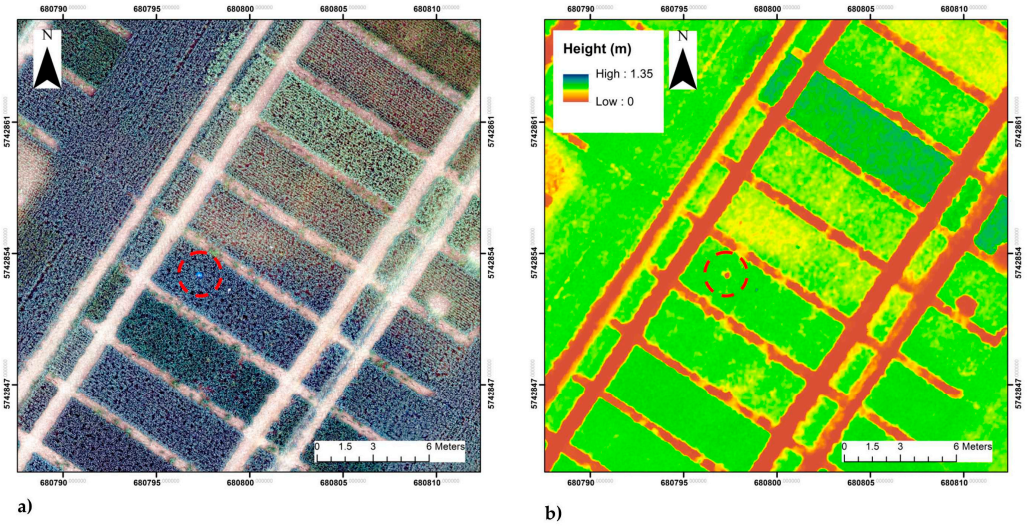

Figure 14. Side-by-side comparison of different cultivar plots in the N4 Treatment highlight the within-plot variability mapping achieved through the UAV based SfM technique. A hole (red circle) in the one of the plots is hard to make out in the orthomosaic (**a**) whilst being clearly visible in the nDSM (**b**). Data captured on 17 June 2015 and coordinates are displayed in WGS 1984 Coordinate System.

3.3. Nitrogen Application and Cultivar Responses

A key focus of this study was to produce a practical high throughput crop measurement system that provides valuable data to crop researchers for use in on-going crop development experiments. The experimental field used in this study was assessing how different wheat varieties were influenced by the quantity of nitrogen (N) fertiliser applied through the season.

The results in Figure 15 show the pattern of crop height increase through the season for each cultivar and the influence of N fertilization. Crop height increases rapidly at the beginning of April in a recognised wheat crop growth phase known as the start of stem elongation (GS30–GS61). The start and rate of stem elongation is earlier and at a greater rate, respectively at the higher N inputs. Maximal height is achieved in mid-June irrespective of the N-treatment but is noticeably lower at the zero N treatment (N1). Individual varieties are characterised by their mature height with Maris Widgeon being notable as a taller cultivar, reflecting the origin of this cultivar as being bred prior to the incorporation of dwarfing alleles. This tall cultivar is very susceptible to wind and rain and may easily lodge (fall over), reflected in the variable data obtained for this cultivar and the apparent decrease seen in some cases during the June period. Plots recover from mild lodging but in severe cases the flattening is irreversible.

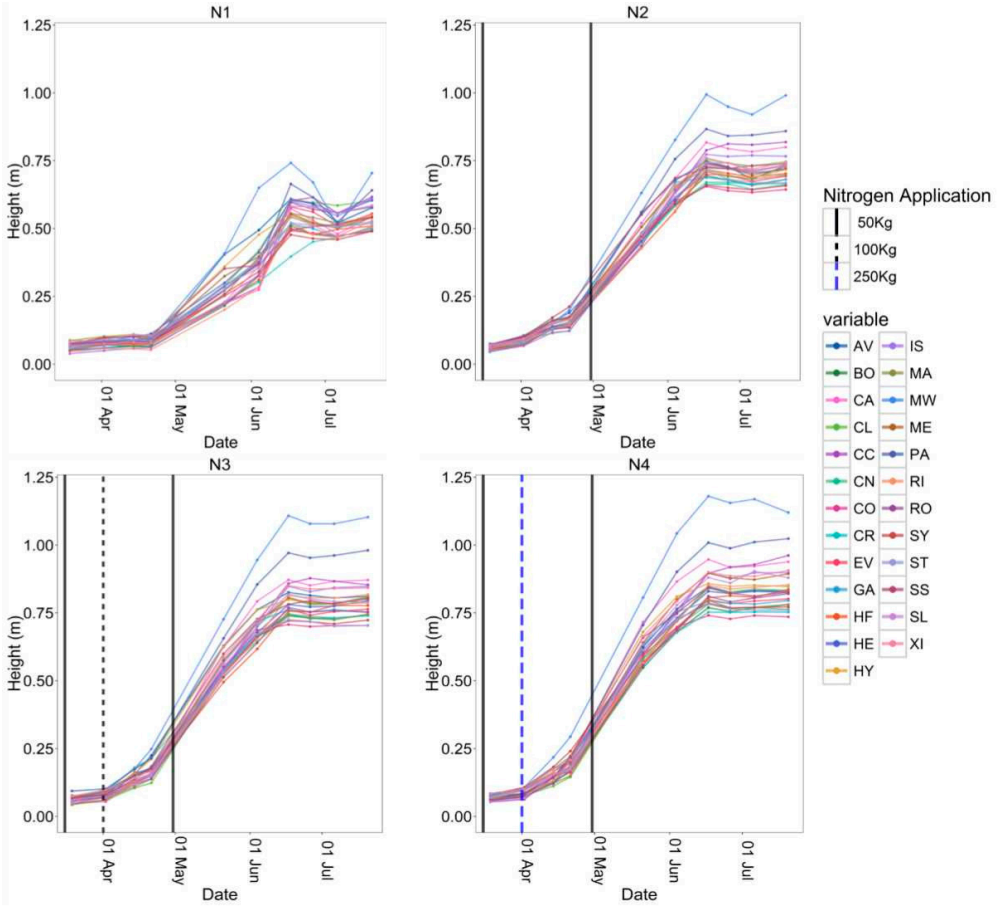

Figure 15. Comparison of crop height over the season grouped by nitrogen treatment. Vertical lines in each figure represent the date and quantity of nitrogen applied to plots for each treatment. All data represent the means of three replicates.

4. Discussion

This study has provided a quantifiable assessment of Unmanned Aerial Vehicle (UAV) based Structure from Motion (SfM) Photogrammetry for deriving accurate measurements of crop height

and crop growth rate, in this case to support field phenotyping efforts of 25 wheat varieties grown under four different nitrogen fertiliser treatments. The method presented is relatively straightforward, easily repeatable, and time and cost efficient in comparison to the terrestrial LiDAR and currently used rule method also investigated in this study.

In terms of accuracy, the data produced provide good agreement with the currently applied procedure of manual measurement with a rule (R2 = $\geq$0.93, Root Mean Squared Error (RMSE) = $\leq$0.077 m) but this approach is more consistent and spatially extensive, reducing user error associated with the ruler measurement [35,44]. Assessment of model derived crop heights from a highly accurate (5 mm) Terrestrial LiDAR (R2 = 0.97, RMSE = 0.027 m) and the best UAV model (R2 = 0.99, RMSE = 0.03 m) shows both system's ability to produce highly accurate results; however extremely high costs and poor time efficiency of the LiDAR due to the high number of individual scans required, severely lower the suitability of LiDAR for this application. The UAV method was found to often underestimate crop heights, as discussed by previous studies [35,37], but overall the results showed an improvement in accuracy compared to similar studies [31,32,45], even when the method was applied over a significantly larger number of trial plots (300).

Collection of crop heights over the growing season has proven the ability of this method to collect valuable phenotypic data at development stages between GS30 and GS61 (Zadoks Scale), and is in agreement with literature [31,46]. A number of field based variables were identified from the study as key influencers on final results; namely canopy structure and density were found to impact on model height accuracy both in early growth stages and in crops grown under nutrient deficient conditions, as also discussed by [36]. The repetition of height measurements from the UAV method allowed crop growth rates to be calculated and assessed. The main results of this study were in agreement with the literature which defines the main period of UK wheat crop growth in terms of height gain between early-April and mid-June [14].

As a high-throughput field phenotyping system, this study has demonstrated that UAV SfM is capable of collecting quality, high volume field based phenotypic data. Comparison to the LiDAR shows the UAV method is able to achieve the same high level of accuracy whilst bettering the LiDAR in terms of time and cost efficiency. Alternative high-throughput platforms that have been developed and investigated further show the value of a system for rapid monitoring of canopy dynamics; such as the Field Scanalyzer [47] as well as movable tractor based systems [48,49]. Advantages of these systems over the UAV focus strongly on the lack of weight restrictions, allowing for multiple sensors to be used to collect very high resolution data from multiple sensors simultaneously. However, these systems are limited in their application over larger areas, or across different field locations, something the UAV is better suited to. The tractor based system proposed by Comar et al. [49], was able to sample ~100 plots per hour, which equates to 1000 plots within three days assuming 4–5 h of measuring per day. The UAV method was able to cover 300 plots within a single flight of maximum 15 min, indicating coverage of 1000 plots could be achieved in less than an hour. Clearly there is a trade-off between the systems discussed here as well as other alternatives. The choice of which system is most suitable will be dependent on the data required, the time frame available and the area of coverage needed.

Whilst the method developed in this study has been shown to produce quality results over the temporal scale of a growing season, there is still room for improvement in the understanding of SfM photogrammetry dependencies. For example, in relation to the camera viewing angle, James and Robson [29] found the inclusion of oblique imagery into a NADIR image data set can further improve 3D model accuracy. In this study, software settings were also found to be influential on accuracy of model outputs, therefore in future these should be carefully selected and accurately reported in order to facilitate further advances in UAV based SfM methods and in the accuracy of results. The use of NIR imagery instead of RGB is also an area of interest, as the increased contrast between plant and soil offered by NIR imagery may improve model processing; a potential solution to the negative influence

of decreased canopy structure on model derived heights as shown by the May accuracy assessment results (Figure 10) and also discussed in the literature [36].

5. Conclusions

The work presented in this paper develops a rapid and accurate method for collecting in-field measurements of crop height using Unmanned Aerial Vehicle (UAV) based remote sensing. The UAV method developed utilises very high resolution UAV imagery and a Structure from Motion photogrammetry workflow to produce 3D topographic reconstructions of the crop trial field. Accuracy assessments of the UAV derived crop heights showed the method was able to produce measures of height comparable in accuracy to those measured by the existing manual, rule based method (R^2 = $\geq$0.92, Root Mean Squared Error (RMSE) = $\leq$0.07m). The very high spatial resolution of the UAV derived data allows for assessment of spatial variability in crop height at both the field and plot scale. UAV flight campaigns throughout the season allowed for the monitoring of changes in crop height as well as the calculation of growth rate.

Future work will look to increase the temporal resolution of the methods in order to provide a more complete picture of this phenotypic trait throughout the development stages of the different cultivars. It will also look to develop methods using other imaging equipment such as multi-spectral [50–52], hyper-spectral [35] and thermal cameras [53,54] to provide information beyond just plant height and growth rate. This should help to open up the opportunity to collect a more complete set of crop phenotype metrics at a spatial and temporal resolution usually unavailable to plant scientists, offering greater insights into varieties behaviours and adaptability under different growing conditions.

Overall, UAV SfM has the potential to become a valuable tool for rapid high-throughput in-field phenotyping of crop heights at very high resolution and accuracy for use in crop trials or more general agricultural applications.

Acknowledgments: This project forms part of and is funded by a BBSRC CASE Studentship (BB/L016516/1), in partnership with Bayer Crop Sciences. Thanks go to Elisa Liras, Michael Schlemmer and Wolfgang Thielert of Bayer Crop Sciences for their support with this work. An equipment grant was also awarded by NERC Geophysical Equipment Facility for the use of the TLS during the pilot study. Martin J. Wooster is supported by the National Centre for Earth Observation (NCEO). A particular thanks goes to Nathan Wooster for assistance in collecting UAV data of the field for the bare ground DEM. The work at Rothamsted Research was supported by the Biotechnology and Biological Sciences Research Council (BBSRC) via the 20:20 Wheat®project (BBS/E/C/00005202) and the Enhancing Diversity in UK wheat through a public sector pre-breeding programme, the Wheat Improvement Strategic Programme (BB/I002278/1), and by the Department for Environment, Food and Rural Affairs (Defra) funded Wheat Genetic Improvement Network (IF0146).

Author Contributions: F.H.H., M.J.W., M.J.H. and A.B.R. conceived and designed the survey procedures. F.H.H., A.B.R. and M.C. performed the surveys. F.H.H., M.C. and A.M. processed and analysed the data. M.J.H., M.J.W. and A.B.R. provided feedback. F.H.H. wrote the paper.

Conflicts of Interest: The authors declare no conflict of interest. The founding sponsors had no role in the design of the study; in the collection, analyses, or interpretation of data; in the writing of the manuscript, and in the decision to publish the results.

References

1. Nelleman, C.; MacDavette, M.; Manders, T.; Eickhout, B.; Svihus, B.; Prins, A.G.; Kaltenborn, B.P. *The Environmental Food Crisis: The Environment's Role in Averting Future Food Crises*; A UNEP Rapid Response Assessment; UNEP/RID-Arendal: Arendal, Norway, 2009.
2. United Nations. *World Population Prospects: The 2015 Revision, Key Findings and Advance Tables*; United Nations: New York, NY, USA, 2015.
3. IDRC—International Development Research Centre. FACTS & FIGURES on Food and Biodiversity. Available online: https://www.idrc.ca/en/article/facts-figures-food-and-biodiversity (accessed on 22 May 2016).
4. Rothamsted Research. 20:20 Wheat. Available online: http://www.rothamsted.ac.uk/our-science/2020-wheat (accessed on 18 May 2016).

5. Cobb, J.N.; DeClerck, G.; Greenberg, A.; Clark, R.; McCouch, S. Next-generation phenotyping: Requirements and strategies for enhancing our understanding of genotype–phenotype relationships and its relevance to crop improvement. *Theor. Appl. Genet.* **2013**, *126*, 867–887. [CrossRef] [PubMed]
6. Gago, J.; Douthe, C.; Coopman, R.E.; Gallego, P.P.; Ribas-Carbo, M.; Flexas, J.; Escalona, J.; Medrano, H. UAVs challenge to assess water stress for sustainable agriculture. *Agric. Water Manag.* **2015**, *153*, 9–19. [CrossRef]
7. Saint Pierre, C.; Crossa, J.L.; Bonnett, D.; Yamaguchi-Shinozaki, K.; Reynolds, M.P. Phenotyping transgenic wheat for drought resistance. *J. Exp. Bot.* **2012**, *63*, 1799–1808. [CrossRef] [PubMed]
8. Araus, J.L.; Cairns, J.E. Field high-throughput phenotyping: The new crop breeding frontier. *Trends Plant Sci.* **2014**, *19*, 52–61. [CrossRef] [PubMed]
9. Chapman, S.C.; Merz, T.; Chan, A.; Jackway, P.; Hrabar, S.; Dreccer, M.F.; Holland, E.; Zheng, B.; Ling, T.J.; Jimenez-Berni, J. Pheno-Copter: A Low-Altitude, Autonomous Remote-Sensing Robotic Helicopter for High-Throughput Field-Based Phenotyping. *Agronomy* **2014**, *4*, 279–301. [CrossRef]
10. Torres, A.; Pietragalla, J. Chapter 19: Crop morphological traits. In *Physiological Breeding II: A Field Guide to Wheat Phenotyping*; Pask, A.J.D., Pietragalla, J., Mullan, D.M., Reynolds, M.P., Eds.; CIMMYT: Mexico D.F., Mexico, 2012; pp. 106–112.
11. Lati, R.N.; Filin, S.; Eizenberg, H. Estimating plant growth parameters using an energy minimization-based stereovision model. *Comput. Electron. Agric.* **2013**, *98*, 260–271. [CrossRef]
12. Zadoks, J.C.; Chang, T.T.; Konzak, C.F. A decimal code for the growth stages of cereals. *Weed Res.* **1974**, *14*, 415–421. [CrossRef]
13. Tottman, D.R. The decimal code for the growth stages of cereals, with illustrations. *Ann. Appl. Biol.* **1987**, *110*, 441–454. [CrossRef]
14. Agriculture and Horticulture Development Board. *Wheat Growth Guide*; AHDB: Warwickshire, UK, 2015.
15. Cornelissen, J.H.C.; Lavorel, S.; Garnier, E.; Díaz, S.; Buchmann, N.; Gurvich, D.E.; Reich, P.B.; Steege, H.T.; Morgan, H.D.; van der Heijden, M.G.A.; et al. A handbook of protocols for standardised and easy measurement of plant functional traits worldwide. *Aust. J. Bot.* **2003**, *51*, 335–380. [CrossRef]
16. Pérez-Harguindeguy, N.; Díaz, S.; Garnier, E.; Lavorel, S.; Poorter, H.; Jaureguiberry, P.; Bret-Harte, M.S.; Cornwell, W.K.; Craine, J.M.; Gurvich, D.E.; et al. New handbook for standardised measurement of plant functional traits worldwide. *Aust. J. Bot.* **2013**, *61*, 167–234. [CrossRef]
17. Tilly, N.; Hoffmeister, D.; Cao, Q.; Huang, S.; Lenz-Wiedemann, V.; Miao, Y.; Bareth, G. Multitemporal crop surface models: Accurate plant height measurement and biomass estimation with terrestrial laser scanning in paddy rice. *J. Appl. Remote Sens.* **2014**, *8*, 083671. [CrossRef]
18. Turner, D.; Lucieer, A.; de Jong, S.M. Time series analysis of landslide dynamics using an Unmanned Aerial Vehicle (UAV). *Remote Sens.* **2015**, *7*, 1736–1757. [CrossRef]
19. Woodget, A.S.; Carbonneau, P.E.; Visser, F.; Maddock, I.P. Quantifying submerged fluvial topography using hyperspatial resolution UAS imagery and structure from motion photogrammetry. *Earth Surf. Process. Landf.* **2015**, *40*, 47–64. [CrossRef]
20. Rango, A.; Laliberte, A.; Steele, C.; Herrick, J.E.; Bestelmeyer, B.; Schmugge, T.; Roanhorse, A.; Jenkins, V. Using unmanned aerial vehicles for rangelands: Current applications and future potentials. *Environ. Pract.* **2006**, *8*, 159–168. [CrossRef]
21. Laliberte, A.S.; Rango, A. Texture and scale in object-based analysis of subdecimeter resolution Unmanned Aerial Vehicle (UAV) imagery. *IEEE Trans. Geosci. Remote Sens.* **2009**, *47*, 761–770. [CrossRef]
22. Koh, L.; Wich, S. Dawn of drone ecology: Low-cost autonomous aerial vehicles for conservation. *Trop. Conserv. Sci.* **2012**, *5*, 121–132. [CrossRef]
23. Fernández-Hernandez, J.; González-Aguilera, D.; Rodríguez-Gonzálvez, P.; Mancera-Taboada, J. Image-based modelling from Unmanned Aerial Vehicle (UAV) photogrammetry: An effective, low-cost tool for archaeological applications. *Archaeometry* **2015**, *57*, 128–145. [CrossRef]
24. Berni, J.A.J.; Zarco-Tejada, P.J.; Gonzalez-Dugo, V.; Fereres, E. Remote sensing of thermal water stress indicators in peach. *Acta Hortic.* **2012**, *962*, 325–331. [CrossRef]
25. Panda, S.S.; Ames, D.P.; Panigrahi, S. Application of vegetation indices for agricultural crop yield prediction using neural network techniques. *Remote Sens.* **2010**, *2*, 673–696. [CrossRef]
26. Zarco-Tejada, P.J.; Suarez, L.; Gonzalez-Dugo, V. Spatial resolution effects on chlorophyll fluorescence retrieval in a heterogeneous canopy using hyperspectral imagery and radiative transfer simulation. *IEEE Geosci. Remote Sens. Lett.* **2013**, *10*, 937–941. [CrossRef]

27. Westoby, M.J.; Brasington, J.; Glasser, N.F.; Hambrey, M.J.; Reynolds, J.M. "Structure-from-Motion" photogrammetry: A low-cost, effective tool for geoscience applications. *Geomorphology* **2012**, *179*, 300–314. [CrossRef]
28. Konecny, G. Geoinformation: Remote Sensing, Photogrammetry and Geographic Information Systems, Second Edition. Available online: https://www.crcpress.com/Geoinformation-Remote-Sensing-Photogrammetry-and-Geographic-Information/Konecny/p/book/9781420068566 (accessed on 18 May 2016).
29. James, M.R.; Robson, S. Mitigating systematic error in topographic models derived from UAV and ground-based image networks: Mitigating systematic error in topographic models. *Earth Surf. Process. Landf.* **2014**, *39*, 1413–1420. [CrossRef]
30. Nex, F.; Remondino, F. UAV for 3D mapping applications: A review. *Appl. Geomat.* **2014**, *6*, 1–15. [CrossRef]
31. Bendig, J.; Willkomm, M.; Tilly, N.; Gnyp, M.L.; Bennertz, S.; Qiang, C.; Miao, Y.; Lenz-Wiedemann, V.I.S.; Bareth, G. Very high resolution crop surface models (CSMs) from UAV-based stereo images for rice growth monitoring in Northeast China. *Int. Arch. Photogramm. Remote Sens. Spat. Inf. Sci.* **2013**, *40*, 45–50. [CrossRef]
32. Bendig, J.; Bolten, A.; Bareth, G. UAV-based Imaging for Multi-Temporal, very high Resolution Crop Surface Models to monitor Crop Growth Variability. *Photogramm. Fernerkund. Geoinf.* **2013**, *2013*, 551–562. [CrossRef]
33. Ruiz, J.J.; Diaz-Mas, L.; Perez, F.; Viguria, A. Evaluating the accuracy of DEM generation algorithms from UAV imagery. *Int. Arch. Photogramm. Remote Sens. Spat. Inf. Sci.* **2013**, *40*, 333–337. [CrossRef]
34. Turner, D.; Lucieer, A.; Watson, C. An automated technique for generating georectified mosaics from Ultra-high resolution Unmanned Aerial Vehicle (UAV) imagery, based on Structure from Motion (SfM) point clouds. *Remote Sens.* **2012**, *4*, 1392–1410. [CrossRef]
35. Aasen, H.; Burkart, A.; Bolten, A.; Bareth, G. Generating 3D hyperspectral information with lightweight UAV snapshot cameras for vegetation monitoring: From camera calibration to quality assurance. *ISPRS J. Photogramm. Remote Sens.* **2015**, *108*, 245–259. [CrossRef]
36. Geipel, J.; Link, J.; Claupein, W. Combined spectral and spatial modeling of corn yield based on aerial images and crop surface models acquired with an unmanned aircraft system. *Remote Sens.* **2014**, *6*, 10335–10355. [CrossRef]
37. Willkomm, M.; Bolten, A.; Bareth, G. Non-destructive monitoring of rice by hyperspectral in-field spectrometry and UAV-based remote sensing: Case study of field-grown rice in north Rhine-Westphalia, Germany. *ISPRS Int. Arch. Photogramm. Remote Sens. Spat. Inf. Sci.* **2016**, *XLI-B1*, 1071–1077. [CrossRef]
38. Barraclough, P.B.; Howarth, J.R.; Jones, J.; Lopez-Bellido, R.; Parmar, S.; Shepherd, C.E.; Hawkesford, M.J. Nitrogen efficiency of wheat: Genotypic and environmental variation and prospects for improvement. *Eur. J. Agron.* **2010**, *33*, 1–11. [CrossRef]
39. Haala, N.; Rothermel, M. Dense multiple stereo matching of highly overlapping UAV imagery. *ISPRS Int. Arch. Photogramm. Remote Sens. Spat. Inf. Sci.* **2012**, *39*, B1. [CrossRef]
40. Hartmann, W.; Tilch, S.; Eisenbeiss, H.; Schindler, K. Determination of the UAV position by automatic processing of thermal images. *ISPRS Int. Arch. Photogramm. Remote Sens. Spat. Inf. Sci.* **2012**, *39*, B6. [CrossRef]
41. Agisoft. *Agisoft PhotoScan User Manual Professional Edition*, version 1.2; AgiSoft LLC, 2016. Available online: http://www.agisoft.com/downloads/user-manuals/ (accessed on 2 February 2016).
42. Granshaw, S.I. Photogrammetric terminology: Third edition. *Photogramm. Rec.* **2016**, *31*, 210–252. [CrossRef]
43. Leica Geosystems. Leica Cyclone 3D Point Cloud Processing Software. Available online: http://leica-geosystems.com/products/laser-scanners/software/leica-cyclone (accessed on 16 April 2016).
44. Pask, A.J.D.; Pietragalla, J.; Mullan, D.M.; Reynolds, M.P. *Physiological Breeding II: A Field Guide to Wheat Phenotyping*; CIMMYT: Mexico, Mexico, 2012.
45. Bareth, G.; Bendig, J.; Tilly, N.; Hoffmeister, D.; Aasen, H.; Bolten, A. A comparison of UAV- and TLS-derived plant height for crop monitoring: Using polygon grids for the analysis of Crop Surface Models (CSMs). *Photogramm. Fernerkund. Geoinf.* **2016**, *2016*, 85–94. [CrossRef]
46. Jay, S.; Rabatel, G.; Hadoux, X.; Moura, D.; Gorretta, N. In-field crop row phenotyping from 3D modeling performed using Structure from Motion. *Comput. Electron. Agric.* **2015**, *110*, 70–77. [CrossRef]
47. Virlet, N.; Sabermanesh, K.; Sadeghi-Tehran, P.; Hawkesford, M.J. Field Scanalyzer: An automated robotic field phenotyping platform for detailed crop monitoring. *Funct. Plant Biol.* **2016**, *44*, 143–153. [CrossRef]

48. Andrade-Sanchez, P.; Gore, M.A.; Heun, J.T.; Thorp, K.R.; Carmo-Silva, A.E.; French, A.N.; Salvucci, M.E.; White, J.W. Development and evaluation of a field-based high-throughput phenotyping platform. *Funct. Plant Biol.* **2014**, *41*, 68–79. [CrossRef]
49. Comar, A.; Burger, P.; de Solan, B.; Baret, F.; Daumard, F.; Hanocq, J.-F. A semi-automatic system for high throughput phenotyping wheat cultivars in-field conditions: Description and first results. *Funct. Plant Biol.* **2012**, *39*, 914–924. [CrossRef]
50. Honkavaara, E.; Saari, H.; Kaivosoja, J.; Pölönen, I.; Hakala, T.; Litkey, P.; Mäkynen, J.; Pesonen, L. Processing and assessment of spectrometric, stereoscopic imagery collected using a lightweight UAV spectral camera for precision agriculture. *Remote Sens.* **2013**, *5*, 5006–5039. [CrossRef]
51. Sankaran, S.; Khot, L.R.; Espinoza, C.Z.; Jarolmasjed, S.; Sathuvalli, V.R.; Vandemark, G.J.; Miklas, P.N.; Carter, A.H.; Pumphrey, M.O.; Knowles, N.R.; et al. Low-altitude, high-resolution aerial imaging systems for row and field crop phenotyping: A review. *Eur. J. Agron.* **2015**, *70*, 112–123. [CrossRef]
52. Bendig, J.; Yu, K.; Aasen, H.; Bolten, A.; Bennertz, S.; Broscheit, J.; Gnyp, M.L.; Bareth, G. Combining UAV-based plant height from crop surface models, visible, and near infrared vegetation indices for biomass monitoring in barley. *Int. J. Appl. Earth Obs. Geoinf.* **2015**, *39*, 79–87. [CrossRef]
53. Berni, J.; Zarco-Tejada, P.J.; Suarez, L.; Fereres, E. Thermal and narrowband multispectral remote sensing for vegetation monitoring from an unmanned aerial vehicle. *IEEE Trans. Geosci. Remote Sens.* **2009**, *47*, 722–738. [CrossRef]
54. Prashar, A.; Jones, H.G. Infra-red thermography as a high-throughput tool for field phenotyping. *Agronomy* **2014**, *4*, 397–417. [CrossRef]

3.3 Published article additions.

In addition to the published article, additional information with regards specific aspects of the developed method and results are provided in the following sections.

3.3.1 Lens replacement and calibration parameters.

As stated on page 9 of the published article, replacement of the UAV camera lens occurred due to damage to the original. This damage and replacement occurred between the 21st April 2015 and 21st May 2015 flights. As part of the Agisoft Photoscan SfM workflow, geometric lens calibration corrections were performed on each flight dataset. Details of the parameters used to perform these corrections are detailed in **Table 3.1.** Details of the different correction parameters determined and applied by Agisoft Photoscan when applying geometric lens distortion corrections to imagery. (Agisoft, 2016).

Table 3.1. Details of the different correction parameters determined and applied by Agisoft Photoscan when applying geometric lens distortion corrections to imagery.

Agisoft Parameter	Description
fx, fy	Focal length in the x and y dimensions measured in pixels.
cx, cy	Principal point coordinates i.e. the interception of lens optical axis and sensor plane
Skew	Skew transformation coefficient
k1, k2, k3, k4	Radial distortion coefficients
p1, p2, p3, p4	Tangential distortion coefficients

3.3.2 Model accuracy and RMSE calculation

Assessments of the predictive capabilities of the derived models presented in the published article are provided through the calculation of root mean square error (RMSE). For this work, RMSE were calculated on all available data points, for example 10 points for the preliminary study, and 300 for the main study in June and July assessments. As the two-crop height (ruler and UAV) datasets were independent of each other, i.e. one was not used to calibrate the other, it was deemed appropriate to calculate RMSE on all available data points.

3.3.3 LiDAR vs. UAV heights.

Within the paper, focus was on recreating ruler measured heights, and as such accuracy assessments were compared to the ruler. Figure 3.1 presents accuracy assessments of the UAV derived mean plot heights compared to LiDAR derived mean heights for the 10 plots used in the 2014 pilot study. Results indicate comparable mean plot height measurements from the two techniques, $R^2 \geq 0.93$. Interestingly comparison of these two methods shows less negative impact on height errors from the higher altitude (90A) and combined UAV models. This trend is likely to be a result of the spatial nature of both methods in comparison to the ruler measurements. As discussed in the paper, the 90A and combined models suffer from smoothing or filtering of small plant features as a result of lower spatial resolutions, which will include the specific features measured by the ruler method. By contrast the LiDAR and UAV methods, both include and subsequently average out all layers or components of the canopy into a

single result, increasing the comparability seen in the results. The UAV heights still indicate underestimation compared to the LiDAR, as also seen when compared to the ruler measurements. This is likely a result of the superior resolution of the LiDAR versus the UAV, achieving 0.05cm and 0.5cm resolutions respectively.

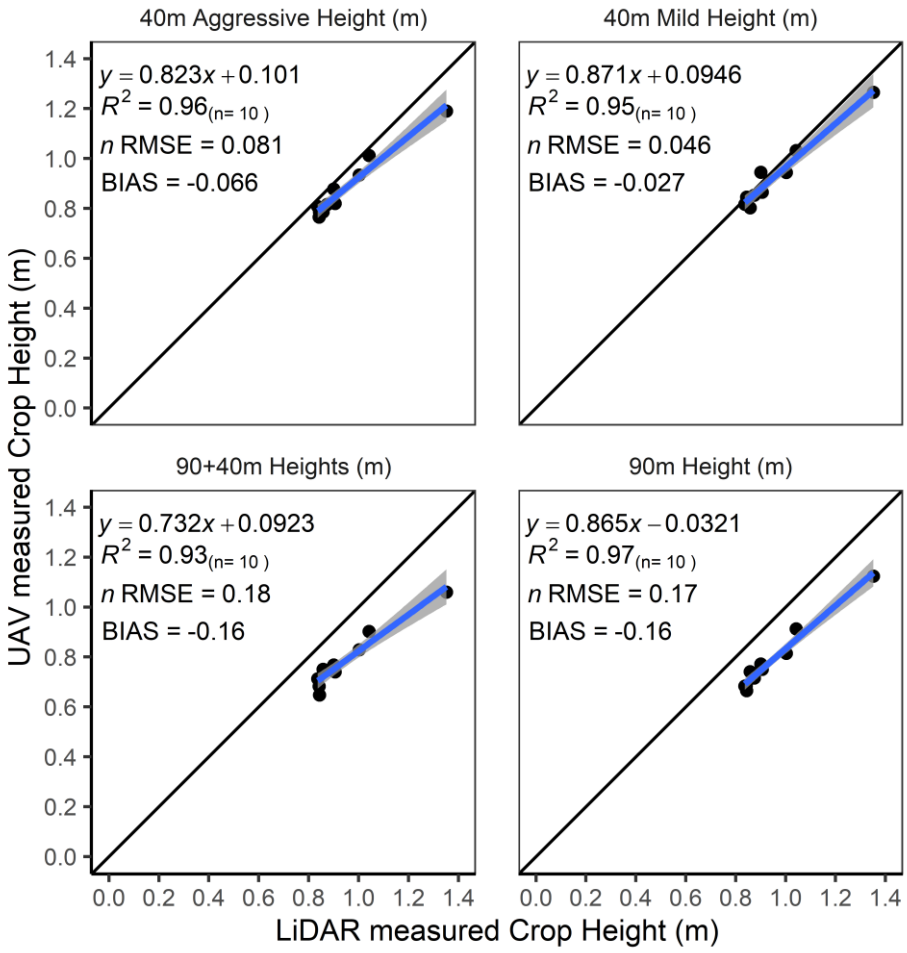

Figure 3.1. Correlation plots comparing LiDAR and UAV derived crop heights for 10 wheat plots measured in the 2014 pilot study. These results are initially presented as Figure 8 of the published article in this chapter (Holman *et al.* 2016). Solid black line indicates the 1:1 line.

3.3.4 Digital Elevation Models

For the published article, two methods for creating bare ground DEMs were presented and tested. For the buffer zone DEM, a more detailed description of the method used for generating these DEMs is provided. Buffer zone DEMs were generated for each UAV flight date to remove underlying field topography from the generated models and isolate pure crop heights. To generate the buffer zone DEMs, first single points were placed manually at the corner of each plot and within the buffer zones (Figure 3.2). This step was performed manually and repeated for each date to ensure the points were positioned on true bare ground rather than crops. From these points, the Z (height) values from the DSM were interpolated spatially using the Triangulated Irregular Network (TIN) tool in ArcMap. The resulting TIN was then rasterised at the same spatial resolution as the original DSM, before subtracting it from the DSM to generate the nDSM.

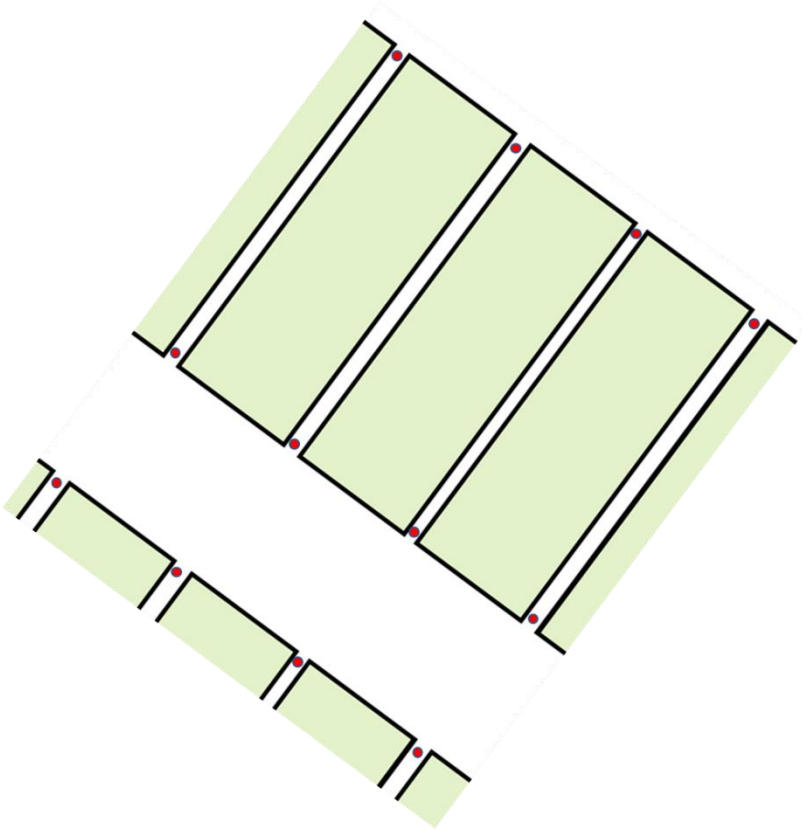

Figure 3.2. Example of point placement used to extract bare ground heights for generation of bare ground Digital Elevation Models. Red points indicate typical location of points used, though placement was manually performed for each separate DSM generated.

3.3.5 Normalising Digital Surface Models

The work presented within this section builds on the findings of the published article, presenting further analysis of SfM software settings and processing workflows, with a focus on understanding how they can be altered to optimise processing efficiency.

Typically, previous studies, including the work in this Chapter, have utilised an 'as high as possible' approach when selecting processing settings in SfM software. This is done in an attempt to ensure that model resolutions and quality is maximised and hopefully ensures the best reconstruction and accuracy are obtained. However, this can lead to significantly longer processing times for only relatively minor and perhaps insignificant gains in model accuracy. Results from previous studies have shown that ultra-high and medium quality require vastly different processing times (ultra-high = 64 hours *vs.* medium = 9 hours), and produce differing model resolutions of 2.5cm and 10cm for ultra-high and medium quality respectively (Schirrmann et al., 2016a; Ziliani et al., 2018). Comparison of the UAV derived maize crop heights to LiDAR heights from these two models indicated only slight improvements in accuracy were obtained in R^2 (ultra-high = 0.99 *vs.* medium = 0.98), and RMSE (ultra-high = 0.0199m *vs.* medium = 0.0241m). These results and processing times were obtained using high powered computing equipment and Agisoft Photoscan and highlight how the 'as high as possible' approach does not necessarily provide the best option for height measurements. On the other hand, for some applications the loss of resolution may be significant; for example, where fine 3D detail within canopies is required or desired, the loss of resolution from lower quality models will be detrimental to this.

In addition to assessing processing settings, it was theorised that the combination of models processed at different qualities, during normalisation of DSMs, may offer improved results. Specifically, can a high-quality (HQ) DEM be used to normalise a medium quality (MQ) DSM and achieve any improvement in accuracy of derived crop heights. The theory underlying this being that the reduced error in the DEM will improve accuracies; whilst the shorter processing times of the multiple DSMs will improve overall throughput of the SfM process. Therefore, further investigation was performed to better understand the impact of model processing quality on accuracy and turn-around time of crop height retrieval in wheat experiments from UAV imagery.

3.3.6 Methods

UAV imagery of the same experimental field at Rothamsted Research, was collected for the 2017 season using the same procedure as outlined in the published article in Section 3.2. A bare ground DEM was produced from an early season flight (11th November 2016), shortly after the experiment was planted. A single DSM was produced from a flight carried out on 4th July 2017, the closest date to when manual measurements of height were collected. For both the DEM and DSM, two versions were produced, of medium and high-quality processing. Full details of processing settings and model parameters are outlined in Table 3.2.

Table 3.2. Agisoft Photoscan model processing parameters for bare ground and crop DSMs.

Model	GSD (m)	No. of photos	Alignment parameters	Dense point Cloud parameters	DEM parameters	Orthomosaic Parameters	DEM Resolution (m)
High Quality (HQ)	0.01	573	Accuracy = Highest	High - Disabled	Dense cloud	Blending - Disabled	0.02
Medium Quality (MQ)	0.01	573	Accuracy = Highest	Medium - Disabled	Dense cloud	Blending - Disabled	0.04

3.3.7 Results and Discussion

3.3.7.1 Processing Times

Total processing times for the medium and high-quality models are detailed in Table 3.3 below. Results show a marked difference in processing times between the MQ and HQ settings, despite the settings being different by only one step in quality. The HQ models takes an extra 11 hours to produce, results which fit with those found by other studies (Ziliani et al., 2018). A seven-hour processing time for the MQ model, indicates that in theory results could be obtained on the same day as data collection.

Table 3.3. Agisoft Photoscan processing times for each processing step involved in generating DSMs. Total time is also provided.

Model	Alignment time (hh:mm:ss)	Dense point Cloud time (hh:mm:ss)	DEM time (hh:mm:ss)	Orthomosaic time (hh:mm:ss)	Total Time (hh:mm:ss)
High Quality (HQ)	01:24:00	15:34:00	00:02:40	00:53:51	17:54:34
Medium Quality (MQ)	01:24:00	04:40:00	00:02:59	00:53:51	07:00:50

3.3.7.2 Accuracy Assessments

Comparison of UAV and ruler derived crop heights was used to assess accuracy of the UAV models (Figure 3.3). Results show the model generated from high quality DEM and DSM (HQ+HQ) produces the best results in terms of R^2, RMSE and bias. As expected, the MQ+MQ model produces good accuracy but lower than that achieved by the HQ+HQ model. This trend fits with the results achieved by Ziliani *et al.* (2018), who also found that all models gave good accuracy, though increasing processing quality did improve accuracy. The new combined model of high-quality DEM and medium quality DSM, showed good results outperforming the MQ model, but still below the HQ model. These results suggest that some of the drop-in accuracy of the MQ model is related to errors associated with either resolution or processing, which can be reduced with the inclusion of the HQ bare ground DEM. It is known that reducing the model quality level leads to an increase in the filtering applied by the SfM software, which in turn lowers the spatial resolutions. As discussed in Chapter 2.3.2, reduced spatial resolutions, have been identified as a source of increased error in SfM derived height models (Sadeghi-Tehran et al., 2017). The use of the medium quality CSM in the combined model results,

will still suffer from loss of fine-scale crop structures, ultimately resulting in an increase in underestimation of mean plot height as seen in Figure 3.3.

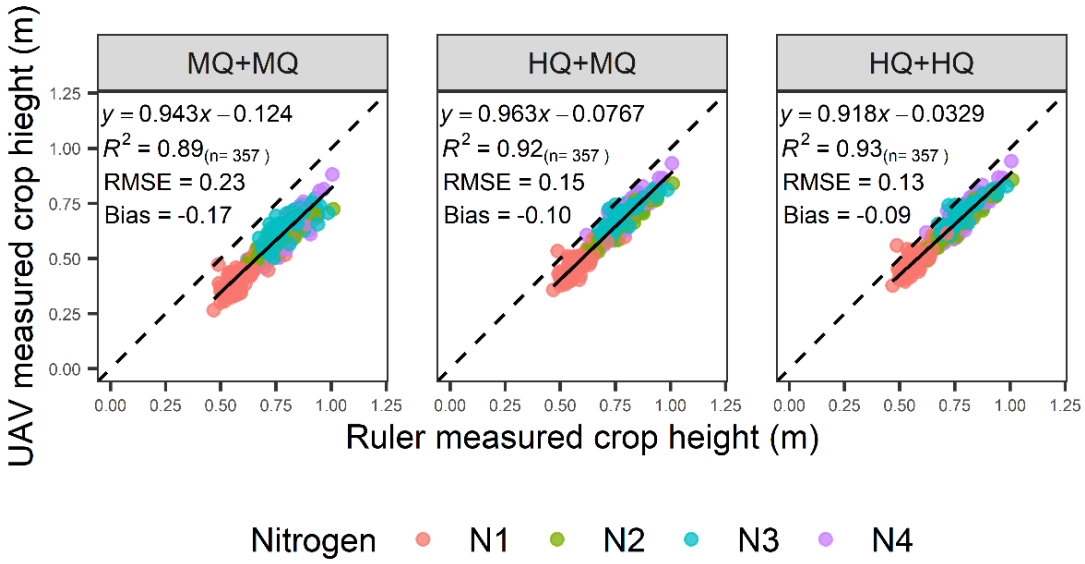

Figure 3.3. Comparisons of accuracy assessments for UAV and ruler derived wheat crop heights from the three different normalised Digital Surface Models (nDSMs). From right to left the subplots are produced from medium quality (MQ) Digital Elevation Model (DEM) and Digital Surface Model (DSM); medium-quality DSM and high-quality (HQ) DEM; and high-quality models DEM and DSM.

The results highlight the impact of processing settings on both processing time, model accuracy, and model resolution. These results and trends fit with those of other studies, though processing times were shorter for this study compared to those of Ziliani et al., (2018). This is likely to be a result of smaller spatial area covered and the smaller number of images. Use of higher quality bare ground DEMs for normalisation of lower quality DSMs produced gains in accuracy over the use of lower quality DEMs and DSMs. This mixed model approach also produces positive improvements on processing times, an advantage where results in reduced return time are important. Clearly selection of processing settings is important, not only for accuracy, but resolution and processing

speeds as well. Future studies should look to include more detail on the processing parameters, including software version and settings, hardware used and imagery details, to improve understanding, development, and optimisation of SfM processing workflows.

3.4 Summary and Conclusion

This chapter has presented work which developed methods for high throughput measurement of wheat crop height, using Structure from Motion photogrammetric processing workflows and RGB imagery collected from a rotary wing UAV. A clear and complete workflow has been presented and tested against the traditional standard used for measuring crop heights of field-based wheat trials, a meter rule. Results of accuracy assessments showed the UAV photogrammetry reconstructions of wheat plots heights to be comparable to ruler measurements ($R^2 \geq 0.92$), though the UAV did present consistent underestimation errors of heights in the main study (RMSE ≤ 0.07m and Bias ≤ -0.064).

Comparison of these results to the initial studies of (Bendig et al., 2013a, 2013b; Bendig, 2015) and (Aasen et al., 2015a) shows improvements in both consistency of height measurements ($R^2 \geq 0.93$ compared to $0.71 \geq R^2 \leq 0.22$). The trend for the UAV results to underestimate true plant heights remained, though it was significantly reduced by the method improvements developed by the work in this chapter with biases ≤ -0.064 compared to -0.19 achieved by (Aasen et al., 2015a). These results demonstrate successful development and improvement of the SfM method to reduce the sources of error and their impacts as identified by Bendig *et al.*, (2015, 2013). Even so, the negative

biases and underestimation of height remained within the results of this study. Further comparison of results to other studies, post publication of this chapter, show comparable accuracies over large scale trials and a range of crop types. Madec et al., (2017) investigated both LiDAR and UAV methods applied to measuring 1137 field-based wheat trial plots. UAV accuracies achieved over this greater number of plots were comparable to the results in this chapter (R^2: 0.9 vs 0.92, and RMSE: 0.08m vs. 0.07m). Another study by Malambo et al., (2018) provided greater temporal accuracy tests of UAV derived maize and sorghum heights against a LiDAR system. Although not assessing the exact same crop, using the same technique, the authors were able to achieve similar R^2 values (≥0.88) and RMSE (≤0.02m) and importantly these accuracies were maintained over 6 separate measurements and crop growth stages. Ziliani et al., (2018) also provided accuracy assessments of UAV SfM modelled heights for maize crops over a significantly larger area, totalling 50 hectares. Assessment of accuracies against a terrestrial LiDAR system found similar levels of accuracy obtained by the UAV SfM method as obtained within this chapter and other studies. Of interest when comparing results from all these studies is that despite different target crops, results are consistent including the common underestimation of crop heights from the UAV SfM method. The question still remains, as to whether this is an error associated with the UAV results, or with the source of validation data used for accuracy assessments. Aasen et al., (2015) highlighted the difficulty of obtaining true accuracy assessments of new methods such as SfM photogrammetry, when using a ruler as this method itself is prone to various user errors and subjectivities between measurements. In addition, the lack of spatial measurements, limits how well the ruler measurements can represent all spatial

variability within a trial plot. Geipel et al., (2014) concluded that results should be validated against 'perfectly co-registered' high resolution LiDAR data in order to ascertain true tests of accuracy for the UAV method. Additional work in this chapter compared UAV and LiDAR measured heights and highlighted the accuracy achieved from UAVs compared to a high spatial resolution and accuracy terrestrial LiDAR system. However, spatial and temporal coverage of plots with the LiDAR used in this chapter was limited by the laborious and slow data collection workflows required for LiDAR. The study by Madec et al., (2017), using both a vehicle-based LiDAR and a UAV to measure a large volume of experimental plots, found the trend to underestimate of crop heights persisted even when using highly accurate LiDAR measurements for validation data. The consistent negative biases displayed by the SfM results in all studies, has been hypothesised to be a result of the spatial resolution of UAV imagery limiting the SfM software's ability to reconstruct fine canopy structures (e.g. grain heads) thus reducing the apparent canopy height within the final 3D models (Bareth et al., 2016; Grenzdörffer, 2014; Voort, 2016). Further work presented in this chapter investigated the impact of spatial resolution, defined by model quality, in combination with normalising of DEMs on final height accuracies. Increasing of model quality, and in turn spatial resolution, did produce very slight improvements in both R^2 and RMSE, indicating that increasing resolution may reduce model error. However, Brocks et al., (2016) found increasing spatial resolutions too much, introduced unacceptable levels of noise into models, negating any improvements in error.

Clearly, further work is needed to understand the sources and reasons for the underestimation, and whether these trends can be improved further. Despite this consistent error presented by SfM results, it continues to be widely adopted and applied to phenotyping for predictions of biomass, yield and stress tolerance in field-based trials (Araus and Kefauver, 2018; Shakoor et al., 2017; Yang et al., 2017). The superior throughput and spatial coverage achieved using SfM and UAVs makes the slight loss in accuracy an acceptable trade-off for the application of phenotyping crop height.

Overall the work presented in this chapter has successfully developed and applied the use of UAVs and Structure from Motion photogrammetry image processing to generate accurate measures of crop heights in the field. The superior throughput obtained using UAVs over ground-based alternatives (e.g. ruler or LiDAR) allows for the monitoring of crop heights in the field at high spatial and temporal resolutions previously unachievable with traditional standard practices. This offers new insights into how crop height changes over time and space, for example the calculation of growth rates as presented in this chapter. However, as discussed, this method is still subject to errors in height, specifically underestimation. Clearly this consistent trend, found in several studies, needs further investigation before UAVs and SfM can be classed as the new standard method for obtaining crop heights. Other opportunities for future work should look to include additional equipment and/or methods to facilitate measurement of multiple phenotypes simultaneously, e.g. multi-spectral and thermal cameras. This will allow for better analysis of the complex and dynamic interaction of multiple phenotypic traits in response to genes and growing environment.

Chapter 4: Radiometric Calibration of Commercial 'Off the Shelf' Cameras for UAV-based High-Resolution Crop Phenotyping of Reflectance and NDVI

4.1 Introduction

The spectral reflectance of plant canopies is influenced by the optical properties of the plant and the plant's structural properties. These properties produce a unique spectral signature, measurements of which have been shown useful for relating to physiological traits, as highlighted in Chapter 2. Methods for measuring the spectral reflectance of canopies are widely used for field-based phenotyping; however, many conventional techniques suffer from low throughput and poor spatial information (e.g. are point-based or offer low spatial resolutions). Therefore, much of the dynamic temporal and spatial expressions of target traits in response to environmental conditions are lost. Unmanned Aerial Vehicles (UAVs) and multispectral remote sensing imagers have the potential to overcome the limitations associated with ground-based methods. However, many commercial imagers suffer from lack of spatial resolution or high costs, or a combination of the two. Adaptation of Commercial 'Off the Shelf' (COTS) cameras are an alternative low-cost option, which offer superior spatial resolutions and ease of use. However, lack of complete and validated radiometric calibration workflows, as well as derived reflectance measures, restricts their application for high throughput UAV phenotyping.

This Chapter presents the development and assessment of a custom dual camera system for measuring four band multi-spectral reflectance imagery from Unmanned Aerial Vehicles (UAV). The equipment and methods are developed to improve the spatial and temporal resolution of measured canopy reflectance, with to the aim of obtaining sufficient spatial resolutions to isolate the key components of canopy reflectance, canopy size and canopy quality. The work utilises two Commercial 'Off the Shelf' (COTS) digital cameras, one modified to collect imagery in near infrared (NIR); while the second, unmodified to collect multi-spectral, visible and near-infrared imagery of wheat canopies. Custom developed calibration workflows are applied to convert the pixel values from these two data sources to measures of reflectance. The work undertaken for this chapter culminated in a published research article in the journal Remote Sensing, for which primary authorship, method development, data processing and analysis was performed by the thesis author. M. Castle assisted in data collection and processing; A. Riche assisted in method development, data collection and manuscript editing; M. Wooster and M. Hawkesford assisted in method development and editing of manuscript. The article is included within this chapter following the requirements of King's College London PhD thesis rules.

In addition to the published article, Section 4.3 provides more detail on the derived spectral responses of the two COTS cameras used in this chapter. This includes details of the methodology used and results obtained.

4.2 Published Article

remote sensing

MDPI

Article

Radiometric Calibration of 'Commercial off the Shelf' Cameras for UAV-Based High-Resolution Temporal Crop Phenotyping of Reflectance and NDVI

Fenner H. Holman [1,*], Andrew B. Riche [2], March Castle [2], Martin J. Wooster [1,3] and Malcolm J. Hawkesford [2]

1 Department of Geography, King's College London, London WC2B 4BG, UK
2 Rothamsted Research, Harpenden, Hertfordshire AL5 2JQ, UK
3 National Centre for Earth Observation (NCEO), King's College London, London WC2B 4BG, UK
* Correspondence: fenner.holman@kcl.ac.uk

Received: 3 June 2019; Accepted: 9 July 2019; Published: 11 July 2019

Abstract: Vegetation indices, such as the Normalised Difference Vegetation Index (NDVI), are common metrics used for measuring traits of interest in crop phenotyping. However, traditional measurements of these indices are often influenced by multiple confounding factors such as canopy cover and reflectance of underlying soil, visible in canopy gaps. Digital cameras mounted to Unmanned Aerial Vehicles offer the spatial resolution to investigate these confounding factors, however incomplete methods for radiometric calibration into reflectance units limits how the data can be applied to phenotyping. In this study, we assess the applicability of very high spatial resolution (1 cm) UAV-based imagery taken with commercial off the shelf (COTS) digital cameras for both deriving calibrated reflectance imagery, and isolating vegetation canopy reflectance from that of the underlying soil. We present new methods for successfully normalising COTS camera imagery for exposure and solar irradiance effects, generating multispectral (RGB-NIR) orthomosaics of our target field-based wheat crop trial. Validation against measurements from a ground spectrometer showed good results for reflectance ($R^2 \geq 0.6$) and NDVI ($R^2 \geq 0.88$). Application of imagery collected through the growing season and masked using the Excess Green Red index was used to assess the impact of canopy cover on NDVI measurements. Results showed the impact of canopy cover artificially reducing plot NDVI values in the early season, where canopy development is low.

Keywords: Unmanned Aerial Vehicle; reflectance; radiometric calibration; NDVI; digital cameras; canopy reflectance

1. Introduction

In crop phenotyping, vegetation indices (e.g., NDVI) derived from canopy reflectance are commonly used to assess certain physiological traits of interest [1], including (i) plant vigour [2,3], (ii) plant biomass [4,5], (iii) plant nitrogen status [6], (iv) plant Leaf Area Index (LAI) [7,8] and (v) final crop yield [9]. However, these indices are typically influenced by both the target vegetation condition and variables such as background soil properties and canopy cover/density [10]. The combined influence of each variable quite often remains unacknowledged when associating vegetation indices (VIs) to traits of interest—a problem when there are multiple situations (e.g., low canopy cover and high vegetation vigour versus high canopy cover and low vegetation vigour) that may equate to similar VI measures. Such situations can provide significant uncertainty, and even false indications of plant status [11]. Traditional methods of measuring canopy spectral reflectance (e.g., ground spectrometers and/or satellite based remote sensing) offer insufficient spatial resolution to investigate and dissect

the influences of the many variables involved in controlling VI measures. Unmanned Aerial Vehicle (UAV) based remote sensing systems may, however, offer this capability, and are becoming a prominent method for high throughput phenotyping of field-based crop trials, largely thanks to their very high spatial resolution imagery [12].

In combination with modified digital cameras or commercially available multispectral imagers, low-cost UAVs are increasingly being used for high temporal resolution crop condition monitoring and field phenotyping. More recently, modified single and dual 'commercial off the shelf' (COTS) digital camera systems are being used for collection of multispectral (RGB-NIR) imagery at spatial resolutions superior to those achieved by commercial cameras such as the Parrot Sequoia [13]. However, captured imagery is still subject to distortions from camera (exposure, vignetting, file format and spectral sensitivity), and environmental factors (predominantly solar spectral irradiance) [14–23], weakening the capacity to extract accurate quantitative information [15,24]. Whilst calibration methods for the bulk of these factors have been investigated, shortcomings remain in relation to long-term consistency, particularly with respect to variable solar irradiance. Firstly, obtaining temporally relevant measures of irradiance for individual UAV images is a challenge. Berra et al. [25] used ground-based artificial targets of known reflectance, along with the empirical line method, to convert camera measures to reflectance units. However, inconsistent capturing of targets within individual images limited calibration to final orthomosaics. Therefore, variations in irradiance during the flight were not corrected for, increasing errors in the derived reflectance datasets [26]. Furthermore, the temporal stability of reflectance of such artificial targets left out in the field can vary by up to 16% over a season [27]. An alternative is to use a supplementary device measuring irradiance concurrently with COTS camera data collection, providing the information to convert individual images into reflectance units. The Parrot Sequoia employs this method, utilising its own downwelling light sensor operating at the same spectral bands as the imager itself. The second shortcoming identified relates to the fixing of exposure settings (aperture, shutter speed and ISO) to remove influence of camera exposure settings on the amount of light reaching the sensor, or the sensitivity of the sensor to light. This "fixed settings" approach increases risk of under or over exposure of images—which equates to lost data [28]. Linear relationships between image Digital Number (DN) and varying ISO, shutter speed and aperture have been previously demonstrated [29], indicating post-capture normalising of images of varying exposure can be achieved. As far as we can tell, this feature has not been utilised for this purpose before.

Given the above, the aim of the current study is to calibrate individual wavebands of dual COTS cameras to reflectance, with a focus to include individual image irradiance corrections from a separate irradiance sensor and allowance for non-fixing of camera exposure. Then, within a field phenotyping setting, using a low-cost UAV utilise the very high-resolution reflectance imagery to temporally analyse the influence of canopy structure and soil reflectance on derived vegetation indices, specifically NDVI. Within this framework, specific objectives are to:

1. Develop a method for full radiometric calibration of COTS camera imagery, with new methods for exposure normalisation and individual image incoming solar irradiance adjustment.
2. Quantitatively assess the influence of the radiometric calibration steps and the final quality of the derived reflectance and NDVI datasets.
3. Utilise the very high-resolution maps derived from the UAV imagery to analyse the influence of canopy cover on NDVI trends for a field-based wheat crop trial.

2. Materials and Methods

2.1. Field Site

All data were collected at the experimental farm operated by Rothamsted Research, UK (51°48'34.56"N, 0°21'22.68"W). We focused on the Defra-funded Wheat Genetic Improvement Network (WGIN) Diversity Field Experiment [24], whose aim is to test the influence of applying different nitrogen fertiliser treatments to different wheat cultivars. A total of 30 different cultivars were grown

at 4 different nitrogen application rates, with three replicates making a total of 360 plots. (Table 1) [25]. Each plot consisted of a 9 m × 3 m non-destructive plot and a 2.5 m × 3 m plot reserved for destructive sampling. This study focuses on the non-destructive part only.

Table 1. Details of the four nitrogen treatments applied to the diversity field experiment for 2017.

Treatment Code	Total Nitrogen Application (kg N ha^{-1})	Application Date	Nitrogen Applied (kg n ha^{-1})
N1	0	-	0
		-	0
		-	0
N2	100	15/03/2017	50
		05/04/2017	50
		09/05/2017	0
N3	200	15/03/2017	50
		05/04/2017	100
		09/05/2017	50
N4	350	15/03/2017	50
		05/04/2017	250
		09/05/2017	50

2.2. UAV Imagery

A DJI S900 UAV [30] fitted with a DJI flight controller was flown on a pre-determined flight plan at 45 m altitude over the field site nine times between 7 March 2017 and 4 July 2017. The flight plan was designed to ensure 80% overlap between concurrent images was obtained. Two Sony (Tokyo, Japan) α5100 mirrorless digital cameras [31] mounted on the UAV were used for the image collection. These cameras contain 24.3 mega pixel complementary metal-oxide semiconductor (CMOS) sensors, and both were fitted with 20 mm F2.8 Sony prime lenses. One camera was left as standard to record RGB imagery, and one had had its internal NIR-blocking filter replaced with an 830 nm long pass filter to block visible light and enable recording of NIR waveband imagery. The 830 nm filter was selected to ensure minimal capturing of visible light in the imagery, as seen with the 660 nm filter used by Berra et al. [25,32].

All images were captured at 1-sec intervals and in Raw format, with focus set to 45 m to reflect the UAV flying height. Aperture and ISO were left on automatic, whilst shutter speed was fixed to 1/500sec to ensure minimisation of motion blur. The UAV and cameras were flown over the field site at a time relatively close to local solar noon, with actual recording times varying from 10:11 to 13.25. Twelve Ground Control Points, whose positions were measured with a Trimble Geo 7 DGPS [33], were used for georeferencing final orthomosaics. To provide measures of total incoming solar irradiance, a Tec5 HandySpec Field spectrometer (Oberursel, Germany) [34] fitted with a cosine corrected downwelling optic was deployed at a fixed location next to the field and set to measure at 1-second intervals. Spectral measurements were collected at 10 nm spectral resolution across the wavelength range 360–1000 nm.

2.3. Validation Data

Mean plot canopy reflectance, measured with the Tec5 HandySpec Field spectrometer, was used for validation of UAV derived canopy reflectance measures. To collect the spectrometer measurements, a single scan of each plot's canopy was collected with the spectrometer optic held approximately 1 m above the plot; the standard procedure employed by Rothamsted Research. Each scan produced one spectral reflectance measure for the plot at 10 nm spectral resolution across the wavelength range 360–1000 nm. This procedure was repeated for all 360 plots on three separate dates during the growing season between 19 April and 4 July 2017. The Tec5 HandySpec adjusts for changes in solar illumination between measurements using a downwelling optic fitted with a cosine diffuser; reflectance is calculated using proprietary software. Before comparing to UAV results, the Tec5 results

were convolved to the same spectral wavebands as the cameras. These ground-based measurements were not always collected on the same days as UAV flights due to logistical constraints, but were within 3 days. Additional validation data was obtained by flying a Parrot Sequoia multispectral imager [13] simultaneously with the dual camera system for a single date (21 June 2017). The Sequoia was set to capture images every second and the Sequoia's downwelling sunshine sensor was mounted atop the UAV for collection of irradiance measurements. The Sequoia images were processed using Pix4D (Lausanne, Switzerland) (Version 4.3.1) [35] using standard recommended settings, downwelling light sensor data and manufacturer derived calibrations, producing Green, Red, and NIR reflectance orthomosaics at a ground sampling distance (GSD) of 5 cm.

Due to the differences between COTS camera and Parrot Sequoia spectral responses (Table 2), direct comparison between the cameras was not possible. Therefore, assessment of accuracy of the individual UAV-based imaging systems was conducted by comparing both against the Tec5.

Table 2. Spectral sensitivities for the Parrot Sequoia's four spectral bands.

Camera Channel	Wavelength Range (nm)
Green	530–570
Red	640–680
Red Edge	730–740
NIR	770–810

2.4. Post-Processing of Captured Imagery

The processing of the dual-camera imagery followed the workflow outlined in Figure 1. Specific details on the main correction steps, including the novel exposure corrections are provided.

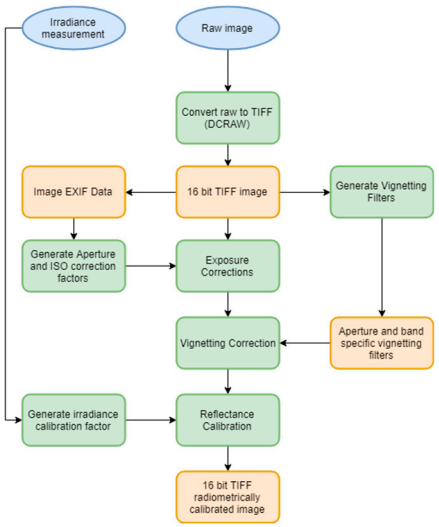

Figure 1. Flow chart of key processing steps used to convert raw images to reflectance images. The blue circles indicate inputs, green squares indicate processing steps and yellow squares derived products.

2.4.1. Relative Spectral Response

Relative Spectral Responses (RSR), Figure 2, of both cameras were determined using a double monochromator fitted with an integrating sphere, using the method described by Berra et al. [32]. The unmodified RGB camera shows greatest sensitivity in the green channel, as expected from a Bayer matrix colour filter array [32]. For the modified NIR camera, overall sensitivity was similar in all three bands that originally measured Red, Green and Blue waveband light. Whilst now mostly sensitive to NIR wavelength light, all channels show some sensitivity to light below 830 nm (i.e., sensitivity to radiation outside the NIR spectral range remained), indicating that the modified internal filter was

not performing at 100% at 830 nm. The 'Blue' channel of the NIR-adapted camera displayed the least sensitivity to light below 830 nm, therefore was best suited for use as the NIR channel. The wavebands determined for each channel of the RGB and NIR channels are presented in Table 3.

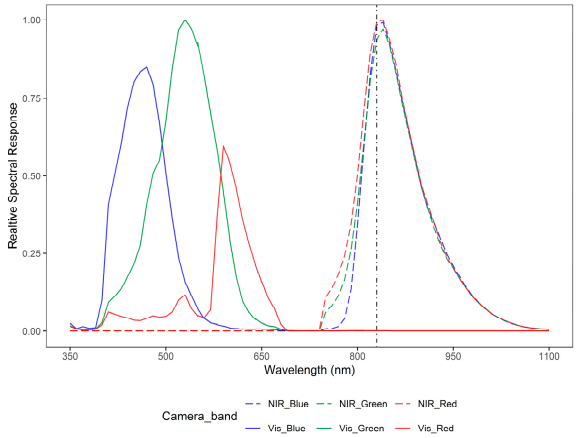

Figure 2. Relative Spectral response of the two Sony cameras used in this study. Vertical dotted line indicates the 830 nm blocking filter present in the adapted Sony NIR camera.

Table 3. Sony α5100 camera band sensitivities. Sensitivities were measured using a double monochromator fitted with an integrating sphere.

Model	Channel	Wavelength Range (nm)
"RGB" Camera	Red	580–660
	Green	420–610
	Blue	410–540
"NIR" Camera	NIR (blue channel)	800–900

2.4.2. RAW Conversion

Images were collected in RAW format before conversion to 16-bit Tagged Image File Format (TIFF) format using DCRAW 9.27 [36]. This was done using bilinear conversion algorithms and a dark current correction, to maintain original sensor DN measurements. The exact settings are presented in Table 4. Dark current correction images for each camera were captured in complete darkness (i.e., lens cap on and lights turned off), and used for the DCRAW processing.

Table 4. Details of DCRAW settings used to convert images from raw to Tagged Image File Format (TIFF).

DCRAW Command	Action
–v	Print verbose messages
–6	Write 16bit
–W	No automatic image brightening
–g 1 1	Apply unadjusted gamma curve
–T	Write Tiff format
–r 1 1 1 1	Set unadjusted white balance
–t 0	Do not rotate image
–q 0	Apply linear demosaicing
–o 0	Raw output colour space
–K darkimage.pgm	Apply dark image correction using file specified

2.4.3. Exposure Corrections

To determine the relationships between DN and exposure settings (aperture and ISO), a series of images were collected of a Lambertian spectralon reflectance panel, set up indoors under constant

illumination with a white incandescent bulb light. For each exposure setting (aperture, ISO and shutter speed), a series of images were captured under the settings full range (e.g., ISO100–ISO1000), whilst other settings remained fixed. As illumination remained constant; three image sets were produced, each modelling the influence of changing one exposure setting on image DNs.

Linear relationships between pixel DN and aperture and ISO were observed (Figure 3). From these relationships, the aperture correction factor (CF_{app}) was derived to normalise images captured under varied aperture to an aperture value of 1 (Equations (1) and (2)).

$$Image_{app} = \frac{Image_{RAW}}{CF_{app}} \tag{1}$$

where

$$CF_{app} = \frac{1}{\left(fstop_{image}\right)^2} \tag{2}$$

where *f-stop* is the aperture value the image was captured with and $Image_{RAW}$ is the DCRAW converted TIFF image and $Image_{app}$ is the aperture corrected image.

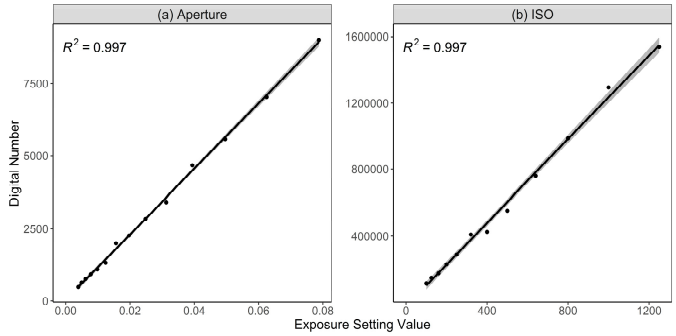

Figure 3. Linear relationships and R^2 between camera exposure settings, (**a**) aperture and (**b**) ISO, and image digital numbers. For (**a**) Aperture, f-numbers have been converted from 'stops' to aperture diameter via 1/f-stop^2.

For ISO, Equation (3) was used to normalise images to an ISO value of 100, the lowest and most commonly used setting on the cameras.

$$Image_{ISO} = \frac{Image_{app}}{\left(\frac{ISO_{image}}{100}\right)} \tag{3}$$

where ISO_{image} is the ISO setting used to capture the image; $Image_{app}$ is the aperture corrected image; and $Image_{ISO}$ is the ISO and aperture corrected image.

2.4.4. Vignetting Correction

An adapted version of the method outlined by LeLong et al. [16] was used in this study; such that camera, band and aperture-specific vignetting correction filters were generated for each data collection date. For each flight, the following steps were taken to produce vignetting filters:

1. Images of matching camera, band and aperture settings were summed together and averaged.
2. The radial vignetting profile of the averaged image was modelled using the median of evenly spaced concentric rings.
3. A 2nd degree polynomial function interpolated the vignetting profile from the median of rings.
4. The interpolation values were then divided by the minimum value to produce a multiplicative correction factor which brightened the corners.

5. The concentric rings are given the value of the correction factor corresponding to its distance from the centre to produce the final vignetting filter (Figure 4 middle).

Unlike LeLong et al. [16], the vignetting filter was applied as a multiplicative filter rather than additive—this is in order to preserve the underlying patterns within the original images.

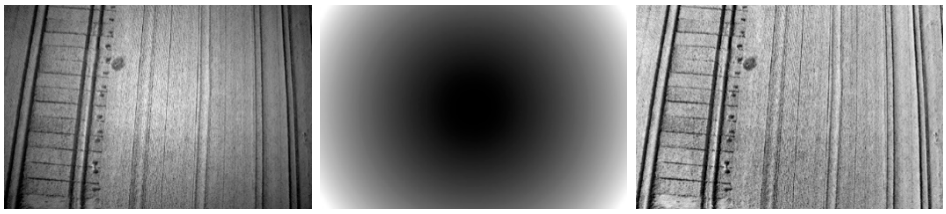

Figure 4. The input NIR image (**left**), generated vignetting filter (**middle**) and vignetting corrected image (**right**).

2.4.5. Cross Calibration Factor and Reflectance Calibration

Before converting image DNs to reflectance, it was necessary to cross calibrate the Tec5 downwelling sensor and the cameras. To do this, the empirical line method was used to retrieve the relationship between Tec5 irradiance measures and exposure and vignetting corrected image DN, over 5 Lambertian reference targets (Figure 5).

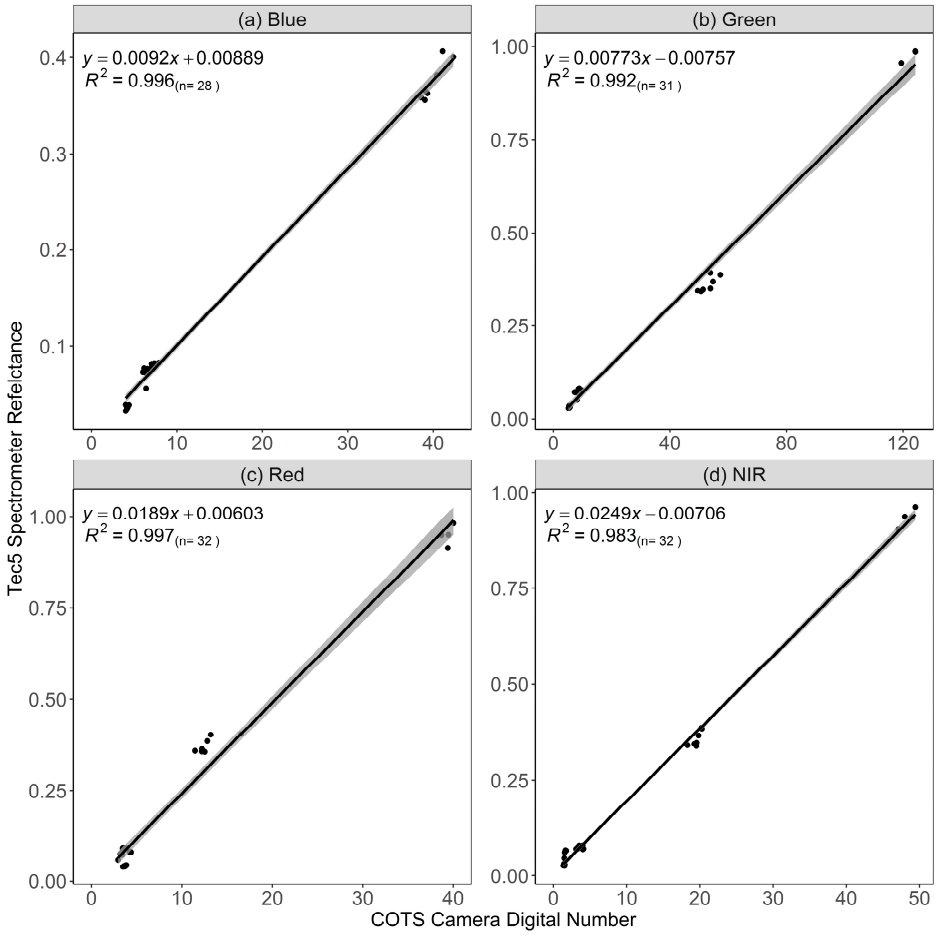

Figure 5. Results of relationships between exposure and vignetting corrected image DNs and Tec5 spectrometer reflectance in wavebands (**a**) Blue, (**b**) Green, (**c**) Red and (**d**) Near Infrared (NIR). All camera bands show strong linear agreements with Tec5 reflectance. Measurements of five black, grey and white spectral reflectance targets were used for this.

The camera and band specific calibration factors, Table 5, were applied to individual images, before Equation (4) was used to convert images from DN to reflectance using time matched Tec5 irradiance measurements.

$$R_{b,t} = \frac{Image_{b,t}}{Tec5\ irradiance_{b,t}} \quad (4)$$

where $R_{b,t}$ is the final reflectance image at time t and waveband b, $Image_{b,t}$ is the single image captured at time t and band b, and $Tec5\ irradiance_{b,t}$ is the Tec5 irradiance measurement captured at the same time, t and convolved to the same band b as the image.

Table 5. Calibration equations for each of the four camera bands. Equations were derived from comparison of camera and Tec5 measurements of five reference targets.

Camera and Band	Calibration Equation
RGB-Blue	$0.0092 \times DN + 0.00889$
RGB-Green	$0.00773 \times DN + 0.00757$
RGB-Red	$0.0189 \times DN + 0.00603$
NIR-Blue	$0.0249 \times DN - 0.00706$

2.4.6. Orthomosaic Generation

Agisoft Photoscan (St. Petersburg, Russia) (1.4.3) [37] was used to process final imagery to orthomosaics, including automatic lens correction. For each date, two orthomosaics were generated, RGB and NIR. Agisoft processing settings, Table 6, were kept consistent for all orthomosaics. In order to minimise the impact of geometric distortion and variation, the disabled blending mode was used to generate the orthomosaic [38]. This mode takes pixel data from the image whose view is closest to nadir. Orthomosaics were generated and exported at 1 cm Ground Sampling Distance (GSD).

Table 6. Processing settings for Agisoft Photoscan. The same settings were used for all Orthomosaics generated.

Processing Step	Setting
Align photos	High
Generate dense point cloud	Medium
Generate mesh	High
Generate orthomosaic	Disabled

NDVI orthomosaics were generated using Equation (5), before mean values for each plot in each camera band and NDVI were extracted using custom Python-based processing tools. As in Holman et al. [12], a 50 cm buffer was applied to each plot before extracting mean values in order to prevent the influence of the plot edge effect.

$$NDVI = \frac{R_{NIR} - R_r}{R_{NIR} + R_r} \quad (5)$$

where R_{NIR} is measured reflectance in the NIR band and R_r is measured reflectance in the red band.

2.5. Canopy Masking

To dissect green canopy from background variables, the Excess Green Red (ExGR) index was used (Equation (6)), with a threshold of > 0 to classify green vegetation [39,40]. Figure 6 shows an example of the produced mask, with reasonable agreement between visual green canopy and pixels classified as green by ExGR. The masks were used to extract mean plot NDVI of green pixels only.

$$ExGR = (2 \times G - R - B) - (1.4 \times R - G) \quad (6)$$

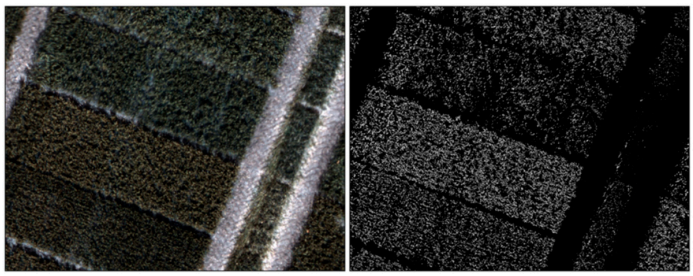

Figure 6. Example image of an RGB image of wheat trial plots and right the ExGR mask output. In the ExGR mask, white represents green classified pixels and black non-green pixels. Imagery is from the 21 June 2017 UAV data collection campaign.

3. Results

3.1. Validation of Calibrations

The influence of the calibration steps applied to COTS camera imagery on precision of results was first assessed. For a single date (21 June 2017), camera imagery was processed with corrections applied cumulatively to understand their influence on results. For clarity, extracted mean plot results for the red and NIR bands have been scaled to a range 0–1.

Red band results (Figure 7) show little impact on linear trend and intercept from correction steps, with consistent slopes around 1.2 and intercepts of 0.07. Correlations show improvement with addition of corrections, $R^2_{RAW} = 0.82$ up to $R^2_{Vignetting} = 0.89$, with camera-related exposure and vignetting offering the greatest gains. No meaningful effect on nRMSE and bias is gained from corrections.

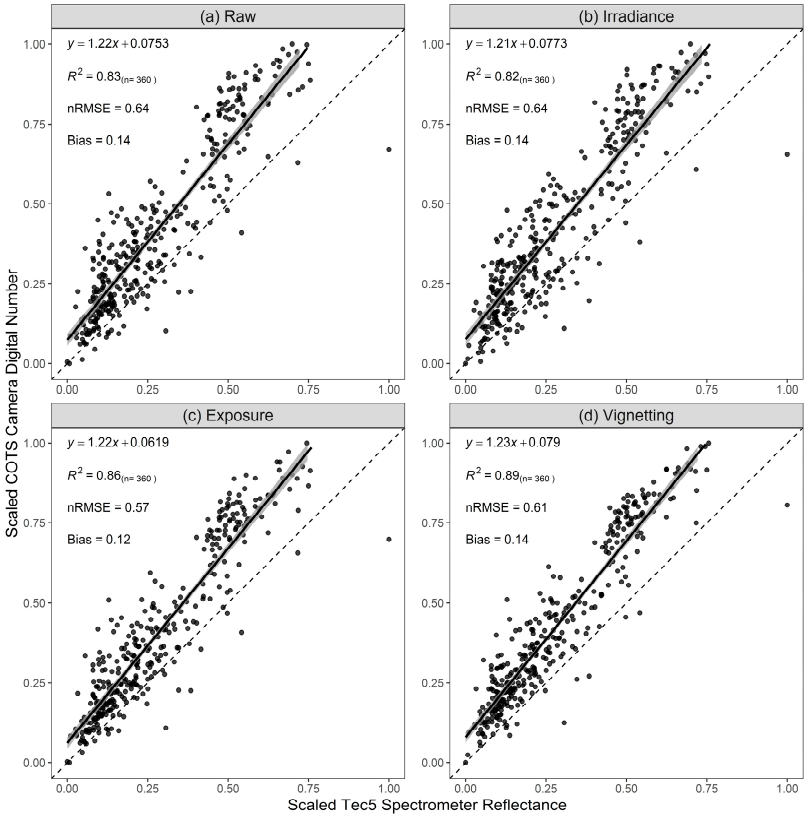

Figure 7. Assessment of the cumulative influence of correction steps on the precision of scaled mean plot measurements in the Red band. Scaled reflectance for (**a**) Raw, (**b**) Irradiance, (**c**) Exposure and (**d**) Vignetting corrected images are compared to scaled COTS camera convolved Tec5 measurements of mean plot reflectance. The dashed line represents the 1:1 line.

For the NIR band (Figure 8), a more significant impact of correction steps is observed. Gains in both the linear fit and R^2 are achieved at each step, with vignetting indicating the most significant influence. Both nRMSE and bias decline in accuracy with the addition of correction steps.

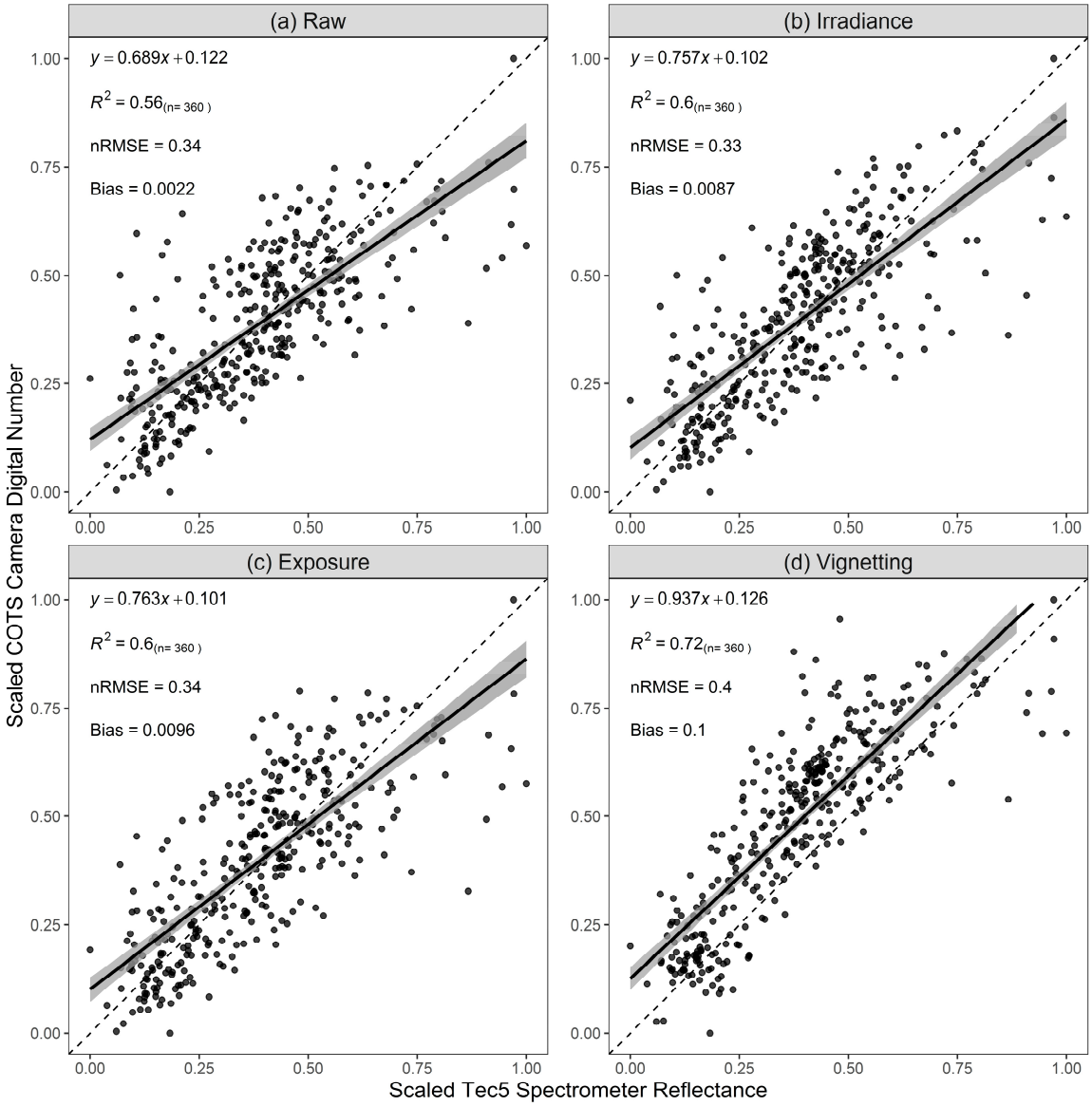

Figure 8. Assessment of the cumulative influence of correction steps on the precision of scaled mean plot measurements in the NIR band. Scaled reflectance for (**a**) Raw, (**b**) Irradiance, (**c**) Exposure and (**d**) Vignetting corrected images are compared to scaled COTS camera convolved Tec5 measurements of mean plot reflectance. The dashed line represents the 1:1 line.

The influence of corrections on NDVI, calculated from non-scaled data (Figure 9), indicates high precision (R^2 = 0.91) but poor accuracy (nRMSE = 0.85, Bias = −0.57) compared to the ground validation data. Addition of irradiance correction greatly improves accuracy, particularly nRMSE, bias and linear trend. Exposure corrections improve correlation, though drops in nRMSE and bias are also introduced. Finally, the addition of vignetting improves all statistics, indicating that the complete collection of calibration steps produces best results in terms of both accuracy and precision.

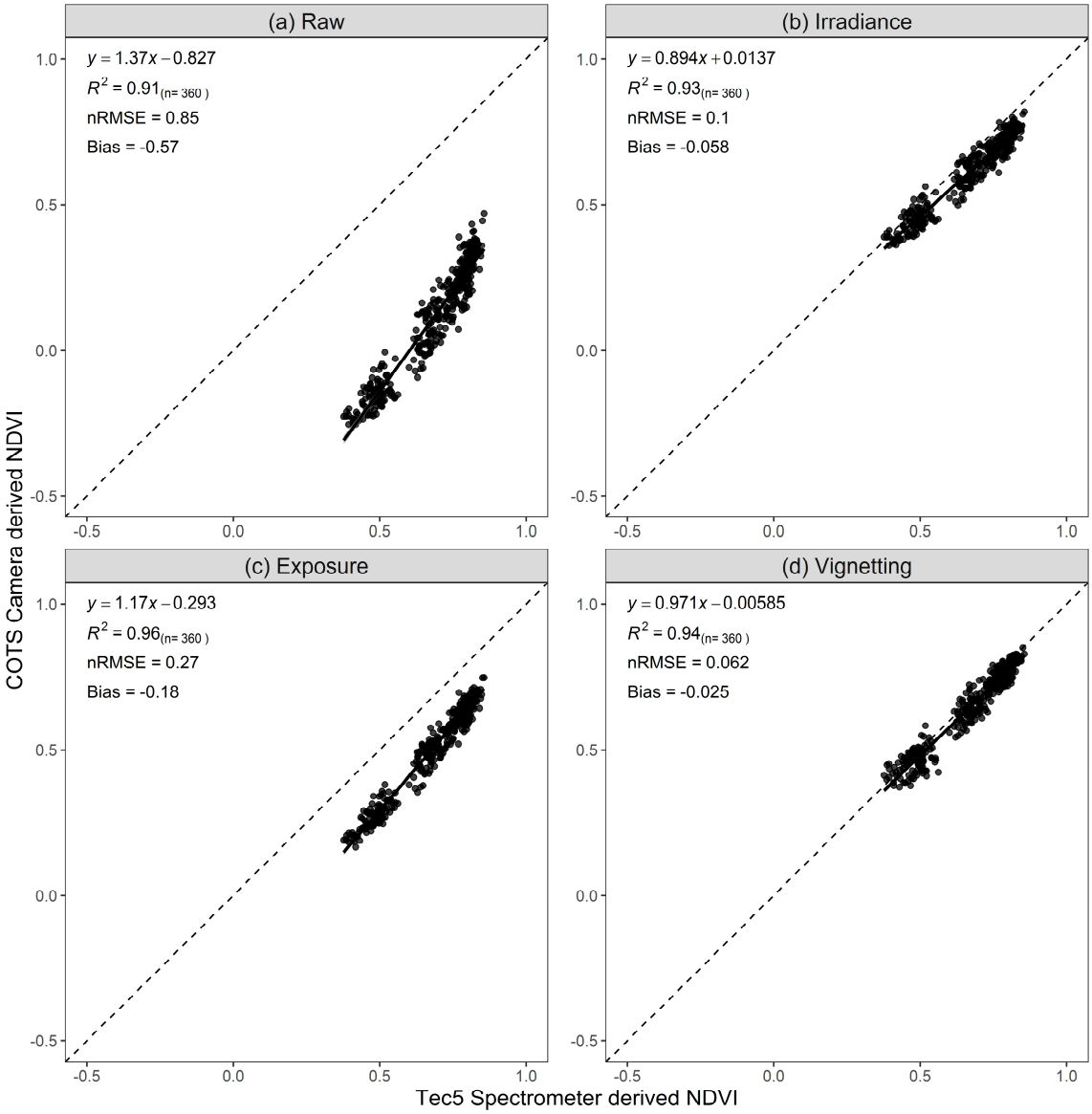

Figure 9. Assessment of the cumulative influence of radiometric corrections applied to COTS camera-derived NDVI. Results for (**a**) Raw, (**b**) Irradiance, (**c**) Exposure and (**d**) Vignetting corrected NDVI are compared to scaled COTS camera convolved Tec5 measurements of mean plot NDVI. Dashed line indicates the 1:1 line.

Further investigation of camera settings (Figure 10), via calculation on Exposure Value (Equation (7)), highlights how the cameras adjusted exposure independently during UAV flight. This independence explains the poor accuracy of NDVI from raw images, where variable camera settings (which can vary between the independent cameras used to gather RGB and NIR data) artificially altering the red to NIR ratio. Inclusion of the varying solar spectral irradiance data corrects this, improving the data consistency greatly; inclusion of exposure and vignetting corrections removes all influence of variable exposure settings, producing even higher accuracy data.

$$ExposureValue_i = 2 \times log_2(f_i) - log_2(t_i) - log_2(ISO_i/100) \quad (7)$$

where f_i is the image aperture, t_i is the image shutter speed and ISO_i is the image ISO value.

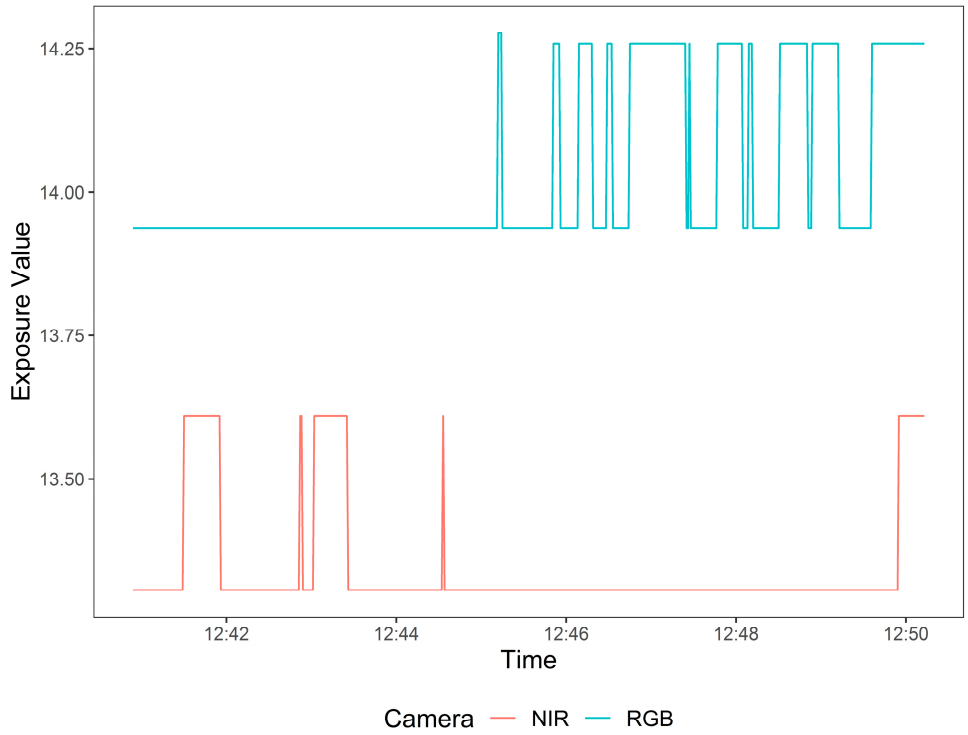

Figure 10. Exposure value for the RGB and NIR cameras over the duration of a flight showing the cameras adjusting exposure independently. Data is from the flight on 21 June 2017.

3.2. Accuracy Assessment of COTS Camera Reflectance

For three dates (19 April 2017, 21 June 2017, and 4 July 2017), the COTS camera-derived mean plot reflectance and calculated NDVI were assessed against Tec5 results. Results for the blue reflectance band (Figure 11) show good fit against the Tec5 in the first two dates ($R^2 > 0.79$), with slopes close to 1 and intercepts close to 0. Small nRMSE and biases also indicate good agreement with the spectrometer. Poorer results in all statistics in the last date (4 July 2017) show reduced agreement with Tec5 reflectance measurements. At this later date, onset of senescence will increase the variability in canopy reflectance both within and between plots, as seen by the increase in vertical error bars. This spatial non-uniformity of senescence onset is better measured by the UAV data as opposed to the spectrometer, leading to poorer statistics at this time point.

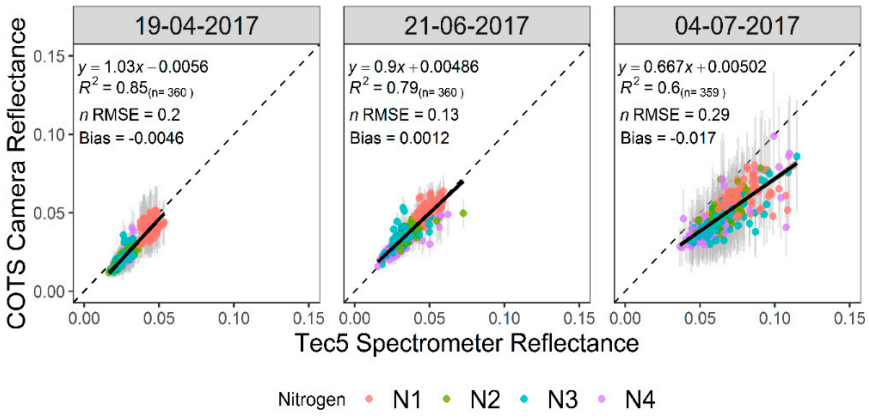

Figure 11. Accuracy assessments of blue band reflectance for three dates. Tec5 reflectance is convolved to the spectral response of the COTS cameras for comparison. The points are coloured based on nitrogen treatment applied to the plot. Standard deviation of reflectance measured by the COTS cameras is presented by vertical error bars. The dashed line represents the 1:1 line.

The green (Figure 12) and red bands (Figure 13) show very similar trends in accuracy to the blue band. Both bands show good fit ($R^2 \geq 0.84$) and consistent small negative biases, indicating slight underestimation of reflectance from the cameras. The same trend between nitrogen treatments over time is also present, as well as the greater within-plot variation for the last date compared to the earlier two.

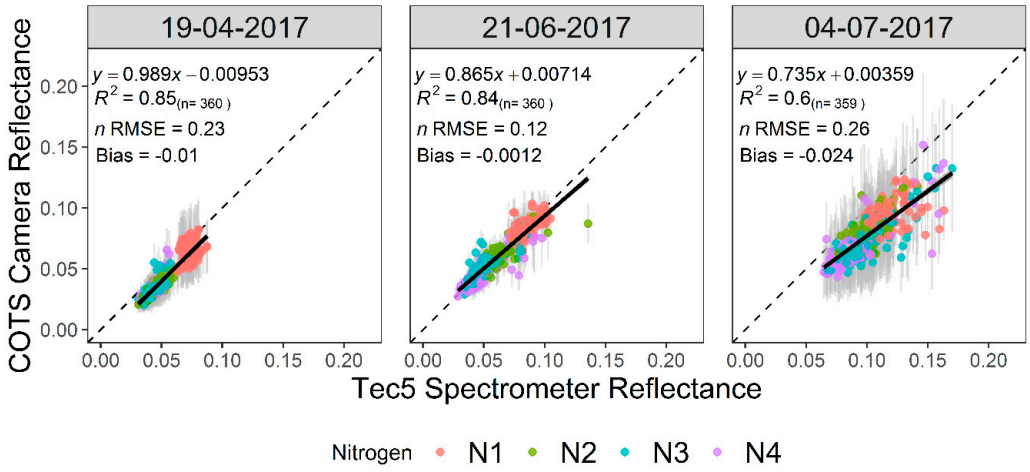

Figure 12. Accuracy assessments of green band reflectance for three dates. Tec5 reflectance is convolved to the spectral response of the COTS cameras for comparison. The points are coloured based on nitrogen treatment applied to the plot. Standard deviation of reflectance measured by the COTS cameras is presented by vertical error bars. The dashed line represents the 1:1 line.

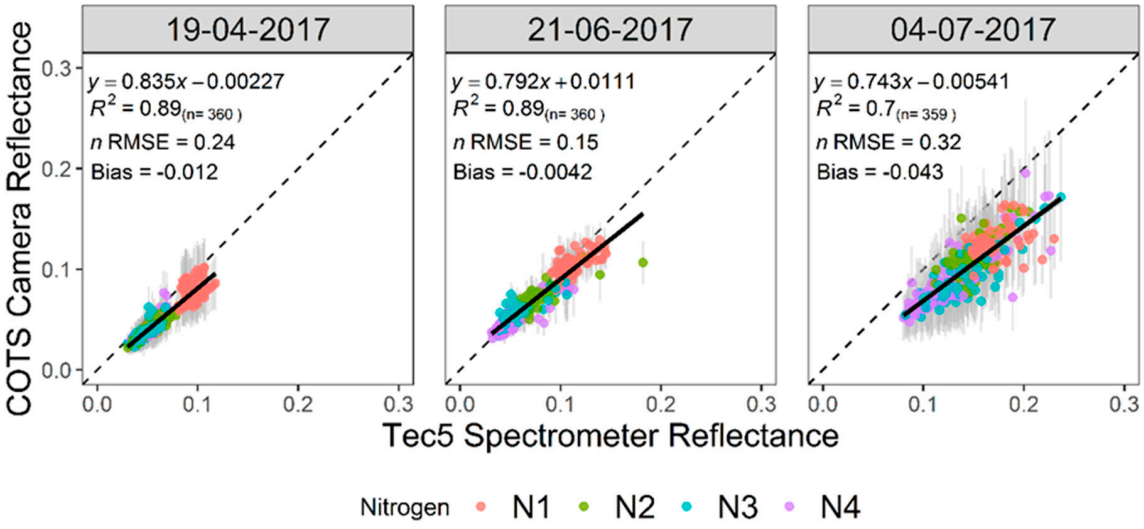

Figure 13. Accuracy assessments of red band reflectance for three dates. Tec5 reflectance is convolved to the spectral response of the COTS cameras for comparison. The points are coloured based on nitrogen treatment applied to the plot. Standard deviation of reflectance measured by the COTS cameras is presented by vertical error bars. The dashed line represents the 1:1 line.

The NIR band (Figure 14) shows reduced fit in comparison to the visible bands ($0.64 \geq R^2 \leq 0.7$) and larger biases indicate lower accuracies achieved in the NIR band. In contrast to the visible bands, the NIR shows lowest accuracy in the first date before improving for the subsequent two dates. Trends between nitrogen treatments show that N1 treatments consistently have the lowest reflectance, indicating reduced vegetation in these plots, as expected. Standard deviations show the same increased variability in plot reflectance of the last date. Overall, the results of the NIR camera indicate lower sensitivity to higher canopy reflectance compared to the Tec5.

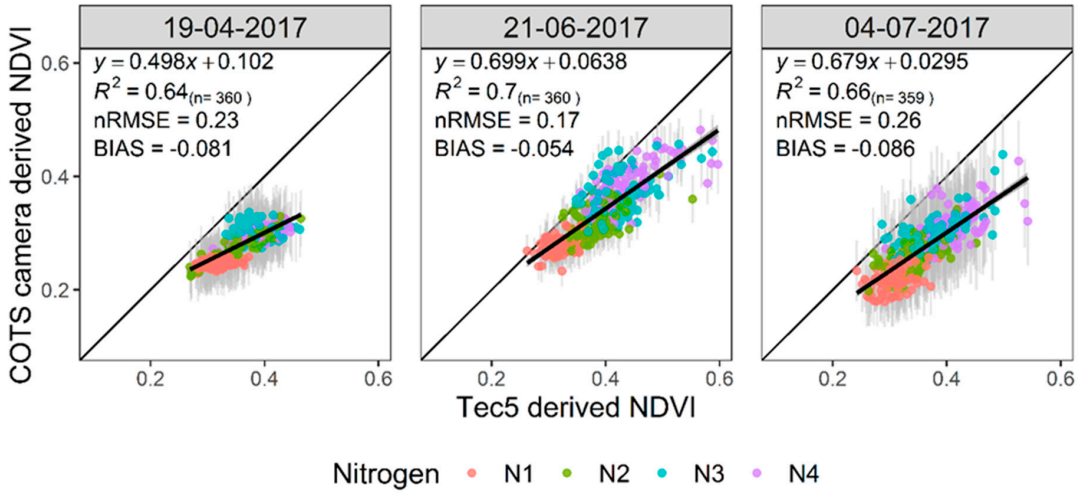

Figure 14. Accuracy assessments of NIR band reflectance for three dates. Tec5 reflectance is convolved to the spectral response of the COTS cameras for comparison. The points are coloured based on nitrogen treatment applied to the plot. Standard deviation of reflectance measured by the COTS cameras is presented by vertical error bars. The dashed line represents the 1:1 line.

Accuracy assessments of calculated NDVI (Figure 15) show high correlations ($R^2 \geq 0.88$) and low nRMSE. Additionally, biases indicating overall very good accuracy are achieved from the COTS cameras. Temporal accuracy shows a similar drop in accuracy for the final date, as seen in the visible bands, but overall good stability is achieved. The lower accuracy of the NIR band appears to not impact the accuracy of calculated NDVI.

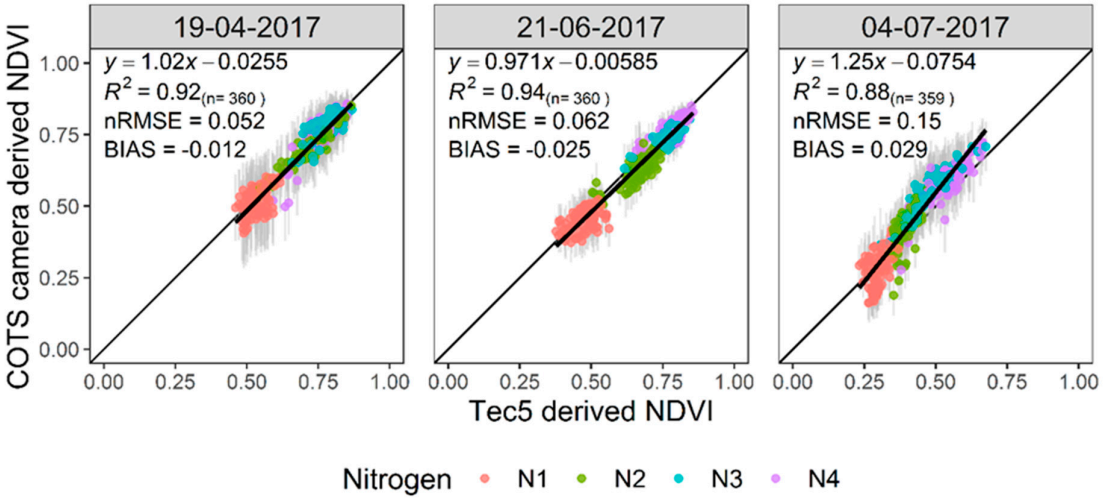

Figure 15. Accuracy assessments COTS camera-derived NDVI for three dates. The points are coloured based on nitrogen treatment applied to the plot. Standard deviation of reflectance measured by the COTS cameras is presented by vertical error bars. The dashed line represents the 1:1 line.

Additional assessment compared results from the COTS cameras with the Parrot Sequoia (Figure 16), a commercially available multispectral imager whose data is processed using proprietary calibrations. Of the individual bands, green showed the strongest agreement between the two camera systems, with comparable R^2, nRMSE and bias. The red band indicated poorer accuracy achieved by the Sequoia, with large nRMSE, negative biases and poorer linear agreement with the Tec5. In the NIR band, both camera systems showed comparable accuracy levels and precision. NDVI results show greater accuracy achieved by the COTS cameras, with the Sequoia overestimating NDVI compared to the TEC5 (as indicated by positive bias). The similarity in results between the COTS cameras and Parrot

Sequoia, particularly in the NIR waveband, suggests discrepancy between imaging and non-imaging spectral monitoring technologies.

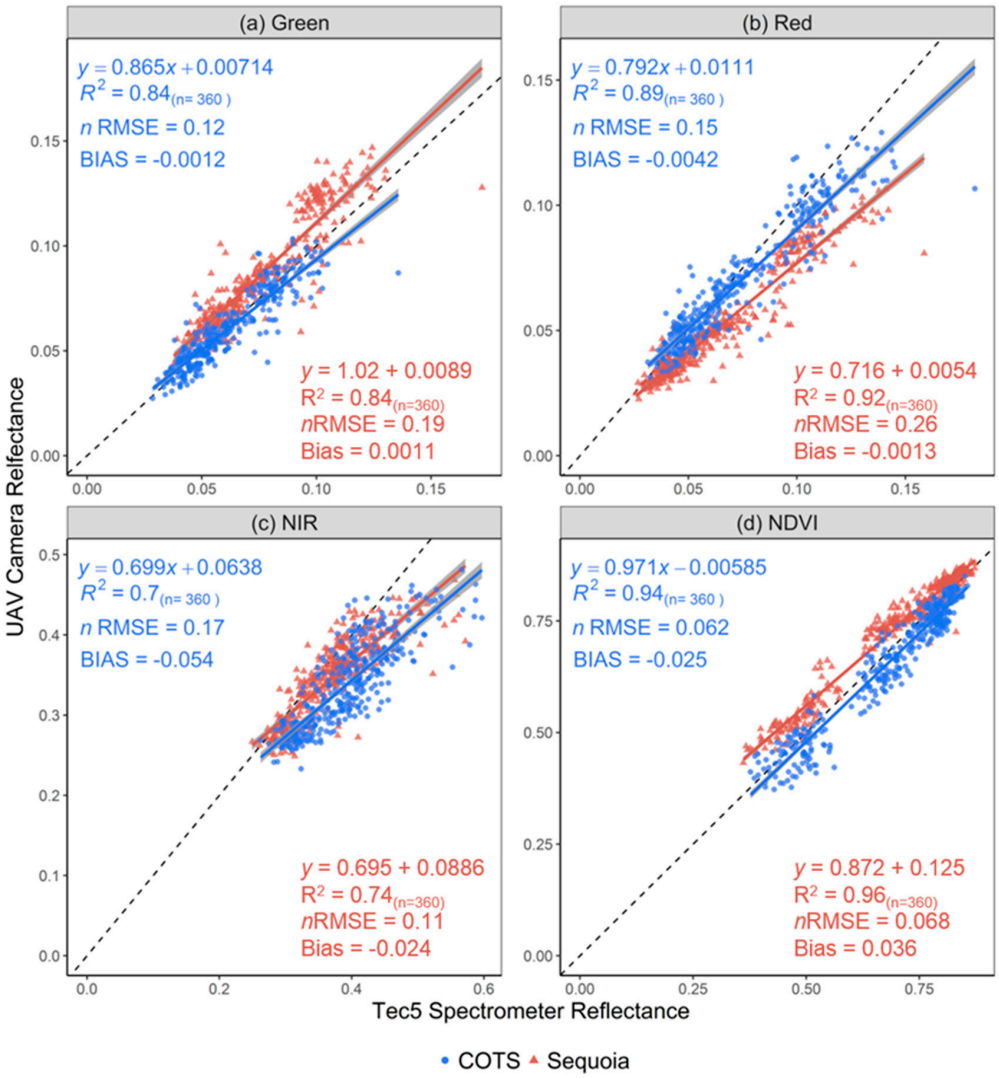

Figure 16. Comparison of accuracies achieved by COTS (blue) cameras and Parrot Sequoia (red) in (**a**) green, (**b**) red and (**c**) NIR reflectance and (**d**) NDVI. Comparisons are made against Tec5 measure reflectances and NDVI. Reflectance was measured from both cameras on the same date (21 June 2017), whilst Tec5 measurements were collected two days later. The dashed line represents the 1:1 line.

3.3. Influence of Canopy on NDVI

The focus of this component of the study was to investigate the potential for high spatial resolution imagery to be used to dissect the influence of canopy cover on derived vegetation indices. For nine dates, the COTS camera imagery was calibrated, processed and NDVI calculated. For one date, 18 May 2017, significant shadowing impacted on the results of masking; as such, this date was removed from further processing. For the remaining eight dates, a subset of ten cultivars have been used. Examples of cropped NDVI orthomosaics for three dates highlight the temporal and spatial variation achieved from the COTS cameras (Figure 17).

Assessment of $NDVI_{unmasked}$ (Figure 18a, top row) shows typical trends over time and between nitrogen treatments. All cultivars and treatment levels show a starting NDVI value around 0.4, increasing to a peak in late-May before dropping off at the end of the season. Comparison between nitrogen treatments shows clear differences between plots with (N2, N3 and N4) and without (N1)

fertiliser application, with the N1 treatment showing lower maximum NDVI, despite similar initial NDVI values (~0.4). The drop in NDVI values at the end of the season is likely a result of senescence and the browning of crop canopy. Application of ExGR derived masks (Figure 18b, second row) to extract NDVI of green classified pixels only, produces new trends between treatments and over time. For all treatments, shallower temporal trends in NDVI are observed, with the N1 treatment displaying a close to horizontal trend with the peak in late-May no longer featuring. Comparing the difference between $NDVI_{unmasked}$ and $NDVI_{ExGR}$ (Figure 18c, third row) shows the greatest influence of masking occurs early season where % green pixel is lowest (Figure 18d, bottom row).

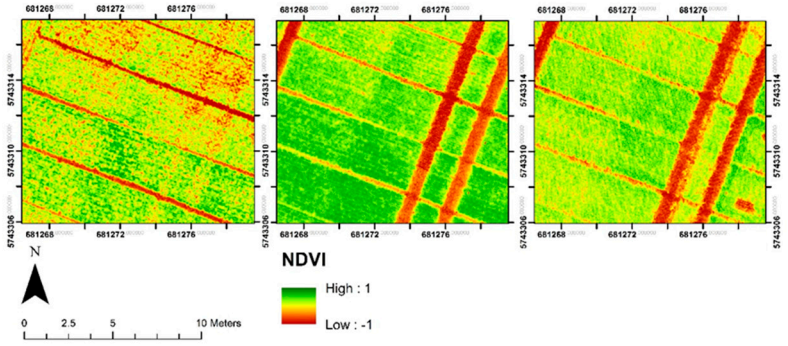

Figure 17. Example subset of NDVI orthomosaics from three dates—27 March 2017 (**left**), 18 May 2017 (**middle**), 21 June 2017 (**right**). Orthomosaics highlight the spatial variability of NDVI both between and within plots.

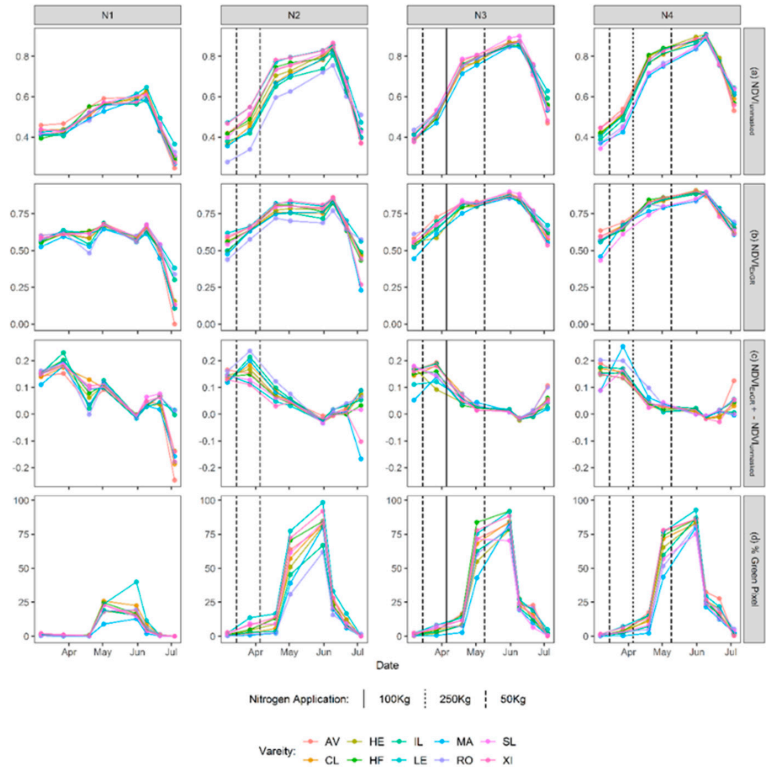

Figure 18. Temporal trends of ten wheat cultivars grown under four different nitrogen treatments for: (**a**) the standard unmasked mean NDVI; (**b**) mean NDVI derived from ExGR masked plots to remove the influence of background soil; (**c**) displaying temporal differences between masked and unmasked NDVI results; (**d**) percentage green pixel as calculated from the ExGR masks. Nitrogen application dates and quantities for the N2, N3 and N4 treatments are presented by the vertical lines. All data represent the means of three replicates.

4. Discussion

This study has provided a quantitative assessment of commercial off the shelf (COTS) digital cameras for supporting the UAV-based remote sensing of field-based crop trials. COTS cameras provide very high spatial resolution imagery, potentially enabling the separation of canopy influences on vegetation indices from those of the background soil and thus making the derived information more relevant to crop health assessment and monitoring.

We have designed and tested a data processing workflow to radiometrically calibrate COTS camera imagery into reflectance units, in blue, green, red and NIR wavebands. Cameras were allowed to vary their exposure settings during flight, to cope with varying solar illumination conditions, whilst having a fixed shutter speed to avoid blurring from the UAV-motion. We find that our processing workflow can cope with this setup, and that the influence of the different pre-processing steps varies by band. In particular, the NIR band showed greater impact from vignetting corrections than the visible wavebands, agreeing with past studies which found that the modified internal filters used in NIR COTS cameras increase the impact of vignetting in images by up to 30% [16,25]. The influence of varied exposure settings as well as the success of the developed corrections was perhaps most clear during calculations of NDVI, because the separate visible and NIR COTS cameras used did not necessarily change their exposure settings in the same way at the same time, leading to artificial changes in derived NDVI. Even without corrections, good precision is observed in COTS camera calculated NDVI. However, NDVI values calculated from such raw camera data (or that calibrated into radiances rather than reflectances) are always significantly different to those derived from calibrated reflectances, and this difference is sensor specific [41]. Ultimately, this means VIs calculated from different sensors can only be intercompared in a fully meaningful way if calculated from calibrated reflectance measures.

Temporal consistency of the developed workflow was tested over three dates via comparison of COTS camera and Tec5 field-spectrometer-derived mean plot reflectance. Results showed good accuracy with NDVI results ($R^2 \geq 0.88$, nRMSE ≤ 0.15) comparable to those achieved by other studies [25,42,43]. Consistency of results over this period indicates a good level of robustness in the developed methods for variable weather conditions both during and between data collection flights. Some variability occurred between time points in all bands and NDVI; likely a result of the UAV and Tec5 spectrometer obtaining measurements at different spatial resolutions [38] and datasets not being collected on the same date. Rossi et al. [44] demonstrated the impact of non-concurrent data collection when comparing different reflectance from different sensors, with a single day lag negatively impacting on correlation results. Variability in accuracy also occurred between bands, particularly for visible versus NIR, which was observed consistently over time. The same variations were also observed in the Parrot Sequoia results, as well as by Aasen and Bolten [38], who found that the varying field of views between cameras and spectrometers coupled with varying bidirectional reflectance factors in visible and NIR wavelengths impacted on correlations in the NIR band. Lack of influence of the NIR results on NDVI accuracy further indicates disparity between imaging and non-imaging measurement systems, as opposed to error in the NIR band. Investigation of this variability between bands and data sources should be a focus of future work.

Application of the very high resolution (GSD = 1 cm) reflectance imagery over time was used to investigate the impact of canopy cover and background soil on derived NDVI. Results of the unmasked NDVI presented temporal trends over a season in relation to differing nitrogen treatments and for different wheat cultivars. Masking of background soil pixels, via Excess Green Red, offered new insights into temporal NDVI trends in relation to canopy cover. Greatest differences between $NDVI_{unmasked}$ and $NDVI_{ExGR}$ (Figure 18d) occurred in the early season, where canopy cover is lowest [45], indicating that background soil and canopy cover can artificially influence measured vegetation indices. Isolation of the crop canopy for VI measurements should provide improved relationships between VI and traits of interest such as yield, canopy quality, senescence and canopy chlorophyll content [10,46], and therefore should be a focus of future studies.

5. Conclusions

This study has presented methods for radiometric calibration of commercial off the shelf digital camera imagery to reflectance for use in plant phenotyping. New calibrations for image exposure normalisation, combined with robust vignetting and irradiance corrections produced accurate reflectance and NDVI, comparable to a Parrot Sequoia multispectral camera and Tec5 ground spectrometer. The very high-resolution imagery obtained provided new insights into the influence of canopy cover and background soil on derived plot NDVI, especially in the early season. Future studies should look to incorporate additional UAV phenotyping methods such as 3D structure and thermal measurements to provide a more extensive low-cost phenotyping UAV-based system.

Author Contributions: Conceptualization, F.H.H., M.J.W., M.J.H. and A.B.R.; data curation, F.H.H., M.C. and A.B.R.; methodology, F.H.H and M.J.W. and A.B.R.; resources, M.J.W., M.J.H. and A.B.R; software, F.H.H; supervision, M.J.W., M.J.H. and A.B.R; validation, F.H.H; visualization, F.H.H; writing—original draft, F.H.H; writing—review and editing, F.H.H., M.J.W., M.J.H. and A.B.R.

Funding: This project forms part of and is funded by a BBSRC CASE Studentship (BB/L016516/1), in partnership with Bayer Crop Sciences. Martin J. Wooster is supported by the National Centre for Earth Observation (NCEO). The work at Rothamsted Research was supported by the Biotechnology and Biological Sciences Research Council (BBSRC) the Designing Future Wheat programme (BB/P016855/1) and the United Kingdom Department for Environment, Food and Rural Affairs funding of the Wheat Genetic Improvement Network (CH1090).

Acknowledgments: The authors would like to thank Dr C. MacLellan and the NERC Field Spectroscopy Facility for his assistance in camera calibration; Professor Serge Wich (Liverpool John Moores) for loaning of the Parrot Sequoia; Dr Pouria Sadeghi-Tehran for his advice and support with data analysis.

Conflicts of Interest: The authors declare no conflict of interest.

References

1. Pask, A.J.D.; Pietragalla, J.; Mullan, D.M.; Reynolds, M.P. *Physiological Breeding II: A Field Guide to Wheat Phenotyping*; CIMMYT: Mexico City, Mexico, 2012.
2. Khan, Z.; Chopin, J.; Cai, J.; Eichi, V.R.; Haefele, S.; Miklavcic, S.J. Quantitative Estimation of Wheat Phenotyping Traits Using Ground and Aerial Imagery. *Remote Sens.* **2018**, *10*, 950. [CrossRef]
3. Kipp, S.; Mistele, B.; Baresel, P.; Schmidhalter, U. High-throughput phenotyping early plant vigour of winter wheat. *Eur. J. Agron.* **2014**, *52*, 271–278. [CrossRef]
4. Cabrera-Bosquet, L.; Molero, G.; Stellacci, A.M.; Bort, J.; Nogues, S.; Araus, J.L. NDVI as a potential tool for predicting biomass, plant nitrogen content and growth in wheat genotypes subjected to different water and nitrogen conditions. *Cereal Res. Commun.* **2011**, *39*, 147–159. [CrossRef]
5. Bendig, J.; Bolten, A.; Bennertz, S.; Broscheit, J.; Eichfuss, S.; Bareth, G. Estimating Biomass of Barley Using Crop Surface Models (CSMs) Derived from UAV-Based RGB Imaging. *Remote Sens.* **2014**, *6*, 10395–10412. [CrossRef]
6. Muñoz-Huerta, R.F.; Guevara-Gonzalez, R.G.; Contreras-Medina, L.M.; Torres-Pacheco, I.; Prado-Olivarez, J.; Ocampo-Velazquez, R.V. A Review of Methods for Sensing the Nitrogen Status in Plants: Advantages, Disadvantages and Recent Advances. *Sensors* **2013**, *13*, 10823–10843. [CrossRef] [PubMed]
7. Ali, M.; Montzka, C.; Stadler, A.; Menz, G.; Thonfeld, F.; Vereecken, H. Estimation and Validation of RapidEye-Based Time-Series of Leaf Area Index for Winter Wheat in the Rur Catchment (Germany). *Remote Sens.* **2015**, *7*, 2808–2831. [CrossRef]
8. Zheng, G.; Moskal, L.M. Retrieving Leaf Area Index (LAI) Using Remote Sensing: Theories, Methods and Sensors. *Sensors* **2009**, *9*, 2719–2745. [CrossRef]
9. Lopresti, M.F.; Di Bella, C.M.; Degioanni, A.J. Relationship between MODIS-NDVI data and wheat yield: A case study in Northern Buenos Aires province, Argentina. *Inf. Process. Agric.* **2015**, *2*, 73–84. [CrossRef]
10. Jay, S.; Gorretta, N.; Morel, J.; Maupas, F.; Bendoula, R.; Rabatel, G.; Dutartre, D.; Comar, A.; Baret, F. Estimating leaf chlorophyll content in sugar beet canopies using millimeter- to centimeter-scale reflectance imagery. *Remote Sens. Environ.* **2017**, *198*, 173–186. [CrossRef]
11. Duan, T.; Chapman, S.; Guo, Y.; Zheng, B. Dynamic monitoring of NDVI in wheat agronomy and breeding trials using an unmanned aerial vehicle. *Field Crop. Res.* **2017**, *210*, 71–80. [CrossRef]

12. Holman, F.H.; Riche, A.B.; Michalski, A.; Castle, M.; Wooster, M.J.; Hawkesford, M.J. High Throughput Field Phenotyping of Wheat Plant Height and Growth Rate in Field Plot Trials Using UAV Based Remote Sensing. *Remote Sens.* **2016**, *8*, 1031. [CrossRef]
13. Parrot SEQUOIA+|Parrot Store Official. Available online: https://www.parrot.com/business-solutions-uk/parrot-professional/parrot-sequoia (accessed on 8 April 2019).
14. Young, N.E.; Anderson, R.S.; Chignell, S.M.; Vorster, A.G.; Lawrence, R.; Evangelista, P.H. A survival guide to Landsat preprocessing. *Ecolgy* **2017**, *98*, 920–932. [CrossRef] [PubMed]
15. Lebourgeois, V.; Bégué, A.; Labbé, S.; Mallavan, B.; Prévot, L.; Roux, B. Can Commercial Digital Cameras Be Used as Multispectral Sensors? A Crop Monitoring Test. *Sensors* **2008**, *8*, 7300–7322. [CrossRef] [PubMed]
16. Lelong, C.C.D.; Burger, P.; Jubelin, G.; Roux, B.; Labbé, S.; Baret, F. Assessment of Unmanned Aerial Vehicles Imagery for Quantitative Monitoring of Wheat Crop in Small Plots. *Sensors* **2008**, *8*, 3557–3585. [CrossRef] [PubMed]
17. Mathews, A.J. A Practical UAV Remote Sensing Methodology to Generate Multispectral Orthophotos for Vineyards: Estimation of Spectral Reflectance Using Compact Digital Cameras. *Int. J. Appl. Geospat. Res.* **2015**, *6*, 65–87. [CrossRef]
18. Gibson-Poole, S.; Humphris, S.; Toth, I.; Hamilton, A. Identification of the onset of disease within a potato crop using a UAV equipped with un-modified and modified commercial off-the-shelf digital cameras. *Adv. Anim. Biosci.* **2017**, *8*, 812–816. [CrossRef]
19. Filippa, G.; Cremonese, E.; Migliavacca, M.; Galvagno, M.; Sonnentag, O.; Humphreys, E.; Hufkens, K.; Ryu, Y.; Verfaillie, J.; Di Cella, U.M.; et al. NDVI derived from near-infrared-enabled digital cameras: Applicability across different plant functional types. *Agric. For. Meteorol.* **2018**, *249*, 275–285. [CrossRef]
20. Petach, A.R.; Toomey, M.; Aubrecht, D.M.; Richardson, A.D. Monitoring vegetation phenology using an infrared-enabled security camera. *Agric. For. Meteorol.* **2014**, *195*, 143–151. [CrossRef]
21. Sakamoto, T.; Shibayama, M.; Kimura, A.; Takada, E. Assessment of digital camera-derived vegetation indices in quantitative monitoring of seasonal rice growth. *ISPRS J. Photogramm. Remote Sens.* **2011**, *66*, 872–882. [CrossRef]
22. Sakamoto, T.; Gitelson, A.A.; Nguy-Robertson, A.L.; Arkebauer, T.J.; Wardlow, B.D.; Suyker, A.E.; Verma, S.B.; Shibayama, M. An alternative method using digital cameras for continuous monitoring of crop status. *Agric. For. Meteorol.* **2012**, *154*, 113–126. [CrossRef]
23. Luo, Y.; El-Madany, T.S.; Filippa, G.; Ma, X.; Ahrens, B.; Carrara, A.; Gonzalez-Cascon, R.; Cremonese, E.; Galvagno, M.; Hammer, T.W.; et al. Using Near-Infrared-Enabled Digital Repeat Photography to Track Structural and Physiological Phenology in Mediterranean Tree-Grass Ecosystems. *Remote Sens.* **2018**, *10*, 1293. [CrossRef]
24. Kelcey, J.; Lucieer, A. Sensor Correction of a 6-Band Multispectral Imaging Sensor for UAV Remote Sensing. *Remote Sens.* **2012**, *4*, 1462–1493. [CrossRef]
25. Berra, E.F.; Gaulton, R.; Barr, S. Commercial Off-the-Shelf Digital Cameras on Unmanned Aerial Vehicles for Multitemporal Monitoring of Vegetation Reflectance and NDVI. *IEEE Trans. Geosci. Remote Sens.* **2017**, *55*, 4878–4886. [CrossRef]
26. Smith, G.M.; Milton, E.J. The use of the empirical line method to calibrate remotely sensed data to reflectance. *Int. J. Remote Sens.* **1999**, *20*, 2653–2662. [CrossRef]
27. Anderson, K.; Milton, E.J. Characterisation of the apparent reflectance of a concrete calibration surface over different time scales. In Proceedings of the Ninth International Symposium on Physical Measurements and Signatures in Remote Sensing (ISPMSRS), Beijing, China, 17–19 October 2005.
28. Ritchie, G.L.; Sullivan, D.G.; Perry, C.D.; Hook, J.E.; Bednarz, C.W. Preparation of a Low-Cost Digital Camera System for Remote Sensing. *Appl. Eng. Agric.* **2008**, *24*, 885–894. [CrossRef]
29. Hiscocks, P.D. Measuring Luminance with a Digital Camera. Available online: https://www.atecorp.com/atecorp/media/pdfs/data-sheets/Tektronix-J16_Application.pdf (accessed on 10 August 2017).
30. Spreading Wings S900–Highly Portable, Powerful Aerial System for the Demanding Filmmaker. Available online: https://www.dji.com/uk/spreading-wings-s900 (accessed on 8 April 2019).
31. Smart Camera|a5100 NFC & Wi-Fi Enabled Digital Camera|Sony UK. Available online: https://www.sony.co.uk/electronics/interchangeable-lens-cameras/ilce-5100-body-kit (accessed on 8 April 2019).

32. Berra, E.; Gibson-Poole, S.; MacArthur, A.; Gaulton, R.; Hamilton, A. Estimation of the spectral sensitivity functions of un-modified and modified commercial off-the-shelf digital cameras to enable their use as a multispectral imaging system for UAVs. *ISPRS–Int. Arch. Photogramm. Remote Sens. Spat. Inf. Sci.* **2015**, *XL-1/W4*, 207–214. [CrossRef]
33. Geo 7X|Handhelds|Trimble Geospatial. Available online: https://geospatial.trimble.com/products-and-solutions/geo-7x (accessed on 8 April 2019).
34. Customized Systems for HandySpec® Field|tec5. Available online: https://www.tec5.com/en/products/custom-solutions/handyspec-field (accessed on 8 April 2019).
35. Professional Photogrammetry and Drone Mapping Software. Available online: https://www.pix4d.com/ (accessed on 10 April 2019).
36. Decoding Raw Digital Photos in Linux. Available online: https://www.cybercom.net/~{}dcoffin/dcraw/ (accessed on 18 February 2019).
37. Agisoft Agisoft PhotoScan User Manual Professional Edition, Version 1.2. Available online: http://www.agisoft.com/pdf/photoscan-pro_1_2_en.pdf (accessed on 24 August 2016).
38. Aasen, H.; Bolten, A. Multi-temporal high-resolution imaging spectroscopy with hyperspectral 2D Imagers–from Theory to Application. *Remote Sens. Environ.* **2018**, *205*, 374–389. [CrossRef]
39. Meyer, G.E.; Neto, J.C. Verification of color vegetation indices for automated crop imaging applications. *Comput. Electron. Agric.* **2008**, *63*, 282–293. [CrossRef]
40. Sadeghi-Tehran, P.; Virlet, N.; Sabermanesh, K.; Hawkesford, M.J. Multi-feature machine learning model for automatic segmentation of green fractional vegetation cover for high-throughput field phenotyping. *Plant Methods* **2017**, *13*, 103. [CrossRef]
41. Zhou, X.; Guan, H.; Xie, H.; Wilson, J.L. Analysis and optimization of NDVI definitions and areal fraction models in remote sensing of vegetation. *Int. J. Remote Sens.* **2009**, *30*, 721–751. [CrossRef]
42. Hassan, M.A.; Yang, M.; Rasheed, A.; Jin, X.; Xia, X.; Xiao, Y.; He, Z. Time-Series Multispectral Indices from Unmanned Aerial Vehicle Imagery Reveal Senescence Rate in Bread Wheat. *Remote Sens.* **2018**, *10*, 809. [CrossRef]
43. Hassan, M.A.; Yang, M.; Rasheed, A.; Yang, G.; Reynolds, M.; Xia, X.; Xiao, Y.; He, Z. A rapid monitoring of NDVI across the wheat growth cycle for grain yield prediction using a multi-spectral UAV platform. *Plant Sci.* **2019**, *282*, 95–103. [CrossRef] [PubMed]
44. Rossi, M.; Niedrist, G.; Asam, S.; Tonon, G.; Tomelleri, E.; Zebisch, M. A Comparison of the Signal from Diverse Optical Sensors for Monitoring Alpine Grassland Dynamics. *Remote Sens.* **2019**, *11*, 296. [CrossRef]
45. Agriculture and Horticulture Development Board (AHDB). *Wheat Growth Guide*; Agriculture and Horticulture Development Board (AHDB): Warwickshire, UK, 2015.
46. Makanza, R.; Zaman-Allah, M.; Cairns, J.E.; Magorokosho, C.; Tarekegne, A.; Olsen, M.; Prasanna, B.M. High-Throughput Phenotyping of Canopy Cover and Senescence in Maize Field Trials Using Aerial Digital Canopy Imaging. *Remote Sens.* **2018**, *10*, 330. [CrossRef]

4.3 Additions to Published Article

Improvements and corrections to two figures from the published article are provided below. Paper figure 6 has been brightened to improve image clarity (Figure 4.2); and paper figure 14 X-axis has been corrected to read NIR reflectance (Figure 4.1).

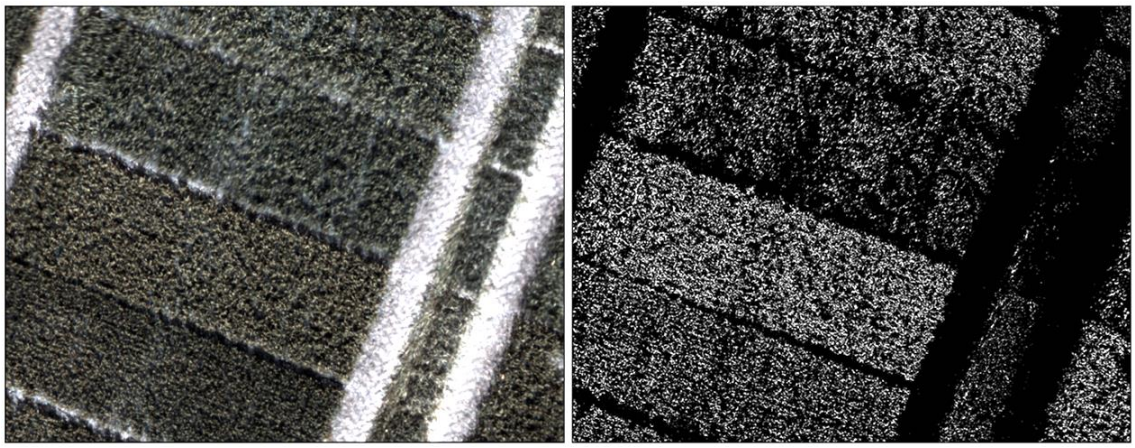

Figure 4.2. Example image of an RGB image of wheat trial plots and right the ExGR mask output. In the ExGR mask, white represents green classified pixels and black non-green pixels. Imagery is from the 21 June 2017 UAV data collection campaign. This figure has been brightened to improve clarity; original image is Figure 6 in Holman *et al.* (2019).

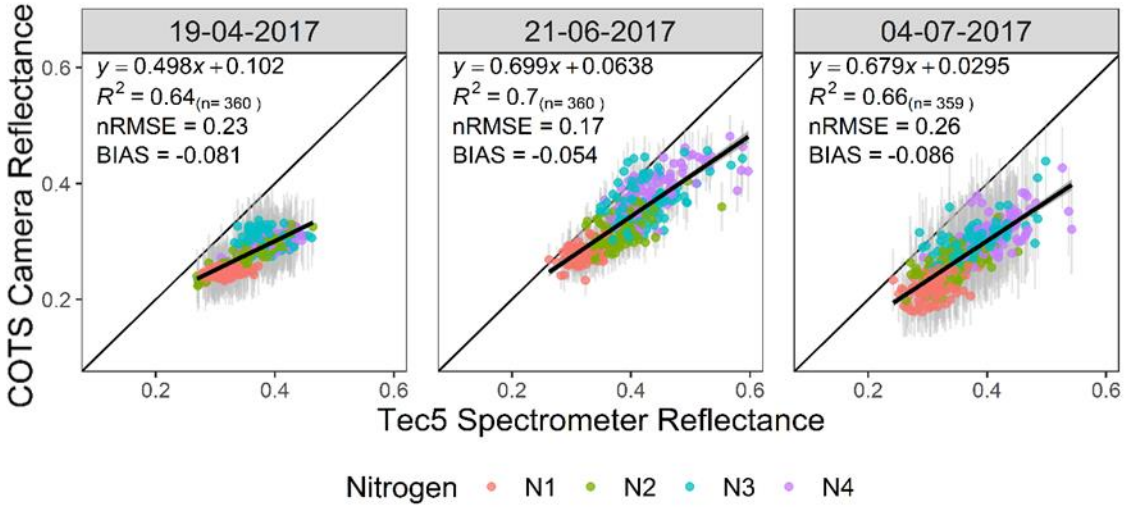

Figure 4.1. Accuracy assessments of NIR band reflectance from three dates. Tec reflectance is convolved to the spectral response of the OCTS cameras for comparison. The points are coloured based on nitrogen treatment applied to the plot. Standard deviation of reflectance measured by the COTS cameras is presented by vertical error bars. The dashed line represents the 1:1 line. Original figure is from Holman *et al.* (2019) and has been corrected for an incorrect x-axis label.

4.4 Camera Spectral Response Determination

As discussed in the published article (Section 4.2), knowing the exact spectral sensitivities and wavebands of COTS cameras is imperative for accurate correction of pixel digital numbers to measures of reflectance (Berra et al., 2015). However, the spectral sensitivity of most digital cameras internal CMOS (Complementary Metal-Oxide-Semiconductor) or CCD (Charge-Coupled Device) sensors are typically not published by manufacturers. Furthermore, when adapting these cameras to make use of their natural sensitivity to NIR, the replacement of the internal NIR blocking filter for an RGB blocking filter will have unknown influence on spectral response of the camera. Therefore, it is necessary for users to estimate the unique spectral response of each individual camera (Darrodi et al., 2015; Jiang et al., 2013). The methods used to do this, and results achieved are outlined with this section of the chapter.

4.4.1 Materials and Methods

A double monochromator (OL 750-M-D Double Grating Monochromator, Optronic Laboratories Inc., Orlando, Florida, USA) was used to produce monochromatic light at user defined wavelengths. An integrating sphere was attached to the exit opening of the monochromator to produce an evenly illuminated surface which could be photographed (Figure 4.3). The camera, whose spectral response was being determined, was positioned with its lens covering the viewing port of the integrating sphere to capture images of monochromatic light (Figure 4.4). All external lights were turned off, and a black cloth placed over the sphere and camera to remove any chances of contamination of imagery from external light sources.

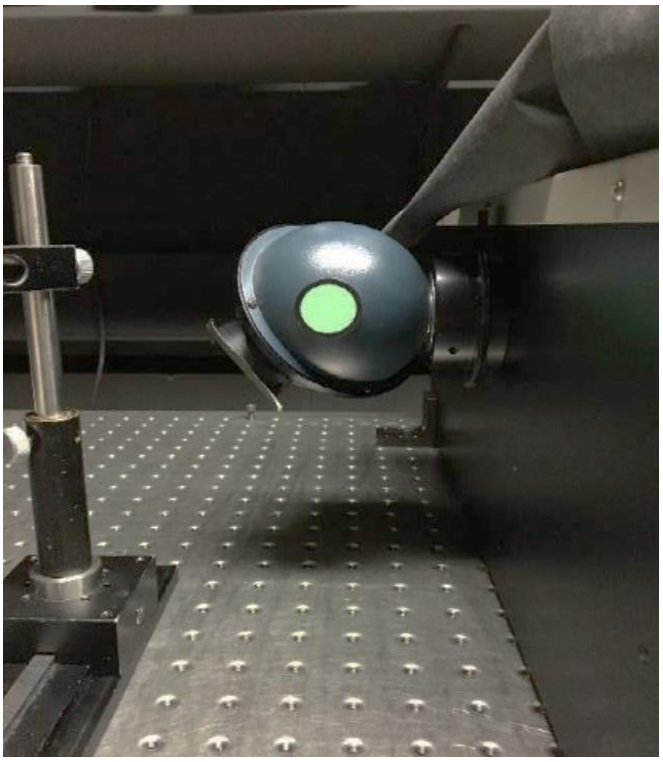

Figure 4.3. An integrating sphere attached to the exit port of the double monochromator. Opening in the integrating sphere shows internal illumination of the sphere from the monochromator.

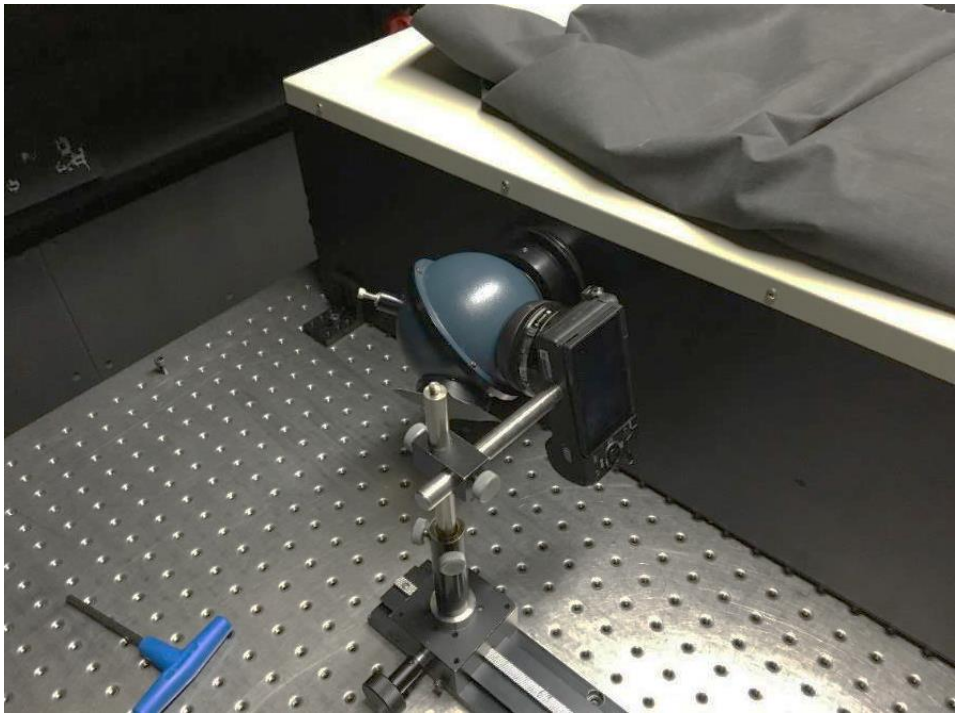

Figure 4.4. Camera positioned with its lens covering the opening of the integrating sphere. A black cloth was used to cover the camera and sphere to block any light from external sources contaminating images.

A tungsten halogen bulb was used as the light source for the monochromator. Lamp current and monochromator slit opening sizes were kept constant for all wavelengths (Table 4.1). The monochromator filter was changed from #2 for 350-650nm wavelengths, to #3 for 550-1100nm wavelength light.

Table 4.1. Lamp and double monochromator set-up setting used for all light wavelengths imaged.

Monochromatic wavelengths (nm)	350-650	550-1100
Lamp Current (Amps)	5.6	5.6
Filter	#2	#3
Slit opening (mm) (entrance/middle/exit)	5/5/5	5/5/5

For both visible (Sony_RGB) and near infrared (Sony_NIR) cameras, all images were captured under constant camera settings specific to each camera, Table 4.2. Imagery was captured in raw format to maintain the linear response of the camera sensors to light.

Table 4.2. Camera exposure settings used to capture single wavelength imagery for both the visible RGB and NIR cameras. Slower settings for the NIR camera are due to reduced sensitivity of the camera to NIR light.

Camera	**Aperture**	**ISO**	**Shutter Speed (seconds)**	**Light range (nm)**
Sony_RGB	f/2.8	100	1/3	350-850
Sony_NIR	f/2.8	100	8	750-1150

For image processing, the raw imagery was converted to TIFF format using DCRAW open source software (Coffin, 2007). After conversion, average values of a 4×4-pixel area in the centre of each image was extracted and used for deriving spectral responses. Due to variations in monochromator settings and filters used for different wavelengths, images required adjustment for variability in brightness of light produced between wavelengths. To do this a reference silicon photodiode spectrometer measured the same wavelengths produced under the same settings as each of the two cameras. Individual images were adjusted in post processing to normalise for variations between wavelengths, using these reference measurements.

4.4.2 Results

Reference measures of monochromatic light wavelengths produced by the monochromator (Figure 4.5) demonstrate how the level of monochromatic light produced varies with wavelength and between filter used.

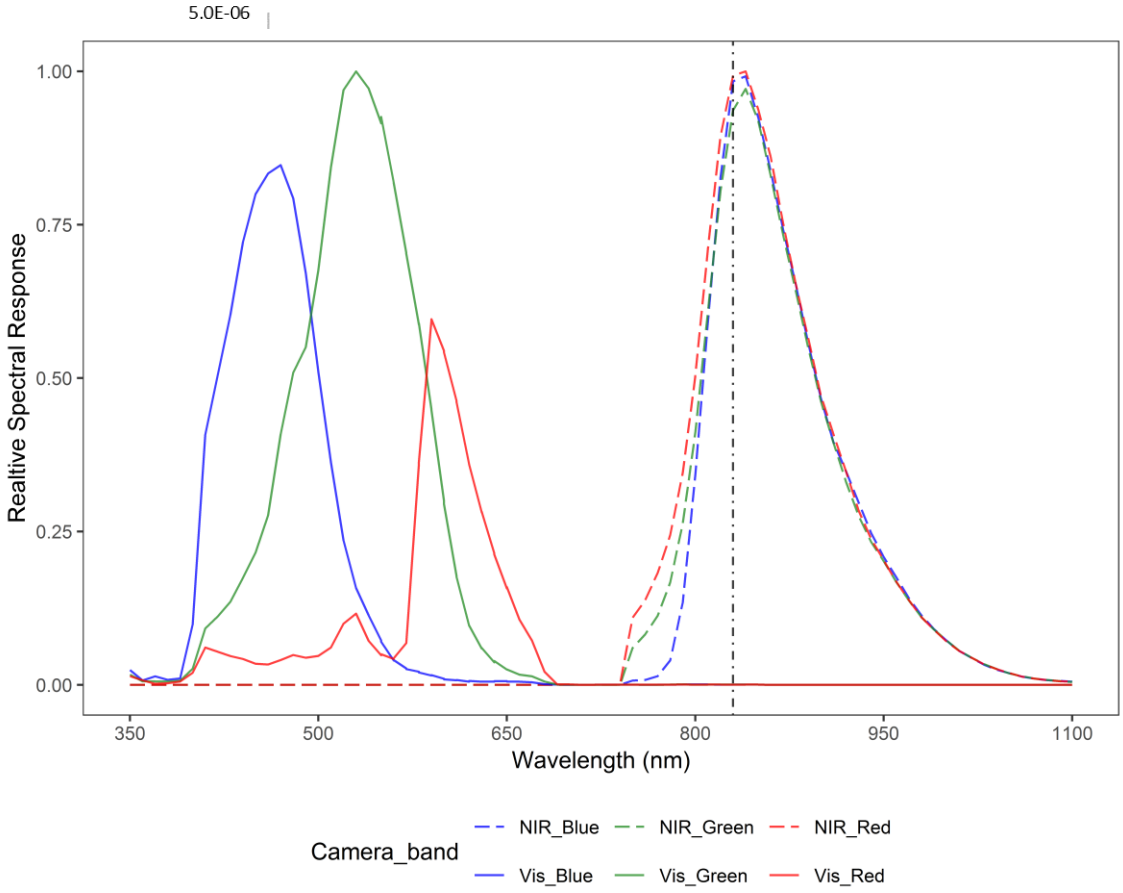

Figure 4.6. Relative spectral responses of each band of the visible RGB (solid lines) and adapted NIR (dashed lines) Sony cameras. Line colours indicate camera band. Vertical dashed line indicates the wavelength location of the 830nm visible blocking filter installed in the NIR camera. settings used for the two different wavelengths ranges measured. Blue = 350-650nm and Filter #2, Orange = 550-1100nm and Filter #3.

Final relative spectral responses for the visible RGB, and NIR cameras are presented in Figure 4.6. Results for the unadapted RGB camera present typical trends expected of a CMOS sensor, as used within these Sony cameras. Increased

sensitivity of the green band is a result of the Bayer matrix filter on the sensors (Nijland et al., 2014). For the adapted NIR camera, results show very similar level and trend in sensitivity between all three bands. All bands show some sensitivity below the 830nm of the blocking filter, suggesting it is not a perfect filter. Of the three bands, the blue band shows the lowest sensitivity below 830nm, making it the most suitable for providing 'pure' NIR imagery. The other two bands are likely to be contaminated by inclusion of red edge wavelengths.

Finally, comparison against, a number of other commercial cameras tested at the same time as the Sony cameras indicates that differences between cameras and manufacturers are present (Figure 4.7). This highlights the importance of measuring each individual camera's spectral responses to ensure the accuracy of derived reflectances.

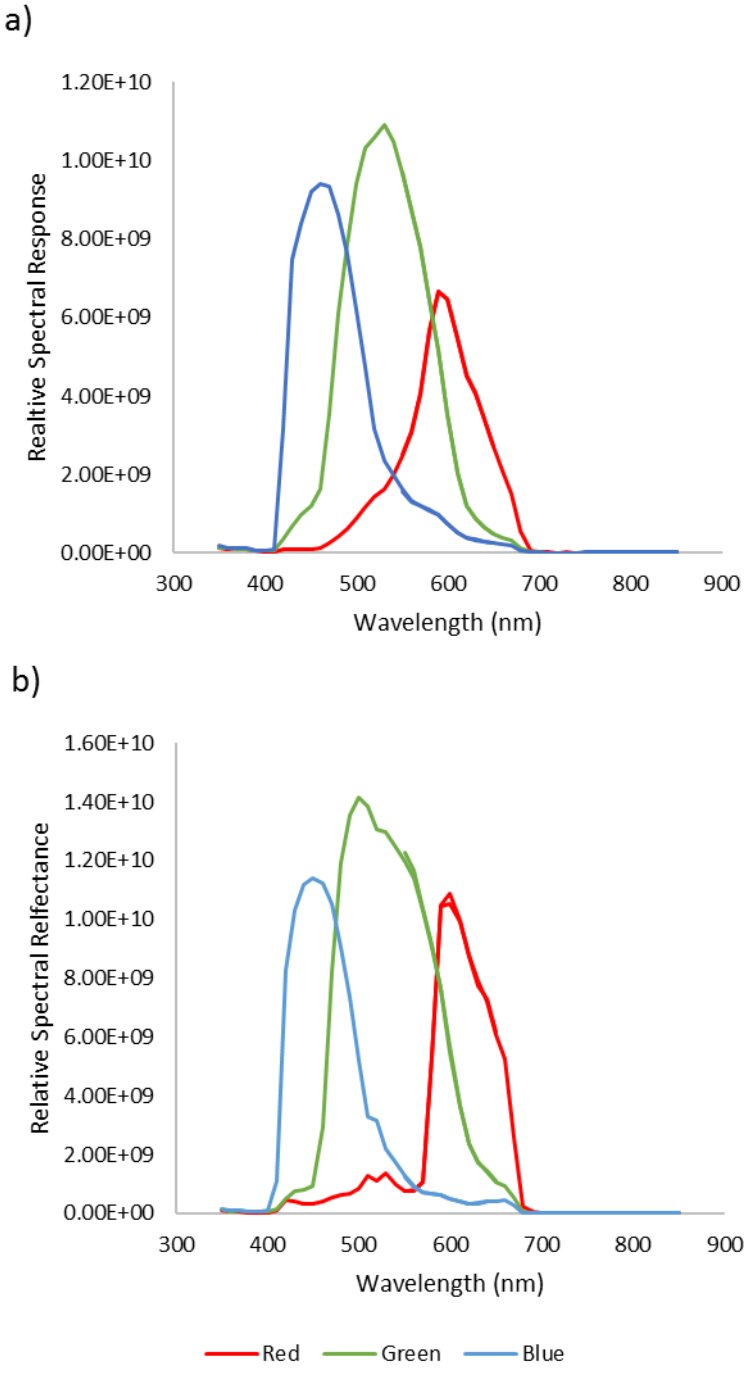

Figure 4.7. Relative spectral responses for (a) Canon 500D RGB camera, and (b) Panasonic DMX-LX7 RGB camera. Line colours indicate camera band.

4.5 Summary and Conclusion

The work in this chapter has detailed the development and assessment of 'commercial off the shelf' (COTS) cameras for capturing very high resolution, radiometrically calibrated reflectance imagery in visible and near-infrared spectral bands. The targeted application of these cameras is for high-throughput canopy reflectance phenotyping of field-based wheat trials, where existing standard methods used (e.g. ground-based spectrometers) often lack spatial resolution. It is known that multiple factors, including canopy structure and background soil, influence measured reflectances and derived vegetation indices. The use of high-resolution COTS cameras should provide the required spatial resolution in order to filter and mask non-vegetation pixels and derive canopy measurements independent of other influencers.

Accuracy assessments were performed against canopy reflectances collected using a ground-based vis-NIR spectrometer. Results indicated variabilities in accuracy between spectral bands and time points during the growing season. Of the camera bands the NIR camera presented notably reduced agreement with the spectrometer compared to the visible bands. This trend dominated in the higher reflectance plots, associated with the N4 treatment level, and was consistent over the different validation dates. Interestingly, the professionally calibrated Parrot Sequoia multispectral imager also presented the same trend between visible and NIR bands when compared to the ground spectrometer. The consistency of these trends in the data obtained by the two camera systems, indicates that its source is a result of differences between measurements by the

spectrometer compared to the imaging systems of the two cameras. Aasen and Bolten, (2018) found similar trends when comparing a UAV-mounted hyperspectral imager and ground spectrometer for wheat canopy reflectances. The authors found that the differences in field of view between the spectrometers and cameras, coupled with varying the bi-directional reflectance factors between visible and NIR spectral bands, had greater impact on the NIR band accuracy compared to the visible bands. For this chapter the difference in field of view between the spectrometer (25°) and the cameras (42°) were significant such that it could be the cause of the differences in accuracy. However, the Parrot Sequoia has a field of view of 32°, which sits between the spectrometer and COTS cameras. Another study by Deng et al., (2018) also presented comparison of a ground spectrometer (ASD) and a UAV based Parrot Sequoia when measuring a 30% reflectance panel. The authors found clear differences between the two systems, with the greatest difference occurring within the red edge and NIR bands. Interestingly, the authors also found this trend remained consistent between cloudy and sunny weather conditions. Further accuracy assessments in this chapter, of wheat canopy NDVI measurements found notably higher levels of agreement between the sensors, compared to the individual spectral bands. With $R^2 \geq 0.88$ and nRMSE ≤ 0.15, these results indicate that in the case of NDVI, the cameras and spectrometers are accurately comparable in their measurements. In addition, the results for the single flight conducted with both camera systems showed the same level of agreement for the COTS cameras ($R^2 \geq 0.94$ and nRMSE ≤ 0.062) and Parrot Sequoia ($R^2 \geq 0.96$ and nRMSE ≤ 0.068). These results indicate that although the NIR band presented reduced accuracy compared to the visible, these reduced accuracies have not carried through into calculated NDVI

measurements. This further points to a non-erroneous difference between point-based spectrometers and imaging-based systems such as the cameras used in this chapter. However, without further investigation it is difficult to identify the cause or reason for these trends.

Building on previous work investigating calibration of COTS cameras, a key area of focus for this chapter was improving the temporal stability of the methods. To do this, cameras were allowed to automatically vary their exposure settings during all flights in order to maximise image quality with the varying solar conditions during flights as well as over the growing season. Linear trends between exposure settings and image DN were identified for both aperture and ISO, agreeing with other studies (Hiscocks, 2011). These trends allowed for the application of custom developed corrections for camera ISO and aperture to normalise all images post capture. Tests of temporal consistency over multiple dates in the growing season were used to test the methods. Despite the varying levels of accuracy obtained between bands, the temporal consistency achieved indicates the good robustness of the methods and data. The added exposure normalisation steps, developed in this chapter, aid in maintaining consistent measures of reflectance over variable weather and irradiance conditions. Some variability did occur between dates, but this was to be expected due to the non-concurrent collection of ground and UAV data. Collection of data occurred up to 5 days apart, with just a single day lag between collections proving to impact negatively on correlation results (Rossi et al., 2019).

The proposed application of the COTS cameras was to utilise the very high resolution (GSD = 1cm) calibrated reflectance imagery collected over time, to investigate the impact of canopy cover and background soil on derived canopy NDVI of experimental wheat plots. Using the popular ExGR index to mask out non-vegetation pixels, the application of COTS cameras to provide true measures of vegetation-only NDVI monitoring was tested and proven. Comparison of masked and unmasked temporal NDVI trends showed that greatest differences occurred in the early season (March - April), where crop ground cover is typically low (AHDB, 2015). Through the middle of the growing period, little difference was observed between masked and unmasked NDVI, indicating canopies were fully established and ground cover was at a maximum. Some differences were also observed within the senescence period of the crops (June - July), where rate of senescence, and therefore loss of green canopy may vary between varieties and nitrogen treatments. Without validation of these trends, it is difficult to ascertain the true relationships between the measured trends in NDVI and the phenotypic trait responsible. Despite these uncertainties, this initial proof of concept has indicated the potential for using very high-resolution imagery in generating greater canopy phenotypic information from spectral reflectance measurements. Proposed areas of work for future studies include the development of the masking techniques used to isolate green vegetation from other background materials. The ExGR method, whilst widely used, is simplistic and does not account for senescing vegetation. Machine learning has been previously demonstrated in the application of identifying specific plant structures, monitoring senescence, and classifying different vegetation (Sadeghi-Tehran et al., 2017). Application of these techniques would likely expand the

applications of COTS camera data for high-throughput phenotyping via UAVs, and therefore should be investigated further.

The work presented in this chapter has developed and refined the data collection and processing workflows of calibrated reflectance imagery from commercial off the shelf cameras. Results demonstrated new correction workflows for camera exposure settings developed in this chapter, in combination with robust vignetting and irradiance corrections were successful; facilitating greater flexibility in image capture under varied illumination conditions. Accuracy assessments between a ground spectrometer and the cameras showed variable levels of accuracy, highlighting potential difficulties in the comparison of scanning-based and image-based reflectance measurements. This trend was found to be consistent between different imaging sensors, e.g. a Parrot Sequoia, and points to the need for further work in understanding the reasons and solutions for this disparity between systems. Application of the COTS cameras to filtering out background soil from canopy NDVI measurements, highlighted the impact of these factors on mean canopy NDVI, especially in the early season. Future studies should look at the incorporation of additional phenotypes, via additional sensors or data processing. For example, the imagery produced by the COTS cameras, can easily be processed to produce both multispectral orthomosaics, and also normalised Digital Surface Models (nDSM) for assessment of crop morphology traits including crop height and growth rate (Chapter 3). This will provide a more complete analysis of the complex interactions between plant phenotypes and genotypes and growing environment.

Chapter 5: Dynamic Quantifying of Canopy Trait Response of Modern Wheat Cultivars to Varied Nitrogen Applications

5.1 Introduction

This chapter focusses on further evaluation of UAV techniques for phenotyping of field-based crop trial experiments. Specifically, the focus is on further assessment of application of the methodologies and technologies developed within this PhD project to ongoing field experiments at Rothamsted Research.

Increases in global wheat yields are a key target for ensuring food security in the face of increasing pressures, such as climate change, competition for resources and demands from growing populations into the future (Furbank and Tester, 2011b). Photosynthesis has previously been identified as a key source of advancement in improving crop yields, playing a major role in determining above-ground biomass and final yield (Parry et al., 2006). Within this, strategies have looked to increase both the light capture efficiency of plant canopies, and the duration of light capture through the life cycle of plants (Parry et al., 2011b). Whilst improvements in canopy light capture efficiency have been largely maximised, there are still opportunities to extend the duration of photosynthetically active canopies by manipulating the plant's life cycle (Dohleman et al., 2009).

Past improvements in the efficiency and duration of canopy light capture of wheat crops have largely been brought about by increased inputs of nitrogen fertiliser, which ensure that canopy size, quality and duration are maximised (Hawkesford, 2014). However, increases in nitrogen fertiliser application come with significant financial and environmental costs. In light of these costs, moves to improve sustainable use of nitrogen in agriculture are required (Bingham et al., 2012; Gaju et al., 2011). In response to these issues, focus has turned to developing new crop genotypes better adapted to efficient nitrogen use, such that photosynthetic capacity, biomass and yield are maximised with reduced nitrogen fertiliser applications. Key phenotypic targets for this include the early development and closure of canopies, and delayed canopy senescence (Hawkesford, 2012). The promotion of early canopy formation, and extended canopy duration, under varied nitrogen conditions, have been identified as important factors in potential yield gains (Shearman et al., 2005).

Both canopy formation and senescence are dynamic phenotypic traits, whose onset and duration will vary between crop varieties, growing seasons, and environmental growing conditions (Hawkesford, 2017; Lopes and Reynolds, 2012). However, commonly used standard methods (e.g. visual scoring) for phenotyping traits associated with canopy formation and senescence are inadequate (Christopher et al., 2014). Past studies have used ground-based temporal NDVI measures to assess dynamic canopy traits over time, specifically focussing on quantifying senescence rates in canopies. Linear regressions, for example, are a simple solution, however temporal senescence curves are inevitably non-linear such that this method lacks sufficient interpretation of dynamic changes (Christopher et al., 2014; Vijayalakshmi et al., 2010).

An alternative approach has used a logistic function to quantify senescence as a two phase, slow, then rapid, process (Gaju et al., 2011). Results indicated strong positive correlations between senescence rate with final grain yield and nitrogen use efficiency. Another study demonstrated how comparisons of integrated weekly NDVI measurements during senescence, produced superior relationships between variety and yield, compared to alternative single timepoint measurements (Christopher et al., 2014). These studies indicate that integration of canopy dynamics over the canopy senescence phase provides useful indicators of crop performance. However, lack of spatial measurements, and limitations with temporal measurements associated with these methods restricts their application for multiple large-scale field trials. Unmanned Aerial Vehicles (UAVs) are an alternative solution capable of high temporal and spatial resolution and proven in the application throughput phenotyping of field based crop trials (Holman et al., 2016; Madec et al., 2017; Malambo et al., 2018).

This chapter aims to utilise UAV phenotyping platforms to evaluate how nitrogen fertiliser application affects canopy formation and senescence dynamics in a modern wheat germplasm breeding panel. To achieve this, the chapter will develop a method for phenotyping dynamic changes in canopy NDVI traits over time, with specific focus on canopy formation and senescence phases.

5.2 Methods

5.2.1 Field Site

All data were collected at the experimental farm operated by Rothamsted Research, UK (51°48′34.56″N, 0°21′22.68″W). The Defra-funded Wheat Genetic Improvement Network (WGIN) Diversity Field Experiment (Barraclough et al., 2010) was used for all data collection. The aim of the WGIN experiment is to test the influence of different nitrogen fertiliser application levels to different wheat cultivars. The data for this chapter was collected over three years, 2016, 2017 and 2018; and for each year 30 cultivars were grown under four different nitrogen treatment levels (Table 5.1, Table 5.2, and Table 5.3). In 2018, weather conditions limited vehicular access to the field early in the season, such that only two nitrogen applications were performed. Nitrogen applications for 2018 were adjusted to ensure total nitrogen applied was consistent with 2016 and 2017 totals. For each cultivar and nitrogen treatment, three replicates were grown in 9m × 3m non-destructive plots and an adjacent 2.5 m × 3 m destructive sampling plots; planting layout maps can be found in Appendix A. Of the 30 cultivars grown each year, 25 were repeated for all years and therefore these 25 will be the focus of this study (Table 5.4). This study focuses on measurements of the non-destructive plots only.

Table 5.1. Nitrogen fertiliser rates and application dates for the four treatments in 2016.

Treatment code	Total N applied (kg-N /ha)	Application 1 (21/03/2016)	Application 2 (08/04/2016)	Application 3 (26/04/2016)
N1	0	-	-	-
N2	100	50	50	-
N3	200	50	100	50
N4	350	50	250	50

Table 5.2. Nitrogen fertiliser rates and application dates for the four treatments in 2017.

Treatment code	Total N applied (kg-N/ha)	Application 1 (15/03/2017)	Application 2 (05/04/2017)	Application 3 (09/05/2017)
N1	0	-	-	-
N2	100	50	50	-
N3	200	50	100	50
N4	350	50	250	50

Table 5.3. Nitrogen fertiliser rates and application dates for the four treatments in 2018.

Treatment code	Total N applied (kg-N /ha)	Application 1 (19/04/2018)	Application 2 (04/05/2018)
N1	0	-	-
N2	100	100	-
N3	200	100	100
N4	350	175	175

Table 5.4. Wheat varieties and codes for the 25 varieties grown over the 3 years 2016, 2017 and 2018.

Variety	Code	Variety	Code
Avalon	AV	**Leeds**	LE
Cadenza	CA	**Lili**	LI
Claire	CL	**Malacca**	MA
Conqueror	CN	**Mercia**	ME
Cordiale	CO	**Maris Widgeon**	MW
Crusoe	CR	**Paragon**	PA
Evolution	EL	**Reflection**	RF
Hereward	HE	**Riband**	RI
Hereford	HF	**Robigus**	RO
Hylux	HL	**Solstice**	SL
Hystar	HY	**Skyfall**	SY
Illustrious	IL	**Xi19**	Xi
Istabraq	IS		

5.2.2 Meteorological Data

Daily measures of meteorological data were collected by the Rothamsted Research's weather station, and made available by the electronic Rothamsted Archive (Perryman et al., 2018). From this daily rainfall (mm), and average, minimum and maximum daily temperatures (°C) were extracted for all three growing seasons and used to assess and understand variability in environmental conditions between seasons.

5.2.3 Crop Measurements

For all three seasons, plots were harvested, and fresh grain weighed using a Haldrup GMbH C-85 specialist plot combine harvester (Haldrup, Ilshofen, Germany). For straw yield, a sub-sample of the destructive plot was cut by hand just before harvest, and fresh weight measured. Dry matter straw and grain weights were determined by oven-drying approximately 80g sub-samples of fresh grain and straw in an oven overnight at 105 °C (80^0C for straw). From these samples, grain yield at 85% dry matter in tonnes per hectare (t/ha), biomass tonnes at 100% dry matter in tonnes per hectare (t/ha) respectively, and total nitrogen uptake in kg of nitrogen per hectare (kg-N/ha) were determined (Barraclough et al., 2010).

5.2.4 UAV imagery

A DJI S900 UAV (DJI, Shengzhen, China) was flown on a pre-determined flight plan at 50m altitude over the experimental field. The flight plan was designed to ensure that an 80% overlap between concurrent images was obtained. Two Sony (Tokyo, Japan) α5100 mirrorless digital cameras mounted on the UAV were used for the spectral visible (RGB) and near infrared (NIR) image collection, as detailed in Chapter 4 (Holman et al., 2019). Both cameras were fitted with 20mm F2.8 Sony prime lenses, and the NIR camera, an internal 830nm long pass blocking filter.

All images were captured at 1-second intervals and in Raw format, with focus set to 50 m to reflect the UAV flying height. Aperture and ISO were left on automatic, whilst shutter speed was fixed to 1/500sec to ensure minimisation of motion blur. The UAV and cameras were flown over the field site at a time as close as possible to local solar noon.

Twelve Ground Control Points, whose positions were measured with a Trimble Geo 7 DGPS (Trimble, Sunnyvale, USA), were used for georeferencing final orthomosaics. To provide measurements of total incoming solar irradiance, a Tec5 HandySpec Field spectrometer (Tec5, Oberursel, Germany) fitted with a cosine corrected downwelling optic was deployed at a fixed location next to the field and set to measure at 1-second intervals. Spectral measurements were collected at 10 nm spectral resolution across the wavelength range 360–1000 nm.

5.2.5 Reflectance imagery processing

All raw imagery collected by the UAVs was processed to calibrated reflectances using the workflow outlined in Chapter 4. Corrections for vignetting, exposure settings and reflectance calibration were all applied (Holman et al., 2019). For the 2016 data, misaligned clocks between cameras meant that calibration of individual images to reflectance using Tec5 downwelling was not possible. As the total flight times were below 15 minutes, a single reflectance calibration value can be used, whilst still achieving good accuracy (Miura and Huete, 2009). Therefore, for the 2016 flights an average of the Tec5 downwelling measurements for the entire flight time was used to calibrate each camera band into reflectance.

5.2.6 Orthomosaic processing

Agisoft Photoscan (Agisoft, St. Petersburg, Russia) (Version 1.4.3) was used to process final imagery to orthomosaics, including automatic lens correction. For each date, two orthomosaics were generated, RGB and NIR. Agisoft processing settings, Table 5.5, were kept consistent for all orthomosaics. Orthomosaics were generated and

exported at 1 cm Ground Sampling Distance (GSD). NDVI orthomosaics were generated using Equation 2.

$$NDVI = \frac{R_{NIR} - R_R}{R_{NIR} + R_R} \quad (2)$$

Where R_R is the measured reflectance in the red waveband, and R_{NIR} is measured reflectance in the near infrared waveband.

Table 5.5. Agisoft processing steps and parameter settings relevant to each step.

Processing Step	Setting
Align photos	High
Generate dense point cloud	Medium
Generate mesh	High
Generate orthomosaic	Disabled

The Excess Green Red (ExGR) (Equation 3) was calculated and used to mask NDVI orthomosaics and remove the influence of background soil reflectance. A threshold of >0 to classify green vegetation, was set to produce 'vegetation only' measures of plot canopy NDVI.

$$ExGR = (2 \times R_G - R_R - R_B) - (1.4 \times R_R - R_G) \quad (3)$$

Where R_R is the measured reflectance in the red waveband, and R_G is reflectance measured in the green waveband, and R_B is reflectance measured in the blue waveband.

In addition to masking NDVI, the percentage of vegetation within each plot was calculated from the ExGR derived vegetation masks. This was derived by the number of pixels classified as vegetation (>0 ExGR) over the total number of pixels within each plot.

Three different orthomosaics were generated to assess canopy traits, NDVI, ExGR_NDVI, and GreenPixel as described in Table 5.6. From each orthomosaic, mean plot values were extracted for each plot. As in Holman *et al.* (2016, 2019) a 50cm buffer was applied to each plot to remove the influence of plot edge effect.

Table 5.6. Definitions of the phenotypic traits generated from orthomosaics derived from UAV imagery.

Model	Description
NDVI	NDVI calculated from red and NIR reflectance imagery.
ExGR_NDVI	NDVI of pixels classified as green vegetation by ExGR values > 0.
GreenPixel	The percentage of pixels within each plot classified as green vegetation by ExGR > 0.

5.2.7 Quantification of development phases

To isolate the three development phases, canopy formation, full canopy, and senescence, thresholding was applied to mean NDVI values for all plots (Figure 5.1). Formation phase was isolated as the period from $NDVI_{min}$ to $NDVI_{90\%}$. Senescence phase was identified as the period post second $NDVI_{90\%}$ until the end of the season. Full canopy was identified as the period between formation and senescence thresholds, where canopy NDVI was at its maximum and top 10%. For each defined phase, the integral (area under the curve) of the curve was calculated using the trapezoid method via R computer software (Jurasinski et al., 2014). Comparison of derived integrals for each of

the nitrogen fertiliser application level was used, via Kruskal Wallis tests, to assess the impact of nitrogen fertiliser on each of these three development phases. The specific metrics used to define the different periods ($NDVI_{min}$ and $NDVI_{90\%}$) were selected in line with the expected seasonal trend in wheat canopy green area index (AHDB, 2015), as well as with discussions with crop researchers at Rothamsted Research, UK. The proposed metrics were designed to isolate the period of maximum canopy, as well as the phases either side, namely the development and senescence of the canopy.

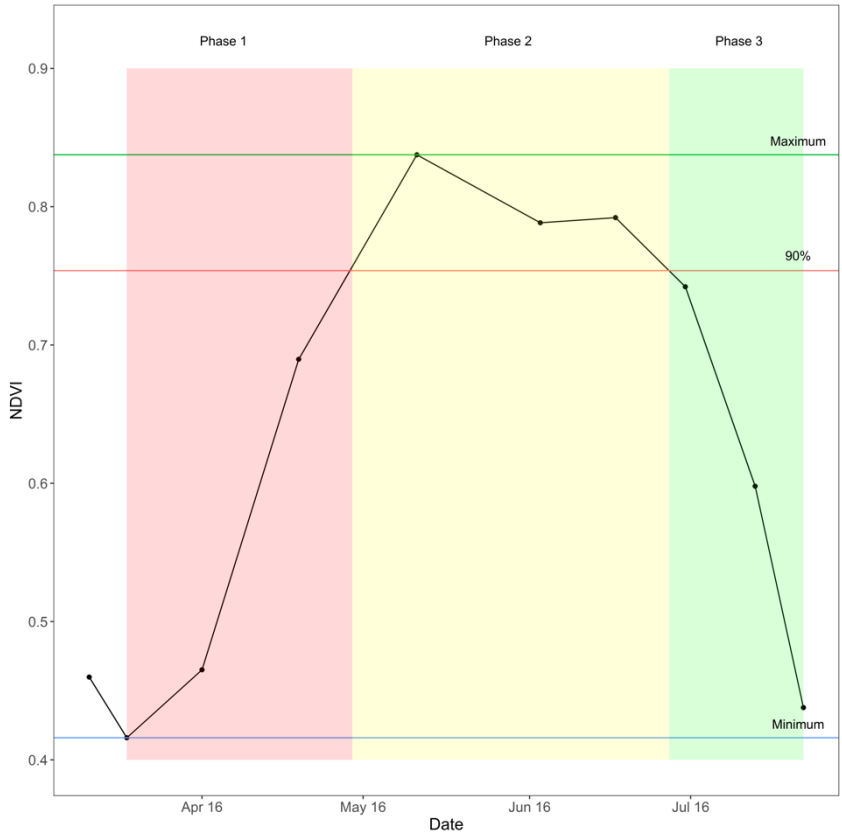

Figure 5.1. Example of the isolation of three development phases based on the minimum, maximum and 90% NDVI values. Phase 1 = Formation phase; Phase 2 = Full canopy phase; Phase 3 = Senescence phase.

5.3 Results

5.3.1 Crop parameters

5.3.1.1 Grain Yield

Grain yield varied between 2.49 and 12.86 tonnes per hectare (t/ha, 85% dry matter) depending on variety, season, and nitrogen treatment level (Figure 5.2). Variation between years was apparent, with 2018 yields lower for all varieties and nitrogen treatments compared to 2016 and 2017. The variety Maris Widgeon (MW) consistently presented lowest yields, though this trend was reduced in the 2018 growing season. Comparison between nitrogen treatments indicates the greatest differences to occur between N1 and all other treatment levels. Variability between the N2, N3 and N4 treatment levels is less consistent between years.

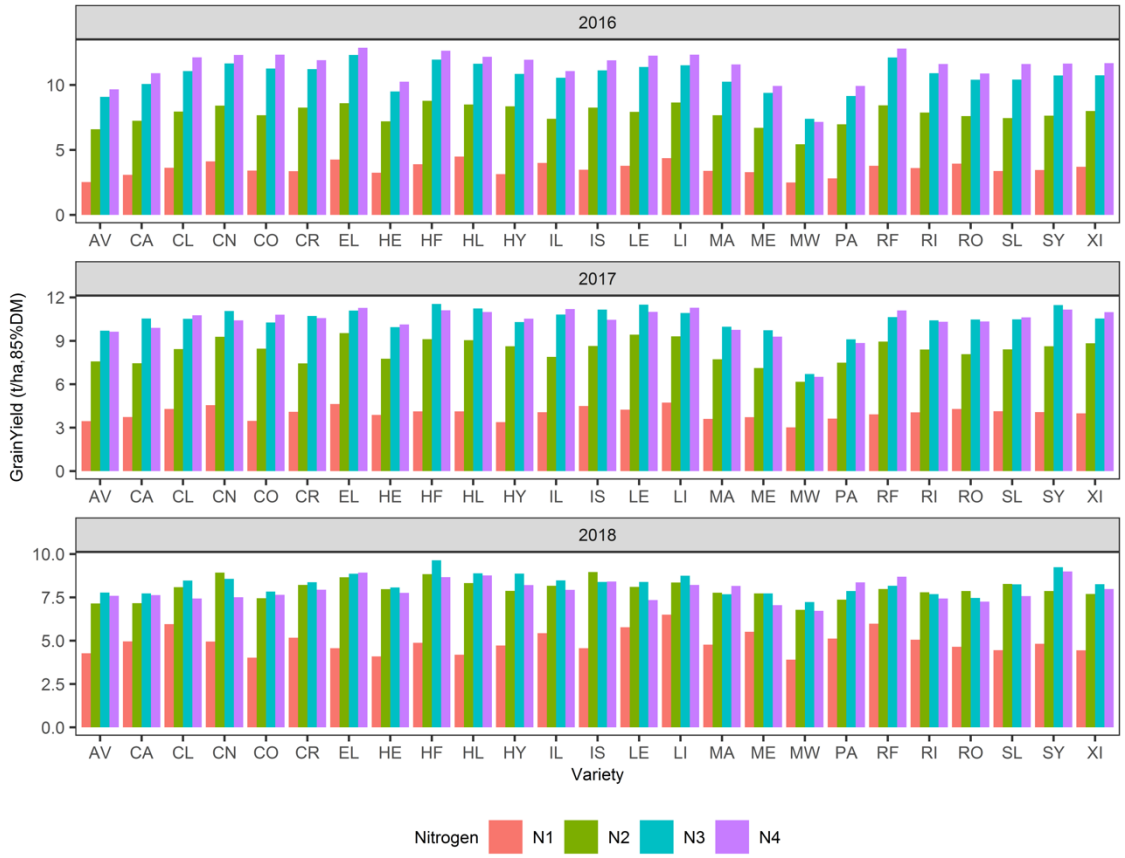

Figure 5.2. Grain yields (t/ha, 85% dry matter) for 25 wheat varieties over three growing seasons (2016, 2017 and 2018) and four nitrogen treatment levels. N1 = 0 kg-N/ha, N2 = 100 kg-N/ha, N3 = 200 kg-N/ha, N4 = 350 kg-N/ha.

5.3.1.2 Biomass (100% Dry Matter)

Final biomass measurements ranged between 3.56 and 22.06 t/ha depending on variety, season, and nitrogen treatment level (Figure 5.3). For all growing seasons, clear differences in biomass occur between N1 and other nitrogen treatments. In 2016, MW shows markedly reduced biomass compared to all other varieties. Variability in biomass as a factor of nitrogen treatment is present between wheat varieties, and this occurs within all seasons. Though as with yield, the 2018 season shows much reduced variability with the N2, N3 and N4 application levels.

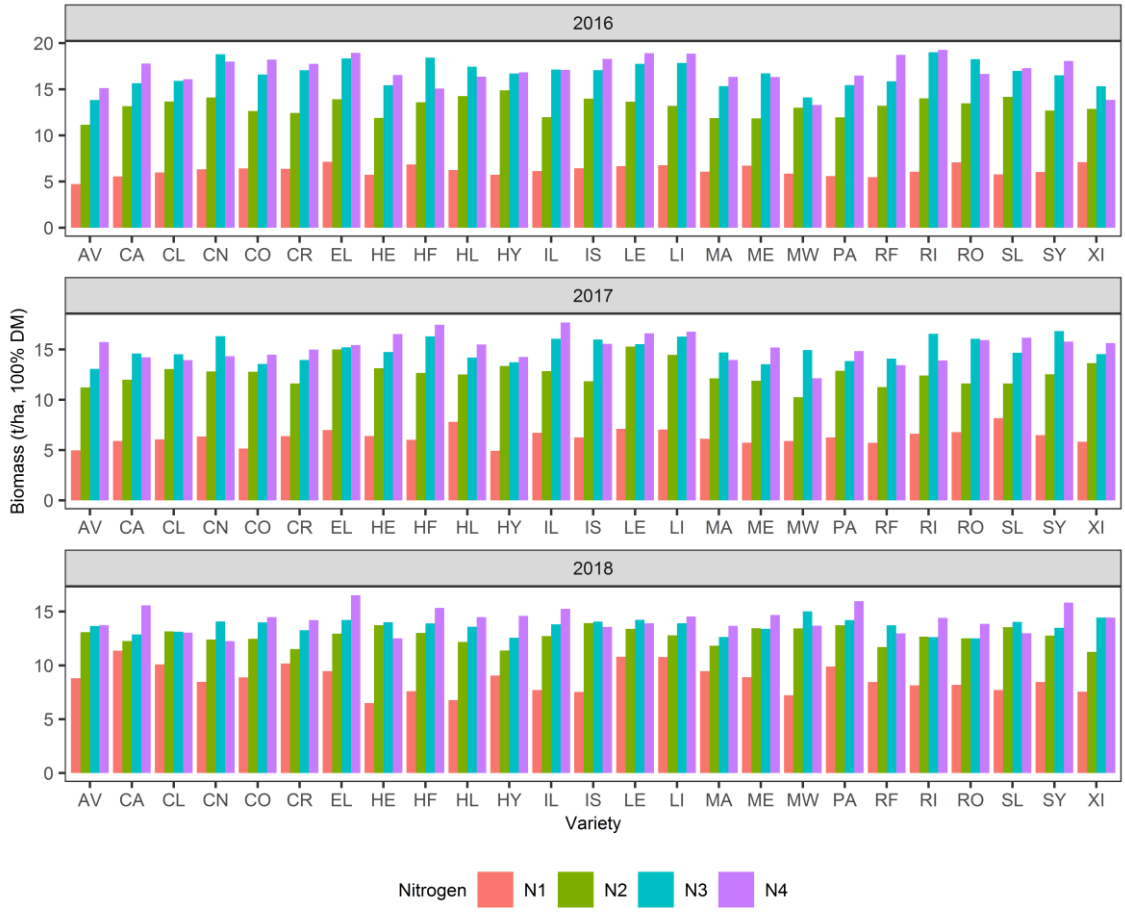

Figure 5.3. Total biomass (t/ha, 100% dry matter) for 25 wheat varieties over three growing seasons (2016, 2017 and 2018) and four nitrogen treatment levels. N1 = 0 kg-N/ha, N2 = 100 kg-N/ha, N3 = 200 kg-N/ha, N4 = 350 kg-N/ha.

5.3.1.3 Total Nitrogen Uptake

Total nitrogen uptake, measured at anthesis, ranged from 21.49 to 281.68 kg-N/ha depending on variety, season, and nitrogen treatment level (Figure 5.4). Unlike yield and biomass results, there was a clear impact of nitrogen treatments on total nitrogen uptake for all three seasons. Variability between wheat varieties is present though these trends are inconsistent between seasons.

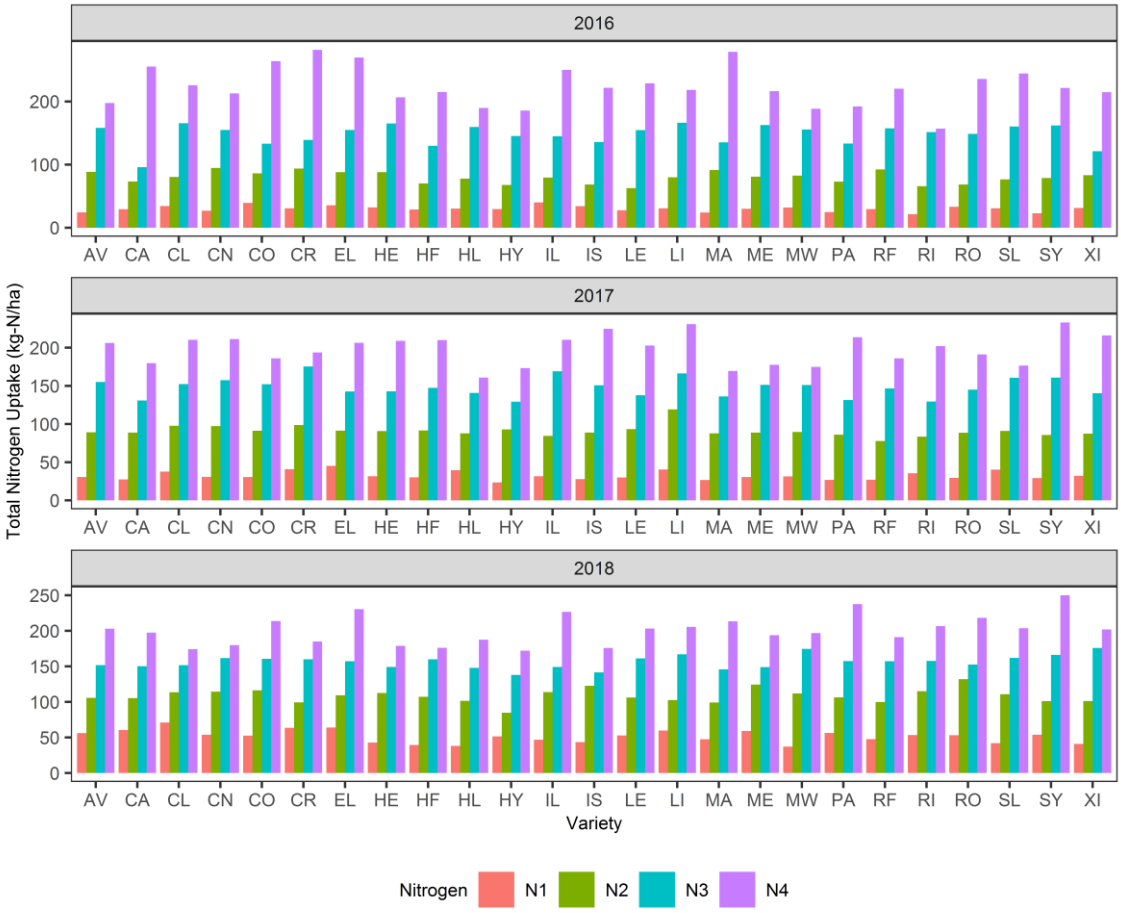

Figure 5.4. Total nitrogen uptake (kg-N/ha) for 25 wheat varieties over three growing seasons (2016, 2017 and 2018) and four nitrogen treatment levels. N1 = 0 kg-N/ha, N2 = 100 kg-N/ha, N3 = 200 kg-N/ha, N4 = 350 kg-N/ha.

5.3.2 UAV Results

For the 2016 growing season (Figure 5.5), mean canopy NDVI values derived from UAV imagery present low values in the early season. Some noise between varieties during this early stage, including some drops in NDVI, could be a result of older leaves senescing before full canopy formation begins. A rapid increase in NDVI from early-April to mid-May is followed by a plateau in NDVI until mid-June. Finally, values show rapid decrease from mid-June until the end of the season. The lower NDVI values for the N1 nitrogen treatment compared to N2, N3 and N4 is clear, whilst any variation between the higher three treatment levels is less distinguishable. Between wheat varieties, most variability in NDVI is seen in the early season, before the main period of increasing NDVI from early-April. For the remainder of the growing season, all varieties follow the same temporal trends for each nitrogen treatment, showing no clear differences between varieties. For ExGR_NDVI, results show very similar temporal trends to NDVI as well as between the different nitrogen treatments. More variability between wheat varieties is seen for the N1 treatment at the beginning of the growing season. Whilst, as with NDVI, little discernible variations between varieties is seen in higher nitrogen treatments. Finally, for percentage of green pixels (GreenPixel), temporal trends for N2, N3 and N4 treatments are the same as NDVI and ExGR_NDVI. A consistent drop and recovery in GreenPixel towards the end of June is of interest. The consistency between nitrogen treatment levels indicates either a field-wide influencer, or some variation in the UAV data for that date, e.g. more variable lighting conditions for this flight. For the N1 treatments, very little increase in GreenPixel over time is seen. Between wheat varieties, variability in GreenPixel is much clearer compared to NDVI

and ExGR_NDVI, with the variety MW sticking out in the N1, N2 and N3 treatments with higher maximum GreenPixel. The variety Maris Widgeon is an older variety, known to express greater biomass yields and lower grain yields implying higher canopy cover.

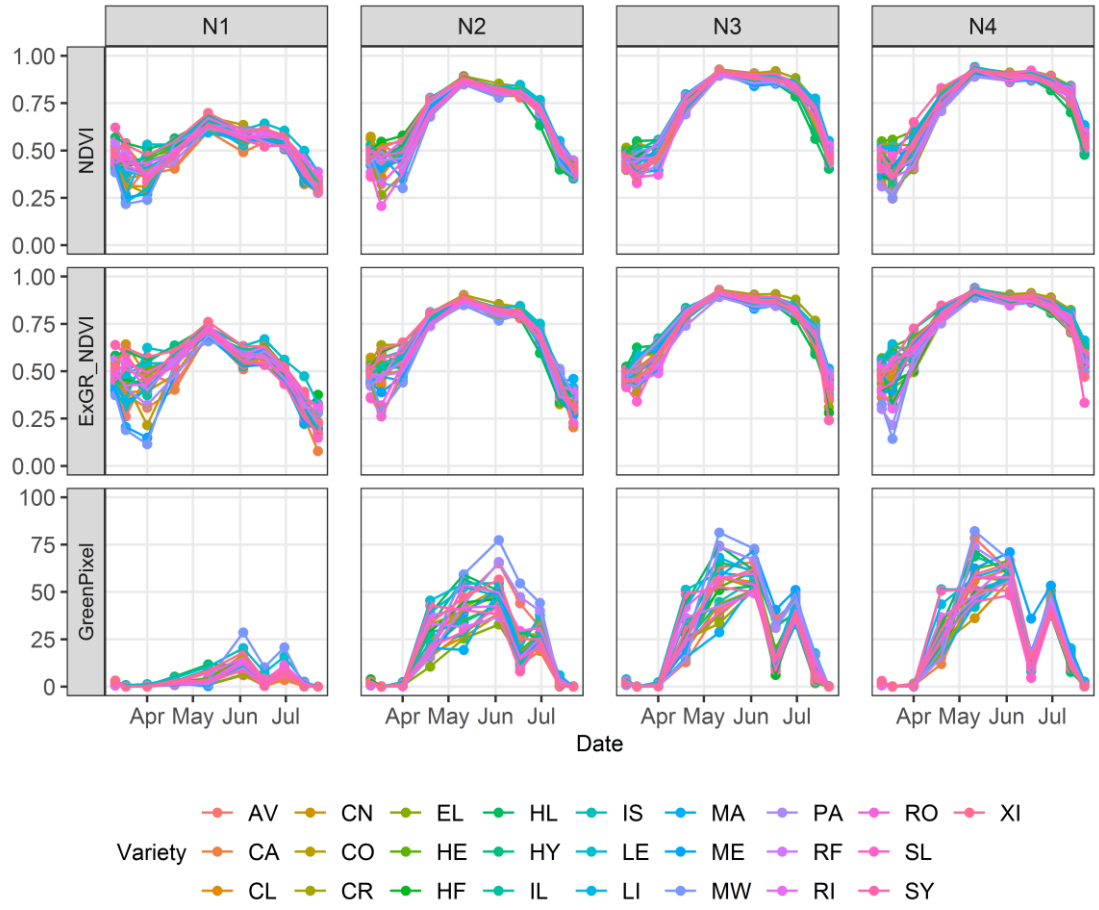

Figure 5.5. 2016 growing season temporal trends of canopy NDVI, ExGR masked NDVI (ExGR_NDVI) and percentage green pixels (GreenPixel) derived from UAV imagery. Results provided for 25 wheat varieties grown under 4 different nitrogen fertiliser treatment levels. N1 = 0 kg-N/ha, N2 = 100 kg-N/ha, N3 = 200 kg-N/ha, N4 = 350 kg-N/ha.

Results for the 2017 (Figure 5.6) growing season show the same 3 phases of increase, plateau, and subsequent decrease observed in 2016, however, differences are present. For NDVI, a drop and then recovery in values in the plateau period is a noticeable difference to the 2016 growing season. A potential explanation for this is the occurrence of ear emergence during this period, altering the reflective and structural properties of the canopies. Though this does not explain the recovery observed subsequently. Similar variation between nitrogen treatments is observed, whilst there is less variability between wheat varieties in the 2017 results compared to 2016. For ExGR_NDVI, very similar results are again seen in comparison to NDVI. For N1 treatments, the trend for increasing values early in the season is noticeably flatter in the ExGR_NDVI results. For GreenPixel, higher maximum values are achieved by all nitrogen levels compared to 2016, though the period of high green pixel percentage is shorter. Overall less variability is seen between wheat varieties compared to 2016.

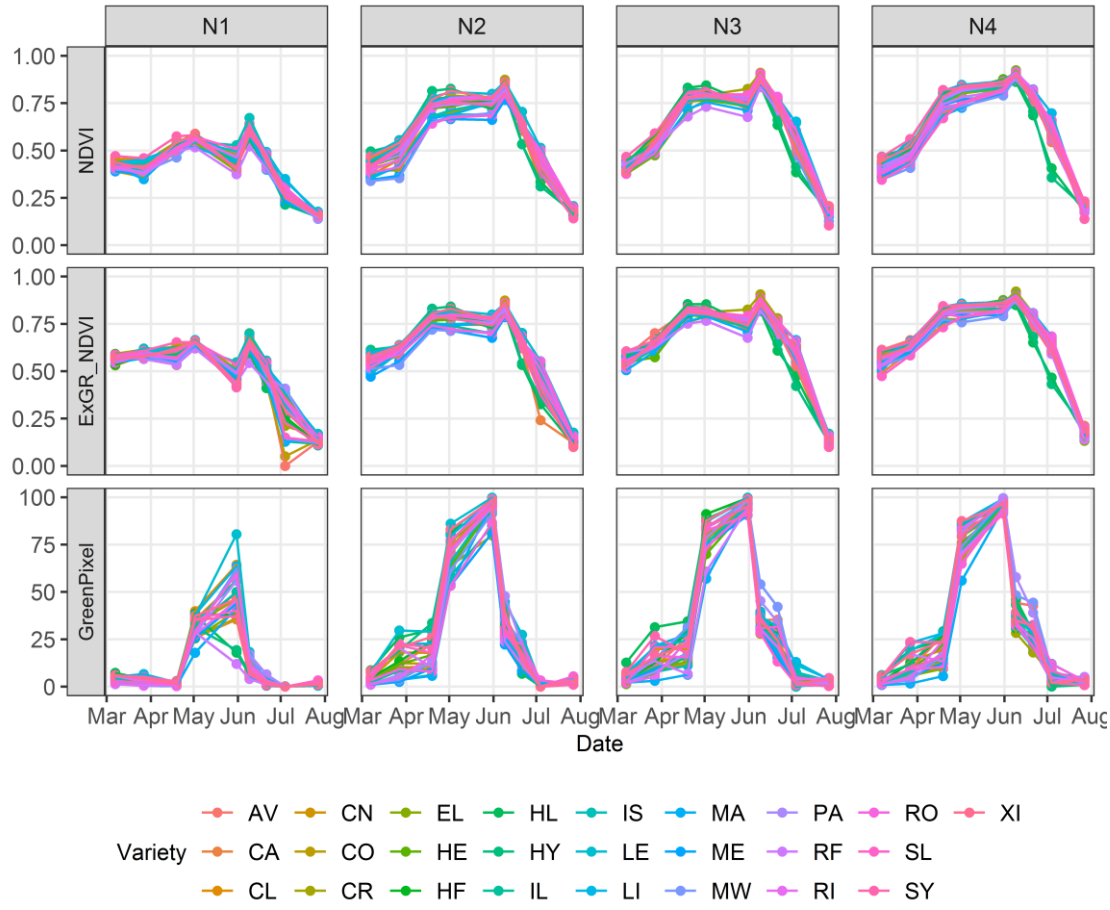

Figure 5.6. 2017 growing season temporal trends of canopy NDVI, ExGR masked NDVI (ExGR_NDVI) and percentage green pixels (GreenPixel) derived from UAV imagery. Results provided for 25 wheat varieties grown under 4 different nitrogen fertiliser treatment levels. N1 = 0 kg-N/ha, N2 = 100 kg-N/ha, N3 = 200 kg-N/ha, N4 = 350 kg-N/ha.

Results for 2018 (Figure 5.7) again show the same temporal trends over the season as in 2016 and 2017. As in 2017, NDVI and ExGR results show a slight drop and recovery in values during the plateau phase, though the drop is smaller in 2018 compared to 2017. Variations between nitrogen treatments show the same trends as 2016 and 2017 results. For wheat varieties, more variability is seen for NDVI and ExGR_NDVI in the early part of season, as expressed in the 2016 results. GreenPixel results also show similar variation between both nitrogen treatments and wheat varieties. Again, the variety MW, stands out as having higher GreenPixel values compared to other varieties.

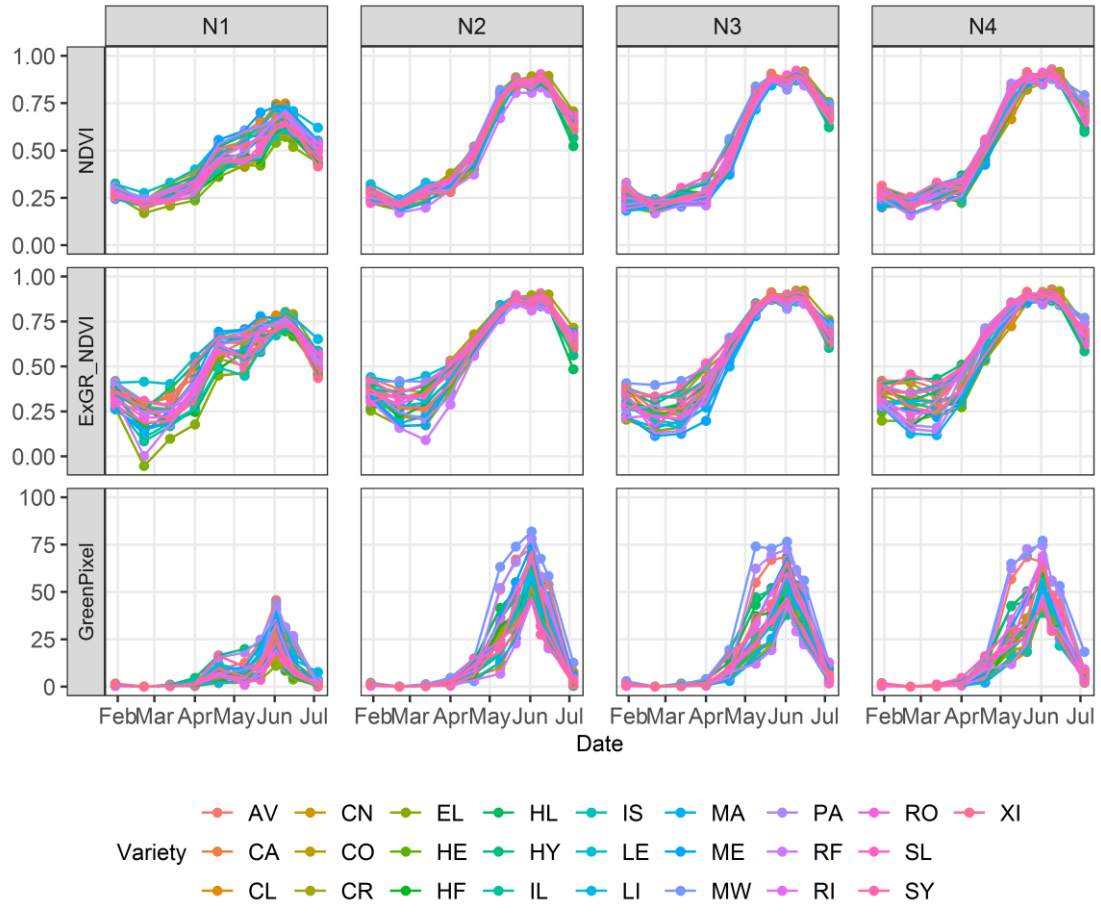

Figure 5.7. 2018 growing season temporal trends of canopy NDVI, ExGR masked NDVI (ExGR_NDVI) and percentage green pixels (GreenPixel) derived from UAV imagery. Results provided for 25 wheat varieties grown under 4 different nitrogen fertiliser treatment levels. N1 = 0 kg-N/ha, N2 = 100 kg-N/ha, N3 = 200 kg-N/ha, N4 = 350 kg-N/ha.

Correlation plots comparing the three canopy metrics for each year are provided in Appendix B. The results of the plots show strong linear agreement between NDVI and EXGR_NDVI metrics, and much weaker linear agreement between the two NDVI based metrics and canopy green pixel counts.

5.3.3 Development phase determination

Exact development phase periods for each growing season were calculated from mean NDVI values for all plots in each season. Results in Table 5.7 show the start and end dates for each phase vary between growing seasons.

Table 5.7. Derived phase start and end dates as well as durations for each growing season.

Year	Phase	Start date	End date	Duration (days)
2016	Formation	18/03/2016	29/04/2016	42
	Full Canopy	29/04/2016	27/06/2016	59
	Senescence	27/06/2016	22/07/2016	25
2017	Formation	07/03/2017	01/05/2017	55
	Full Canopy	01/05/2017	15/06/2017	45
	Senescence	15/06/2017	27/07/2017	42
2018	Formation	21/02/2018	16/05/2018	84
	Full Canopy	16/05/2018	21/06/2018	36
	Senescence	21/06/2018	04/07/2018	13

Figure 5.8 presents results for derived development phases, as well as daily rainfall for the same period. Results show formation phase does not begin at first UAV data collection date, but at the second flight instead. Canopy formation lasts 42 days in total, and interestingly encompasses all nitrogen fertiliser applications for the 2016 season. Full canopy phase succeeds formation, lasting for 59 days; and finally,

senescence, which lasts just 25 days from late-June until the last UAV flight of the season. Comparison of mean NDVI trends for each of the nitrogen treatment levels shows the N1 treatment NDVI values are clearly below the other treatment levels, and this trend begins after the first nitrogen fertiliser application. Between the N2, N3 and N4 treatments, there is little variability in the formation phase. For full canopy, the N2 treatment NDVI results start to separate from the N3 and N4, and this separation becomes greater and clearer in senescence. Daily rainfall trends for the 2016 growing season show several noticeable rainfall events occur through the season, particularly in March, April and June. These events do not appear to have influenced NDVI trends over time however.

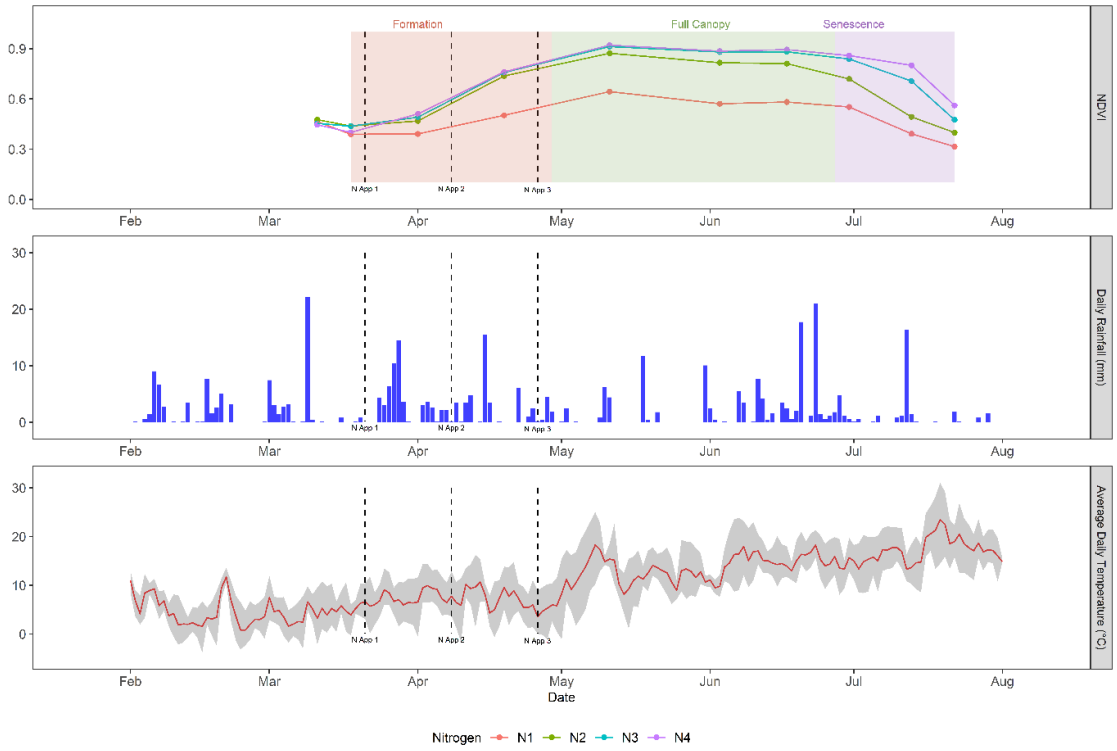

Figure 5.8. Mean NDVI trends for the four nitrogen treatments for the 2016 growing season, with nitrogen application dates and derived development phases shown. NDVI trends are calculated from means of 25 varieties. N1 = 0 kg-N/ha, N2 = 100 kg-N/ha, N3 = 200 kg-N/ha, N4 = 350 kg-N/ha. Daily rainfall (mm) data shows several noticeable rainfall events occurring through the 2016 growing season. Daily average temperature (°C) is represented by the red line, the grey error area indicates the range between daily minimum and maximum temperatures. All meteorological data is obtained from the electronic Rothamsted Archive (Perryman *et al.*, 2018).

Results for the 2017 growing season (Figure 5.9) present a longer formation phase compared to 2016, 55 days compared to 42. The phase started earlier, and finished later in 2017. For a full canopy, 2017 results produced a shorter phase of only 45 days compared to 59. Senescence results show a longer phase of 42 days from mid-June until the last UAV flight in late July. As for nitrogen fertiliser application, formation covers only two of the applications, whilst the third is applied during full canopy. Rainfall results demonstrate that 2017 was a drier year compared to 2016, although there was one significant rainfall event in mid-May. Visually, this rainfall event appears to coincide with a drop in N1 and N3 NDVI values. Again, NDVI trends between treatment levels

show the clear difference between N1 and all other treatment levels through all development phases. Between the higher treatment levels, results show little obvious differences until the start of senescence. In the senescence period, as with 2016, the N2 treatment shows a drop in NDVI values away from those of N3 and N4.

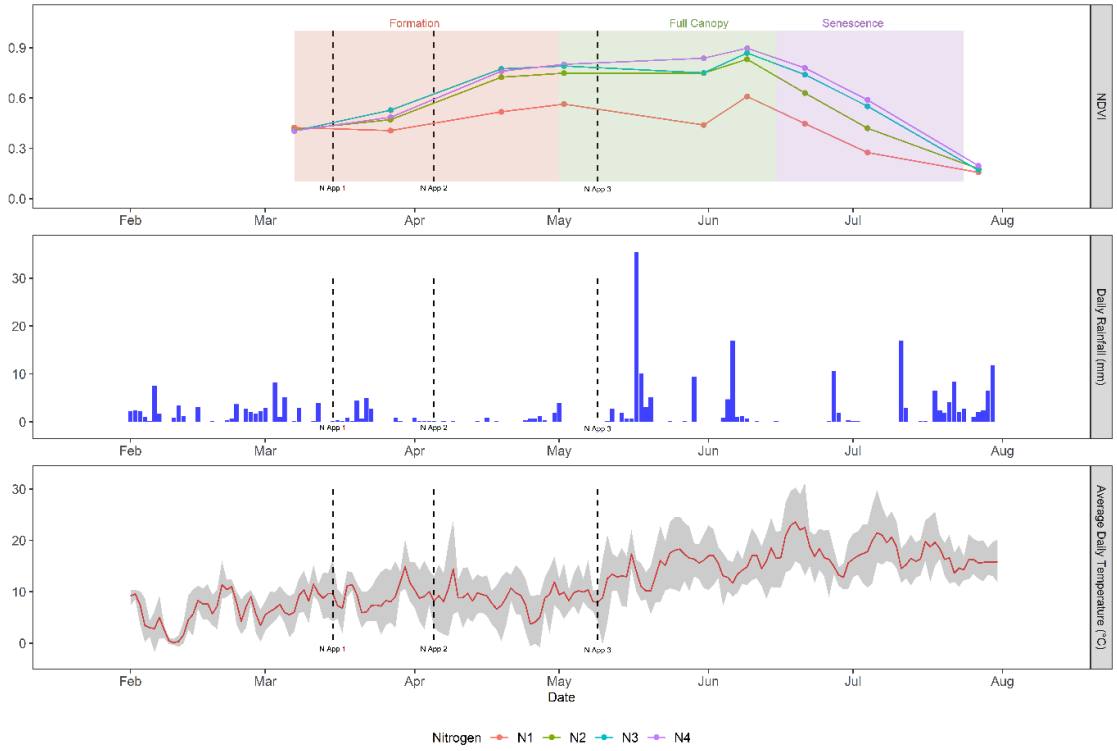

Figure 5.9. Mean NDVI trends for the four nitrogen treatments for the 2017 growing season, with nitrogen application dates and derived development phases shown. NDVI trends are calculated from means of 25 varieties. N1 = 0 kg-N/ha, N2 = 100 kg-N/ha, N3 = 200 kg-N/ha, N4 = 350 kg-N/ha. Daily rainfall (mm) data shows one noticeable rainfall events occurring in the 2017 growing season. Daily average temperature (°C) is represented by the red line, the grey error area indicates the range between daily minimum and maximum temperatures. All meteorological data is obtained from the electronic Rothamsted Archive (Perryman *et al.*, 2018).

The 2018 growing season results (Figure 5.10) show the longest formation period, lasting 84 days. This is in part due to the earlier UAV flights, starting in February 2018 compared to March 2016 and 2017. However, the 2018 formation phase also finished later compared to 2016 and 2017, suggesting that the longer phase was not solely due to the earlier flights. Full canopy occurs from mid-May and lasts only 36 days, whilst senescence lasts only 13 days. The short senescence period is more than likely to be a result of the lack of UAV flights after 04/07/2018. Flights in 2016 and 2017 finished at later date; at the end of August. Only two nitrogen applications occurred in 2018, and both occurred within the formation period. Comparison of NDVI results between nitrogen treatments once again shows the N1 treatment to be noticeably lower, with an apparent date of divergence in mid-April. As for the other treatment levels, no clear differentiation is present between N2, N3 and N4 treatments across all three phases. Finally, rainfall results show that 2018 was a wet season, like 2016. A high volume of rainfall early in the season was the main reason for a third nitrogen application not being applied. Two larger rainfall events occur in late April and late May 2018. Reduced rainfall is observed from May onwards, after the second and final nitrogen application date. No obvious impact from the first event is seen in NDVI trends whilst a small dip in NDVI values for N2, N3 and N4 is seen shortly after the late May rainfall event.

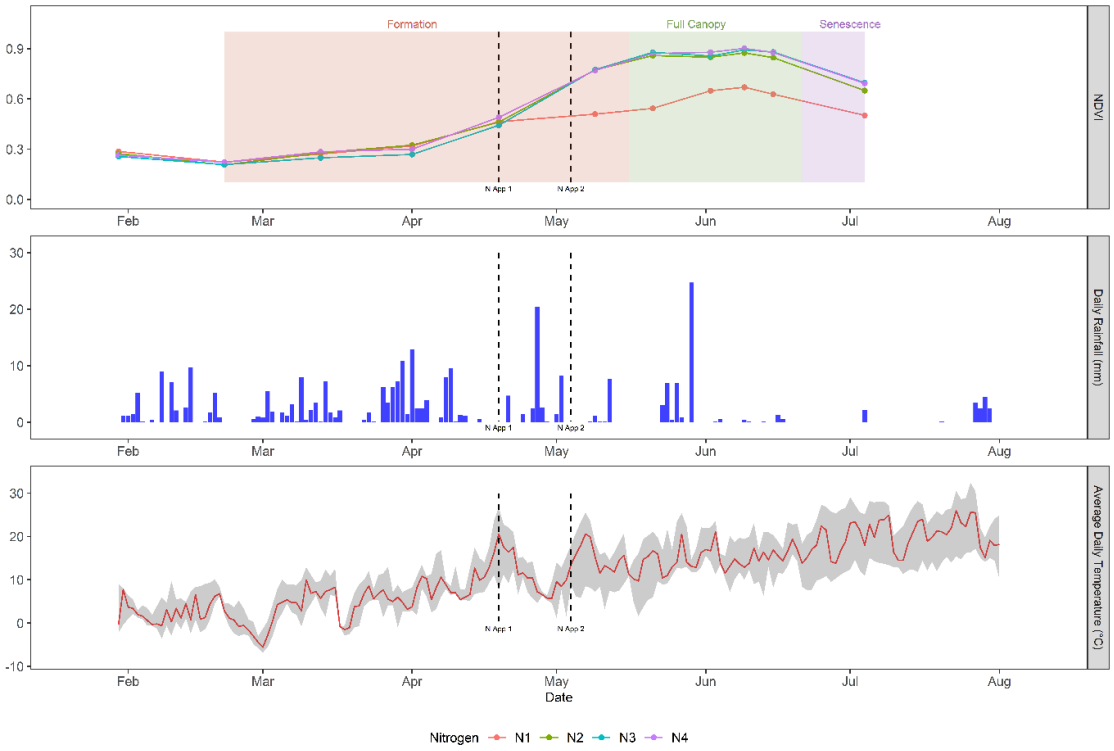

Figure 5.10. Mean NDVI trends for the four nitrogen treatments for the 2018 growing season, with nitrogen application dates and derived development phases shown. NDVI trends are calculated from means of 25 varieties. N1 = 0 kg-N/ha, N2 = 100 kg-N/ha, N3 = 200 kg-N/ha, N4 = 350 kg-N/ha. Daily rainfall (mm) data shows two noticeable rainfall events occurring in the 2018 growing season. Daily average temperature (°C) is represented by the red line, the grey error area indicates the range between daily minimum and maximum temperatures. All meteorological data is obtained from the electronic Rothamsted Archive (Perryman *et al.*, 2018).

5.3.4 Development phase integrals

Using the derived phases presented in the previous section, 'area under curve' integrals were calculated for each development phase, canopy trait (NDVI, ExGR_NDVI, and GreenPixel), and growing season. Additional analysis was also performed focussing on differences between the grown wheat varieties, but was not the main focus of this chapter; these results are provided in Appendix C.

Figure 5.11 and Table 5.8 presents boxplots of phase-derived integrals comparing nitrogen treatment, growing season and canopy trait. P-values for Kruskall Wallis tests of significant differences between nitrogen treatments for canopy formation integrals are also provided (Table 5.8). Results for the canopy formation phase show that the N1 treatment results are significantly lower than all other treatment levels across all canopy traits and growing seasons. Differences between the higher treatment levels (N2, N3 and N4) are visually less clear. For 2016, no significant differences were observed between the higher treatment levels in NDVI and ExGR_NDVI canopy traits. GreenPixel results do, however, show the N2 treatment to be significantly lower then N3 and N4, whilstlt there is no differences between N3 and N4. 2017 results present a different trend in all traits, most noticeably no significant differences for GreenPixel in N2, N3 and N4 treatments. With NDVI, N2 is significantly lower then N3, and ExGR_NDVI N2 is significantly lower than both N3 and N4. Finally 2018, GreenPixel trait presents no differences between N2, N3 and N4 treatments as seen in 2017. For NDVI N3 is signifincalty lower then N4, but interestingly not N2. ExGR_NDVI results show N3 treatments lower then both N2 and N4.

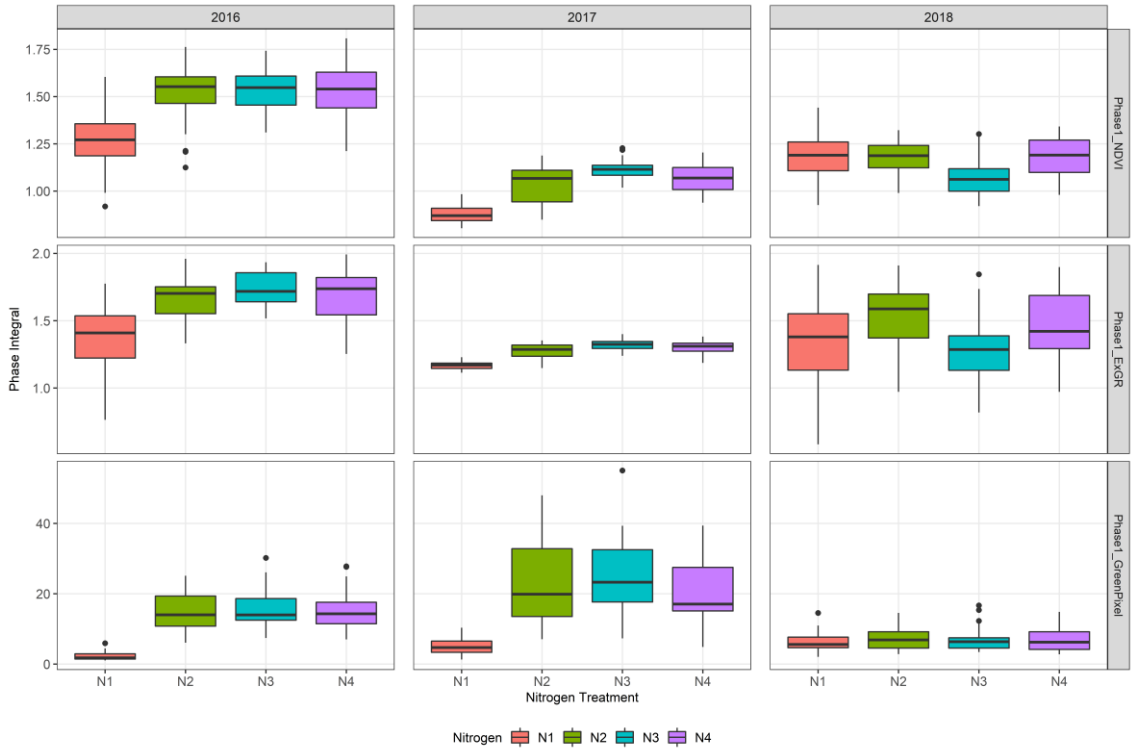

Figure 5.11. Boxplots describing differences in derived integral values for the Formation phase (Phase 1). Comparisons are between growing season (columns), canopy trait (rows) and nitrogen treatment levels (colours). N1 = 0 kg-N/ha, N2 = 100 kg-N/ha, N3 = 200 kg-N/ha, N4 = 350 kg-N/ha.

Table 5.8. P-values for Kruskal Wallis tests of significant difference between Formation phase derived integrals. Test of significant differences are performed between all the four nitrogen treatments for each canopy trait and growing season. Green shading indicates significant results, red shading indicates a nonsignificant result. N1 = 0 kg-N/ha, N2 = 100 kg-N/ha, N3 = 200 kg-N/ha, N4 = 350kg-N/ha.

Year	Metric	N1 × N2	N1 × N3	N1 × N4	N2 × N3	N2 × N4	N3 × N4
2016	NDVI	< 0.01	< 0.01	< 0.01	0.20	0.19	0.82
	ExGR_NDVI	< 0.01	< 0.01	< 0.01	0.11	0.11	0.85
	GreenPixel	< 0.01	< 0.01	< 0.01	0.03	0.03	0.92
2017	NDVI	< 0.01	< 0.01	< 0.01	< 0.01	0.08	0.17
	ExGR_NDVI	< 0.01	< 0.01	< 0.01	< 0.01	0.01	0.50
	GreenPixel	< 0.01	< 0.01	< 0.01	0.18	0.55	0.40
2018	NDVI	< 0.01	< 0.01	< 0.01	0.06	0.14	< 0.01
	ExGR_NDVI	< 0.01	< 0.01	< 0.01	0.05	0.90	0.05
	GreenPixel	< 0.01	< 0.01	< 0.01	1	1	0.78

For the full canopy phase (Figure 5.12, Table 5.9), results again show the N1 treatments are significantly lower across all canopy traits and growing season. NDVI also demonstrate that the differences between all nitrogen levels are significant in all three growing seasons (Table 5.9). ExGR_NDVI and GreenPixel results in 2016 show N2 is significantly lower than N3 and N4, and no difference is seen between N3 and N4. For 2017, differences between nitrogen treatments for ExGR_NDVI are all significant. For GreenPixel, N2 was significantly lower than N4. Finally, 2018 shows no difference between N3 and N4 of significance in ExGR_NDVI. GreenPixel results continue to show no significant differences between N2, N3 and N4 treatments.

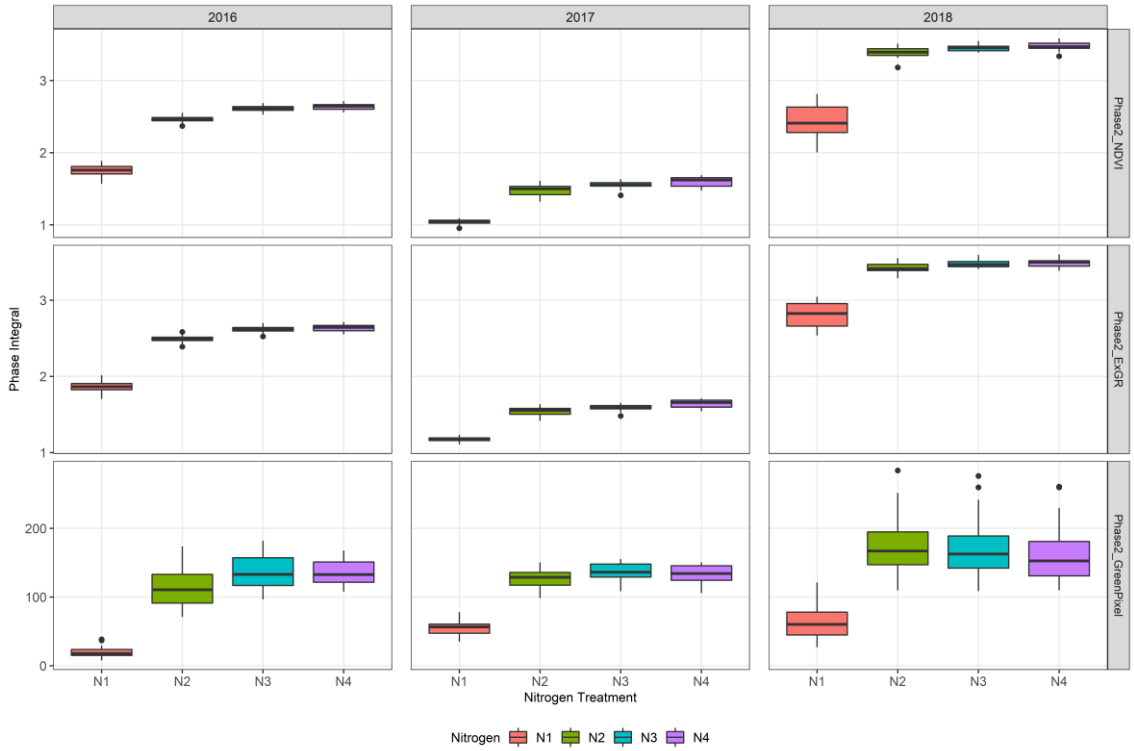

Figure 5.12. Boxplots describing differences in derived integral values for the Full Canopy phase (Phase 2). Comparisons are between growing season (columns), canopy trait (rows) and nitrogen treatment levels (colours). N1 = 0 kg-N/ha, N2 = 100 kg-N/ha, N3 = 200 kg-N/ha, N4 = 350 kg-N/ha.

Table 5.9. P-values for Kruskal Wallis tests of significant difference between Full Canopy phase derived integrals. Test of significant differences are performed between all the four nitrogen treatments for each canopy trait and growing season. Green shading indicates significant results, red shading indicates a nonsignificant result. N1 = 0 kg-N/ha, N2 = 100 kg-N/ha, N3 = 200 kg-N/ha, N4 = 350kg-N/ha.

Year	Metric	N1 × N2	N1 × N3	N1 × N4	N2 × N3	N2 × N4	N3 × N4
2016	NDVI	< 0.01	< 0.01	< 0.01	< 0.01	< 0.01	0.05
	ExGR_NDVI	< 0.01	< 0.01	< 0.01	< 0.01	< 0.01	0.07
	GreenPixel	< 0.01	< 0.01	< 0.01	< 0.01	< 0.01	0.46
2017	NDVI	< 0.01	< 0.01	< 0.01	< 0.01	< 0.01	< 0.01
	ExGR_NDVI	< 0.01	< 0.01	0.03	< 0.01	< 0.01	< 0.01
	GreenPixel	< 0.01	< 0.01	< 0.01	0.12	0.01	0.21
2018	NDVI	< 0.01	< 0.01	0.01	< 0.01	< 0.01	0.03
	ExGR_NDVI	< 0.01	< 0.01	0.02	< 0.01	< 0.01	0.07
	GreenPixel	< 0.01	< 0.01	< 0.01	0.58	0.12	0.31

Again, senescence results show lower N1 results for all canopy traits are significantly different in all three years (Figure 5.13, Table 5.10). Significant differences between all treatment levels were recorded in 2016 results for all canopy traits (Table 5.10). The 2017 results demonstrate that all differences, except for GreenPixel N2, N3 and N4 were significant. Finally, the 2018 results showed no differences between N3 and N4 in any of the canopy traits, whilst again, GreenPixel showed no significant differences between N2, N3 and N4 treatments.

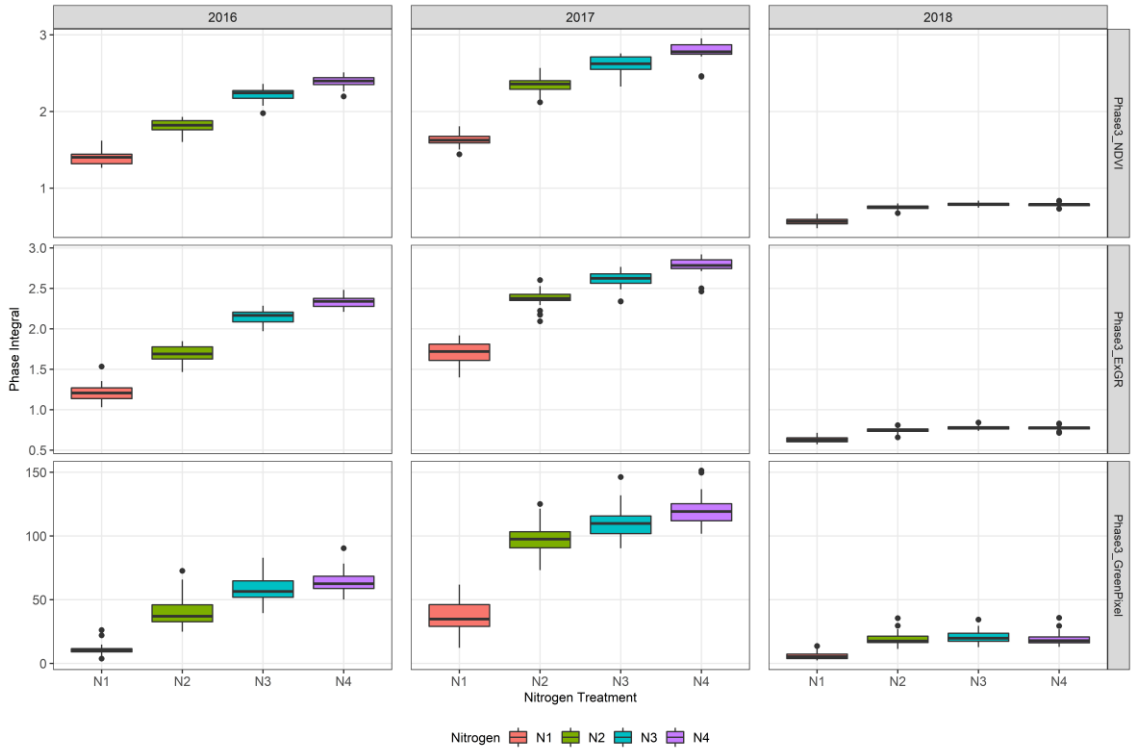

Figure 5.13. Boxplots describing differences in derived integral values for the Senescence phase (Phase 3). Comparisons are between growing season (columns), canopy trait (rows) and nitrogen treatment levels (colours). N1 = 0 kg-N/ha, N2 = 100 kg-N/ha, N3 = 200 kg-N/ha, N4 = 350 kg-N/ha.

Table 5.10. P-values for Kruskal Wallis tests of significant difference between Senescence phase derived integrals. Test of significant differences are performed between all the four nitrogen treatments for each canopy trait and growing season. Green shading indicates significant results, red shading indicates a nonsignificant result. N1 = 0 kg-N/ha, N2 = 100 kg-N/ha, N3 = 200 kg-N/ha, N4 = 350kg-N/ha.

Year	Metric	N1 × N2	N1 × N3	N1 × N4	N2 × N3	N2 × N4	N3 × N4
2016	NDVI	< 0.01	< 0.01	< 0.01	< 0.01	< 0.01	< 0.01
	ExGR_NDVI	< 0.01	< 0.01	< 0.01	< 0.01	< 0.01	< 0.01
	GreenPixel	< 0.01	< 0.01	< 0.01	< 0.01	< 0.01	< 0.01
2017	NDVI	< 0.01	< 0.01	< 0.01	< 0.01	< 0.01	< 0.01
	ExGR_NDVI	< 0.01	< 0.01	< 0.01	< 0.01	< 0.01	< 0.01
	GreenPixel	< 0.01	< 0.01	< 0.01	0.39	0.85	0.37
2018	NDVI	< 0.01	< 0.01	0.01	< 0.01	< 0.01	0.75
	ExGR_NDVI	< 0.01	< 0.01	0.02	< 0.01	< 0.01	0.82
	GreenPixel	< 0.01	< 0.01	< 0.01	0.39	0.85	0.37

5.3.5 Correlations with crop metrics

Statistically significant positive correlations between phase integrals of canopy traits and crop metrics were found in all seasons and development phases Figure 5.14, Figure 5.15, and Figure 5.16). Strong positive correlations ($r > 0.70$) between all three canopy traits and final grain yield were seen in both 2016 and 2017 seasons. Correlations for 2018, were weaker overall, particularly in formation where the highest correlating trait was NDVI ($r = 0.52$). Of the three canopy traits, NDVI showed the most consistency over phases and growing seasons. Strongest correlations were achieved in full canopy and senescence phases for all growing seasons. The same trend was observed for correlations between phase integrals derived from the three canopy traits and final biomass yields for each growing season. Again, NDVI showed the best and most

consistent positive correlations for development phase integral and growing season. Strongest correlations were again found in full canopy and senescence for all growing seasons. Correlations for 2018, stand out for their overall weaker associations compared to previous years. Finally, correlations with total nitrogen uptake, show increasing strength of correlation from formation through to the strongest correlations in senescence. Finally, NDVI indicates the most consistent correlations over phase and growing season, closely followed by ExGR_NDVI. GreenPixel correlations were consistently weaker compared to the other traits except for formation in 2016.

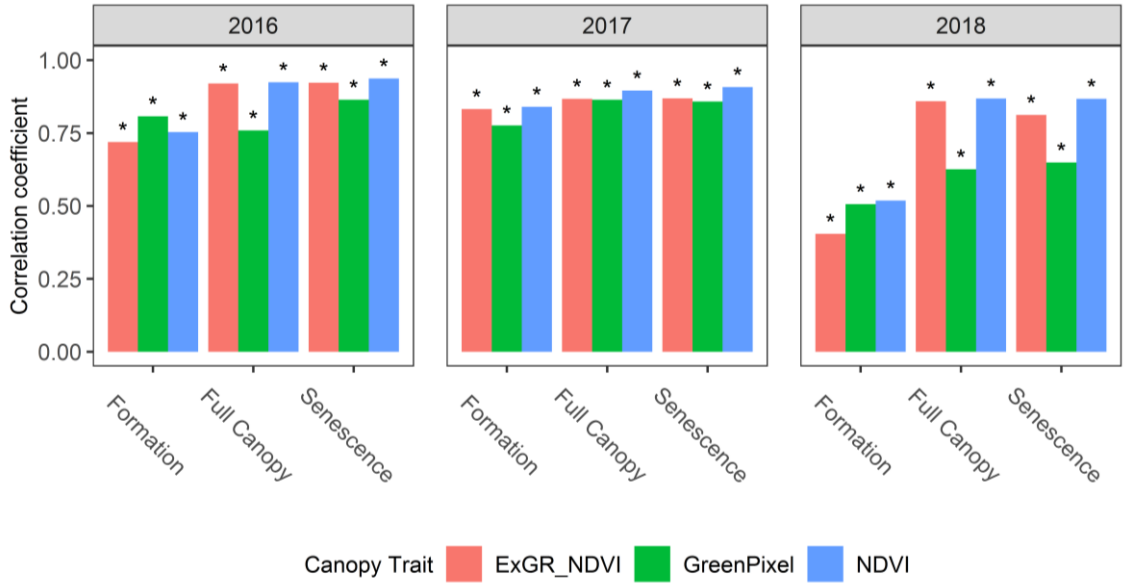

Figure 5.14. Pearson's correlation coefficient results between canopy development phase integrals derived from the UAV time series and final grain yields (t/ha at 85% dry matter) for all three growing seasons and canopy traits. * indicates statistically significant results (p-value < 0.05).

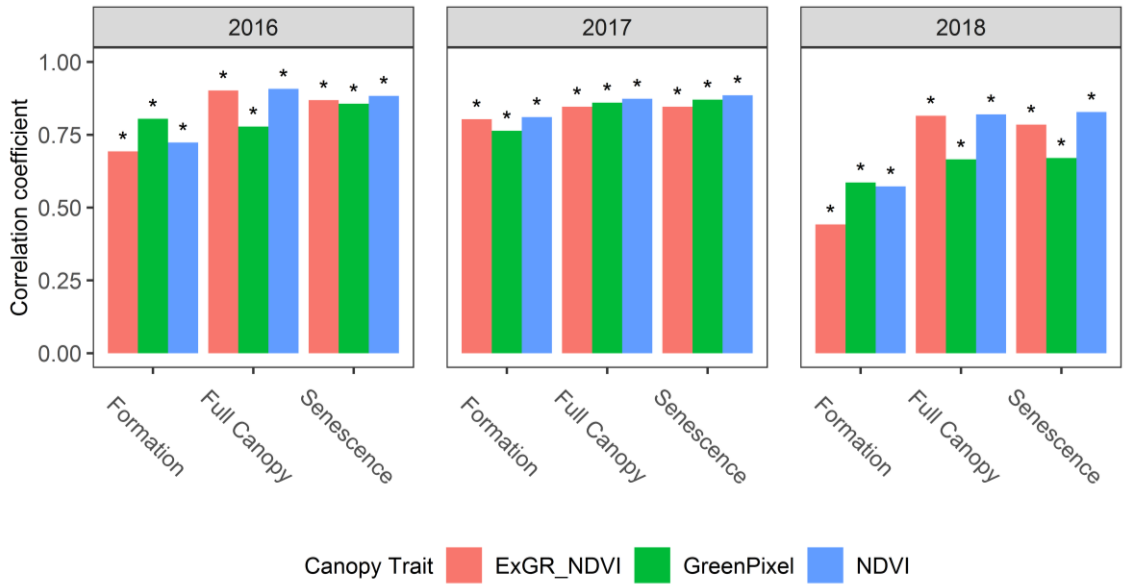

Figure 5.15. Pearson's correlation coefficient results between canopy development phase integrals derived from the UAV time series and final biomass yields (t/ha at 100% dry matter) for all three growing seasons and canopy traits. * indicates statistically significant results (p-value < 0.05).

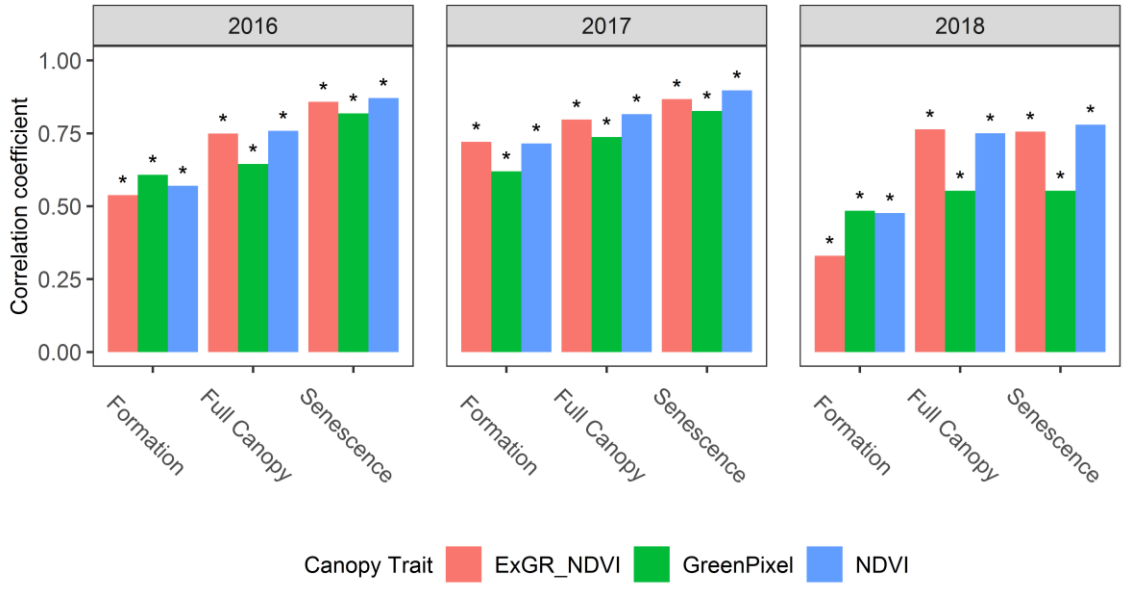

Figure 5.16. Pearson's correlation coefficient results between canopy development phase integrals derived from the UAV time series and phase integrals and total nitrogen uptake (kg-N/ha) measured at anthesis for all three growing seasons and canopy traits * indicates statistically significant results (p-value < 0.05).

5.4 Discussion

The aim of this chapter was to produce a method for phenotyping dynamic canopy development phases; specifically, the periods related to canopy formation and senescence. Using measured 'area under the curve', single metrics were produced to quantify these dynamic phases, in order to gain better understanding of how nitrogen fertiliser application concentrations impact on canopy dynamics.

The devised method utilised temporal trends in canopy NDVI to identify and isolate three phases; formation, full canopy and senescence. These phases were based on monitoring the temporal trends in canopy 'greenness' as measured by NDVI and identifying and isolating the two periods of considerable change in measured NDVI, considered to relate to canopy formation and senescence. A third phase was identified as the transition period of full canopy and maximum canopy 'greenness' which was bracketed between the formation and senescence phases. An interesting trend was identified in the UAV time series, with an early season drop in NDVI between the first and second flights presented in 2016 and 2018 growing seasons. Possible explanations for this include the influence of background soil. Su et al., (2019) found a similar trend and attributed it to irrigation of wheat plots between the two UAV flights increasing the soil moisture content. In combination with lower ground cover, this would increase the influence of background soil reflectance on derived mean plot NDVI values. However, temporal ExGR masked NDVI results show this trend remains somewhat in both 2016 and 2018, where the soil has been removed from the measurements. Alternatively, senescence of early leaves could also result in a dip in NDVI, though again it would be expected that the ExGR_NDVI would filter this out if this was the cause. Crop damage

is another potential source for this trend be it from rainfall as seen in mid-May of the 2017 growing season, or frost damage as a result of cold temperatures early in the year. Visual assessment of meteorological data from the 3 growing seasons (Figure 5.8, Figure 5.9, and Figure 5.10) indicate no consistent rainfall or cold weather events that may explain the dipping trend. An alternative option that may explain the fact that the trend remains in the ExGR masked NDVI results, is a change in canopy structure and form as the crops begin to grow. Canopy reflectance is a result of the interaction between irradiance and canopy architecture leading to scattering of light in multiple directions (Jay et al., 2017a). After emergence, the initial shoots maintain a dome shape canopy in order to maximise light interception. After a period, the wheat plant begins to grow and the canopy transitions from a dome shape to elongation; therefore, altering the canopy architecture (Satorre and Slafer, 1999). This transition in canopy architecture occurs naturally, and therefore could explain the consistent dipping trend observed in 2016 and 2018. Further investigation of these periods in the wheat growth, ideally using 3D observations, is needed in order to identify the exact reason for their occurrence. Using 3D observations, for example LiDAR, should facilitate the modelling any changes in canopy architecture over time.

Comparison of the temporal trends and defined phases to those of Green Area Index (Figure 5.17) demonstrates the same temporal trend is obtained (Agriculture and Horticulture Development Board, 2015). Specifically, the main period of rapid increase occurs between March/April to May, and the period of decrease occurs from June until August. In terms of development phases, comparison to the published wheat development phases (Figure 5.17) indicates that the Foundation and Construction

phases cover different time periods to formation and full canopy phases in this study. The Production phases, however, does align well with the senescence phase (phase 3) data in this chapter.

Though reasonable agreement is obtained in phases derived in this chapter and expected according to published growth trends (Agriculture and Horticulture Development Board, 2015), the data and results obtained in this chapter are limited presenting opportunities for further study. The use of mean NDVI values across all varieties and nitrogen treatments to defined development phases, will have reduced the ability to dissect differences between crop varieties, a key focus of crop breeders. As highlighted in Section 5.1, a target trait for many breeders is the ability of wheat varieties to prolong a full canopy and delay senescence (Christopher et al., 2014). By applying a single method to all varieties, any discrete differences in the timings of transition between phases (e.g. early canopy establishment or delayed senescence) will be concealed. This is further hampered by the lack of temporal resolution and coverage of UAV data utilised in this chapter. Data from bi-weekly UAV flights was used to monitor temporal changes in canopy phenotypes. This low temporal resolution means derived phase integrals, and in particular the specific transition timings between phases, are strongly influenced by the timings of UAV flights, as opposed to the changes in crop canopy traits. For example, in both the 2016 and 208 datasets, flights end before convergence of NDVI across all nitrogen treatments, as would be expected at the end of senescence. Furthermore, senescence phase for the 2018 season, as classified in this chapter, is covered by only two UAV flights. It must be recognised that it is difficult to associate trends with target phenotypic traits, as the temporal trend is incomplete and

influenced more by the number and timings of UAV flights as opposed to the target crops. Increasing the total number of UAV flights whilst also decreasing the time gap (e.g. > weekly flights) between flights should provide the ability for complete development phases and their transition points to be defined independent of UAV flight times.

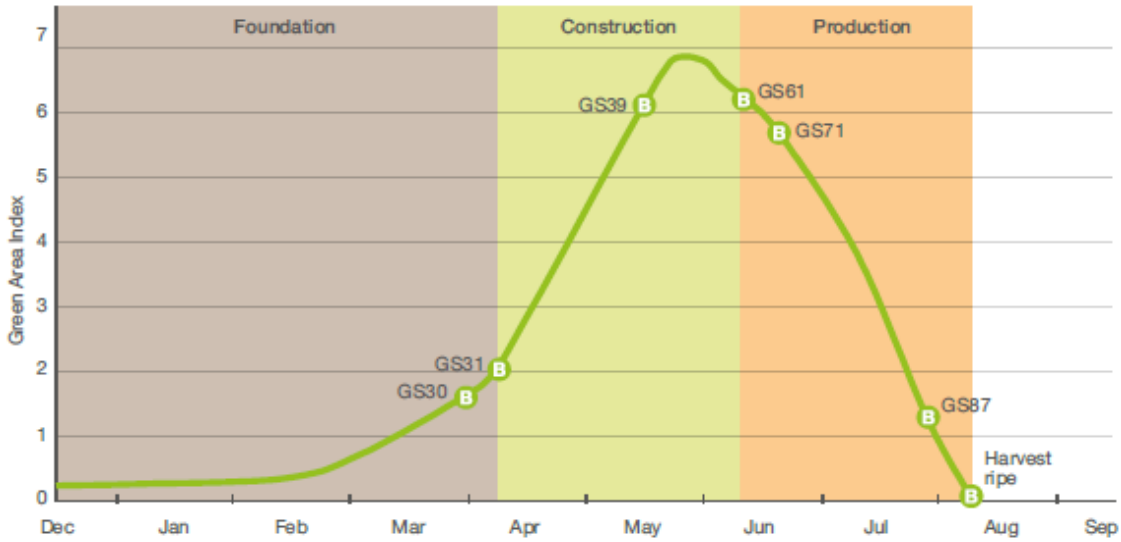

Figure 5.17. Expected temporal trends for winter wheat green area index from December to August. Also detailed are the three main wheat development phases outlined by Agriculture and Horticulture Development Board (AHDB) use for monitoring wheat development and crop management practices. GS = growth stage. (Agriculture and Horticulture Development Board, 2015).

Statistical comparison of canopy dynamics highlighted the influence of nitrogen application concentration within all isolated canopy development phases. The lack of nitrogen applied within the N1 plots is a clear and consistent trend throughout development phases, canopy traits and growing seasons. Insufficient nitrogen is clearly demonstrated to be a limiting factor on canopy dynamics throughout the crop life cycle. Of the other nitrogen treatments, the results indicate a non-linear trend in increasing phase integrals with increasing nitrogen. Most notable is the lack of consistent

differences between N3 and N4. These trends fit with the known impacts of increasing nitrogen concentrations on grain yield (Figure 5.18) (Hawkesford, 2014). The limited improvement in crop yield from nitrogen applications above 200 kg-N/ha (the N2 treatment level) correlate with the apparent limited improvements in canopy development traits seen in the results of this chapter.

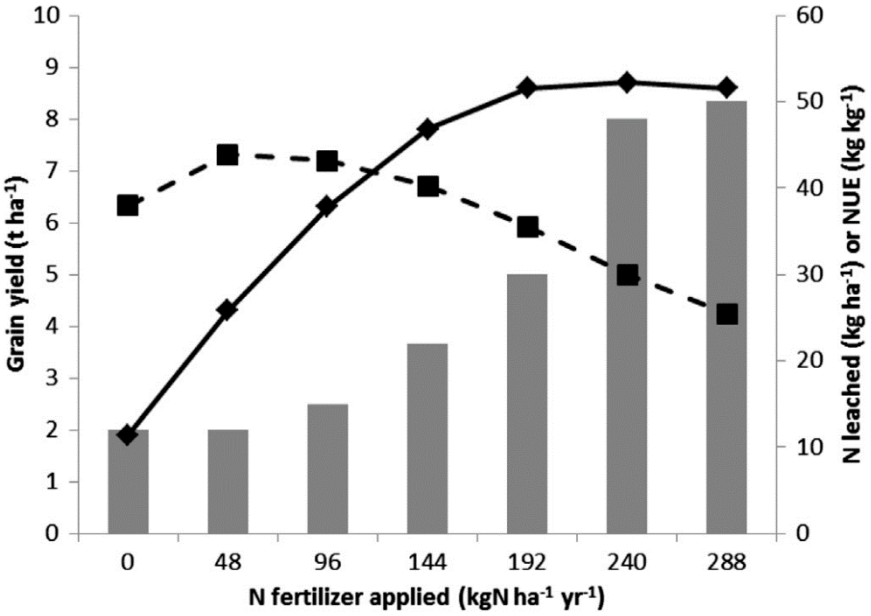

Figure 5.18. Comparison of nitrogen fertiliser application (bars) and final grain yield (solid line) showing a non-linear trend of increasing fertiliser and grain yields. Dotted line indicates estimated nitrogen use efficiency (Hawkesford, 2014).

Strong correlations between derived temporal canopy trait dynamics and harvest metrics (final grain yield, biomass and nitrogen uptake) were observed in the results of this study. Interestingly, standard NDVI tended to perform as well as, or even outperform the other canopy traits when testing correlations against key harvest metrics. The incorporation of canopy quality and coverage into the standard NDVI measure clearly outperforms either of these factors isolated. Further, comparison of these correlations to those of other studies indicates that the dynamic phenotyping of traits

does produce increased correlations against those of single time point measurements (Hassan et al., 2019; Magney et al., 2016). The results of this study are consistent with other assessments of NDVI versus harvest metric correlations (Bendig et al., 2015; Hassan et al., 2019; Pietragalla and Madrigal Vega, 2012) in that they show that the best correlations are found at the later development stages, around anthesis (flowering). Interestingly, of the canopy traits, NDVI provided the most consistent correlations with final crop metrics, despite the known limitations of spatially averaged NDVI measures of incorporating reflectance from multiple sources including background soil (Jay et al., 2017b).

The results in this chapter clearly demonstrate the potential value of integrated temporal phenotyping of crop trials for providing greater insight into how the dynamic development of plants is influenced by fertiliser application. Key to this, has been the ability to phenotype at sufficiently high temporal resolutions. The use of UAVs for this application produces significant time saving when compared to manual ground-based systems, as well as the ability to customise temporal resolution. Previous studies have shown that increased temporal resolution and integrated measurements of senescence improve understanding of genetic variation between individual genotypes, both within and between environments (Christopher et al., 2014). The simplicity and flexibility of UAVs makes it possible to achieve sufficient temporal resolution in order to dynamically phenotype the full life cycle of crop canopy.

Although the work of this chapter demonstrates the ability to phenotype dynamic canopy development phases, the 'area under the curve' method is relatively simplistic and does not highlight any inevitable non-linear trends during phases. Some

alternative methods, designed to better incorporate these within-phase trends, have been identified and should form part of the focus of future work. These include modified logistical models (Baret, 1986; Kouadio et al., 2012; Lauvernet, 2005); found to adequately estimate decreases in Green Area Index measured from satellites as a result of canopy senescence. Alternatively, Gaju et al., (2011), applied a function developed by (Genard et al., 1999) to quantify senescence as a two phase (slow and rapid) process, thereby incorporating non-linear trends into the final senescence metric derived. Key to the success of this function was obtaining data twice per week throughout the growing season up until canopy senescence was fully completed. This further highlights the temporal resolution of data in this chapter as a key limitation, for which future work should strongly focus on improving. Additional future work should look to apply the quantification of development phases method (Section 5.2.7) to individual varieties, rather than the entire field. This should allow better interpretation of phase integral trends as a result of varietal responses to varied nitrogen fertiliser application.

5.5 Conclusion

This chapter evaluated the application of high temporal UAV phenotyping to assess the effect of nitrogen fertiliser on canopy development phases. Integration of NDVI time series was used to quantify temporal trends in canopy traits over three growing seasons. Statistical comparison of phase integrals highlighted the impact of nitrogen on canopy dynamics, whilst strong correlations with harvest metrics showed the applicability of these dynamic phenotypes for association with final yields and biomass. Future work should look to increase temporal resolution of NDVI time series, and also adapt the applied methods in order investigate the impact of genetic variability between wheat varieties in response to nitrogen applications.

Chapter 6: 'Cost-throughput' Analysis of UAVs for Long Term Phenotyping of Field-based Crop Trial Experiments

6.1 Introduction

Advances in crop yields are needed to satisfy global food production demands, whilst countering biotic and abiotic stresses (Furbank and Tester, 2011b). Identification of current phenotyping abilities as a key bottle-neck to meaningful advances in crop yield gains has pushed the development of high throughput phenotyping technologies to the fore (Araus and Cairns, 2014b). This is especially true for phenotyping of field-based crop experiments, where traditional methods are seen to be largely labour intensive, inefficient, and often subjective. Several new platform types have been developed, with a focus on increasing the precision, resolution and throughput of phenotyping of field-based experiments. These include static ground platforms (e.g. Scanalyzer (Virlet et al., 2016)), moving ground-based vehicles (e.g. Pheno-mobiles (Kise and Zhang, 2008)), and low-altitude Unmanned Aerial Vehicles (UAVs); all of which present both advantages and disadvantages. The success of any of these platforms will largely rely on the validation of results, validation of high throughput abilities, data management and affordability (Araus et al., 2008).

In the case of UAVs, numerous studies have presented development and validation of acquired phenotypic data, often promoting these platforms as cost efficient or low cost, high throughput phenotyping platforms. However, few studies have offered

any assessment of the requirements for validation of throughput, data management and affordability. As such the focus of this chapter will be to evaluate and discuss the costs and throughput related to UAVs for field phenotyping.

6.1.1 Throughput

The throughput of any crop phenotyping platform equates to the number of plots or plants measured per period of time, e.g. per day (Fiorani and Schurr, 2013b). For large scale field experiments (>10,000 plots), the need for higher throughputs of phenotyping is clear. For an experiment of 20,000 plots, it was estimated that manual measurements of 30s per plot would require 192 hours of continuous work to complete (White et al., 2012a). Comparison of UAVs to tractor-based phenotyping, indicated superior throughput achieved by the UAVs (900 plots per hours vs. 100 plots per hour) (Comar et al., 2012; Holman et al., 2016). However, to define throughput as just the data collection phase, ignores the various additional steps required to produce phenotypic results. This includes calibration, correction, processing and analysis of data. For manual methods, e.g. rulers, slow data collection is countered by minimal data processing times. By contrast UAVs vastly improve data collection rates over conventional manual methods. However, extensive processing requirements, upwards of 64 hours (Ziliani et al., 2018), complicates the interpretation of true high throughput abilities of UAVs. For a fifteen-minute flight, to cover a 50-hectare field, this means that SfM processing can equate to as much as 99% of total throughput time. Automated data processing, via SfM software does allow for the majority of this to be performed with minimal input; however, this delay in obtaining phenotypic results can be significant.

6.1.2 Cost

As with the definition of throughput, definitions of cost must acknowledge a range of variables to provide a true cost analysis. Equipment is most often the focus when assessing costs; however, equipment often only represents a variable fraction of the total cost of a typical phenotyping program. Previous analysis of total costs related to a typical phenotypic program have indicated that data analysis alone can equate to up to 20% of total costs (Reynolds et al., 2019). This figure was based on estimated costs for UAV phenotyping of 4000 micro plots (4-10m^2), and total investment of $103,000. Total investment included $10,000 for a UAV and sensor; $24,545 per year for labour and training; $2,000 per year for maintenance; and $68,000 on field running costs (Reynolds et al., 2019). However, this review does not provide any details on target phenotypic traits, sensors used, or throughput achieved. Interpretation of this analysis is therefore difficult, particularly as costs related to both UAV platforms and sensors can vary significantly. For example, height measurements of a field experiment can be achieved using a low cost UAV (DJI Phantom 4 (DJI, Shenzhen, China)), proprietary RGB camera and SfM processing at a cost of £2,000 (Malambo et al., 2018). Alternatively, a UAV suitable LiDAR could be used in combination with a UAV capable of carrying 10kg (Freefly Alta (Freefly, Washington, USA)), at a cost upwards of £50,000 for the platform and sensor. Neither of these costs include the additional computing hardware and software licenses required to process and store data. Despite both offering phenotyping of crop height, the equipment cost related is significant.

Both cost and throughput associated with phenotyping systems are complex, highly variable, and at present insufficiently characterised to fully validate the affordability and efficiency of UAV phenotyping. In response to this current situation, this chapter will provide a more comprehensive and detailed breakdown of the costs and throughput associated with UAV phenotyping. In addition, comparison with manual ground-based methods will provide a clearer definition of the comparative low cost and high throughput abilities of UAVs. Utilising work from previous chapters, as well as discussions with Rothamsted Research, quantitative assessments of cost and throughput for a typical phenotyping program will be presented.

6.2 Study Site and Assessment Parameters

To ensure relevance of derived values, Rothamsted Research was used as the example research station. This was to ensure all parameters of the analysis, such as number of plots measured, and throughput rates were true and relatable to the real-world scenarios. Manual and UAV methods were based on those methods already applied to field phenotyping at Rothamsted Research. For the analysis, the following parameters were used: The total number of plots to be measured per growth season was set at 10,000 of two different sizes, large (9m x 3m) and small (1m x 1m). Analysis was set to cover five growing seasons, with 26 repeat measurements per season to measure phenotypes dynamically. For both methods, throughput was adjusted to reflect the increased throughput associated with smaller plots.

In terms of phenotyping methods, the manual method was assigned to phenotype two traits, height and canopy reflectance. Crop heights were measured using a meter rule and required two technicians for measurement and recording of heights. Canopy reflectances were measured with a hand-held Tec5 Handyspec field spectrometer (Tec5, Oberursel, Germany), requiring one technician to undertake phenotyping of canopy reflectance. UAV-based phenotyping, covered three categories of phenotype. Firstly, crop heights were determined using Structure from Motion photogrammetry with the same workflow as outlined in Chapter 3 and Holman *et al.* (2016). Phenotyping of canopy spectral reflectances was performed using the cameras and workflows developed in Chapter 4 and Holman *et al.* (2019). Additional custom-made image calibration software, produced by the author of this thesis, was implemented by Rothamsted Research to maximise automation of the image calibration and data analysis steps. Further information about this software can be found in Appendix B. Finally, phenotyping of canopy temperatures was performed using a thermal imager, as implemented by Rothamsted research.

Throughput assessments were based on typical plot and data throughput achieved by field technicians at Rothamsted Research. Cost assessments were calculated based on the exact field equipment, backup equipment, training, computer hardware and software used by Rothamsted Research.

6.3 Results

6.3.1 Cost Assessment

A full breakdown of the costs associated with manual phenotyping of crop height and canopy reflectance in the field is provided in Table 6.1. Costs include the employment of two technicians to undertake all measurements and data processing. For crop height, a simple meter rule was used for all measurements, adding very little to overall costs. A Tec5 HandySpec field spectrometer (Tec5, Oberursel, Germany) was used for measurements of plot canopy spectral reflectance, costing £13,362. The greatest cost associated with the manual method is for the two technicians, costing £100,000 per year for salaries and additional overheads. This is a significant cost, compared to the other phenotyping tools utilised; however, the necessity for skilled field technicians makes this cost unavoidable. Overall results show a total cost of £515,257 for the full five years of phenotyping. Expressed as cost per plot, this equates to £10.31 per plot for five years of measurements.

Table 6.1. Details of costs per year associated with manual phenotyping for crop height and canopy spectral reflectance. Costs include required equipment, labour and data processing.

Requirement	Details	Cost (£)	Additional Costs (£)	Five Year cost (£)
Ruler	Measuring crop height	5	-	5
Computer	Recording crop height measurements	200	-	200
Spectrometer	Tec 5 field spectrometer	13,362	1,690 software	15,052
Labour	Salary plus overheads. (Minimum 2 people required for measuring height)	100,000	100,000 per annum	500,000
Total				**515,257 (103,051 year^{-1})**
Cost per plot (£) – 50,000 plots over five years				**10.31**

Cost analysis for the UAV shows a requirement for more equipment compared to the manual methods (Table 6.2). Rothamsted Research owns two identical UAVs, both with custom gimbles to facilitate carrying different sensors simultaneously; with one acting primarily as a back-up in case of damage. A total of 16 Lithium Polymer (LiPO) batteries are required to fly all field experiments. Spare LiPO batteries are also included in case of loss of batteries due to damage or end of life span, as well as a high-powered battery charger to ensure timely charging of all batteries. Visible RGB and NIR cameras with lenses and spare parts are included for both the height and reflectance phenotyping. A FLIR thermal infrared camera is used for phenotyping canopy temperatures. Insurance and Civil Aviation Authority (CAA) permissions are required by UK law, as well as the proximity of Rothamsted Research to Luton Airport. Computing requirements included software license for Agisoft Photoscan (Agisoft, St. Petersburg, Russia), storage for imagery and computer hardware for processing of imagery. Custom open source Python-based software, developed within this PhD project, was used for data analysis and calibration of spectral imagery. Miscellaneous costs include spare parts, Ground Control Points (GCPS) in the fields, and access to a GPS for locating of GCPs. Finally, training and employment of one field technician is required to run the UAV phenotyping platform. Overall results present a total cost of £291, 885 for five years of phenotyping via UAV. Cost per plot was calculated at £6.20 for the five years. As with the manual method, labour costs were the greatest single outlay for UAV phenotyping.

Table 6.2. Details of costs per year associated with UAV phenotyping for crop height and canopy spectral reflectance. Costs include required equipment, labour and data processing.

Requirement	Details	Cost (£)	Additional Costs (£)	5-year Cost (£)
UAV	DJI S900+ with custom gimbal.	5,000	Spare drone – 5,000	10,000
Laptop	Standard laptop able to run flight controller software	1,000	-	1,000
Batteries	16x LiPO* batteries	3,040	Spare batteries – 1,520	4,560
Charger	LiPO* battery charger	450		450
RGB camera + lens	Sony α5100 + 20mm pancake lens	700	Spare camera - 700	1,400
NIR camera + lens	Sony α5100 + 20mm pancake lens + 780nm blocking filter replacement.	1,000	Spare camera – 1,000	2,000
TIR Camera	FLIR thermal imaging camera	5,800	-	5,800
Spectrometer	Tec 5 field spectrometer	13,362	1,690 software	15,052
Insurance	Covers equipment and 3rd party liability (required in the UK)	1,500	1,500 per annum cost	7,500
CAA Permission	Permission for Commercial Operation (PfCO) annual renewal	185	185 per annum cost	925
Software/ computing	Data processing software and hardware††, storage (HDD)	550† + 5000	-	5550
Miscellaneous	Spare parts, Ground Control Points etc.	3,000	750	3,750
Training (per person)	Training to achieve PfCO.	2,000	-	2,000
Labour	Salary for one person plus overheads.	50,000	50,000 per annum	250,000
Total Cost				**309,987 (61,997 year^{-1})**
Cost per plot (£) – 50,000 plots over five years				**6.20**

** Lithium Polymer Battery. ** Permission for Commercial Operation. † Education License.*

†† Example processing computer: i7 processor (3.0ghz), 32gb Ram, 8gb Nvidia GTX 1080 Graphics Card, 1Tb SSD.

6.3.2 Throughput Assessment

Results of calculated throughput rates for both the manual and UAV methods are presented in Table 6.3. For the manual method, there was variation in throughput between the two different plot sizes and the two different phenotypes measured. Unsurprisingly, the reflectance measurements were quicker than the height measurements, due to the ruler requiring multiple manual measurements from within a single plot. Data processing times for both measurements were quick (3 hours) as little data processing was required, except input of height measurements into a computer. Despite this, the total time required to phenotype the 10,000 plots with 26 repeats was 386 days for a single year. Clearly this is impossible with the current level of labour employed at Rothasmted Research. One solution would be to employ more labourers; however, this would drive up costs. If broken down to time per measurement repetition, the manual methods require 15 days to collect data for what should be weekly measurements.

For the UAV, throughput did not vary between phenotypic measurements, because they are undertaken with the same flight. Throughput did vary however with plot size, as a greater number of small plots were contained within a field and therefore a single data collection flight. Furthermore, the deployment of multiple sensors, or the ability to phenotype multiple traits from the same image sets, increased throughput. The main disadvantage of the UAV method for throughput was the time required for data processing; an additional 36 hours. This was slower in comparison to the manual methods, and will be a problem if speed of data turnaround is a priority. The total time

for the UAV method to phenotype height, spectral reflectance and canopy temperature was 49 days for all 26 repeated measurements. This equates to 5 days per round of phenotyping measurements.

The key difference between the manual and UAV methods, is that the most time-consuming aspect of the manual methods is the actual collection of the data. In contrast, the UAV method is slowed by the processing of data compared to data collection. The benefit of using the UAV comes from the ability to semi-automate the processing workflow to 24/7, at a time more convenient to the user. The manual method does not have this ability.

Table 6.3. Comparison of plot throughput per day, data processing time and total work days per year required for the manual and UAV phenotyping methods.

Method	Measurement	Plot Size*	Number of Plots	Throughput per day	Data Processing Time (Days)	Days per measurement	Measurements per Year	Days per year	Total work days per year
Manual	Height	Large	4000	600	0.125	7	26	177	386
		Small	6000	1500	0.125	4	26	107	
	Reflectance	Large	4000	1500	0.125	3	26	73	
		Small	6000	6000	0.125	1	26	29	
UAV	Height	Large	4000	3000	1.5	3	26	74	117
		Small	6000	40000	1.5	2	26	43	
	Reflectance	Large	4000	3000	1.5	3	26	74	
		Small	6000	40000	1.5	2	26	43	
	Thermal	Large	4000	3000	1.5	3	8	23	
		Small	6000	40000	1.5	2	8	13	

** Large = 3m x 9m plot; Small = 1m x 1*

6.4 Discussion

This chapter aimed to provide a detailed assessment of costs and throughput of the UAV phenotyping field experiments undertaken at Rothamsted Research, a UK-based crop research centre. To achieve this, financial costs and plot throughputs were calculated for a five-season phenotyping campaign covering 10,000 plots per year.

Cost assessment results show that overall the UAV offers superior cost per plot (£6.20) compared with manual methods (£10.31). Results highlight the influence of what may be considered hidden costs associated with both phenotyping methods. Labour accounted for 97% of costs for the manual method, and 80% of costs associated with UAV phenotyping. The importance of trained technicians for both methods clearly has to be acknowledged in future studies. The results also highlight the further hidden costs of the UAVs associated with data processing. In addition, the requirements for software licenses, sensor calibrations, data processing workflows and storage add considerable investment to the UAV. Comparison of these results to those of Reynolds *et al.* (2019) show disparity in the costs related to each aspect of the UAV method. Higher costs in all aspects of this study, highlights the need for more transparency in relation to costs in future studies of UAV-based phenotyping.

For throughput, results strongly emphasise the benefits gained from the UAVs. The inability for the manual method to complete the required repeat measurements within each season is a considerable limitation. The throughput of UAVs is considerably higher in comparison and is assisted by the ability to carry multiple sensors, phenotyping traits simultaneously. Throughput of UAVs is, on the other hand, hindered

by throughput of data after capture. Unlike the data from manual methods, UAV data requires significant post-capture processing to extract the phenotypic data. Software packages are available which automate some of the steps required, though user input is still required at various stages of the process. Full automation of data processing is beginning to appear in some software packages, e.g. Pix4Dfields now offers 'instant' 2D mapping in the field without the need for an internet connection (Pix4D, 2019). Alternatively, further development of open source workflows could improve automation, throughput and software cost savings related to image processing.

It should be noted that the costs and throughputs quantified in this chapter are specific to the phenotyping programme and equipment used as set out in Section 6.2. Therefore, costs and throughputs presented should not be applied as general costs for UAV phenotyping. Costs will undoubtedly fluctuate between locations, applications and durations of phenotyping experiments, for example labour in one country will vary with another (Reynolds et al., 2019).

6.5 Conclusions

Remote sensing-based monitoring from UAVs is regularly promoted as a new low-cost, high-throughput phenotyping solution to solve much of the phenotyping bottleneck associated with current crop development research. However, the lack of analyses in previous studies into the true costs and throughputs associated with obtaining phenotypic data from UAVs means these claims were relatively unproven. Results from this chapter demonstrate the superior throughput and cost savings associated with UAV phenotyping; ultimately confirming that UAVs can indeed provide low cost, high throughput phenotyping of field-based experiments. In the scenario presented within this chapter, the UAV equated to a 40% cost saving per plot over a five-year period.

These advantages of UAVs can be enhanced even further as future work continues development of the data processing side of UAV workflows to improve the speed and automation of data analysis workflows. Whilst the provision and reporting of quantitative measures of cost and throughput associated with future studies is important.

Chapter 7: Summary of Findings, Conclusions and Future Work

7.1 Research Aims and Objectives

As introduced in Chapter 1 and revisited throughout this thesis, the need for new, high throughput phenotyping methods, technologies and protocols of field-based crop experiments is being strongly driven by the necessity to achieve a 50% increase in global crop yields (Food and Agriculture Organization of the United Nations, 2017; Furbank and Tester, 2011b; United Nations, 2015). The development of UAV-based remote sensing tools, offers a potential solution to overcome these current inadequacies in field phenotyping, specifically resolution, precision and speed of throughput (Virlet et al., 2016). However, prior to the commencement of this PhD project, evaluation and validation of the ability of UAVs to provide phenotypically accurate, high throughput and cost-efficient data was insufficient. This chapter evaluates the extent to which the research aims and objectives set out in Chapters 1 and 2 of this thesis respectively, have been met. The overall aims of this thesis were to (i) investigate the use of UAV-based remote sensing technologies, data capture methods, and processing methodologies for providing high throughput data collection of phenotypic traits in the field; (ii) validate derived phenotypic measures against current standard measurement techniques; (iii) prove integration and application of developed methods to phenotyping of on-going field-based wheat crop experiments, (iv) assess affordability and high throughput capacity. To address these research aims, a series of specific objectives were defined (Chapter 2, Section 2.4), and addressed and evaluated (Chapters 3 – 6). The following

section reviews the general findings and outcomes of each of these chapters with references to these aims and the relevant objectives of this thesis.

Chapter 3: Crop morphology was identified as a key category of crop phenotypes, not only suitable for its measurement via remote sensing, but also as a group of valuable phenotypic traits applicable to crop development. Specific traits identified within crop morphology, were crop height and lodging risk. Structure from Motion Photogrammetry was identified as a potential solution for generating 3D reconstructions of plant morphology. However, existing examples of this application for crop height measurements lacked the accuracy required for phenotyping (Aasen et al., 2015b; Bendig et al., 2015, 2013a). Specifically, these studies suffered from significant underestimation of crop heights (Bias = 0.19m) as well as poor temporal consistency in results ($0.77 \leq R^2 \geq 0.22$). This first data chapter sought to develop and validate the application of UAV derived imagery in **combination with Structure from Motion Photogrammetric processing workflows for spatial and temporal measuring of field-based wheat crop trials**. A complete method for collection and processing of UAV imagery, via SfM photogrammetry, was developed. Validation of the derived mean plot heights was performed against both ruler and LiDAR measures of crop heights, producing consistently accurate results ($R^2 \geq 0.92$, RMSE ≤ 0.07m, Bias ≤ 0.064m) over three measurement dates (May, June and July). Superior throughput of measurements allowed the UAV method to be applied at multiple time points, from which measures of crop growth rate could be calculated. Higher spatial resolutions, facilitated the assessment of both inter- and intra-plot crop height variability, even highlighting features within plots unseen from ground assessments (Figure 7.1). Additional

investigation of SfM processing workflows also highlighted the influence of model processing parameters on model accuracy, resolution and processing times; all important factors to be considered when applying this method to real world scenarios. Future work should look to evaluate alternative imaging systems suitable for incorporation into UAV use, ultimately to facilitate measurement of multiple phenotypes simultaneously. This will allow for better analyses of the complex and dynamic interaction of multiple phenotypic traits in response to genes and growing

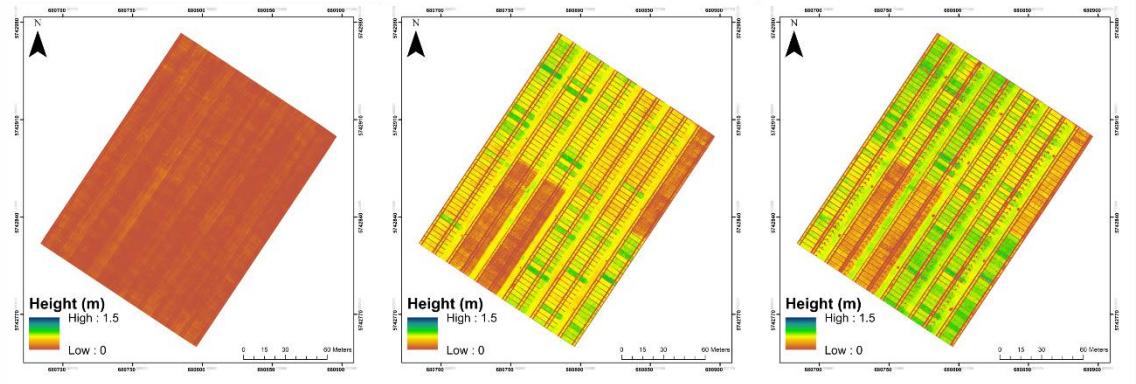

Figure 7.1. Normalised Digital Surface Models (nDSM) for three different wheat development stages captured during the 2015 growing season. The dates of the nDSMs are, from left to right 21st April, 4th June, and 6th July respectively. Originally Figure 13 in Holman *et al.* (2016) and Chapter 3 of this thesis.

environment.

Chapter 4: Spectral reflectance of plant canopies was the other category of phenotyping focussed on within this thesis. Conventional methods for measuring spectral reflectance, typically suffer from low throughput and little to no spatial resolution. UAV compatible spectral imagers offer improved spatial resolutions, though this is still limited by a trade-off between the costs and spatial resolutions of available sensors. Commercial digital cameras are a low cost, high resolution alternative for multi-spectral imaging; however, validation of workflows and accuracy of results means their

application remains unproven. This chapter sought **to develop and validate the application of modified Commercial 'Off the Shelf' (COTS) digital cameras and UAVs for the collection of radiometrically calibrated high-resolution spectral imagery of canopy reflectance**. The development of a complete radiometric calibration workflow was a key focus of this chapter, in order to generate accurate reflectance measures. New adjustments for variable image capture settings, specifically ISO and aperture value, were established to facilitate greater flexibility and ease of use of these cameras during image capture campaigns. Additional corrections for vignetting, camera spectral sensitivity, and temporal irradiance measures, combined to produce a system capable of accurate capture of high spatial resolution reflectance imagery in visible and near infrared wavebands. Validation of measured canopy reflectance against an alternative commercial UAV imager (Parrot Sequoia), and a ground-based spectrometer, highlighted disparity in accuracy between spectral bands when comparing imaging (cameras) and non-imaging (Tec5) spectrometers. Despite these trends, accuracy assessments of derived NDVI indicated successful calibration of COTS camera imagery into accurate canopy NDVI measurements ($R^2 \geq 0.88$, nRMSE ≤ 0.15). COTS cameras were investigated because they offer superior spatial resolutions over alternative UAV imagers. This aspect was investigated and applied to canopy reflectance measurements to highlight the impact of background soil inclusion in mean canopy reflectance measures (Figure 7.2). Isolation of pure vegetation pixels through the filtering of pixels, highlighted how early season measurements where greatly influenced by incomplete canopy coverage. Future work should focus on utilising the high spatial resolution to further enhance phenotypic measurements obtained from this camera system.

Application of machine learning and computer vision processing of the imagery could facilitate better monitoring of temporal phases of crops, for example, canopy formation, onset and duration of senescence, and grain head development.

Chapter 5: The focus of the previous chapters was on the evaluation,

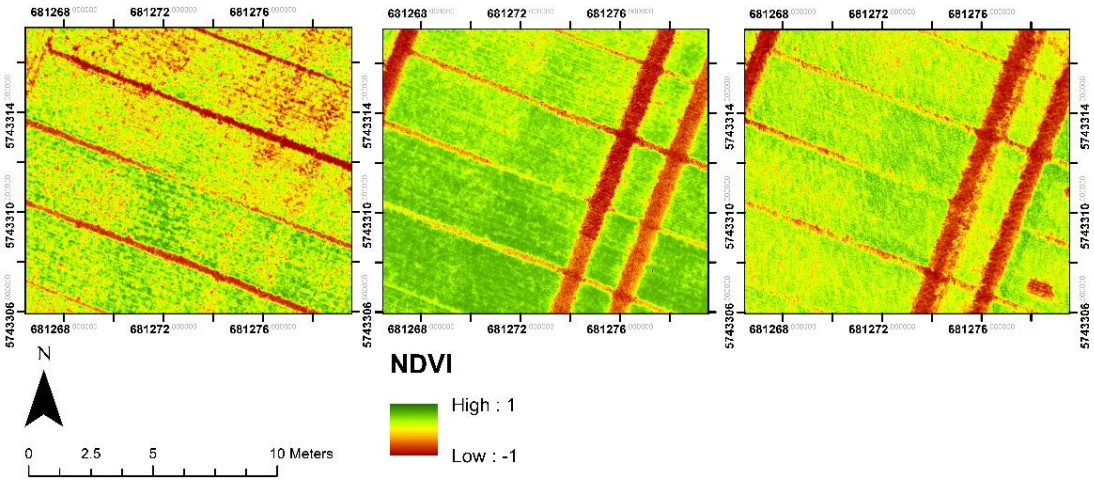

Figure 7.2. Subsets of NDVI orthomosaics from three dates, 27/03/2017 (left), 18/05/2017 (middle), 21/06/2017 (right). Orthomosaics derived from multispectral imagery captured with Commercial 'Off the Shelf' (COTS) cameras, and calibrated using custom corrections developed in this PhD. Originally Figure 17 in Holman *et al.* (2019) and Chapter 4 of this thesis.

development and validation of technologies and methodologies to produce accurate phenotypic data from UAV remote sensing platforms. However, as highlighted in Chapter 1, the full and proper evaluation and validation of the application of any new phenotyping strategy to phenotyping of existing real-world field-based crop improvement experiments is vital to their success. To provide a more complete evaluation of UAVs for phenotyping, it was appropriate to investigate what additional benefits that UAV phenotyping may offer over conventional field phenotyping strategies. In particular, to focus on the benefits gained from improvements to temporal and spatial resolutions provided by UAVs. Therefore, this chapter sought **to evaluate the applicability of UAV phenotyping methods, developed within this thesis, to long**

term, dynamic phenotyping of nitrogen fertiliser application on canopy development traits of a modern wheat germplasm panel. Using the high temporal resolution measurements, collected over the life cycle of the crops, methods were developed to phenotype temporal trends in canopy NDVI. The method was designed to isolate and quantify dynamic trends within canopy formation, full canopy and senescence phases of crop development. Statistical analysis of differences between dynamic canopy traits under different nitrogen treatments highlighted the negative impact that limiting nitrogen fertiliser can have on crop canopy formation, full canopy and senescence dynamics. Assessment of correlations with key harvest metrics showed strong correlations with final grain yield, biomass yield and total nitrogen uptake. The results highlight the applicability of the increased temporal resolution phenotyping to gaining new insights into how crops respond to changes in environmental growing conditions through their life cycles. Though they also highlight some shortcomings with the applied methods and datasets utilised, providing key areas of focus for future work in order to further develop the methods and results. Further work must include obtaining even greater temporal resolution to facilitate greater insight into crop growth dynamics. Additionally, work should look to investigate genetic variation in response to nitrogen treatments or other environmental variables to further enhance the application of UAVs to phenotyping and crop development, results were provided within this thesis (Appendix C), though analysis of these results.

Chapter 6: UAVs and remote sensing techniques are widely promoted as being high-throughput and low cost, making them an ideal solution to current bottlenecks in field phenotyping strategies. However, studies often provide little or no quantitative

assessment of the throughput rates or the associated financial costs required in order to implement UAVs into long term phenotyping studies. As highlighted in Chapter 1, cost and throughput benefits are as important factors as phenotypic accuracy in defining the success of any new phenotyping system. Considering these factors, this chapter sought **to assess and quantify the true costs and throughput associated with a UAV-based phenotyping system for long term field experiments.** Comparison of financial cost and throughput rates achieved by Rothamsted Research for ground-based and UAV-based phenotyping strategies, were used to provide quantitative assessment of the cost and throughput benefits. Evaluation of all financial costs associated with both strategies highlighted the significance of 'hidden' costs (e.g. labour and training) on the total investment required; with labour costs amounting to 97% of total cost for ground-based and 85% for UAV-based phenotyping. Overall, the UAV could achieve a 47% cost saving per plot over ground-based manual methods when considered for a five-year time period. As for throughput, the UAV provided significant advantages, ultimately achieving a throughput rate 3x greater than those of ground-based phenotyping per year for the scenario presented. This superiority is achieved largely due to the rapid data collection facilitated by UAVs and the remote sensing techniques. Slower data processing times for UAVs compared to ground-based techniques, were overcome by automation of the subsequent processing steps. Overall, for the scenarios presented in Chapter 6, UAVs offered significant advantages in all aspects of cost and throughput compared to ground-based alternatives.

7.2 Recommendations for Future Work

Unmanned Aerial Vehicles and remote sensing are no longer considered 'potential' solutions or concepts for phenotyping of field-based crop trials. Work in this thesis has made a valuable contribution to the development and validation of UAVs in this application and has identified areas for future study. These include:

- The incorporation of a wider range of sensors for phenotyping should be investigated to increase phenotyping capabilities. Development of low cost, UAV specific sensors including LiDAR and hyperspectral cameras are making them a feasible option for use. LiDAR offers the opportunity to generate much greater three-dimensional information of height, growth rates, and canopy architecture (Hosoi and Omasa, 2009; Jimenez-Berni et al., 2018; Liu et al., 2017); whilst hyperspectral increases the number and range of wavebands available for phenotyping, increasing the number of phenotypes available for measurement (Bohnenkamp et al., 2019; Li et al., 2019; Liu et al., 2020). However, as with the technologies and methods evaluated in this thesis, key to the success of any new sensor technology will be the successful development and validation of data capture, processing, analysis, and accuracy.
- Standardisation of data handling, processing, analysis and storage must be addressed in future work, to ensure compatibility of phenotypic results from different years and/or locations. As the adoption of UAVs into many different phenotyping strategies increases, there is a necessity to develop standard protocols for the important steps of data analysis and storage. The methods developed in chapters 3 and 4, generate significant volumes of imagery data (>10

GB per flight), which requires sufficient storage and processing solutions. Fine-tuning of these aspects of the entire phenotyping solution will further improve the overall capacity of UAVs as a high-throughput phenotyping system.

- This PhD project has provided only a small example of the potential applications and phenotypes that can be derived from the UAV imagery and sensors developed. Further work should consider the additional phenotypic metrics that can be derived from high spatial and temporal resolution data available from UAV platforms. More advanced data analysis techniques such as machine learning and computer vision should be investigated for their potential in offering more robust and automated analysis methods for increased phenotyping of UAV-based datasets. This area of data processing, and analysis is seeing large and rapid developments. An area of particular interest is the use of machine learning to train computers in automated image recognition and classification. Examples applications of these techniques in the field of crop phenotyping include senescence monitoring and quantification from UAV imagery (Makanza et al., 2018). Elsewhere, studies have trained models to classify vegetation and soil pixels in order to quantify ground cover and crop establishment from aerial RGB imagery (Sadeghi-Tehran et al., 2017). Other applications that have shown promise include the monitoring of disease and pest establishment in plants (Bah et al., 2019; Faical et al., 2016; Pérez-Ortiz et al., 2016; Puig et al., 2015) as well as yield prediction models from a collection of phenotypic input data (Arroyo et al., 2017; Chlingaryan et al., 2018; Hassan et al., 2019).

Integration of additional sensors alongside the dual COTS camera system of this PhD project should be a focus of future work. Specifically, thermal imaging which has been applied in monitoring crop water stress, a key target trait for crops grown in water limited environments (Rutkoski et al., 2016). Studies have utilised thermal imagers from UAVs for crop phenotyping (Berni et al., 2009a; Perez-Priego et al., 2005; Zarco-Tejada et al., 2012). Combining of thermal phenotyping with morphology and spectral reflectances as developed in this thesis should create a system capable high-throughput phenotyping a range of phenotypic data simultaneously in order to better understand how phenotypes interact dynamically over time and space.

7.3 Concluding Remarks

This PhD project has developed and evaluated UAV-based remote sensing technologies and methodologies for high throughput phenotyping of crop morphology and spectral reflectance in field-based crop trials. Conventional manual, ground-based phenotyping has been a bottleneck to meaningful advances in crop and yield development, required to meet the demands of a growing global population. The methods developed in this study offer superior temporal and spatial resolutions whilst achieving comparable accuracy for both crop morphology and spectral reflectance of plots. Improved throughput and cost efficiency of UAV phenotyping strategies over alternative options, provide further confirmation of UAVs application as valid, accurate, precise and high throughput phenotyping systems for application to field-based crop experiments. It is hoped that the work presented in this thesis will contribute to the

adoption of UAVs and remote sensing as the new conventional phenotyping strategy and support the development of crop yield advancements into the future.

References

Aasen, H., Bolten, A., 2018. Multi-temporal high-resolution imaging spectroscopy with hyperspectral 2D imagers – From theory to application. Remote Sensing of Environment 205, 374–389. https://doi.org/10.1016/j.rse.2017.10.043

Aasen, H., Burkart, A., Bolten, A., Bareth, G., 2015a. Generating 3D hyperspectral information with lightweight UAV snapshot cameras for vegetation monitoring: From camera calibration to quality assurance. ISPRS Journal of Photogrammetry and Remote Sensing 108, 245–259. https://doi.org/10.1016/j.isprsjprs.2015.08.002

Aasen, H., Burkart, A., Bolten, A., Bareth, G., 2015b. Generating 3D hyperspectral information with lightweight UAV snapshot cameras for vegetation monitoring: From camera calibration to quality assurance. ISPRS Journal of Photogrammetry and Remote Sensing 108, 245–259. https://doi.org/10.1016/j.isprsjprs.2015.08.002

Aasen, H., Honkavaara, E., Lucieer, A., Zarco-Tejada, P., 2018. Quantitative Remote Sensing at Ultra-High Resolution with UAV Spectroscopy: A Review of Sensor Technology, Measurement Procedures, and Data Correction Workflows. Remote Sensing 10, 1091. https://doi.org/10.3390/rs10071091

Aber, J.S., Marzolff, I., Ries, J.B., 2010. Small-Format Aerial Photography, 1st ed. Elsevier, Amsterdam. https://doi.org/10.1016/C2009-0-18493-3

Agisoft, 2016. Agisoft PhotoScan User Manual Professional Edition, Version 1.2 [WWW Document]. URL http://www.agisoft.com/pdf/photoscan-pro_1_2_en.pdf (accessed 8.24.16).

Agriculture and Horticulture Development Board, 2015. Wheat Growth Guide. AHDB, Warwickshire.

AHDB, 2015. Wheat Growth Guide. Agriculture and Horticulture Development Board (AHDB).

Altieri, M.A., Nicholls, C.I., 2017. The adaptation and mitigation potential of traditional agriculture in a changing climate. Climatic Change 140, 33–45. https://doi.org/10.1007/s10584-013-0909-y

Anderson, K., Gaston, K.J., 2013. Lightweight unmanned aerial vehicles will revolutionize spatial ecology. Frontiers in Ecology and the Environment 11, 138–146. https://doi.org/10.1890/120150

Anderson, K., Milton, E.J., 2005. Characterisation of the apparent reflectance of a concrete calibration surface over different time scales. Proceedings of the Ninth International Symposium on Physical Measurements and Signatures in Remote Sensing (ISPMSRS) pp 417–419.

Andújar, D., Fernández-Quintanilla, C., Dorado, J., 2015. Matching the Best Viewing Angle in Depth Cameras for Biomass Estimation Based on Poplar Seedling Geometry. Sensors (Basel, Switzerland) 15, 12999–13011. https://doi.org/10.3390/s150612999

Araus, J.L., Cairns, J.E., 2014a. Field high-throughput phenotyping: the new crop breeding frontier. Trends in Plant Science 19, 52–61. https://doi.org/10.1016/j.tplants.2013.09.008

Araus, J.L., Cairns, J.E., 2014b. Field high-throughput phenotyping: the new crop breeding frontier. Trends in Plant Science 19, 52–61. https://doi.org/10.1016/j.tplants.2013.09.008

Araus, José L., Kefauver, S.C., 2018. Breeding to adapt agriculture to climate change: affordable phenotyping solutions. Current Opinion in Plant Biology. https://doi.org/10.1016/j.pbi.2018.05.003

Araus, José L, Kefauver, S.C., 2018. Breeding to adapt agriculture to climate change: affordable phenotyping solutions. Current Opinion in Plant Biology. https://doi.org/10.1016/j.pbi.2018.05.003

Araus, J.L., Kefauver, S.C., Zaman-Allah, M., Olsen, M.S., Cairns, J.E., 2018. Translating High-Throughput Phenotyping into Genetic Gain. Trends in Plant Science 23, 451–466. https://doi.org/10.1016/j.tplants.2018.02.001

Araus, J.L., Slafer, G.A., Royo, C., Serret, M.D., 2008. Breeding for Yield Potential and Stress Adaptation in Cereals. Critical Reviews in Plant Sciences 27, 377–412. https://doi.org/10.1080/07352680802467736

Arroyo, J.A., Gomez-Castaneda, C., Ruiz, E., Cote, E.M.D., Gaviz, F., Sucar, L.E., 2017. UAV technology and machine learning techniques applied to the yield improvement in precision agriculture, in: 2017 IEEE Mexican Humanitarian Technology Conference, MHTC 2017. Institute of Electrical and Electronics Engineers Inc., pp. 137–143. https://doi.org/10.1109/MHTC.2017.8006410

Ashraf, M., Harris, P., 2005. Abiotic Stresses: Plant Resistance Through Breeding and Molecular Approaches. CRC Press.

Australian Plant Phenomics Facility, 2019. Phenotyping Technology, Australian Plant Phenomics Facility.

Azzari, G., Goulden, M.L., Rusu, R.B., 2013. Rapid Characterization of Vegetation Structure with a Microsoft Kinect Sensor. Sensors (Basel, Switzerland) 13, 2384–2398. https://doi.org/10.3390/s130202384

Bagherikia, S., Pahlevani, M., Yamchi, A., Zaynalinezhad, K., Mostafaie, A., 2019. Transcript Profiling of Genes Encoding Fructan and Sucrose Metabolism in Wheat Under Terminal Drought Stress. Journal of Plant Growth Regulation 38, 148–163. https://doi.org/10.1007/s00344-018-9822-y

Bah, M.D., Dericquebourg, E., Hafiane, A., Canals, R., 2019. Deep learning based classification system for identifying weeds using high-resolution UAV imagery, in: Advances in Intelligent Systems and Computing. Springer Verlag, pp. 176–187. https://doi.org/10.1007/978-3-030-01177-2_13

Balazadeh, S., Schildhauer, J., Araújo, W.L., Munné-Bosch, S., Fernie, A.R., Proost, S., Humbeck, K., Mueller-Roeber, B., 2014. Reversal of senescence by N resupply to N-starved Arabidopsis thaliana: transcriptomic and metabolomic consequences. Journal of Experimental Botany 65, 3975–3992. https://doi.org/10.1093/jxb/eru119

Barbedo, J.G.A., 2019. A Review on the Use of Unmanned Aerial Vehicles and Imaging Sensors for Monitoring and Assessing Plant Stresses. Drones 3, 40. https://doi.org/10.3390/drones3020040

Baret, F., 1986. Contribution au suivi radiométrique de cultures de céréales. http://www.theses.fr.

Bareth, G., Bendig, J., Tilly, N., Hoffmeister, D., Bolten, H.A.& A., 2016. A Comparison of UAV-and TLS-derived Plant Height for Crop Monitoring: Using Polygon Grids for the Analysis of Crop Surface Models (CSMs). Photogrammetrie Fernerkundung Geoinormation 2, 85–94. https://doi.org/10.1127/pfg/2016/0289

Barraclough, P.B., Howarth, J.R., Jones, J., Lopez-Bellido, R., Parmar, S., Shepherd, C.E., Hawkesford, M.J., 2010. Nitrogen efficiency of wheat: Genotypic and environmental variation and prospects for improvement. European Journal of Agronomy 33, 1–11. https://doi.org/10.1016/j.eja.2010.01.005

Bendig, J., Bolten, A., Bareth, G., 2013a. UAV-based Imaging for Multi-Temporal, very high Resolution Crop Surface Models to monitor Crop Growth Variability. Photogrammetrie - Fernerkundung - Geoinformation 2013a, 551–562. https://doi.org/10.1127/1432-8364/2013/0200

Bendig, J., Bolten, A., Bennertz, S., Broscheit, J., Eichfuss, S., Bareth, G., 2014. Estimating Biomass of Barley Using Crop Surface Models (CSMs) Derived from UAV-Based RGB Imaging. Remote Sensing 6, 10395–10412. https://doi.org/10.3390/rs61110395

Bendig, J., Willkomm, M., Tilly, N., Gnyp, M.L., Bennertz, S., Qiang, C., Miao, Y., Lenz-Wiedemann, V.I.S., Bareth, G., 2013b. Very high resolution crop surface models (CSMs) from UAV-based stereo images for rice growth monitoring in Northeast China. Int. Arch. Photogramm. Remote Sens. Spat. Inf. Sci 40, 45–50.

Bendig, J., Yu, K., Aasen, H., Bolten, A., Bennertz, S., Broscheit, J., Gnyp, M.L., Bareth, G., 2015. Combining UAV-based plant height from crop surface models, visible, and near infrared vegetation indices for biomass monitoring in barley. International Journal of Applied Earth Observation and Geoinformation 39, 79–87. https://doi.org/10.1016/j.jag.2015.02.012

Bendig, J.V., 2015. Unmanned aerial vehicles (UAVs) for multi-temporal crop surface modelling. A new method for plant height and biomass estimation based on RGB-imaging. Universität zu Köln.

Berni, J.A.J., Zarco-Tejada, P.J., Gonzalez-Dugo, V., Fereres, E., 2012. Remote Sensing of Thermal Water Stress Indicators in Peach. Acta Horticulturae 962, 325–331. https://doi.org/10.17660/ActaHortic.2012.962.45

Berni, J.A.J., Zarco-Tejada, P.J., Suarez, L., Fereres, E., 2009a. Thermal and Narrowband Multispectral Remote Sensing for Vegetation Monitoring From an Unmanned Aerial Vehicle. IEEE Transactions on Geoscience and Remote Sensing 47, 722–738. https://doi.org/10.1109/TGRS.2008.2010457

Berni, J.A.J., Zarco-Tejada, P.J., Suárez, L., González-Dugo, V., Fereres, E., 2009b. Remote sensing of vegetation from UAV platforms using lightweight multispectral and thermal imaging sensors. Int. Arch. Photogramm. Remote Sens. Spatial Inform. Sci 38.

Berra, E., Gibson-Poole, S., MacArthur, A., Gaulton, R., Hamilton, A., 2015. Estimation of the spectral sensitivity functions of un-modified and modified commercial off-theshelf digital cameras to enable their use as a multispectral imaging system for UAVs. ISPRS - International Archives of the Photogrammetry, Remote Sensing and Spatial Information Sciences XL-1/W4, 207–214. https://doi.org/10.5194/isprsarchives-XL-1-W4-207-2015

Berra, E.F., Gaulton, R., Barr, S., 2017. Commercial Off-the-Shelf Digital Cameras on Unmanned Aerial Vehicles for Multitemporal Monitoring of Vegetation Reflectance and NDVI. IEEE Transactions on Geoscience and Remote Sensing 55, 4878–4886. https://doi.org/10.1109/TGRS.2017.2655365

Bevilacqua, A., Piccinini, F., Gherardi, A., 2011. Vignetting correction by exploiting an optical microscopy image sequence, in: 2011 Annual International Conference of the IEEE Engineering in Medicine and Biology Society. Presented at the 2011

Annual International Conference of the IEEE Engineering in Medicine and Biology Society, pp. 6166–6169. https://doi.org/10.1109/IEMBS.2011.6091523

Bingham, I.J., Karley, A.J., White, P.J., Thomas, W.T.B., Russell, J.R., 2012. Analysis of improvements in nitrogen use efficiency associated with 75 years of spring barley breeding. European Journal of Agronomy, Designing Crops for new challenges 42, 49–58. https://doi.org/10.1016/j.eja.2011.10.003

Blonquist, J.M., Norman, J.M., Bugbee, B., 2009. Automated measurement of canopy stomatal conductance based on infrared temperature. Agricultural and Forest Meteorology 149, 2183–2197. https://doi.org/10.1016/j.agrformet.2009.10.003

Bohnenkamp, D., Behmann, J., Mahlein, A.-K., 2019. In-Field Detection of Yellow Rust in Wheat on the Ground Canopy and UAV Scale. Remote Sensing 11, 2495. https://doi.org/10.3390/rs11212495

Botwright, T.L., Condon, A.G., Rebetzke, G.J., Richards, R.A., 2002. Field evaluation of early vigour for genetic improvement of grain yield in wheat. Australian Journal of Agricultural Research 53, 1137. https://doi.org/10.1071/AR02007

Brocks, S., Bendig, J., Bareth, G., 2016. Toward an automated low-cost three-dimensional crop surface monitoring system using oblique stereo imagery from consumer-grade smart cameras. Journal of Applied Remote Sensing 10, 046021. https://doi.org/10.1117/1.jrs.10.046021

Bull, D.R., 2014. Chapter 4 - Digital Picture Formats and Representations, in: Bull, D.R. (Ed.), Communicating Pictures. Academic Press, Oxford, pp. 99–132. https://doi.org/10.1016/B978-0-12-405906-1.00004-0

Bullock, D.G., Anderson, D.S., 1998. Evaluation of the Minolta SPAD-502 chlorophyll meter for nitrogen management in corn. Journal of Plant Nutrition 21, 741–755. https://doi.org/10.1080/01904169809365439

Burud, I., Lange, G., Lillemo, M., Bleken, E., Grimstad, L., Johan From, P., 2017. Exploring Robots and UAVs as Phenotyping Tools in Plant Breeding. IFAC-PapersOnLine, 20th IFAC World Congress 50, 11479–11484. https://doi.org/10.1016/j.ifacol.2017.08.1591

CAA, 2019. Civil Aviation Authority [WWW Document]. URL https://www.caa.co.uk/home/ (accessed 4.12.20).

Castro, A.I. de, Jurado-Expósito, M., Peña-Barragán, J.M., López-Granados, F., 2012. Airborne multi-spectral imagery for mapping cruciferous weeds in cereal and legume crops. Precision Agriculture 13, 302–321. https://doi.org/10.1007/s11119-011-9247-0

Chapman, S.C., Merz, T., Chan, A., Jackway, P., Hrabar, S., Dreccer, M.F., Holland, E., Zheng, B., Ling, T.J., Jimenez-Berni, J., 2014. Pheno-Copter: A Low-Altitude, Autonomous Remote-Sensing Robotic Helicopter for High-Throughput Field-Based Phenotyping. Agronomy 4, 279–301. https://doi.org/10.3390/agronomy4020279

Chlingaryan, A., Sukkarieh, S., Whelan, B., 2018. Machine learning approaches for crop yield prediction and nitrogen status estimation in precision agriculture: A review. Computers and Electronics in Agriculture 151, 61–69. https://doi.org/10.1016/j.compag.2018.05.012

Christopher, J.T., Veyradier, M., Borrell, A.K., Harvey, G., Fletcher, S., Chenu, K., 2014. Phenotyping novel stay-green traits to capture genetic variation in senescence dynamics. Functional Plant Biol. 41, 1035. https://doi.org/10.1071/FP14052

Chu, T., Starek, M., Brewer, M., Murray, S., Pruter, L., 2017. Assessing Lodging Severity over an Experimental Maize (Zea mays L.) Field Using UAS Images. Remote Sensing 9, 923. https://doi.org/10.3390/rs9090923

Cobb, J.N., DeClerck, G., Greenberg, A., Clark, R., McCouch, S., 2013. Next-generation phenotyping: requirements and strategies for enhancing our understanding of genotype–phenotype relationships and its relevance to crop improvement. Theoretical and Applied Genetics 126, 867–887. https://doi.org/10.1007/s00122-013-2066-0

Coffin, D., 2007. Decoding raw digital photos in Linux [WWW Document]. Decoding raw digital photos in Linux. URL https://www.cybercom.net/~dcoffin/dcraw/ (accessed 2.18.19).

Coleman, R.K., Gill, G.S., Rebetzke, G.J., 2001. Identification of quantitative trait loci for traits conferring weed competitiveness in wheat (Triticum aestivum L.). Australian Journal of Agricultural Research 52, 1235–1246. https://doi.org/10.1071/ar01055

Colomina, I., Molina, P., 2014. Unmanned aerial systems for photogrammetry and remote sensing: A review. ISPRS Journal of Photogrammetry and Remote Sensing 92, 79–97. https://doi.org/10.1016/j.isprsjprs.2014.02.013

Comar, A., Burger, P., de Solan, B., Baret, F., Daumard, F., Hanocq, J.-F., 2012. A semi-automatic system for high throughput phenotyping wheat cultivars in-field conditions: description and first results. Functional Plant Biology 39, 914. https://doi.org/10.1071/FP12065

Conrady, A.E., 2013. Applied Optics and Optical Design, Part One. Courier Corporation.

Coops, N.C., Johnson, M., Wulder, M.A., White, J.C., 2006. Assessment of QuickBird high spatial resolution imagery to detect red attack damage due to mountain pine beetle infestation. Remote Sensing of Environment 103, 67–80. https://doi.org/10.1016/j.rse.2006.03.012

Dandois, J.P., Ellis, E.C., 2013. High spatial resolution three-dimensional mapping of vegetation spectral dynamics using computer vision. Remote Sensing of Environment 136, 259–276. https://doi.org/10.1016/j.rse.2013.04.005

Darrodi, M.M., Finlayson, G., Goodman, T., Mackiewicz, M., 2015. Reference data set for camera spectral sensitivity estimation. J Opt Soc Am A Opt Image Sci Vis 32, 381–391. https://doi.org/10.1364/JOSAA.32.000381

Daughtry, C.S.T., Walthall, C.L., Kim, M.S., Colstoun, E.B. de, McMurtrey, J.E., 2000. Estimating Corn Leaf Chlorophyll Concentration from Leaf and Canopy Reflectance. Remote Sensing of Environment 74, 229–239. https://doi.org/10.1016/S0034-4257(00)00113-9

Deery, D., Jimenez-Berni, J., Jones, H., Sirault, X., Furbank, R., 2014. Proximal Remote Sensing Buggies and Potential Applications for Field-Based Phenotyping. Agronomy 4, 349–379. https://doi.org/10.3390/agronomy4030349

Deng, L., Mao, Z., Li, X., Hu, Z., Duan, F., Yan, Y., 2018. UAV-based multispectral remote sensing for precision agriculture: A comparison between different cameras. ISPRS Journal of Photogrammetry and Remote Sensing 146, 124–136. https://doi.org/10.1016/j.isprsjprs.2018.09.008

Distelfeld, A., Avni, R., Fischer, A.M., 2014. Senescence, nutrient remobilization, and yield in wheat and barley. Journal of Experimental Botany ert477. https://doi.org/10.1093/jxb/ert477

Doelling, D., Helder, D., Schott, J., Stone, T., Pinto, C.T., 2018. 1.17 - Vicarious Calibration and Validation, in: Liang, S. (Ed.), Comprehensive Remote Sensing.

Elsevier, Oxford, pp. 475–518. https://doi.org/10.1016/B978-0-12-409548-9.10329-X

Dohleman, F.G., Heaton, E.A., Leakey, A.D.B., Long, S.P., 2009. Does greater leaf-level photosynthesis explain the larger solar energy conversion efficiency of Miscanthus relative to switchgrass? Plant Cell Environ. 32, 1525–1537. https://doi.org/10.1111/j.1365-3040.2009.02017.x

Du, M., Noguchi, N., 2017. Monitoring of Wheat Growth Status and Mapping of Wheat Yield's within-Field Spatial Variations Using Color Images Acquired from UAV-camera System. Remote Sensing 9, 289. https://doi.org/10.3390/rs9030289

Duan, T., 2017. Dynamic monitoring of NDVI in wheat agronomy and breeding trials using an unmanned aerial vehicle. Field crops research v. 210, 71–80. https://doi.org/10.1016/j.fcr.2017.05.025

Erten, E., Lopez-Sanchez, J.M., Yuzugullu, O., Hajnsek, I., 2016. Retrieval of agricultural crop height from space: A comparison of SAR techniques. Remote Sensing of Environment 187, 130–144. https://doi.org/10.1016/j.rse.2016.10.007

European Plant Phenotyping Network, 2019. Infrastructure DB.

Evenson, R.E., Gollin, D., 2003. Assessing the Impact of the Green Revolution, 1960 to 2000. Science 300, 758–762. https://doi.org/10.1126/science.1078710

Evert, R.F., Eichhorn, S.E., 2013. Raven Biology of Plants., 8th ed. W.H Freeman and Company.

Faical, B.S., Ueyama, J., Carvalho, A.C.P.L.F. de, 2016. The Use of Autonomous UAVs to Improve Pesticide Application in Crop Fields. Institute of Electrical and Electronics Engineers (IEEE), pp. 32–33. https://doi.org/10.1109/mdm.2016.96

Fernández-Hernandez, J., González-Aguilera, D., Rodríguez-Gonzálvez, P., Mancera-Taboada, J., 2015. Image-Based Modelling from Unmanned Aerial Vehicle (UAV) Photogrammetry: An Effective, Low-Cost Tool for Archaeological Applications. Archaeometry 57, 128–145. https://doi.org/10.1111/arcm.12078

Fiorani, F., Schurr, U., 2013a. Future Scenarios for Plant Phenotyping. Annual Review of Plant Biology 64, 267–291. https://doi.org/10.1146/annurev-arplant-050312-120137

Fiorani, F., Schurr, U., 2013b. Future Scenarios for Plant Phenotyping. Annual Review of Plant Biology 64, 267–291. https://doi.org/10.1146/annurev-arplant-050312-120137

Fonstad, M.A., Dietrich, J.T., Courville, B.C., Jensen, J.L., Carbonneau, P.E., 2013. Topographic structure from motion: a new development in photogrammetric measurement. Earth Surface Processes and Landforms 38, 421–430. https://doi.org/10.1002/esp.3366

Food and Agriculture Organization of the United Nations (Ed.), 2017. The future of food and agriculture: trends and challenges. Food and Agriculture Organization of the United Nations, Rome.

Furbank, R.T., Tester, M., 2011a. Phenomics – technologies to relieve the phenotyping bottleneck. Trends in Plant Science 16, 635–644. https://doi.org/10.1016/j.tplants.2011.09.005

Furbank, R.T., Tester, M., 2011b. Phenomics – technologies to relieve the phenotyping bottleneck. Trends in Plant Science 16, 635–644. https://doi.org/10.1016/j.tplants.2011.09.005

G. L. Ritchie, D. G. Sullivan, C. D. Perry, J. E. Hook, C. W. Bednarz, 2008. Preparation of a Low-Cost Digital Camera System for Remote Sensing. Applied Engineering in Agriculture 24, 885–894. https://doi.org/10.13031/2013.25359

Gago, J., Douthe, C., Coopman, R.E., Gallego, P.P., Ribas-Carbo, M., Flexas, J., Escalona, J., Medrano, H., 2015. UAVs challenge to assess water stress for sustainable agriculture. Agricultural Water Management 153, 9–19. https://doi.org/10.1016/j.agwat.2015.01.020

Gaju, O., Allard, V., Martre, P., Snape, J.W., Heumez, E., LeGouis, J., Moreau, D., Bogard, M., Griffiths, S., Orford, S., Hubbart, S., Foulkes, M.J., 2011. Identification of traits to improve the nitrogen-use efficiency of wheat genotypes. Field Crops Research 123, 139–152. https://doi.org/10.1016/j.fcr.2011.05.010

Gaju, O., DeSilva, J., Carvalho, P., Hawkesford, M.J., Griffiths, S., Greenland, A., Foulkes, M.J., 2016. Leaf photosynthesis and associations with grain yield, biomass and nitrogen-use efficiency in landraces, synthetic-derived lines and cultivars in wheat. Field Crops Research 193, 1–15. https://doi.org/10.1016/j.fcr.2016.04.018

Gaudin, A.C.M., Henry, A., Sparks, A.H., Slamet-Loedin, I.H., 2013. Taking transgenic rice drought screening to the field. Journal of Experimental Botany 64, 109–117. https://doi.org/10.1093/jxb/ers313

Gehrke, R., Greiwe, A., 2014. RGBI images with UAV and off-the-shelf compact cameras: an investigation of linear sensor characteristics. https://doi.org/10.12760/02-2014-1-10

Geipel, J., Link, J., Claupein, W., 2014. Combined Spectral and Spatial Modeling of Corn Yield Based on Aerial Images and Crop Surface Models Acquired with an Unmanned Aircraft System. Remote Sensing 6, 10335–10355. https://doi.org/10.3390/rs61110335

Genard, M., Reich, M., Lobit, P., Besset, & J., 1999. Correlations between sugar and acid content and peach growth. The Journal of Horticultural Science and Biotechnology 74, 772–776. https://doi.org/10.1080/14620316.1999.11511187

Ghanem, M.E., Marrou, H., Sinclair, T.R., 2015. Physiological phenotyping of plants for crop improvement. Trends in Plant Science 20, 139–144. https://doi.org/10.1016/j.tplants.2014.11.006

Gibson-Poole, S., Humphris, S., Toth, I., Hamilton, A., 2017. Identification of the onset of disease within a potato crop using a UAV equipped with un-modified and modified commercial off-the-shelf digital cameras. Advances in Animal Biosciences 8, 812–816. https://doi.org/10.1017/S204047001700084X

Gómez-Candón, D., Castro, A.I.D., López-Granados, F., 2014. Assessing the accuracy of mosaics from unmanned aerial vehicle (UAV) imagery for precision agriculture purposes in wheat. Precision Agriculture 15, 44–56. https://doi.org/10.1007/s11119-013-9335-4

Govaerts, B., Verhulst, N., 2010. The normalized difference vegetation index (NDVI) GreenSeekerTM handheld sensor: Toward the integrated evaluation of crop management. CIMMYT.

Grenzdörffer, G.J., 2014. Crop height determination with UAS point clouds. ISPRS - International Archives of the Photogrammetry, Remote Sensing and Spatial Information Sciences XL–1, 135–140. https://doi.org/10.5194/isprsarchives-XL-1-135-2014

Guan, S., Fukami, K., Matsunaka, H., Okami, M., Tanaka, R., Nakano, H., Sakai, T., Nakano, K., Ohdan, H., Takahashi, K., 2019. Assessing Correlation of High-Resolution NDVI with Fertilizer Application Level and Yield of Rice and Wheat Crops using Small UAVs. Remote Sensing 11, 112. https://doi.org/10.3390/rs11020112

Guo, W., Zheng, B., Potgieter, A.B., Diot, J., Watanabe, K., Noshita, K., Jordan, D.R., Wang, X., Watson, J., Ninomiya, S., Chapman, S.C., 2018. Aerial Imagery Analysis – Quantifying Appearance and Number of Sorghum Heads for Applications in Breeding and Agronomy. Frontiers in Plant Science 9, 1544. https://doi.org/10.3389/fpls.2018.01544

Hassan, M.A., Yang, M., Rasheed, A., Yang, G., Reynolds, M., Xia, X., Xiao, Y., He, Z., 2019. A rapid monitoring of NDVI across the wheat growth cycle for grain yield prediction using a multi-spectral UAV platform. Plant Science, The 4th International Plant Phenotyping Symposium 282, 95–103. https://doi.org/10.1016/j.plantsci.2018.10.022

Hawkesford, M.J., 2012. Improving Nutrient Use Efficiency in Crops. eLS. https://doi.org/10.1002/9780470015902.a0023734

Hawkesford, M.J., 2014. Reducing the reliance on nitrogen fertilizer for wheat production. Journal of Cereal Science, Cereal Science for Food Security,Nutrition and Sustainability 59, 276–283. https://doi.org/10.1016/j.jcs.2013.12.001

Hawkesford, M.J., 2017. Genetic variation in traits for nitrogen use efficiency in wheat. J Exp Bot 68, 2627–2632. https://doi.org/10.1093/jxb/erx079

Heyneke, E., Watanabe, M., Erban, A., Duan, G., Buchner, P., Walther, D., Kopka, J., Hawkesford, M.J., Hoefgen, R., 2019. Effect of Senescence Phenotypes and Nitrate Availability on Wheat Leaf Metabolome during Grain Filling. Agronomy 9, 305. https://doi.org/10.3390/agronomy9060305

Hiscocks, P.D., 2011. Measuring Luminance with a digital camera [WWW Document]. Syscomp Electronic Design Limited. URL https://www.atecorp.com/atecorp/media/pdfs/data-sheets/Tektronix-J16_Application.pdf (accessed 8.10.17).

Hoffmeister, D., Curdt, C., Tilly, N., Bendig, J., 2010. 3D TERRESTRIAL LASER SCANNING FOR FIELD CROP MODELLING. p. 6.

Holman, F.H., Riche, A.B., Castle, M., Wooster, M.J., Hawkesford, M.J., 2019. Radiometric Calibration of 'Commercial off the Shelf' Cameras for UAV-Based High-Resolution Temporal Crop Phenotyping of Reflectance and NDVI. Remote Sensing 11, 1657. https://doi.org/10.3390/rs11141657

Holman, F.H., Riche, A.B., Michalski, A., Castle, M., Wooster, M.J., Hawkesford, M.J., 2016. High Throughput Field Phenotyping of Wheat Plant Height and Growth Rate in Field Plot Trials Using UAV Based Remote Sensing. Remote Sensing 8, 1031. https://doi.org/10.3390/rs8121031

Hosoi, F., Omasa, K., 2009. Estimating vertical plant area density profile and growth parameters of a wheat canopy at different growth stages using three-dimensional portable lidar imaging. ISPRS Journal of Photogrammetry and Remote Sensing 64, 151–158. https://doi.org/10.1016/j.isprsjprs.2008.09.003

Houle, D., Govindaraju, D.R., Omholt, S., 2010. Phenomics: the next challenge. Nature Reviews Genetics 11, 855–866. https://doi.org/10.1038/nrg2897

Huete, A.R., 1988. A soil-adjusted vegetation index (SAVI). Remote Sensing of Environment 25, 295–309. https://doi.org/10.1016/0034-4257(88)90106-X

Hunt, E.R., Hively, W.D., Daughtry, C.S., McCarty, G.W., Fujikawa, S.J., Ng, T.L., Tranchitella, M., Linden, D.S., Yoel, D.W., 2008. Remote sensing of crop leaf area index using unmanned airborne vehicles, in: Proceedings of the Pecora 17 Symposium, Denver, CO.

Hunt Jr., E.R., Doraiswamy, P.C., McMurtrey, J.E., Daughtry, C.S.T., Perry, E.M., Akhmedov, B., 2013. A visible band index for remote sensing leaf chlorophyll

content at the canopy scale. International Journal of Applied Earth Observation and Geoinformation 21, 103–112. https://doi.org/10.1016/j.jag.2012.07.020

Hunter, M.C., Smith, R.G., Schipanski, M.E., Atwood, L.W., Mortensen, D.A., 2017. Agriculture in 2050: Recalibrating Targets for Sustainable Intensification. BioScience 67, 386–391. https://doi.org/10.1093/biosci/bix010

James, M.R., Robson, S., d'Oleire-Oltmanns, S., Niethammer, U., 2017. Optimising UAV topographic surveys processed with structure-from-motion: Ground control quality, quantity and bundle adjustment. Geomorphology 280, 51–66. https://doi.org/10.1016/j.geomorph.2016.11.021

Jay, S., Gorretta, N., Morel, J., Maupas, F., Bendoula, R., Rabatel, G., Dutartre, D., Comar, A., Baret, F., 2017a. Estimating leaf chlorophyll content in sugar beet canopies using millimeter- to centimeter-scale reflectance imagery. Remote Sensing of Environment 198, 173–186. https://doi.org/10.1016/j.rse.2017.06.008

Jay, S., Gorretta, N., Morel, J., Maupas, F., Bendoula, R., Rabatel, G., Dutartre, D., Comar, A., Baret, F., 2017b. Estimating leaf chlorophyll content in sugar beet canopies using millimeter- to centimeter-scale reflectance imagery. Remote Sensing of Environment 198, 173–186. https://doi.org/10.1016/j.rse.2017.06.008

Jay, S., Rabatel, G., Hadoux, X., Moura, D., Gorretta, N., 2015. In-field crop row phenotyping from 3D modeling performed using Structure from Motion. Computers and Electronics in Agriculture 110, 70–77. https://doi.org/10.1016/j.compag.2014.09.021

Jiang, J., Liu, D., Gu, J., Süsstrunk, S., 2013. What is the space of spectral sensitivity functions for digital color cameras?, in: 2013 IEEE Workshop on Applications of Computer Vision (WACV). Presented at the 2013 IEEE Workshop on Applications of Computer Vision (WACV), pp. 168–179. https://doi.org/10.1109/WACV.2013.6475015

Jiang, Y., Li, C., Paterson, A.H., 2016. High throughput phenotyping of cotton plant height using depth images under field conditions. Computers and Electronics in Agriculture 130, 57–68. https://doi.org/10.1016/j.compag.2016.09.017

Jimenez-Berni, J.A., Deery, D.M., Rozas-Larraondo, P., Condon, A. (Tony) G., Rebetzke, G.J., James, R.A., Bovill, W.D., Furbank, R.T., Sirault, X.R.R., 2018. High Throughput Determination of Plant Height, Ground Cover, and Above-Ground Biomass in Wheat with LiDAR. Frontiers in Plant Science 9. https://doi.org/10.3389/fpls.2018.00237

Jones, H.G., Archer, N., Rotenberg, E., Casa, R., 2003. Radiation measurement for plant ecophysiology. Journal of Experimental Botany 54, 879–889. https://doi.org/10.1093/jxb/erg116

Jurasinski, G., Koebsch, F., Guenther, A., Beetz, S., 2014. flux: Flux rate calculation from dynamic closed chamber measurements.

Kanning, M., Kühling, I., Trautz, D., Jarmer, T., 2018. High-Resolution UAV-Based Hyperspectral Imagery for LAI and Chlorophyll Estimations from Wheat for Yield Prediction. Remote Sensing 10, 2000. https://doi.org/10.3390/rs10122000

Khan, Z., Chopin, J., Cai, J., Eichi, V.-R., Haefele, S., Miklavcic, S., Khan, Z., Chopin, J., Cai, J., Eichi, V.-R., Haefele, S., Miklavcic, S.J., 2018a. Quantitative Estimation of Wheat Phenotyping Traits Using Ground and Aerial Imagery. Remote Sensing 10, 950. https://doi.org/10.3390/rs10060950

Khan, Z., Rahimi-Eichi, V., Haefele, S., Garnett, T., Miklavcic, S.J., 2018b. Estimation of vegetation indices for high-throughput phenotyping of wheat using aerial imaging. Plant Methods 14, 20. https://doi.org/10.1186/s13007-018-0287-6

Kim, S.J., Pollefeys, M., 2008. Robust Radiometric Calibration and Vignetting Correction. IEEE Transactions on Pattern Analysis and Machine Intelligence 30, 562–576. https://doi.org/10.1109/TPAMI.2007.70732

Kise, M., Zhang, Q., 2008. Development of a stereovision sensing system for 3D crop row structure mapping and tractor guidance. Biosystems Engineering 101, 191–198. https://doi.org/10.1016/j.biosystemseng.2008.08.001

Knyazikhin, Y., Schull, M.A., Stenberg, P., Mottus, M., Rautiainen, M., Yang, Y., Marshak, A., Carmona, P.L., Kaufmann, R.K., Lewis, P., Disney, M.I., Vanderbilt, V., Davis, A.B., Baret, F., Jacquemoud, S., Lyapustin, A., Myneni, R.B., 2013. Hyperspectral remote sensing of foliar nitrogen content. Proceedings of the National Academy of Sciences 110, E185–E192. https://doi.org/10.1073/pnas.1210196109

Koh, L., Wich, S., 2012. Dawn of drone ecology: low-cost autonomous aerial vehicles for conservation. Tropical Conservation Science 5, 121–132.

Kouadio, L., Duveiller, G., Djaby, B., Jarroudi, M.E., Defourny, P., Tychon, B., 2012. Estimating regional wheat yield from the shape of decreasing curves of green area index temporal profiles retrieved from MODIS data. International Journal of Applied Earth Observation and Geoinformation 18, 111–118. https://doi.org/10.1016/j.jag.2012.01.009

Küng, O., Strecha, C., Beyeler, A., Zufferey, J.-C., Floreano, D., Fua, P., Gervaix, F., 2011. The Accuracy of Automatic Photogrammetric Techniques on Ultra-light UAV Imagery.

Kyratzis, A.C., Skarlatos, D.P., Menexes, G.C., Vamvakousis, V.F., Katsiotis, A., 2017. Assessment of Vegetation Indices Derived by UAV Imagery for Durum Wheat Phenotyping under a Water Limited and Heat Stressed Mediterranean Environment. Front. Plant Sci. 8. https://doi.org/10.3389/fpls.2017.01114

Laliberte, A.S., Rango, A., 2009. Texture and Scale in Object-Based Analysis of Subdecimeter Resolution Unmanned Aerial Vehicle (UAV) Imagery. IEEE Transactions on Geoscience and Remote Sensing 47, 761–770. https://doi.org/10.1109/TGRS.2008.2009355

Lati, R.N., Filin, S., Eizenberg, H., 2013. Estimating plant growth parameters using an energy minimization-based stereovision model. Computers and Electronics in Agriculture 98, 260–271. https://doi.org/10.1016/j.compag.2013.07.012

Latorre-Carmona, P., Knyazikhin, Y., Alonso, L., Moreno, J.F., Pla, F., Yan, Y., 2014. On hyperspectral remote sensing of leaf biophysical constituents: Decoupling vegetation structure and leaf optics using CHRIS-PROBA data over crops in barrax. IEEE Geoscience and Remote Sensing Letters 11, 1579–1583. https://doi.org/10.1109/LGRS.2014.2305168

Lauvernet, C., 2005. Assimilation variationnelle d'observations de télédétection dans les modèles de fonctionnement de la végétation : utilisation du modèle adjoint et prise en compte de contraintes spatiales. Université Joseph-Fourier - Grenoble I.

Lebourgeois, V., Bégué, A., Labbé, S., Mallavan, B., Prévot, L., Roux, B., 2008. Can Commercial Digital Cameras Be Used as Multispectral Sensors? A Crop Monitoring Test. Sensors 8, 7300–7322. https://doi.org/10.3390/s8117300

Lelong, C.C.D., Burger, P., Jubelin, G., Roux, B., Labbé, S., Baret, F., 2008. Assessment of Unmanned Aerial Vehicles Imagery for Quantitative Monitoring of Wheat Crop in Small Plots. Sensors (Basel) 8, 3557–3585. https://doi.org/10.3390/s8053557

Leong, F.J.W.-M., Brady, M., McGee, J.O., 2003. Correction of uneven illumination (vignetting) in digital microscopy images. J Clin Pathol 56, 619–621.

Li, L., Zhang, Q., Huang, D., 2014. A Review of Imaging Techniques for Plant Phenotyping. Sensors 14, 20078–20111. https://doi.org/10.3390/s141120078

Li, Y., Chen, D., Walker, C.N., Angus, J.F., 2010. Estimating the nitrogen status of crops using a digital camera. Field Crops Research 118, 221–227. https://doi.org/10.1016/j.fcr.2010.05.011

Li, Zhenhai, Li, Zhenhong, Fairbairn, D., Li, N., Xu, B., Feng, H., Yang, G., 2019. Multi-LUTs method for canopy nitrogen density estimation in winter wheat by field and UAV hyperspectral. Computers and Electronics in Agriculture 162, 174–182. https://doi.org/10.1016/j.compag.2019.04.005

Liang, X., Liu, Y., Chen, J., Adams, C., 2018. Late-season photosynthetic rate and senescence were associated with grain yield in winter wheat of diverse origins. Journal of Agronomy and Crop Science 204, 1–12. https://doi.org/10.1111/jac.12231

Liebisch, F., Kirchgessner, N., Schneider, D., Walter, A., Hund, A., 2015. Remote, aerial phenotyping of maize traits with a mobile multi-sensor approach. Plant Methods 11, 9. https://doi.org/10.1186/s13007-015-0048-8

Liu, H., Zhu, H., Li, Z., Yang, G., 2020. Quantitative analysis and hyperspectral remote sensing of the nitrogen nutrition index in winter wheat. International Journal of Remote Sensing 41, 858–881. https://doi.org/10.1080/01431161.2019.1650984

Liu, S., Baret, F., Abichou, M., Boudon, F., Thomas, S., Zhao, K., Fournier, C., Andrieu, B., Irfan, K., Hemmerlé, M., Solan, B. de, 2017. Estimating wheat green area index from ground-based LiDAR measurement using a 3D canopy structure model. Agricultural and Forest Meteorology 247, 12–20. https://doi.org/10.1016/j.agrformet.2017.07.007

Liu, S., Li, L., Gao, W., Zhang, Y., Liu, Y., Wang, S., Lu, J., 2018. Diagnosis of nitrogen status in winter oilseed rape (Brassica napus L.) using in-situ hyperspectral data and unmanned aerial vehicle (UAV) multispectral images. Computers and Electronics in Agriculture 151, 185–195. https://doi.org/10.1016/j.compag.2018.05.026

Lobos, G.A., Camargo, A.V., Pozo, A. del, Araus, J.L., Ortiz, R., Doonan, J.H., 2017. Editorial: Plant Phenotyping and Phenomics for Plant Breeding. Frontiers in Plant Science 8. https://doi.org/10.3389/fpls.2017.02181

Lopes, M.S., Reynolds, M.P., 2012. Stay-green in spring wheat can be determined by spectral reflectance measurements (normalized difference vegetation index) independently from phenology. J Exp Bot 63, 3789–3798. https://doi.org/10.1093/jxb/ers071

Lyra, D.H., Virlet, N., Sadeghi-Tehran, P., Hassall, K.L., Wingen, L.U., Orford, S., Griffiths, S., Hawkesford, M.J., Slavov, G.T., 2020. Functional QTL mapping and genomic prediction of canopy height in wheat measured using a robotic field phenotyping platform. Journal of Experimental Botany 71, 1885–1898. https://doi.org/10.1093/jxb/erz545

Madec, S., Baret, F., de Solan, B., Thomas, S., Dutartre, D., Jezequel, S., Hemmerlé, M., Colombeau, G., Comar, A., 2017. High-Throughput Phenotyping of Plant Height: Comparing Unmanned Aerial Vehicles and Ground LiDAR Estimates. Front. Plant Sci. 8. https://doi.org/10.3389/fpls.2017.02002

Magney, T.S., Eitel, J.U.H., Huggins, D.R., Vierling, L.A., 2016. Proximal NDVI derived phenology improves in-season predictions of wheat quantity and quality.

Agricultural and Forest Meteorology 217, 46–60. https://doi.org/10.1016/j.agrformet.2015.11.009

Magorokosho, C., 2010. Characterization of Maize Germplasm Grown in Eastern and Southern Africa: Results of the 2009 Regional Trials Coordinated by CIMMYT. CIMMYT, Zimbabwe.

Mahlein, A.-K., 2015. Plant Disease Detection by Imaging Sensors – Parallels and Specific Demands for Precision Agriculture and Plant Phenotyping. Plant Disease 100, 241–251. https://doi.org/10.1094/PDIS-03-15-0340-FE

Makanza, R., Zaman-Allah, M., Cairns, J., Magorokosho, C., Tarekegne, A., Olsen, M., Prasanna, B., Makanza, R., Zaman-Allah, M., Cairns, J.E., Magorokosho, C., Tarekegne, A., Olsen, M., Prasanna, B.M., 2018. High-Throughput Phenotyping of Canopy Cover and Senescence in Maize Field Trials Using Aerial Digital Canopy Imaging. Remote Sensing 10, 330. https://doi.org/10.3390/rs10020330

Malambo, L., Popescu, S.C., Murray, S.C., Putman, E., Pugh, N.A., Horne, D.W., Richardson, G., Sheridan, R., Rooney, W.L., Avant, R., Vidrine, M., McCutchen, B., Baltensperger, D., Bishop, M., 2018. Multitemporal field-based plant height estimation using 3D point clouds generated from small unmanned aerial systems high-resolution imagery. International Journal of Applied Earth Observation and Geoinformation 64, 31–42. https://doi.org/10.1016/j.jag.2017.08.014

Maresma, Á., Ariza, M., Martínez, E., Lloveras, J., Martínez-Casasnovas, J., 2016. Analysis of Vegetation Indices to Determine Nitrogen Application and Yield Prediction in Maize (Zea mays L.) from a Standard UAV Service. Remote Sensing 8, 973. https://doi.org/10.3390/rs8120973

Mathews, A.J., 2015. A Practical UAV Remote Sensing Methodology to Generate Multispectral Orthophotos for Vineyards: Estimation of Spectral Reflectance Using Compact Digital Cameras. International Journal of Applied Geospatial Research 6, 65–87. https://doi.org/10.4018/ijagr.2015100104

Meyer, G.E., Hindman, T.W., Laksmi, K., 1999. Machine vision detection parameters for plant species identification. Presented at the Proc.SPIE.

Meyer, George.E., Camargo Neto, J., Jones, D.D., Hindman, T.W., 2004. Intensified fuzzy clusters for classifying plant, soil, and residue regions of interest from color images. Computers and Electronics in Agriculture 42, 161–180. https://doi.org/10.1016/j.compag.2003.08.002

Miura, T., Huete, A.R., 2009. Performance of Three Reflectance Calibration Methods for Airborne Hyperspectral Spectrometer Data. Sensors 9, 794–813. https://doi.org/10.3390/s90200794

Motohka, T., Nasahara, K.N., Oguma, H., Tsuchida, S., 2010. Applicability of Green-Red Vegetation Index for Remote Sensing of Vegetation Phenology. Remote Sensing 2, 2369–2387. https://doi.org/10.3390/rs2102369

Mullan, D., Barcello Garcia, M., 2012. Chapter 10. Crop Ground Cover, in: Pask, A.J.D., Pietragalla, J., Mullan, D.M., Reynolds, M.P. (Eds.), Physiological Breeding II: A Field Guide to Wheat Phenotyping. CIMMYT, pp. 46–53.

Mullan, D.J., Reynolds, M.P., 2010. Quantifying genetic effects of ground cover on soil water evaporation using digital imaging. Functional Plant Biology 37, 703. https://doi.org/10.1071/FP09277

Nex, F., Remondino, F., 2014. UAV for 3D mapping applications: a review. Applied Geomatics 6, 1–15. https://doi.org/10.1007/s12518-013-0120-x

Niethammer, U., James, M.R., Rothmund, S., Travelletti, J., Joswig, M., 2012. UAV-based remote sensing of the Super-Sauze landslide: Evaluation and results. Engineering Geology 128, 2–11. https://doi.org/10.1016/j.enggeo.2011.03.012

Nijland, W., de Jong, R., de Jong, S.M., Wulder, M.A., Bater, C.W., Coops, N.C., 2014. Monitoring plant condition and phenology using infrared sensitive consumer grade digital cameras. Agricultural and Forest Meteorology 184, 98–106. https://doi.org/10.1016/j.agrformet.2013.09.007

Oerke, E.-C., 2006. Crop losses to pests. The Journal of Agricultural Science 144, 31–43. https://doi.org/10.1017/S0021859605005708

Pajares, G., 2015. Overview and Current Status of Remote Sensing Applications Based on Unmanned Aerial Vehicles (UAVs). Photogrammetric Engineering & Remote Sensing 81, 281–330. https://doi.org/10.14358/PERS.81.4.281

Panda, S.S., Ames, D.P., Panigrahi, S., 2010. Application of Vegetation Indices for Agricultural Crop Yield Prediction Using Neural Network Techniques. Remote Sensing 2, 673–696. https://doi.org/10.3390/rs2030673

Parrot SEQUOIA+ [WWW Document], 2017. . Parrot Business Solutions. URL https://www.parrot.com/business-solutions-us/parrot-professional/parrot-sequoia (accessed 6.4.18).

Parry, M.A.J., Hawkesford, M.J., 2010. Food security: increasing yield and improving resource use efficiency. Proceedings of the Nutrition Society 69, 592–600. https://doi.org/10.1017/S0029665110003836

Parry, M.A.J., Madgwick, P.J., Carvalho, J.F.C., Andralojc, P.J., 2006. Prospects for increasing photosynthesis by overcoming the limitations of Rubisco. J. Agric. Sci. 145, 31–43. https://doi.org/10.1017/S0021859606006666

Parry, M.A.J., Reynolds, M., Salvucci, M.E., Raines, C., Andralojc, P.J., Zhu, X.-G., Price, G.D., Condon, A.G., Furbank, R.T., 2011a. Raising yield potential of wheat. II. Increasing photosynthetic capacity and efficiency. Journal of Experimental Botany erq304. https://doi.org/10.1093/jxb/erq304

Parry, M.A.J., Reynolds, M., Salvucci, M.E., Raines, C., Andralojc, P.J., Zhu, X.-G., Price, G.D., Condon, A.G., Furbank, R.T., 2011b. Raising yield potential of wheat. II. Increasing photosynthetic capacity and efficiency. J. Exp. Bot. erq304. https://doi.org/10.1093/jxb/erq304

Pask, A., Pietragalla, J., 2012. Chapter 12: Leaf area, green crop area and senescence, in: Pask, A.J.D., Pietragalla, J., Mullan, D.M., Reynolds, M.P. (Eds.), Physiological Breeding II: A Field Guide to Wheat Phenotyping. CIMMYT, pp. 58–62.

Pask, A., Pietragalla, J., Mullan, D., Reynolds, M.P., 2012. Physiological breeding II: a field guide to wheat phenotyping.

Passioura, J.B., 2006. The perils of pot experiments. Functional Plant Biology 33, 1075–1079. https://doi.org/10.1071/FP06223

Peña-Barragán, J.M., Ngugi, M.K., Plant, R.E., Six, J., 2011. Object-based crop identification using multiple vegetation indices, textural features and crop phenology. Remote Sensing of Environment 115, 1301–1316. https://doi.org/10.1016/j.rse.2011.01.009

Pérez-Ortiz, M., Peña, J.M., Gutiérrez, P.A., Torres-Sánchez, J., Hervás-Martínez, C., López-Granados, F., 2016. Selecting patterns and features for between- and within- crop-row weed mapping using UAV-imagery. Expert Systems with Applications 47, 85–94. https://doi.org/10.1016/j.eswa.2015.10.043

Perez-Priego, O., Zarco-Tejada, P.J., Miller, J.R., Sepulcre-Canto, G., Fereres, E., 2005. Detection of water stress in orchard trees with a high-resolution spectrometer

through chlorophyll fluorescence in-filling of the O/sub 2/-A band. IEEE Transactions on Geoscience and Remote Sensing 43, 2860–2869. https://doi.org/10.1109/TGRS.2005.857906

Perryman, S.A.M., Castells-Brooke, N.I.D., Glendining, M.J., Goulding, K.W.T., Hawkesford, M.J., Macdonald, A.J., Ostler, R.J., Poulton, P.R., Rawlings, C.J., Scott, T., Verrier, P.J., 2018. The electronic Rothamsted Archive (e-RA), an online resource for data from the Rothamsted long-term experiments. Scientific Data 5, 180072. https://doi.org/10.1038/sdata.2018.72

Pettorelli, N., 2013. The Normalized Difference Vegetation Index. OUP Oxford.

Pettorelli, N., Vik, J.O., Mysterud, A., Gaillard, J.-M., Tucker, C.J., Stenseth, N.C., 2005. Using the satellite-derived NDVI to assess ecological responses to environmental change. Trends in Ecology & Evolution 20, 503–510. https://doi.org/10.1016/j.tree.2005.05.011

Pieruschka, R., Schurr, U., 2019. Plant Phenotyping: Past, Present, and Future [WWW Document]. Plant Phenomics. URL https://spj.sciencemag.org/plantphenomics/2019/7507131/ (accessed 4.12.20).

Pietragalla, J., Madrigal Vega, A., 2012. Chapter 8. Normalised difference vegetation index, in: Pask, A.J.D., Pietragalla, J., Mullan, D.M., Reynolds, M.P. (Eds.), Physiological Breeding II: A Field Guide to Wheat Phenotyping. CIMMYT, Mexico, pp. 37–40.

Pietragalla, J., Mullan, D., Sereno Mendoza, R., 2012. Chapter 7: Spectral reflectance, in: Pask, A.J.D., Pietragalla, J., Mullan, D.M., Reynolds, M.P. (Eds.), Physiological Breeding II: A Field Guide to Wheat Phenptyping. CIMMYT.

Pingali, P.L., 2012. Green Revolution: Impacts, limits, and the path ahead. Proceedings of the National Academy of Sciences of the United States of America 109, 12302–12308. https://doi.org/10.1073/pnas.0912953109

Pittman, J.J., Arnall, D.B., Interrante, S.M., Moffet, C.A., Butler, T.J., 2015. Estimation of Biomass and Canopy Height in Bermudagrass, Alfalfa, and Wheat Using Ultrasonic, Laser, and Spectral Sensors. Sensors 15, 2920–2943. https://doi.org/10.3390/s150202920

Pix4D, 2019. Pix4Dfields: Drone software for agriculture mapping [WWW Document]. Pix4D. URL https://www.pix4d.com/product/pix4dfields (accessed 9.29.19).

Poorter, H., Bühler, J., Dusschoten, D. van, Climent, J., Postma, J.A., 2012. Pot size matters: a meta-analysis of the effects of rooting volume on plant growth. Functional Plant Biology 39, 839–850.

Prabhakara, K., Hively, W.D., McCarty, G.W., 2015. Evaluating the relationship between biomass, percent groundcover and remote sensing indices across six winter cover crop fields in Maryland, United States. International Journal of Applied Earth Observation and Geoinformation 39, 88–102. https://doi.org/10.1016/j.jag.2015.03.002

Puig, E., Gonzalez, F., Hamilton, G., Grundy, P., 2015. Assessment of crop insect damage using unmanned aerial systems: A machine learning approach, in: Proceedings of MODSIM2015, 21st International Congress on Modelling and Simulation:. Modelling and Simulation Society of Australia and New Zealand Inc. (MSSANZ). pp. 1420–1426.

Qi, J., Chehbouni, A., Huete, A.R., Kerr, Y.H., Sorooshian, S., 1994. A modified soil adjusted vegetation index. Remote Sensing of Environment 48, 119–126. https://doi.org/10.1016/0034-4257(94)90134-1

Rabatel, G., Gorretta, N., Labbé, S., 2011. Getting NDVI spectral bands from a single standard RGB digital camera: a methodological approach, in: 14th Conference of the Spanish Association for Artificial Intelligence, CAEPIA 2011. Springer-Verlag, La Laguna, Spain, p. 10 p.

Rabatel, G., Gorretta, N., Labbé, S., 2014. Getting simultaneous red and near-infrared band data from a single digital camera for plant monitoring applications: Theoretical and practical study. Biosystems Engineering, Image Analysis in Agriculture 117, 2–14. https://doi.org/10.1016/j.biosystemseng.2013.06.008

Rango, A., Laliberte, A., Herrick, J.E., Winters, C., Havstad, K.M., Steele, C., Browning, D.M., 2009. Unmanned aerial vehicle-based remote sensing for rangeland assessment, monitoring, and management. Journal of Applied Remote Sensing 3, 33542. https://doi.org/10.1117/1.3216822

Rango, A., Laliberte, A., Steele, C., Herrick, J.E., Bestelmeyer, B., Schmugge, T., Roanhorse, A., Jenkins, V., 2006. RESEARCH ARTICLE: Using Unmanned Aerial Vehicles for Rangelands: Current Applications and Future Potentials. Environmental Practice null, 159–168. https://doi.org/10.1017/S1466046606060224

Rathmann, R., Szklo, A., Schaeffer, R., 2010. Land use competition for production of food and liquid biofuels: An analysis of the arguments in the current debate. Renewable Energy 35, 14–22. https://doi.org/10.1016/j.renene.2009.02.025

Rebetzke, G.J., Richards, R.A., 1999. Genetic improvement of early vigour in wheat. Australian Journal of Agricultural Research 50, 291. https://doi.org/10.1071/A98125

Reynolds, D., Baret, F., Welcker, C., Bostrom, A., Ball, J., Cellini, F., Lorence, A., Chawade, A., Khafif, M., Noshita, K., Mueller-Linow, M., Zhou, J., Tardieu, F., 2019. What is cost-efficient phenotyping? Optimizing costs for different scenarios. Plant Science, The 4th International Plant Phenotyping Symposium 282, 14–22. https://doi.org/10.1016/j.plantsci.2018.06.015

Reynolds, M.P., Pask, A.J.D., Mullan, D.M., 2012. Physiological breeding I: interdisciplinary approaches to improve crop adaptation. CIMMYT.

Roberts, D., Roth, K., Perroy, R., 2011. Hyperspectral Vegetation Indices. Hyperspectral Remote Sensing of Vegetation 309–327. https://doi.org/10.1201/b11222-20

Rossi, M., Niedrist, G., Asam, S., Tonon, G., Tomelleri, E., Zebisch, M., 2019. A Comparison of the Signal from Diverse Optical Sensors for Monitoring Alpine Grassland Dynamics. Remote Sensing 11, 296. https://doi.org/10.3390/rs11030296

Roy, R., Miller, J., 2017. Miniaturization of image sensors: The role of innovations in complementary technologies in overcoming technological trade-offs associated with product innovation. Journal of Engineering and Technology Management 44, 58–69. https://doi.org/10.1016/j.jengtecman.2017.01.002

Ruiz, J.J., Diaz-Mas, L., Perez, F., Viguria, A., 2013. Evaluating the accuracy of DEM generation algorithms from UAV imagery. Int. Arch. Photogramm. Remote Sens. Spatial Inf. Sci 40, 333–337.

Rutkoski, J., Poland, J., Mondal, S., Autrique, E., Pérez, L.G., Crossa, J., Reynolds, M., Singh, R., 2016. Canopy temperature and vegetation indices from high-throughput phenotyping improve accuracy of pedigree and genomic selection for grain yield in wheat. G3: Genes, Genomes, Genetics 6, 2799–2808. https://doi.org/10.1534/g3.116.032888

Sadeghi-Tehran, P., Virlet, N., Sabermanesh, K., Hawkesford, M.J., 2017. Multi-feature machine learning model for automatic segmentation of green fractional vegetation cover for high-throughput field phenotyping. Plant Methods 13, 103. https://doi.org/10.1186/s13007-017-0253-8

Sankaran, S., Khot, L.R., Carter, A.H., 2015. Field-based crop phenotyping: Multispectral aerial imaging for evaluation of winter wheat emergence and spring stand. Computers and Electronics in Agriculture 118, 372–379. https://doi.org/10.1016/j.compag.2015.09.001

Satorre, E.H., Slafer, G.A., 1999. Wheat: Ecology and Physiology of Yield Determination. CRC Press.

Schirrmann, M., Giebel, A., Gleiniger, F., Pflanz, M., Lentschke, J., Dammer, K.-H., 2016a. Monitoring Agronomic Parameters of Winter Wheat Crops with Low-Cost UAV Imagery. Remote Sensing 8, 706. https://doi.org/10.3390/rs8090706

Schirrmann, M., Hamdorf, A., Garz, A., Ustyuzhanin, A., Dammer, K.-H., 2016b. Estimating wheat biomass by combining image clustering with crop height. Computers and Electronics in Agriculture 121, 374–384. https://doi.org/10.1016/j.compag.2016.01.007

Scotford, I.M., Miller, P.C.H., 2004. Combination of Spectral Reflectance and Ultrasonic Sensing to monitor the Growth of Winter Wheat. Biosystems Engineering 87, 27–38. https://doi.org/10.1016/j.biosystemseng.2003.09.009

Shakoor, N., Lee, S., Mockler, T.C., 2017. High throughput phenotyping to accelerate crop breeding and monitoring of diseases in the field. Current Opinion in Plant Biology, 38 Biotic interactions 2017 38, 184–192. https://doi.org/10.1016/j.pbi.2017.05.006

Shearman, V.J., Sylvester-Bradley, R., Scott, R.K., Foulkes, M.J., 2005. Physiological processes associated with wheat yield progress in the UK. Crop science.

Singh, D., Wang, X., Kumar, U., Gao, L., Noor, M., Imtiaz, M., Singh, R.P., Poland, J., 2019. High-Throughput Phenotyping Enabled Genetic Dissection of Crop Lodging in Wheat. Frontiers in Plant Science 10, 394. https://doi.org/10.3389/fpls.2019.00394

Slafer, G.A., 2012. Wheat development: its role in phenotyping adn improving crop adaptation, in: Physiological Breeding I: Interdisciplinary Approaches to Improve Crop Adaptation. CIMMYT.

Smith, M.W., Vericat, D., 2015. From experimental plots to experimental landscapes: topography, erosion and deposition in sub-humid badlands from Structure-from-Motion photogrammetry. Earth Surface Processes and Landforms 40, 1656–1671. https://doi.org/10.1002/esp.3747

Snavely, N., 2011. Scene Reconstruction and Visualization from Internet Photo Collections: A Survey. IPSJ Transactions on Computer Vision and Applications 3, 44–66. https://doi.org/10.2197/ipsjtcva.3.44

Snavely, N., Seitz, S.M., Szeliski, R., 2006. Photo Tourism: Exploring Photo Collections in 3D. ACM Transactions on Grpahics 25, 12.

Snavely, N., Seitz, S.M., Szeliski, R., 2008. Modeling the World from Internet Photo Collections. International Journal of Computer Vision 80, 189–210. https://doi.org/10.1007/s11263-007-0107-3

Steele, M., Gitelson, A.A., Rundquist, D.C., 2008. A Comparison of Two Techniques for Nondestructive Measurement of Chlorophyll Content in Grapevine Leaves. https://doi.org/10.2134/agronj2007.0254n

Stroppiana, D., Migliazzi, M., Chiarabini, V., Crema, A., Musanti, M., Franchino, C., Villa, P., 2015. Rice yield estimation using multispectral data from UAV: A preliminary experiment in northern Italy, in: International Geoscience and Remote Sensing Symposium (IGARSS). Institute of Electrical and Electronics Engineers Inc., pp. 4664–4667. https://doi.org/10.1109/IGARSS.2015.7326869

Su, J., Liu, C., Hu, X., Xu, X., Guo, L., Chen, W.H., 2019. Spatio-temporal monitoring of wheat yellow rust using UAV multispectral imagery. Computers and Electronics in Agriculture 167, 105035. https://doi.org/10.1016/j.compag.2019.105035

Tanger, P., Klassen, S., Mojica, J.P., Lovell, J.T., Moyers, B.T., Baraoidan, M., Naredo, M.E.B., McNally, K.L., Poland, J., Bush, D.R., Leung, H., Leach, J.E., McKay, J.K., 2017. Field-based high throughput phenotyping rapidly identifies genomic regions controlling yield components in rice. Scientific Reports 7. https://doi.org/10.1038/srep42839

Tattaris, M., Reynolds, M.P., Chapman, S.C., 2016. A Direct Comparison of Remote Sensing Approaches for High-Throughput Phenotyping in Plant Breeding. Frontiers in Plant Science 7. https://doi.org/10.3389/fpls.2016.01131

Tilly, N., Hoffmeister, D., Cao, Q., Huang, S., Lenz-Wiedemann, V., Miao, Y., Bareth, G., 2014. Multitemporal crop surface models: accurate plant height measurement and biomass estimation with terrestrial laser scanning in paddy rice. Journal of Applied Remote Sensing 8, 83671. https://doi.org/10.1117/1.JRS.8.083671

Torres, A., Pietragalla, J., 2012. Chapter 19: Crop morphological traits, in: Pask, A.J.D., Pietragalla, J., Mullan, D.M., Reynolds, M.P. (Eds.), Physiological Breeding II: A Field Guide to Wheat Phenotyping. CIMMYT.

Torres-Sánchez, J., Peña, J.M., Castro, A.I. de, López-Granados, F., 2014. Multi-temporal mapping of the vegetation fraction in early-season wheat fields using images from UAV. Computers and Electronics in Agriculture 103, 104–113. https://doi.org/10.1016/j.compag.2014.02.009

Turner, D., Lucieer, A., Jong, S.M. de, 2015. Time Series Analysis of Landslide Dynamics Using an Unmanned Aerial Vehicle (UAV). Remote Sensing 7, 1736–1757. https://doi.org/10.3390/rs70201736

United Nations, 2015. World Population Prospects: The 2015 Revision, Key Findings and Advance Tables. United Nations, New York.

Valentine, J., Clifton-Brown, J., Hastings, A., Robson, P., Allison, G., Smith, P., 2012. Food vs. fuel: the use of land for lignocellulosic 'next generation' energy crops that minimize competition with primary food production. GCB Bioenergy 4, 1–19. https://doi.org/10.1111/j.1757-1707.2011.01111.x

Varela, S., Assefa, Y., Prasad, P.V.V., Peralta, N.R., Griffin, T.W., Sharda, A., Ferguson, A., Ciampitti, I.A., 2017. Spatio-temporal evaluation of plant height in corn via unmanned aerial systems. Journal of Applied Remote Sensing 11, 1. https://doi.org/10.1117/1.jrs.11.036013

Verhoeven, G., 2008. Imaging the invisible using modified digital still cameras for straightforward and low-cost archaeological near-infrared photography. Journal of Archaeological Science 35, 3087–3100. https://doi.org/10.1016/j.jas.2008.06.012

Verhoeven, G.J.J., 2010. It's all about the format – unleashing the power of RAW aerial photography. International Journal of Remote Sensing 31, 2009–2042. https://doi.org/10.1080/01431160902929271

Vijayalakshmi, K., Fritz, A.K., Paulsen, G.M., Bai, G., Pandravada, S., Gill, B.S., 2010. Modeling and mapping QTL for senescence-related traits in winter wheat under high temperature. Mol Breeding 26, 163–175. https://doi.org/10.1007/s11032-009-9366-8

Virlet, N., Sabermanesh, K., Sadeghi-Tehran, P., Hawkesford, M.J., 2016. Field Scanalyzer: An automated robotic field phenotyping platform for detailed crop monitoring. Functional Plant Biol. https://doi.org/10.1071/FP16163

Virlet, N., Sabermanesh, K., Sadeghi-Tehran, P., Hawkesford, M.J., 2017. Field Scanalyzer: An automated robotic field phenotyping platform for detailed crop monitoring. Functional Plant Biology 44, 143–153. https://doi.org/10.1071/FP16163

Voort, D.V.D., 2016. Laboratory of Geo-Information Science and Remote Sensing Exploring the usability of Unmanned Aerial Vehicles for non-destructive phenotyping of small-scale maize breeding trials.

Wackrow, R., Chandler, J.H., 2011. Minimising systematic error surfaces in digital elevation models using oblique convergent imagery. The Photogrammetric Record 26, 16–31. https://doi.org/10.1111/j.1477-9730.2011.00623.x

Wahab, I., Hall, O., Jirström, M., 2018. Remote Sensing of Yields: Application of UAV Imagery-Derived NDVI for Estimating Maize Vigor and Yields in Complex Farming Systems in Sub-Saharan Africa. Drones 2, 28. https://doi.org/10.3390/drones2030028

Walsh, O.S., Shafian, S., Marshall, J.M., Jackson, C., McClintick-Chess, J.R., Blanscet, S.M., Swoboda, K., Thompson, C., Belmont, K.M., Walsh, W.L., 2018. Assessment of UAV Based Vegetation Indices for Nitrogen Concentration Estimation in Spring Wheat. Advances in Remote Sensing 07, 71–90. https://doi.org/10.4236/ars.2018.72006

Walter, A., Liebisch, F., Hund, A., 2015. Plant phenotyping: from bean weighing to image analysis. Plant Methods 11, 14. https://doi.org/10.1186/s13007-015-0056-8

Westoby, M.J., Brasington, J., Glasser, N.F., Hambrey, M.J., Reynolds, J.M., 2012. 'Structure-from-Motion' photogrammetry: A low-cost, effective tool for geoscience applications. Geomorphology 179, 300–314. https://doi.org/10.1016/j.geomorph.2012.08.021

White, J.W., Andrade-Sanchez, P., Gore, M.A., Bronson, K.F., Coffelt, T.A., Conley, M.M., Feldmann, K.A., French, A.N., Heun, J.T., Hunsaker, D.J., Jenks, M.A., Kimball, B.A., Roth, R.L., Strand, R.J., Thorp, K.R., Wall, G.W., Wang, G., 2012a. Field-based phenomics for plant genetics research. Field Crops Research 133, 101–112. https://doi.org/10.1016/j.fcr.2012.04.003

White, J.W., Andrade-Sanchez, P., Gore, M.A., Bronson, K.F., Coffelt, T.A., Conley, M.M., Feldmann, K.A., French, A.N., Heun, J.T., Hunsaker, D.J., Jenks, M.A., Kimball, B.A., Roth, R.L., Strand, R.J., Thorp, K.R., Wall, G.W., Wang, G., 2012b. Field-based phenomics for plant genetics research. Field Crops Research 133, 101–112. https://doi.org/10.1016/j.fcr.2012.04.003

Willkomm, M., Bolten, A., Bareth, G., 2016. NON-DESTRUCTIVE MONITORING OF RICE BY HYPERSPECTRAL IN-FIELD SPECTROMETRY AND UAV-BASED REMOTE SENSING: CASE STUDY OF FIELD-GROWN RICE IN NORTH RHINE-WESTPHALIA, GERMANY, in: The Internation Archives of the Photogrammetry, Remote Sensing and Spatial Informations Sciences. pp. 1071–1077. https://doi.org/10.5194/isprsarchives-XLI-B1-1071-2016

Woebbecke, D.M., Meyer, G.E., Bargen, K.V., Mortensen, D., 1995. Color indices for weed identification under various soil, residue, and lighting conditions. Transactions of the American Society of Agricultural Engineers 38, 259–269.

Woodget, A.S., Carbonneau, P.E., Visser, F., Maddock, I.P., 2015. Quantifying submerged fluvial topography using hyperspatial resolution UAS imagery and structure from motion photogrammetry. Earth Surface Processes and Landforms 40, 47–64. https://doi.org/10.1002/esp.3613

Yang, G., Liu, J., Zhao, C., Li, Zhenhong, Huang, Y., Yu, H., Xu, B., Yang, X., Zhu, D., Zhang, X., Zhang, R., Feng, H., Zhao, X., Li, Zhenhai, Li, H., Yang, H., 2017. Unmanned Aerial Vehicle Remote Sensing for Field-Based Crop Phenotyping: Current Status and Perspectives. Front Plant Sci 8, 1111. https://doi.org/10.3389/fpls.2017.01111

Yang, Q., Shi, L., Han, J., Zha, Y., Zhu, P., 2019. Deep convolutional neural networks for rice grain yield estimation at the ripening stage using UAV-based remotely sensed images. Field Crops Research 235, 142–153. https://doi.org/10.1016/j.fcr.2019.02.022

Yang, W., Guo, Z., Huang, C., Wang, K., Jiang, N., Feng, H., Chen, G., Liu, Q., Xiong, L., 2015. Genome-wide association study of rice (Oryza sativa L.) leaf traits with a high-throughput leaf scorer. Journal of Experimental Botany 66, 5605–5615. https://doi.org/10.1093/jxb/erv100

Yao, H., Qin, R., Chen, X., 2019. Unmanned Aerial Vehicle for Remote Sensing Applications—A Review. Remote Sensing 11, 1443. https://doi.org/10.3390/rs11121443

Yu, W., 2004. Practical anti-vignetting methods for digital cameras. IEEE Transactions on Consumer Electronics 50, 975–983. https://doi.org/10.1109/TCE.2004.1362487

Zarco-Tejada, P.J., González-Dugo, V., Berni, J.A.J., 2012. Fluorescence, temperature and narrow-band indices acquired from a UAV platform for water stress detection using a micro-hyperspectral imager and a thermal camera. Remote Sensing of Environment 117, 322–337. https://doi.org/10.1016/j.rse.2011.10.007

Zarco-Tejada, P.J., Suarez, L., Gonzalez-Dugo, V., 2013. Spatial Resolution Effects on Chlorophyll Fluorescence Retrieval in a Heterogeneous Canopy Using Hyperspectral Imagery and Radiative Transfer Simulation. IEEE Geoscience and Remote Sensing Letters 10, 937–941. https://doi.org/10.1109/LGRS.2013.2252877

Zhang, L., Grift, T.E., 2012. A LIDAR-based crop height measurement system for Miscanthus giganteus. Computers and Electronics in Agriculture 85, 70–76. https://doi.org/10.1016/j.compag.2012.04.001

Zhao, Z., Rebetzke, G.J., Zheng, B., Chapman, S.C., Wang, E., 2019. Modelling impact of early vigour on wheat yield in dryland regions. Journal of Experimental Botany 70, 2535–2548. https://doi.org/10.1093/jxb/erz069

Zheng, Y., Lin, S., Kambhamettu, C., Yu, J., Kang, S.B., 2009. Single-Image Vignetting Correction. IEEE Transactions on Pattern Analysis and Machine Intelligence 31, 2243–2256. https://doi.org/10.1109/TPAMI.2008.263

Zhou, X., Zheng, H.B., Xu, X.Q., He, J.Y., Ge, X.K., Yao, X., Cheng, T., Zhu, Y., Cao, W.X., Tian, Y.C., 2017. Predicting grain yield in rice using multi-temporal vegetation indices from UAV-based multispectral and digital imagery. ISPRS Journal of Photogrammetry and Remote Sensing 130, 246–255. https://doi.org/10.1016/j.isprsjprs.2017.05.003

Ziliani, M.G., Parkes, S.D., Hoteit, I., McCabe, M.F., 2018. Intra-Season Crop Height Variability at Commercial Farm Scales Using a Fixed-Wing UAV. Remote Sensing 10, 2007. https://doi.org/10.3390/rs10122007

Appendix A

Appendix A contains details of the 2016, 2017 and 2018 field experiment used in Chapters 3, 4 and 5 of this thesis. Planting maps (Figures A1, A2 and A3) and a list of individual varieties grown (Table A1) are provided.

Table A. 1. Name and code of all wheat varieties grown in the 2016, 2017 and 2018 growing season experiments. Also detailed is which season each variety was grown in.

Code	Variety	Seasons Grown.
AV	Avalon	2016, 2017, 2018
BA	Barrel	2018
CA	Cadenza	2016, 2017, 2018
CC	Cocoon	201, 2017
CL	Claire	2016, 2017, 2018
CN	Conqueror	2016, 2017, 2018
CO	Cordiale	2016, 2017, 2018
CR	Crusoe	2016, 2017, 2018
EL	Evolution	2016, 2017, 2018
EV	Evoke	2016
GA	Gallant	2016, 2017
GR	Graham	2017, 2018
HE	Hereward	2016, 2017, 2018
HF	Hereford	2016, 2017, 2018
HL	Hylux	2016, 2017, 2018
HY	Hystar	2016, 2017, 2018
IL	RAGT Illustrious	2016, 2017, 2018
IS	Istabraq	2016, 2017, 2018
LE	Leeds	2016, 2017, 2018
LI	KWS Lili	2016, 2017, 2018
MA	Malacca	2016, 2017, 2018
ME	Mercia	2016, 2017, 2018
MW	Maris Widgeon	2016, 2017, 2018
PA	Paragon	2016, 2017, 2018
RF	Reflection	2016, 2017, 2018
RI	Riband	2016, 2017, 2018
RO	Robigus	2016, 2017, 2018
SK	Siskin	2017, 2018
SL	Solstice	2016, 2017, 2018
SS	Soissons	2016, 2018
SS+SL	Soissons + Solstice	2017
ST	Stigg	2016
SY	Skyfall	2016, 2017, 2018
XI	Xi19	2016, 2017, 2018
ZY	Zyatt	2018

2016

Figure A. 1 Planting map detailing plot layout of the 2016 Wheat Genetic Improvement Network (WGIN) field experiment.

2017

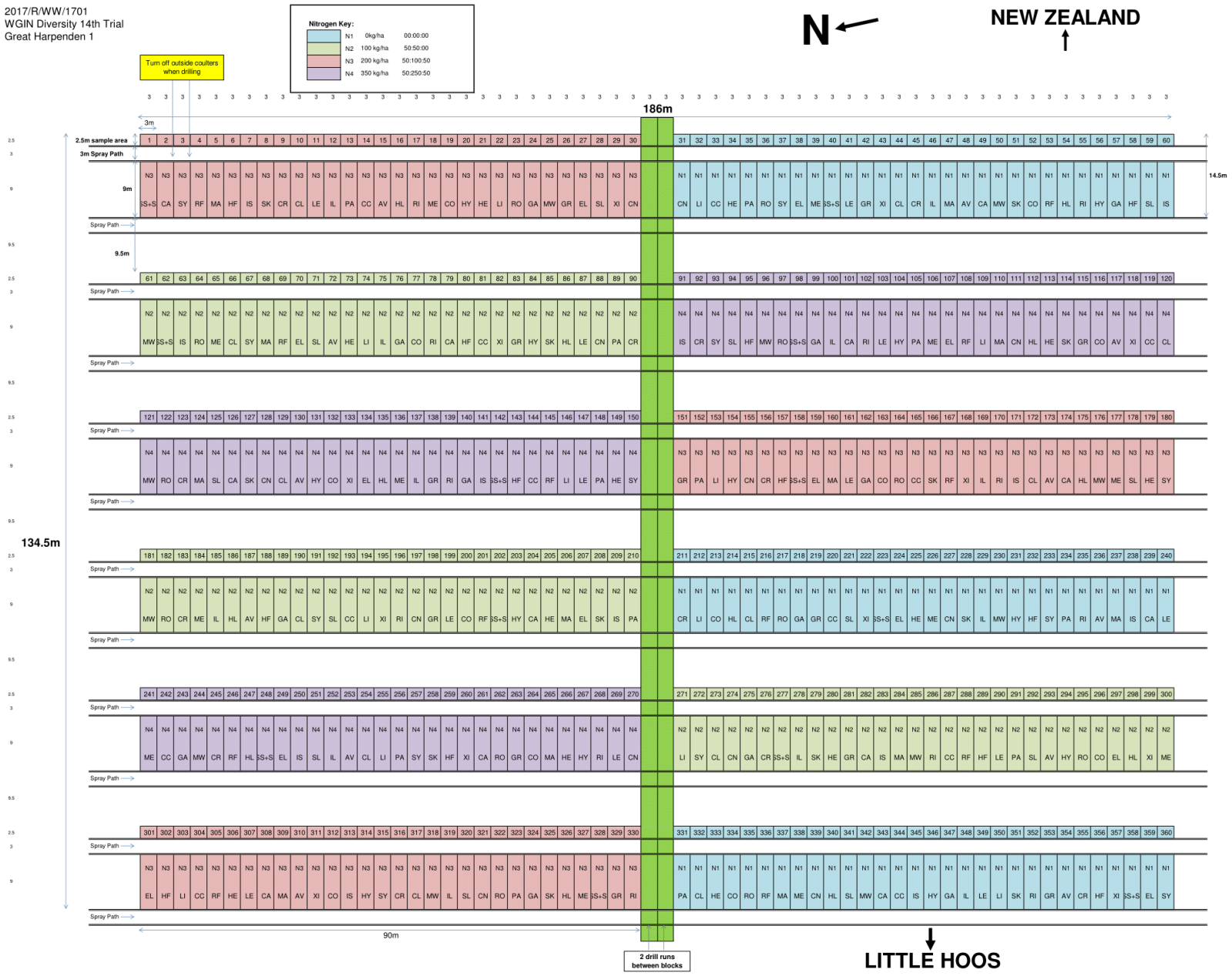

Figure A. 2. Planting map detailing plot layout of the 2017 Wheat Genetic Improvement Network (WGIN) field experiment.

2018

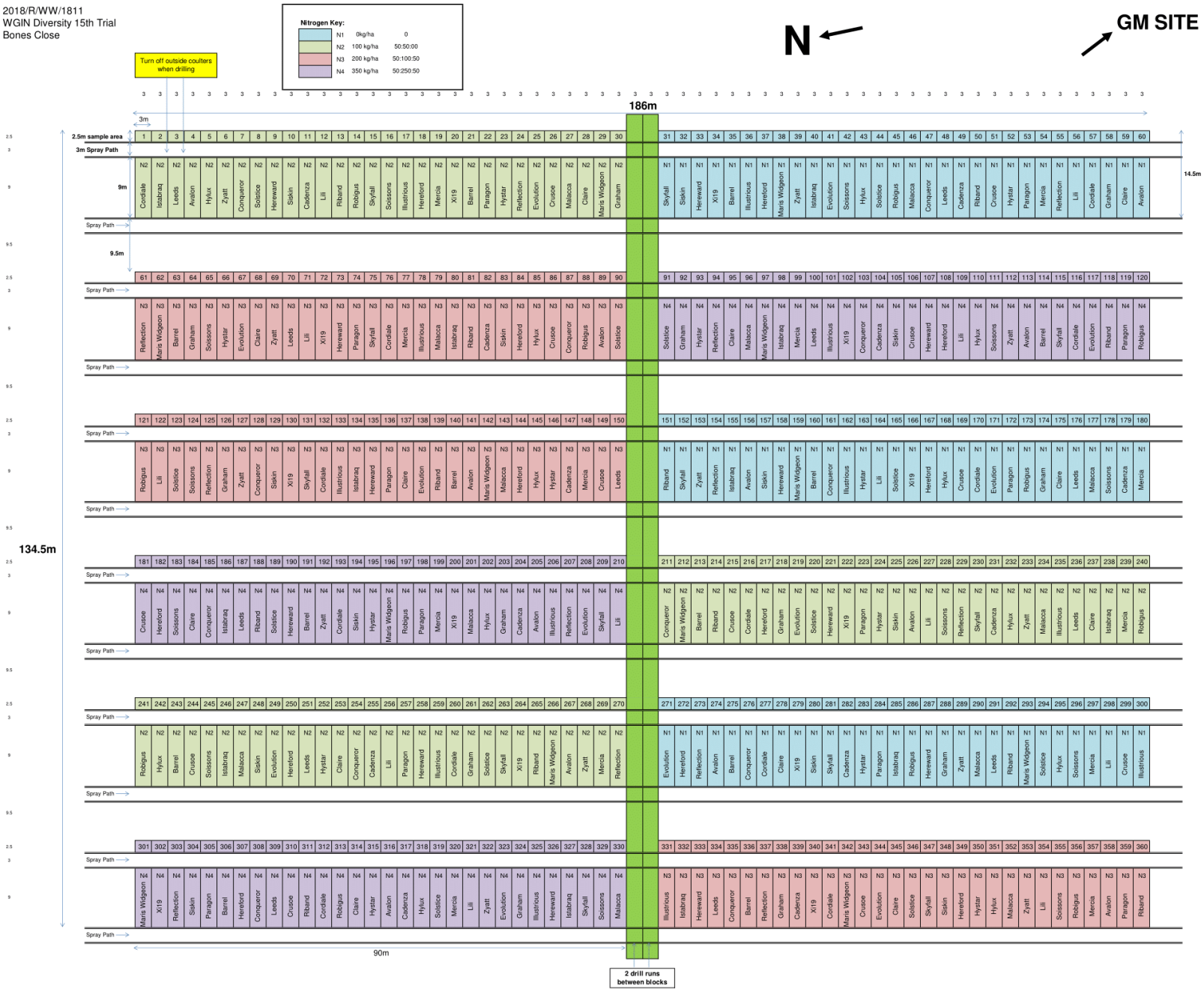

Figure A. 3. Planting map detailing plot layout of the 2018 Wheat Genetic Improvement Network (WGIN) field experiment.

Appendix B

Appendix B contains correlation plots comparing the three different canopy metrics derived in Chapter 5; NDVI, EXGR_NDVI, and GreenPixel. The results indicate positive correlations between NDVI and ExGR_NDVI; whilst Green Pixel shows little to no linear agreement with either of the other two metrics. These trends are consistent across all three years – 2016, 2017 and 2018.

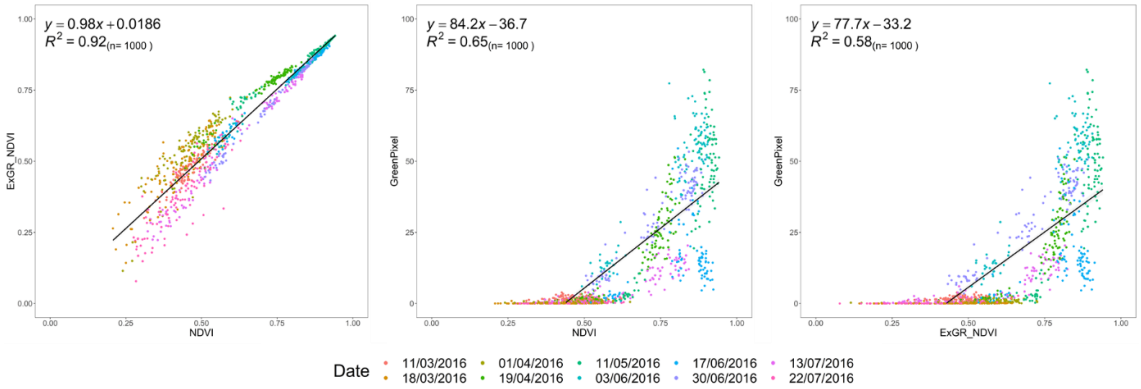

Figure C. 1. Correlation plots between NDVI and ExGR_NDVI (left); NDVI and GreenPixel (middle); and ExGR_NDVI and GreenPixel (right) across all UAV measurement dates in the 2016 growing season. Results show a strong linear trend between NDVI and ExGR masked NDVI, however weaker trends are observed between the NDVI and ExGR_NDVI compared to GreenPixel.

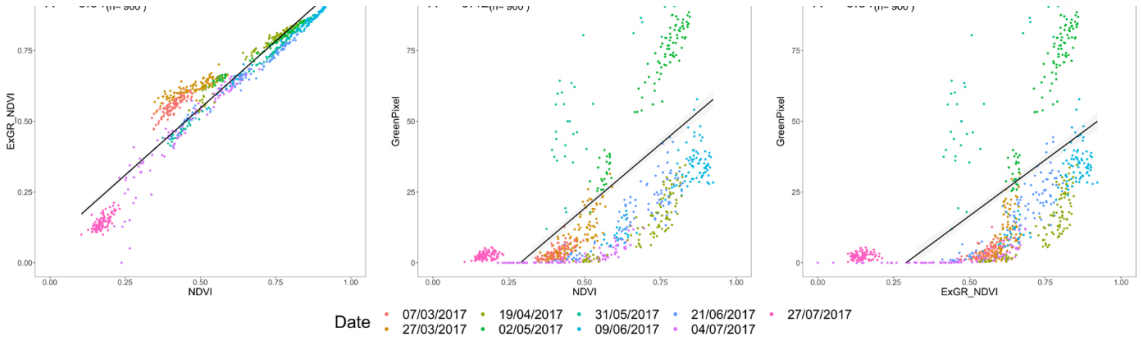

Figure C. 2. Correlation plots between NDVI and ExGR_NDVI (left); NDVI and GreenPixel (middle); and ExGR_NDVI and GreenPixel (right) across all UAV measurement dates in the 2017 growing season. Results show a strong linear trend between NDVI and ExGR masked NDVI, however weaker trends are observed between the NDVI and ExGR_NDVI compared to GreenPixel.

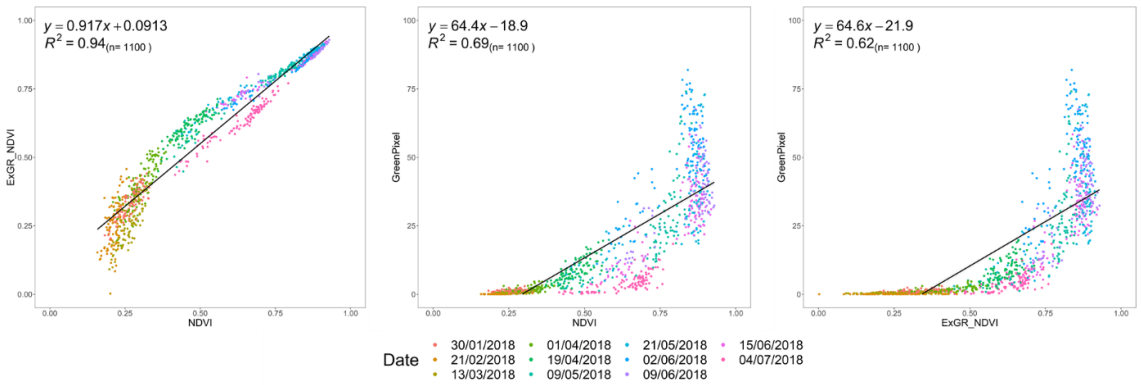

Figure C. 3. Correlation plots between NDVI and ExGR_NDVI (left); NDVI and GreenPixel (middle); and ExGR_NDVI and GreenPixel (right) across all UAV measurement dates in the 2017 growing season. Results show a strong linear trend between NDVI and ExGR masked NDVI, however weaker trends are observed between the NDVI and ExGR_NDVI compared to GreenPixel.

Appendix C

Appendix C contains tabulated results comparing varietal responses to different nitrogen treatments, as measured by each of the three integrated canopy phases as defined in Chapter 5. Results for all phases, canopy reflectance metrics (NDVI, ExGR NDVI, and Green Pixel), and growing year (2016, 2017, 2018) are presented in the following tables.

Table B. 1. P-values for Kruskal Wallis tests of significant difference between Formation phase derived NDVI integrals for the 2016 season. Test of significant differences are performed between all wheat varieties grown. Green shading indicates significant results, red shading indicates a nonsignificant result. N1 = 0 kg-N/ha, N2 = 100 kg-N/ha, N3 = 200 kg-N/ha, N4 = 350kg-N/ha.

Formation Phase – NDVI - 2016						
Variety	**N1 × N2**	**N1 × N3**	**N1 × N4**	**N2 × N3**	**N2 × N4**	**N3 × N4**
AV	0.64	0.12	0.62	0.06	0.70	0.73
CA	0.08	0.21	1.00	0.45	1.00	0.65
CL	0.27	0.36	0.82	0.08	1.00	1.00
CN	0.45	0.27	1.00	0.19	1.00	0.82
CO	0.45	0.21	0.65	0.08	1.00	1.00
CR	0.56	0.21	1.00	0.06	0.77	0.57
EL	0.73	0.03	0.27	0.56	0.57	0.52
HE	0.52	0.45	0.73	0.01	0.36	0.35
HF	0.03	0.12	0.57	0.62	0.28	0.64
HL	0.45	0.06	0.92	0.62	0.57	0.56
HY	0.35	0.14	1.00	0.45	0.82	1.00
IL	0.45	0.14	1.00	0.35	0.82	1.00
IS	0.22	0.21	0.91	0.19	1.00	1.00
LE	0.85	0.25	1.00	0.27	0.99	0.91
LI	0.45	0.16	1.00	0.10	1.00	0.82
MA	0.52	0.45	0.73	0.01	0.36	0.35
ME	0.56	0.16	0.99	0.08	0.92	0.73
MW	0.77	0.03	0.36	0.16	0.62	0.50
PA	0.10	0.27	1.00	0.28	1.00	0.91
RF	0.45	0.03	0.52	0.45	0.91	0.64
RI	0.08	0.21	1.00	0.45	1.00	0.65
RO	0.57	0.56	0.73	0.04	0.16	0.64
SL	0.85	0.35	1.00	0.19	1.00	0.73
SY	0.45	0.56	0.82	0.02	0.43	0.42
Xi	0.04	0.56	0.64	0.27	0.86	0.65

Table B. 2. P-values for Kruskal Wallis tests of significant difference between Formation phase derived NDVI integrals for the 2017 season. Test of significant differences are performed between

all wheat varieties grown. Green shading indicates significant results, red shading indicates a nonsignificant result. N1 = 0 kg-N/ha, N2 = 100 kg-N/ha, N3 = 200 kg-N/ha, N4 = 350kg-N/ha.

Formation Phase – NDVI - 2017						
Variety	**N1 × N2**	**N1 × N3**	**N1 × N4**	**N2 × N3**	**N2 × N4**	**N3 × N4**
AV	0.45	0.25	1.00	0.21	1.00	1.00
CA	1.00	0.14	0.92	0.85	1.00	0.62
CL	0.85	0.09	0.52	0.08	0.64	0.91
CN	0.45	0.04	0.77	0.35	0.82	0.73
CO	0.28	0.27	0.91	0.10	1.00	1.00
CR	0.99	0.14	0.56	1.00	0.82	0.70
EL	0.14	0.27	1.00	0.22	1.00	1.00
HE	0.56	0.27	0.65	0.04	0.64	0.86
HF	0.28	0.21	1.00	0.14	1.00	0.82
HL	0.45	0.10	1.00	0.45	0.91	0.99
HY	0.14	0.21	0.82	0.28	1.00	1.00
IL	0.50	0.08	0.35	0.45	1.00	0.73
IS	0.73	0.08	0.45	0.12	0.52	0.82
LE	0.10	0.27	1.00	0.28	1.00	0.91
LI	0.45	0.36	1.00	0.04	0.92	0.62
MA	0.77	0.10	0.85	0.45	0.57	0.99
ME	0.86	0.08	0.45	0.56	0.50	0.92
MW	0.86	0.08	0.45	0.56	0.50	0.92
PA	0.45	0.14	1.00	0.12	0.99	1.00
RF	0.27	0.22	1.00	0.14	1.00	1.00
RI	0.64	0.04	0.56	0.16	0.73	0.57
RO	1.00	0.33	1.00	0.45	1.00	0.82
SL	0.35	0.10	0.57	1.00	0.64	0.28
SY	0.64	0.04	0.56	0.16	0.73	0.57
Xi	0.19	0.22	1.00	0.21	1.00	0.91

Table B. 3. P-values for Kruskal Wallis tests of significant difference between Formation Phase derived NDVI integrals for the 2018 season. Test of significant differences are performed between all wheat varieties grown. Green shading indicates significant results, red shading indicates a nonsignificant result. N1 = 0 kg-N/ha, N2 = 100 kg-N/ha, N3 = 200 kg-N/ha, N4 = 350kg-N/ha.

Formation Phase – NDVI - 2018						
Variety	**N1 × N2**	**N1 × N3**	**N1 × N4**	**N2 × N3**	**N2 × N4**	**N3 × N4**
AV	0.91	1.00	1.00	1.00	1.00	1.00
CA	1.00	1.00	1.00	1.00	1.00	1.00
CL	1.00	1.00	0.73	0.54	1.00	1.00
CN	0.42	1.00	1.00	0.35	1.00	0.99
CO	1.00	0.82	1.00	1.00	1.00	1.00
CR	0.68	1.00	0.85	0.71	0.91	0.77
EL	0.56	0.42	0.91	0.01	0.28	0.45
HE	1.00	1.00	1.00	1.00	1.00	1.00
HF	0.45	0.56	0.82	0.25	1.00	1.00
HL	0.71	1.00	1.00	0.42	0.73	1.00
HY	1.00	0.85	1.00	1.00	0.73	1.00
IL	0.45	0.85	1.00	0.42	0.91	1.00
IS	0.42	1.00	0.85	0.71	0.73	1.00
LE	1.00	0.91	1.00	1.00	1.00	0.92
LI	1.00	1.00	1.00	1.00	0.91	1.00
MA	0.68	1.00	1.00	1.00	1.00	0.82
ME	1.00	1.00	1.00	0.82	1.00	1.00
MW	0.36	0.25	1.00	0.27	1.00	0.91
PA	1.00	0.91	1.00	1.00	0.85	1.00
RF	0.91	1.00	1.00	1.00	1.00	1.00
RI	0.45	0.91	0.42	0.19	1.00	0.21
RO	0.17	0.57	0.42	0.06	1.00	0.21
SL	0.14	0.56	1.00	0.27	0.73	1.00
SY	0.56	0.45	0.82	0.08	0.92	0.86
Xi	0.45	0.85	1.00	0.42	0.91	1.00

Table B. 4. P-values for Kruskal Wallis tests of significant difference between Full Canopy Phase derived NDVI integrals for the 2016 season. Test of significant differences are performed between all wheat varieties grown. Green shading indicates significant results, red shading indicates a nonsignificant result. N1 = 0 kg-N/ha, N2 = 100 kg-N/ha, N3 = 200 kg-N/ha, N4 = 350kg-N/ha.

Full Canopy Phase – NDVI - 2016						
Variety	**N1 × N2**	**N1 × N3**	**N1 × N4**	**N2 × N3**	**N2 × N4**	**N3 × N4**
AV	0.92	0.21	0.62	0.01	0.17	0.31
CA	0.62	0.16	0.77	0.02	0.22	0.43
CL	0.92	0.21	0.62	0.01	0.17	0.31
CN	0.62	0.06	0.45	0.06	0.42	0.91
CO	0.92	0.21	0.62	0.01	0.17	0.31
CR	0.62	0.12	0.64	0.03	0.28	0.57
EL	0.62	0.06	0.42	0.06	0.45	0.91
HE	0.92	0.21	0.62	0.01	0.17	0.31
HF	0.62	0.04	0.36	0.09	0.52	0.73
HL	0.62	0.16	0.77	0.02	0.22	0.43
HY	0.62	0.16	0.77	0.02	0.22	0.43
IL	0.62	0.12	0.64	0.03	0.28	0.57
IS	0.92	0.21	0.62	0.01	0.17	0.31
LE	0.62	0.09	0.52	0.04	0.36	0.73
LI	0.62	0.16	0.77	0.02	0.22	0.43
MA	0.92	0.21	0.62	0.01	0.17	0.31
ME	0.62	0.16	0.77	0.02	0.22	0.43
MW	0.62	0.16	0.77	0.02	0.22	0.43
PA	0.92	0.21	0.62	0.01	0.17	0.31
RF	0.62	0.12	0.64	0.03	0.28	0.57
RI	0.62	0.12	0.64	0.03	0.28	0.57
RO	0.62	0.06	0.42	0.06	0.45	0.91
SL	0.92	0.21	0.62	0.01	0.17	0.31
SY	0.92	0.21	0.62	0.01	0.17	0.31
Xi	0.92	0.21	0.62	0.01	0.17	0.31

Table B. 5. P-values for Kruskal Wallis tests of significant difference between Full Canopy Phase derived NDVI integrals for the 2017 season. Test of significant differences are performed between all wheat varieties grown. Green shading indicates significant results, red shading indicates a nonsignificant result. N1 = 0 kg-N/ha, N2 = 100 kg-N/ha, N3 = 200 kg-N/ha, N4 = 350kg-N/ha.

Full Canopy Phase – NDVI - 2017						
Variety	**N1 × N2**	**N1 × N3**	**N1 × N4**	**N2 × N3**	**N2 × N4**	**N3 × N4**
AV	0.64	0.27	0.50	0.02	0.36	0.62
CA	0.45	0.21	0.65	0.08	1.00	1.00
CL	0.77	0.16	0.62	0.03	0.36	0.50
CN	0.70	0.12	0.73	0.08	0.77	0.82
CO	0.56	0.45	0.82	0.02	0.42	0.43
CR	0.70	0.10	0.92	0.09	0.62	1.00
EL	0.52	0.35	0.65	0.02	0.45	0.52
HE	0.52	0.27	0.57	0.03	0.56	0.73
HF	0.52	0.35	0.65	0.02	0.45	0.52
HL	0.64	0.21	0.43	0.03	0.45	0.86
HY	0.52	0.35	0.65	0.02	0.45	0.52
IL	0.56	0.35	0.73	0.03	0.52	0.62
IS	0.77	0.27	0.43	0.01	0.22	0.52
LE	0.52	0.35	0.65	0.02	0.45	0.52
LI	0.56	0.45	0.82	0.02	0.42	0.43
MA	0.52	0.27	0.57	0.03	0.56	0.73
ME	0.62	0.06	0.42	0.06	0.45	0.91
MW	0.52	0.09	0.64	0.06	0.56	0.82
PA	0.64	0.21	0.43	0.03	0.45	0.86
RF	0.52	0.35	0.65	0.02	0.45	0.52
RI	0.64	0.35	0.57	0.01	0.28	0.43
RO	0.62	0.09	0.52	0.04	0.36	0.73
SL	0.85	0.09	0.52	0.08	0.64	0.91
SY	0.77	0.21	0.73	0.02	0.28	0.37
Xi	0.52	0.45	0.73	0.01	0.36	0.35

Table B. 6. P-values for Kruskal Wallis tests of significant difference between Full Canopy Phase derived NDVI integrals for the 2018 season. Test of significant differences are performed between all wheat varieties grown. Green shading indicates significant results, red shading indicates a nonsignificant result. N1 = 0 kg-N/ha, N2 = 100 kg-N/ha, N3 = 200 kg-N/ha, N4 = 350kg-N/ha.

Full Canopy Phase – NDVI – 2018						
Variety	**N1 × N2**	**N1 × N3**	**N1 × N4**	**N2 × N3**	**N2 × N4**	**N3 × N4**
AV	0.92	0.21	0.62	0.01	0.17	0.31
CA	0.36	0.27	0.82	0.08	1.00	1.00
CL	0.64	0.16	0.73	0.04	0.56	0.57
CN	0.27	0.28	0.91	0.10	1.00	1.00
CO	0.62	0.12	0.64	0.03	0.28	0.57
CR	0.45	0.16	1.00	0.10	1.00	0.82
EL	0.64	0.35	0.57	0.01	0.28	0.43
HE	0.36	0.21	1.00	0.10	1.00	0.73
HF	0.56	0.12	0.86	0.10	1.00	0.91
HL	0.56	0.16	0.99	0.08	0.92	0.73
HY	0.77	0.21	0.73	0.02	0.28	0.37
IL	0.45	0.21	0.65	0.08	1.00	1.00
IS	0.28	0.27	0.91	0.10	1.00	1.00
LE	0.36	0.27	0.82	0.08	1.00	1.00
LI	0.56	0.16	0.99	0.08	0.92	0.73
MA	0.70	0.16	0.86	0.06	0.64	0.65
ME	0.45	0.16	1.00	0.10	1.00	0.82
MW	0.85	0.09	0.52	0.08	0.64	0.91
PA	0.77	0.27	0.43	0.01	0.22	0.52
RF	0.62	0.09	0.52	0.04	0.36	0.73
RI	0.64	0.35	0.57	0.01	0.28	0.43
RO	0.70	0.21	0.99	0.04	0.52	0.50
SL	0.62	0.16	0.77	0.02	0.22	0.43
SY	0.92	0.21	0.62	0.01	0.17	0.31
Xi	0.70	0.10	0.92	0.09	0.62	1.00

Table B. 7. P-values for Kruskal Wallis tests of significant difference between Senescence Phase derived NDVI integrals for the 2016 season. Test of significant differences are performed between all wheat varieties grown. Green shading indicates significant results, red shading indicates a nonsignificant result. N1 = 0 kg-N/ha, N2 = 100 kg-N/ha, N3 = 200 kg-N/ha, N4 = 350kg-N/ha.

Senescence Phase – NDVI – 2016						
Variety	**N1 × N2**	**N1 × N3**	**N1 × N4**	**N2 × N3**	**N2 × N4**	**N3 × N4**
AV	0.92	0.21	0.62	0.01	0.17	0.31
CA	0.92	0.21	0.62	0.01	0.17	0.31
CL	0.92	0.21	0.62	0.01	0.17	0.31
CN	0.92	0.21	0.62	0.01	0.17	0.31
CO	0.92	0.21	0.62	0.01	0.17	0.31
CR	0.92	0.21	0.62	0.01	0.17	0.31
EL	0.92	0.21	0.62	0.01	0.17	0.31
HE	0.92	0.21	0.62	0.01	0.17	0.31
HF	0.92	0.21	0.62	0.01	0.17	0.31
HL	0.57	0.28	0.64	0.03	0.12	0.62
HY	0.92	0.21	0.62	0.01	0.17	0.31
IL	0.92	0.21	0.62	0.01	0.17	0.31
IS	0.92	0.21	0.62	0.01	0.17	0.31
LE	0.43	0.22	0.77	0.02	0.16	0.62
LI	0.92	0.21	0.62	0.01	0.17	0.31
MA	0.92	0.21	0.62	0.01	0.17	0.31
ME	0.92	0.21	0.62	0.01	0.17	0.31
MW	0.92	0.21	0.62	0.01	0.17	0.31
PA	0.92	0.21	0.62	0.01	0.17	0.31
RF	0.92	0.21	0.62	0.01	0.17	0.31
RI	0.92	0.21	0.62	0.01	0.17	0.31
RO	0.62	0.16	0.77	0.02	0.22	0.43
SL	0.92	0.21	0.62	0.01	0.17	0.31
SY	0.92	0.21	0.62	0.01	0.17	0.31
Xi	0.92	0.21	0.62	0.01	0.17	0.31

Table B. 8. P-values for Kruskal Wallis tests of significant difference between Senescence Phase derived NDVI integrals for the 2017 season. Test of significant differences are performed between all wheat varieties grown. Green shading indicates significant results, red shading indicates a nonsignificant result. N1 = 0 kg-N/ha, N2 = 100 kg-N/ha, N3 = 200 kg-N/ha, N4 = 350kg-N/ha.

Senescence Phase – NDVI – 2017						
Variety	**N1 × N2**	**N1 × N3**	**N1 × N4**	**N2 × N3**	**N2 × N4**	**N3 × N4**
AV	0.62	0.16	0.77	0.02	0.22	0.43
CA	0.62	0.16	0.77	0.02	0.22	0.43
CL	0.92	0.21	0.62	0.01	0.17	0.31
CN	0.52	0.09	0.64	0.06	0.56	0.82
CO	0.92	0.21	0.62	0.01	0.17	0.31
CR	0.92	0.21	0.62	0.01	0.17	0.31
EL	0.92	0.21	0.62	0.01	0.17	0.31
HE	0.92	0.21	0.62	0.01	0.17	0.31
HF	0.62	0.09	0.52	0.04	0.36	0.73
HL	0.92	0.21	0.62	0.01	0.17	0.31
HY	0.73	0.08	0.45	0.12	0.52	0.82
IL	0.62	0.16	0.77	0.02	0.22	0.43
IS	0.92	0.21	0.62	0.01	0.17	0.31
LE	0.62	0.09	0.52	0.04	0.36	0.73
LI	0.92	0.21	0.62	0.01	0.17	0.31
MA	0.92	0.21	0.62	0.01	0.17	0.31
ME	0.92	0.21	0.62	0.01	0.17	0.31
MW	0.64	0.35	0.57	0.01	0.28	0.43
PA	0.62	0.12	0.64	0.03	0.28	0.57
RF	0.92	0.21	0.62	0.01	0.17	0.31
RI	0.62	0.12	0.64	0.03	0.28	0.57
RO	0.92	0.21	0.62	0.01	0.17	0.31
SL	0.92	0.21	0.62	0.01	0.17	0.31
SY	0.43	0.22	0.77	0.02	0.16	0.62
Xi	0.92	0.21	0.62	0.01	0.17	0.31

Table B. 9. P-values for Kruskal Wallis tests of significant difference between Senescence Phase derived NDVI integrals for the 2018 season. Test of significant differences are performed between all wheat varieties grown. Green shading indicates significant results, red shading indicates a nonsignificant result. N1 = 0 kg-N/ha, N2 = 100 kg-N/ha, N3 = 200 kg-N/ha, N4 = 350kg-N/ha.

Senescence Phase – NDVI – 2018						
Variety	**N1 × N2**	**N1 × N3**	**N1 × N4**	**N2 × N3**	**N2 × N4**	**N3 × N4**
AV	0.62	0.06	0.45	0.06	0.42	0.91
CA	0.85	0.08	0.64	0.09	0.52	0.91
CL	0.64	0.03	0.45	0.21	0.43	0.86
CN	0.28	0.14	1.00	0.21	1.00	0.82
CO	0.86	0.06	0.28	0.12	0.42	0.73
CR	0.52	0.06	0.56	0.09	0.64	0.82
EL	0.36	0.16	1.00	0.14	1.00	0.91
HE	0.56	0.08	0.92	0.16	0.99	0.73
HF	0.62	0.03	0.28	0.12	0.64	0.57
HL	0.85	0.08	0.64	0.09	0.52	0.91
HY	0.77	0.04	0.45	0.12	0.52	0.65
IL	0.28	0.27	0.91	0.10	1.00	1.00
IS	0.45	0.16	1.00	0.10	1.00	0.82
LE	0.64	0.02	0.36	0.27	0.50	0.62
LI	0.73	0.19	0.85	0.16	0.64	1.00
MA	0.70	0.21	0.99	0.04	0.52	0.50
ME	0.70	0.06	0.64	0.16	0.86	0.65
MW	0.77	0.12	0.52	0.04	0.45	0.65
PA	0.92	0.21	0.62	0.01	0.17	0.31
RF	0.56	0.45	0.82	0.02	0.42	0.43
RI	0.36	0.08	1.00	0.27	0.82	1.00
RO	0.64	0.12	0.62	0.06	0.70	0.73
SL	0.52	0.03	0.56	0.27	0.57	0.73
SY	0.52	0.08	0.70	0.06	0.52	1.00
Xi	0.64	0.21	0.43	0.03	0.45	0.86

Table B. 10. P-values for Kruskal Wallis tests of significant difference between Formation Phase derived ExGR_NDVI integrals for the 2016 season. Test of significant differences are performed between all wheat varieties grown. Green shading indicates significant results, red shading indicates a nonsignificant result. N1 = 0 kg-N/ha, N2 = 100 kg-N/ha, N3 = 200 kg-N/ha, N4 = 350kg-N/ha.

Formation Phase – ExGR_NDVI – 2016						
Variety	**N1 × N2**	**N1 × N3**	**N1 × N4**	**N2 × N3**	**N2 × N4**	**N3 × N4**
AV	0.36	0.14	1.00	0.16	1.00	0.91
CA	0.10	0.16	0.82	0.45	1.00	1.00
CL	0.25	0.21	1.00	0.17	1.00	1.00
CN	1.00	0.85	1.00	1.00	0.91	1.00
CO	0.70	0.12	0.73	0.08	0.77	0.82
CR	0.27	0.22	1.00	0.14	1.00	1.00
EL	0.91	0.08	0.09	0.64	0.52	0.85
HE	0.64	0.56	0.73	0.03	0.45	0.43
HF	0.12	0.08	0.82	0.73	0.52	0.45
HL	0.71	0.19	0.99	1.00	0.73	0.92
HY	0.56	0.35	1.00	0.33	1.00	0.91
IL	1.00	0.68	0.85	0.71	0.77	0.91
IS	0.22	0.21	0.91	0.19	1.00	1.00
LE	0.56	0.19	1.00	0.56	0.91	1.00
LI	0.85	0.09	0.52	0.08	0.64	0.91
MA	0.64	0.35	0.57	0.01	0.28	0.43
ME	0.56	0.12	0.86	0.10	1.00	0.91
MW	0.64	0.02	0.36	0.27	0.50	0.62
PA	0.21	0.19	1.00	0.22	0.91	1.00
RF	0.56	0.06	0.77	0.56	0.91	0.62
RI	0.33	0.71	1.00	0.70	1.00	0.91
RO	0.50	0.45	1.00	0.08	0.35	0.73
SL	0.85	0.35	1.00	0.19	1.00	0.73
SY	0.56	0.42	0.91	0.01	0.28	0.45
Xi	0.04	0.62	0.36	0.09	0.73	0.52

Table B. 11. P-values for Kruskal Wallis tests of significant difference between Formation Phase derived ExGR_NDVI integrals for the 2017 season. Test of significant differences are performed between all wheat varieties grown. Green shading indicates significant results, red shading indicates a nonsignificant result. N1 = 0 kg-N/ha, N2 = 100 kg-N/ha, N3 = 200 kg-N/ha, N4 = 350kg-N/ha.

Formation Phase – ExGR_NDVI – 2017						
Variety	**N1 × N2**	**N1 × N3**	**N1 × N4**	**N2 × N3**	**N2 × N4**	**N3 × N4**
AV	0.56	0.21	1.00	0.19	1.00	0.91
CA	0.87	0.25	1.00	0.70	1.00	0.99
CL	0.70	0.16	0.86	0.06	0.64	0.65
CN	0.56	0.02	0.42	0.45	0.82	0.43
CO	0.36	0.27	0.82	0.08	1.00	1.00
CR	0.86	0.10	0.56	0.77	0.73	0.85
EL	0.27	0.22	1.00	0.14	1.00	1.00
HE	0.45	0.35	0.82	0.04	0.77	0.73
HF	0.21	0.28	1.00	0.14	0.82	1.00
HL	0.45	0.10	1.00	0.45	0.91	0.99
HY	0.25	0.21	1.00	0.17	1.00	1.00
IL	0.86	0.04	0.22	0.16	0.52	0.57
IS	0.99	0.06	0.22	0.27	0.64	0.50
LE	0.10	0.56	1.00	0.12	0.91	0.86
LI	0.45	0.45	0.91	0.10	0.99	1.00
MA	0.56	0.35	1.00	0.33	1.00	0.91
ME	0.65	0.08	0.21	0.28	0.52	0.99
MW	0.86	0.08	0.45	0.56	0.50	0.92
PA	0.45	0.16	1.00	0.10	1.00	0.82
RF	0.27	0.22	1.00	0.14	1.00	1.00
RI	0.77	0.04	0.45	0.12	0.52	0.65
RO	1.00	0.35	0.86	0.33	1.00	0.91
SL	0.45	0.08	1.00	0.50	0.73	0.35
SY	0.70	0.06	0.64	0.16	0.86	0.65
Xi	0.14	0.28	1.00	0.21	0.82	1.00

Table B. 12. P-values for Kruskal Wallis tests of significant difference between Formation Phase derived ExGR_NDVI integrals for the 2018 season. Test of significant differences are performed between all wheat varieties grown. Green shading indicates significant results, red shading indicates a nonsignificant result. N1 = 0 kg-N/ha, N2 = 100 kg-N/ha, N3 = 200 kg-N/ha, N4 = 350kg-N/ha.

Formation Phase – ExGR_NDVI – 2018						
Variety	**N1 × N2**	**N1 × N3**	**N1 × N4**	**N2 × N3**	**N2 × N4**	**N3 × N4**
AV	1.00	0.91	1.00	1.00	1.00	1.00
CA	1.00	1.00	1.00	1.00	1.00	1.00
CL	1.00	1.00	0.91	1.00	1.00	1.00
CN	0.54	1.00	1.00	0.85	0.65	1.00
CO	1.00	1.00	0.91	1.00	1.00	1.00
CR	1.00	1.00	1.00	1.00	1.00	1.00
EL	0.45	0.36	1.00	0.04	0.92	0.62
HE	1.00	1.00	1.00	1.00	1.00	0.91
HF	0.19	0.71	0.99	1.00	0.92	0.73
HL	0.56	1.00	1.00	0.54	0.91	1.00
HY	1.00	0.87	0.73	0.33	1.00	1.00
IL	0.68	1.00	1.00	0.56	1.00	1.00
IS	0.42	1.00	1.00	1.00	1.00	0.65
LE	1.00	0.91	1.00	1.00	1.00	1.00
LI	1.00	0.82	1.00	1.00	1.00	1.00
MA	1.00	1.00	1.00	0.91	1.00	1.00
ME	1.00	0.56	0.56	1.00	0.91	0.54
MW	0.85	0.71	1.00	0.68	1.00	0.91
PA	1.00	1.00	1.00	1.00	1.00	1.00
RF	1.00	1.00	1.00	1.00	1.00	1.00
RI	1.00	1.00	1.00	1.00	0.91	1.00
RO	0.19	0.91	0.21	0.45	1.00	0.42
SL	0.19	1.00	0.92	0.27	0.82	0.86
SY	1.00	0.85	1.00	0.42	1.00	1.00
Xi	1.00	1.00	1.00	1.00	1.00	0.91

Table B. 13. P-values for Kruskal Wallis tests of significant difference between Full Canopy Phase derived ExGR_NDVI integrals for the 2016 season. Test of significant differences are performed between all wheat varieties grown. Green shading indicates significant results, red shading indicates a nonsignificant result. N1 = 0 kg-N/ha, N2 = 100 kg-N/ha, N3 = 200 kg-N/ha, N4 = 350kg-N/ha.

Full Canopy Phase – ExGR_NDVI – 2016						
Variety	**N1 × N2**	**N1 × N3**	**N1 × N4**	**N2 × N3**	**N2 × N4**	**N3 × N4**
AV	0.92	0.21	0.62	0.01	0.17	0.31
CA	0.62	0.12	0.64	0.03	0.28	0.57
CL	0.92	0.21	0.62	0.01	0.17	0.31
CN	0.62	0.06	0.42	0.06	0.45	0.91
CO	0.92	0.21	0.62	0.01	0.17	0.31
CR	0.62	0.12	0.64	0.03	0.28	0.57
EL	0.62	0.06	0.45	0.06	0.42	0.91
HE	0.92	0.21	0.62	0.01	0.17	0.31
HF	0.62	0.06	0.45	0.06	0.42	0.91
HL	0.62	0.16	0.77	0.02	0.22	0.43
HY	0.62	0.09	0.52	0.04	0.36	0.73
IL	0.62	0.12	0.64	0.03	0.28	0.57
IS	0.92	0.21	0.62	0.01	0.17	0.31
LE	0.62	0.09	0.52	0.04	0.36	0.73
LI	0.62	0.16	0.77	0.02	0.22	0.43
MA	0.62	0.12	0.64	0.03	0.28	0.57
ME	0.62	0.16	0.77	0.02	0.22	0.43
MW	0.62	0.16	0.77	0.02	0.22	0.43
PA	0.92	0.21	0.62	0.01	0.17	0.31
RF	0.62	0.12	0.64	0.03	0.28	0.57
RI	0.62	0.16	0.77	0.02	0.22	0.43
RO	0.62	0.09	0.52	0.04	0.36	0.73
SL	0.92	0.21	0.62	0.01	0.17	0.31
SY	0.92	0.21	0.62	0.01	0.17	0.31
Xi	0.62	0.16	0.77	0.02	0.22	0.43

Table B. 14. P-values for Kruskal Wallis tests of significant difference between Full Canopy Phase derived ExGR_NDVI integrals for the 2017 season. Test of significant differences are performed between all wheat varieties grown. Green shading indicates significant results, red shading indicates a nonsignificant result. N1 = 0 kg-N/ha, N2 = 100 kg-N/ha, N3 = 200 kg-N/ha, N4 = 350kg-N/ha.

Full Canopy Phase – ExGR_NDVI – 2017						
Variety	**N1 × N2**	**N1 × N3**	**N1 × N4**	**N2 × N3**	**N2 × N4**	**N3 × N4**
AV	0.56	0.35	0.73	0.03	0.52	0.62
CA	0.36	0.27	0.82	0.08	1.00	1.00
CL	0.52	0.27	0.57	0.03	0.56	0.73
CN	0.56	0.12	0.86	0.10	1.00	0.91
CO	0.45	0.45	0.91	0.03	0.64	0.52
CR	0.70	0.10	0.92	0.09	0.62	1.00
EL	0.52	0.35	0.65	0.02	0.45	0.52
HE	0.56	0.35	0.73	0.03	0.52	0.62
HF	0.45	0.45	0.91	0.03	0.64	0.52
HL	0.70	0.16	0.86	0.06	0.64	0.65
HY	0.52	0.35	0.65	0.02	0.45	0.52
IL	0.56	0.35	0.73	0.03	0.52	0.62
IS	0.52	0.35	0.65	0.02	0.45	0.52
LE	0.56	0.45	0.82	0.02	0.42	0.43
LI	0.56	0.45	0.82	0.02	0.42	0.43
MA	0.56	0.45	1.00	0.02	0.52	0.35
ME	0.64	0.16	0.73	0.04	0.56	0.57
MW	0.64	0.12	0.62	0.06	0.70	0.73
PA	0.64	0.21	0.43	0.03	0.45	0.86
RF	0.56	0.45	0.82	0.02	0.42	0.43
RI	0.52	0.45	0.73	0.01	0.36	0.35
RO	0.64	0.16	0.73	0.04	0.56	0.57
SL	0.70	0.16	0.86	0.06	0.64	0.65
SY	0.64	0.27	0.50	0.02	0.36	0.62
Xi	0.52	0.27	0.57	0.03	0.56	0.73

Table B. 15. P-values for Kruskal Wallis tests of significant difference between Full Canopy Phase derived ExGR_NDVI integrals for the 2018 season. Test of significant differences are performed between all wheat varieties grown. Green shading indicates significant results, red shading indicates a nonsignificant result. N1 = 0 kg-N/ha, N2 = 100 kg-N/ha, N3 = 200 kg-N/ha, N4 = 350kg-N/ha.

Full Canopy Phase – ExGR_NDVI – 2018						
Variety	**N1 × N2**	**N1 × N3**	**N1 × N4**	**N2 × N3**	**N2 × N4**	**N3 × N4**
AV	0.77	0.16	0.62	0.03	0.36	0.50
CA	0.36	0.27	0.82	0.08	1.00	1.00
CL	0.64	0.12	0.62	0.06	0.70	0.73
CN	0.27	0.28	0.91	0.10	1.00	1.00
CO	0.77	0.16	0.62	0.03	0.36	0.50
CR	0.70	0.10	0.92	0.09	0.62	1.00
EL	0.64	0.27	0.50	0.02	0.36	0.62
HE	0.45	0.16	1.00	0.10	1.00	0.82
HF	0.36	0.21	1.00	0.10	1.00	0.73
HL	0.36	0.27	0.82	0.08	1.00	1.00
HY	0.64	0.27	0.50	0.02	0.36	0.62
IL	0.45	0.21	0.65	0.08	1.00	1.00
IS	0.36	0.21	1.00	0.10	1.00	0.73
LE	0.36	0.27	0.82	0.08	1.00	1.00
LI	0.56	0.16	0.99	0.08	0.92	0.73
MA	0.64	0.16	0.73	0.04	0.56	0.57
ME	0.36	0.21	1.00	0.10	1.00	0.73
MW	0.85	0.09	0.52	0.08	0.64	0.91
PA	0.77	0.27	0.43	0.01	0.22	0.52
RF	0.86	0.09	0.34	0.08	0.36	0.91
RI	0.56	0.45	1.00	0.02	0.52	0.35
RO	0.70	0.16	0.86	0.06	0.64	0.65
SL	0.62	0.09	0.52	0.04	0.36	0.73
SY	0.92	0.21	0.62	0.01	0.17	0.31
Xi	0.56	0.12	0.86	0.10	1.00	0.91

Table B. 16. P-values for Kruskal Wallis tests of significant difference between Senescence Phase derived ExGR_NDVI integrals for the 2016 season. Test of significant differences are performed between all wheat varieties grown. Green shading indicates significant results, red shading indicates a nonsignificant result. N1 = 0 kg-N/ha, N2 = 100 kg-N/ha, N3 = 200 kg-N/ha, N4 = 350kg-N/ha.

Senescence Phase – ExGR_NDVI – 2016						
Variety	**N1 × N2**	**N1 × N3**	**N1 × N4**	**N2 × N3**	**N2 × N4**	**N3 × N4**
AV	0.92	0.21	0.62	0.01	0.17	0.31
CA	0.92	0.21	0.62	0.01	0.17	0.31
CL	0.92	0.21	0.62	0.01	0.17	0.31
CN	0.92	0.21	0.62	0.01	0.17	0.31
CO	0.43	0.22	0.77	0.02	0.16	0.62
CR	0.92	0.21	0.62	0.01	0.17	0.31
EL	0.92	0.21	0.62	0.01	0.17	0.31
HE	0.62	0.16	0.77	0.02	0.22	0.43
HF	0.77	0.27	0.43	0.01	0.22	0.52
HL	0.57	0.28	0.64	0.03	0.12	0.62
HY	0.92	0.21	0.62	0.01	0.17	0.31
IL	0.92	0.21	0.62	0.01	0.17	0.31
IS	0.92	0.21	0.62	0.01	0.17	0.31
LE	0.43	0.22	0.77	0.02	0.16	0.62
LI	0.92	0.21	0.62	0.01	0.17	0.31
MA	0.92	0.21	0.62	0.01	0.17	0.31
ME	0.43	0.22	0.77	0.02	0.16	0.62
MW	0.62	0.09	0.52	0.04	0.36	0.73
PA	0.92	0.21	0.62	0.01	0.17	0.31
RF	0.92	0.21	0.62	0.01	0.17	0.31
RI	0.92	0.21	0.62	0.01	0.17	0.31
RO	0.57	0.17	0.42	0.06	0.21	1.00
SL	0.62	0.09	0.52	0.04	0.36	0.73
SY	0.77	0.27	0.43	0.01	0.22	0.52
Xi	0.92	0.21	0.62	0.01	0.17	0.31

Table B. 17. P-values for Kruskal Wallis tests of significant difference between Senescence Phase derived ExGR_NDVI integrals for the 2017 season. Test of significant differences are performed between all wheat varieties grown. Green shading indicates significant results, red shading indicates a nonsignificant result. N1 = 0 kg-N/ha, N2 = 100 kg-N/ha, N3 = 200 kg-N/ha, N4 = 350kg-N/ha.

Senescence Phase – ExGR_NDVI – 2017						
Variety	**N1 × N2**	**N1 × N3**	**N1 × N4**	**N2 × N3**	**N2 × N4**	**N3 × N4**
AV	0.62	0.16	0.77	0.02	0.22	0.43
CA	0.91	0.45	0.42	0.06	0.06	0.62
CL	0.62	0.16	0.77	0.02	0.22	0.43
CN	0.62	0.09	0.52	0.04	0.36	0.73
CO	0.92	0.21	0.62	0.01	0.17	0.31
CR	0.92	0.21	0.62	0.01	0.17	0.31
EL	0.92	0.21	0.62	0.01	0.17	0.31
HE	0.92	0.21	0.62	0.01	0.17	0.31
HF	0.62	0.06	0.42	0.06	0.45	0.91
HL	0.92	0.21	0.62	0.01	0.17	0.31
HY	0.73	0.27	0.92	0.03	0.22	0.37
IL	0.62	0.12	0.64	0.03	0.28	0.57
IS	0.92	0.21	0.62	0.01	0.17	0.31
LE	0.62	0.16	0.77	0.02	0.22	0.43
LI	0.92	0.21	0.62	0.01	0.17	0.31
MA	0.92	0.21	0.62	0.01	0.17	0.31
ME	0.62	0.12	0.64	0.03	0.28	0.57
MW	0.92	0.21	0.62	0.01	0.17	0.31
PA	0.62	0.12	0.64	0.03	0.28	0.57
RF	0.62	0.16	0.77	0.02	0.22	0.43
RI	0.62	0.16	0.77	0.02	0.22	0.43
RO	0.62	0.16	0.77	0.02	0.22	0.43
SL	0.62	0.16	0.77	0.02	0.22	0.43
SY	0.43	0.22	0.77	0.02	0.16	0.62
Xi	0.92	0.21	0.62	0.01	0.17	0.31

Table B. 18. P-values for Kruskal Wallis tests of significant difference between Senescence Phase derived ExGR_NDVI integrals for the 2018 season. Test of significant differences are performed between all wheat varieties grown. Green shading indicates significant results, red shading indicates a nonsignificant result. N1 = 0 kg-N/ha, N2 = 100 kg-N/ha, N3 = 200 kg-N/ha, N4 = 350kg-N/ha.

Senescence Phase – ExGR_NDVI – 2018						
Variety	**N1 × N2**	**N1 × N3**	**N1 × N4**	**N2 × N3**	**N2 × N4**	**N3 × N4**
AV	0.62	0.06	0.45	0.06	0.42	0.91
CA	0.70	0.10	0.92	0.09	0.62	1.00
CL	0.86	0.03	0.17	0.21	0.64	0.43
CN	0.28	0.21	1.00	0.14	1.00	0.82
CO	0.86	0.06	0.28	0.12	0.42	0.73
CR	0.56	0.10	1.00	0.12	0.86	0.91
EL	0.28	0.21	1.00	0.14	1.00	0.82
HE	0.36	0.14	1.00	0.16	1.00	0.91
HF	0.62	0.06	0.45	0.06	0.42	0.91
HL	0.62	0.08	0.56	0.16	0.77	0.73
HY	0.77	0.04	0.45	0.12	0.52	0.65
IL	1.00	0.87	0.82	0.42	1.00	1.00
IS	0.35	0.45	0.82	0.04	0.73	0.77
LE	0.56	0.02	0.42	0.45	0.82	0.43
LI	1.00	0.25	0.92	0.45	0.99	0.73
MA	0.77	0.12	0.52	0.04	0.45	0.65
ME	0.70	0.04	0.52	0.21	0.99	0.50
MW	0.64	0.16	0.73	0.04	0.56	0.57
PA	0.77	0.16	0.62	0.03	0.36	0.50
RF	0.56	0.35	0.73	0.03	0.52	0.62
RI	0.27	0.14	1.00	0.22	1.00	1.00
RO	0.64	0.21	0.43	0.03	0.45	0.86
SL	0.27	0.08	1.00	0.36	0.82	1.00
SY	0.62	0.06	0.45	0.06	0.42	0.91
Xi	0.52	0.35	0.65	0.02	0.45	0.52

Table B. 19. P-values for Kruskal Wallis tests of significant difference between Formation Phase derived GreenPixel integrals for the 2016 season. Test of significant differences are performed between all wheat varieties grown. Green shading indicates significant results, red shading indicates a nonsignificant result. N1 = 0 kg-N/ha, N2 = 100 kg-N/ha, N3 = 200 kg-N/ha, N4 = 350kg-N/ha.

Formation Phase – GreenPixel – 2016						
Variety	**N1 × N2**	**N1 × N3**	**N1 × N4**	**N2 × N3**	**N2 × N4**	**N3 × N4**
AV	0.77	0.12	0.52	0.04	0.45	0.65
CA	0.45	0.27	0.73	0.06	0.92	0.99
CL	0.62	0.06	0.45	0.06	0.42	0.91
CN	0.64	0.06	0.70	0.12	0.62	0.73
CO	0.35	0.04	0.73	0.45	0.82	0.77
CR	0.16	0.70	0.86	0.06	0.65	0.64
EL	0.62	0.06	0.42	0.06	0.45	0.91
HE	0.64	0.21	0.43	0.03	0.45	0.86
HF	0.14	0.12	1.00	0.45	1.00	0.99
HL	0.27	0.04	0.86	0.56	0.65	0.64
HY	0.28	0.14	1.00	0.21	1.00	0.82
IL	0.64	0.01	0.35	0.28	0.57	0.43
IS	0.56	0.16	0.99	0.08	0.92	0.73
LE	0.45	0.04	0.77	0.35	0.82	0.73
LI	0.36	0.14	1.00	0.16	1.00	0.91
MA	0.52	0.27	0.57	0.03	0.56	0.73
ME	0.77	0.12	0.52	0.04	0.45	0.65
MW	0.52	0.06	0.56	0.09	0.64	0.82
PA	0.62	0.06	0.42	0.06	0.45	0.91
RF	0.45	0.10	1.00	0.16	1.00	0.82
RI	0.42	0.01	0.56	0.45	0.91	0.28
RO	0.85	0.09	0.52	0.08	0.64	0.91
SL	0.70	0.21	0.99	0.04	0.52	0.50
SY	0.62	0.06	0.42	0.06	0.45	0.91
Xi	0.36	0.21	1.00	0.10	1.00	0.73

Table B. 20. P-values for Kruskal Wallis tests of significant difference between Formation Phase derived GreenPixel integrals for the 2017 season. Test of significant differences are performed between all wheat varieties grown. Green shading indicates significant results, red shading indicates a nonsignificant result. N1 = 0 kg-N/ha, N2 = 100 kg-N/ha, N3 = 200 kg-N/ha, N4 = 350kg-N/ha.

Formation Phase – GreenPixel – 2017						
Variety	**N1 × N2**	**N1 × N3**	**N1 × N4**	**N2 × N3**	**N2 × N4**	**N3 × N4**
AV	0.21	0.22	0.91	0.19	1.00	1.00
CA	0.21	0.14	0.82	0.28	1.00	1.00
CL	0.70	0.16	0.86	0.06	0.64	0.65
CN	0.21	0.04	0.99	0.70	0.50	0.52
CO	0.22	0.21	0.91	0.19	1.00	1.00
CR	0.70	0.10	0.92	0.71	0.91	0.73
EL	0.12	0.06	0.73	0.64	0.62	0.70
HE	0.19	0.28	1.00	0.16	1.00	1.00
HF	0.28	0.10	1.00	0.27	0.91	1.00
HL	0.16	0.06	0.65	0.70	0.86	0.64
HY	0.10	0.27	1.00	0.28	1.00	0.91
IL	0.36	0.08	1.00	0.27	0.82	1.00
IS	0.64	0.12	0.62	0.06	0.70	0.73
LE	0.10	0.27	1.00	0.28	1.00	0.91
LI	0.56	0.10	1.00	0.12	0.86	0.91
MA	0.28	0.19	1.00	0.16	1.00	1.00
ME	0.64	0.02	0.36	0.27	0.50	0.62
MW	0.45	0.03	0.64	0.45	0.91	0.52
PA	0.45	0.10	1.00	0.16	1.00	0.82
RF	0.08	0.56	0.92	0.16	0.73	0.99
RI	0.56	0.10	1.00	0.12	0.86	0.91
RO	0.92	0.10	0.70	0.35	0.86	0.57
SL	0.12	0.08	0.82	0.70	0.73	0.77
SY	0.28	0.14	1.00	0.21	1.00	0.82
Xi	0.14	0.36	1.00	0.16	0.91	1.00

Table B. 21. P-values for Kruskal Wallis tests of significant difference between Formation Phase derived GreenPixel integrals for the 2018 season. Test of significant differences are performed between all wheat varieties grown. Green shading indicates significant results, red shading indicates a nonsignificant result. N1 = 0 kg-N/ha, N2 = 100 kg-N/ha, N3 = 200 kg-N/ha, N4 = 350kg-N/ha.

Formation Phase – GreenPixel – 2018						
Variety	**N1 × N2**	**N1 × N3**	**N1 × N4**	**N2 × N3**	**N2 × N4**	**N3 × N4**
AV	0.36	0.25	1.00	0.27	1.00	0.91
CA	0.85	1.00	1.00	1.00	1.00	0.91
CL	0.35	0.08	1.00	0.28	1.00	0.99
CN	0.03	0.52	0.56	0.62	0.35	0.73
CO	0.10	0.36	1.00	0.21	1.00	0.73
CR	0.42	1.00	0.99	1.00	1.00	0.82
EL	0.45	0.14	1.00	0.12	0.99	1.00
HE	0.14	0.35	1.00	0.45	1.00	0.82
HF	0.21	0.10	0.73	0.85	0.86	0.77
HL	0.45	0.33	1.00	0.45	0.91	1.00
HY	0.65	0.10	0.27	0.92	1.00	0.70
IL	0.87	0.70	1.00	0.68	1.00	1.00
IS	0.42	1.00	1.00	1.00	0.99	0.82
LE	0.54	1.00	1.00	0.71	0.82	1.00
LI	0.68	0.87	1.00	0.70	1.00	1.00
MA	0.21	0.19	1.00	0.22	0.91	1.00
ME	0.27	0.45	1.00	0.19	0.82	1.00
MW	0.28	0.14	1.00	0.21	1.00	0.82
PA	0.56	0.12	0.86	0.10	1.00	0.91
RF	1.00	0.33	0.45	0.56	0.64	0.73
RI	0.25	0.21	1.00	0.17	1.00	1.00
RO	0.21	0.28	1.00	0.14	0.82	1.00
SL	0.14	0.21	0.82	0.28	1.00	1.00
SY	1.00	1.00	1.00	1.00	1.00	0.91
Xi	1.00	0.54	1.00	0.56	1.00	0.91

Table B. 22. P-values for Kruskal Wallis tests of significant difference between Full Canopy Phase derived GreenPixel integrals for the 2016 season. Test of significant differences are performed between all wheat varieties grown. Green shading indicates significant results, red shading indicates a nonsignificant result. N1 = 0 kg-N/ha, N2 = 100 kg-N/ha, N3 = 200 kg-N/ha, N4 = 350kg-N/ha.

Full Canopy Phase – GreenPixel – 2016						
Variety	**N1 × N2**	**N1 × N3**	**N1 × N4**	**N2 × N3**	**N2 × N4**	**N3 × N4**
AV	0.21	0.08	1.00	0.45	0.65	1.00
CA	0.92	0.21	0.62	0.01	0.17	0.31
CL	0.64	0.21	0.43	0.03	0.45	0.86
CN	0.62	0.09	0.52	0.04	0.36	0.73
CO	0.27	0.22	1.00	0.14	1.00	1.00
CR	0.21	0.70	0.99	0.04	0.50	0.52
EL	0.62	0.16	0.77	0.02	0.22	0.43
HE	0.62	0.06	0.42	0.06	0.45	0.91
HF	0.64	0.27	0.50	0.02	0.36	0.62
HL	0.56	0.03	0.52	0.35	0.73	0.62
HY	0.56	0.03	0.52	0.35	0.73	0.62
IL	0.62	0.09	0.52	0.04	0.36	0.73
IS	0.62	0.06	0.42	0.06	0.45	0.91
LE	0.27	0.14	1.00	0.22	1.00	1.00
LI	0.52	0.08	0.70	0.06	0.52	1.00
MA	0.52	0.45	0.73	0.01	0.36	0.35
ME	0.62	0.06	0.45	0.06	0.42	0.91
MW	0.04	0.12	0.65	0.77	0.45	0.52
PA	0.09	0.08	0.91	0.85	0.52	0.64
RF	0.64	0.12	0.62	0.06	0.70	0.73
RI	0.62	0.09	0.52	0.04	0.36	0.73
RO	0.27	0.04	0.86	0.56	0.65	0.64
SL	0.85	0.08	0.64	0.09	0.52	0.91
SY	0.62	0.04	0.36	0.09	0.52	0.73
Xi	0.36	0.35	0.91	0.06	1.00	0.86

Table B. 23. P-values for Kruskal Wallis tests of significant difference between Full Canopy Phase derived GreenPixel integrals for the 2017 season. Test of significant differences are performed between all wheat varieties grown. Green shading indicates significant results, red shading indicates a nonsignificant result. N1 = 0 kg-N/ha, N2 = 100 kg-N/ha, N3 = 200 kg-N/ha, N4 = 350kg-N/ha.

Full Canopy Phase – GreenPixel – 2017						
Variety	**N1 × N2**	**N1 × N3**	**N1 × N4**	**N2 × N3**	**N2 × N4**	**N3 × N4**
AV	0.45	0.45	0.91	0.03	0.64	0.52
CA	0.45	0.08	1.00	0.21	0.65	1.00
CL	0.70	0.21	0.99	0.04	0.52	0.50
CN	0.16	0.36	1.00	0.14	0.91	1.00
CO	0.16	0.64	0.73	0.04	0.57	0.56
CR	0.36	0.25	1.00	0.27	1.00	0.91
EL	0.52	0.08	0.70	0.06	0.52	1.00
HE	0.36	0.21	1.00	0.10	1.00	0.73
HF	0.45	0.06	0.92	0.27	0.73	0.99
HL	0.27	0.56	0.65	0.04	0.86	0.64
HY	0.45	0.27	0.73	0.06	0.92	0.99
IL	0.45	0.36	1.00	0.04	0.92	0.62
IS	0.77	0.27	0.43	0.01	0.22	0.52
LE	0.25	0.21	1.00	0.17	1.00	1.00
LI	0.56	0.16	0.99	0.08	0.92	0.73
MA	0.56	0.12	0.86	0.10	1.00	0.91
ME	0.77	0.12	0.52	0.04	0.45	0.65
MW	0.70	0.06	0.64	0.16	0.86	0.65
PA	0.42	0.56	0.91	0.01	0.45	0.28
RF	0.56	0.27	0.65	0.04	0.64	0.86
RI	0.45	0.35	0.82	0.04	0.77	0.73
RO	0.36	0.16	1.00	0.14	1.00	0.91
SL	0.21	0.22	0.91	0.19	1.00	1.00
SY	0.52	0.27	0.57	0.03	0.56	0.73
Xi	0.45	0.16	1.00	0.10	1.00	0.82

Table B. 24. P-values for Kruskal Wallis tests of significant difference between Full Canopy Phase derived GreenPixel integrals for the 2018 season. Test of significant differences are performed between all wheat varieties grown. Green shading indicates significant results, red shading indicates a nonsignificant result. N1 = 0 kg-N/ha, N2 = 100 kg-N/ha, N3 = 200 kg-N/ha, N4 = 350kg-N/ha.

Full Canopy Phase – GreenPixel – 2018						
Variety	**N1 × N2**	**N1 × N3**	**N1 × N4**	**N2 × N3**	**N2 × N4**	**N3 × N4**
AV	0.04	0.21	0.99	0.70	0.52	0.50
CA	0.22	0.21	0.91	0.19	1.00	1.00
CL	0.12	0.08	0.82	0.70	0.73	0.77
CN	0.04	0.16	0.57	0.64	0.56	0.73
CO	0.28	0.10	1.00	0.27	0.91	1.00
CR	0.02	0.56	0.42	0.43	0.45	0.82
EL	0.10	0.45	1.00	0.16	0.82	1.00
HE	0.06	0.27	0.99	0.45	0.92	0.73
HF	0.02	0.27	0.62	0.64	0.36	0.50
HL	0.04	0.27	0.86	0.56	0.64	0.65
HY	0.02	0.16	0.43	0.62	0.22	0.77
IL	0.03	0.71	0.35	0.52	0.56	0.91
IS	0.01	0.56	0.42	0.28	0.45	0.91
LE	0.06	0.09	0.82	0.52	0.56	0.64
LI	0.10	0.12	0.91	0.56	1.00	0.86
MA	0.19	0.16	1.00	0.28	1.00	1.00
ME	0.06	0.16	0.65	0.70	0.64	0.86
MW	0.06	0.27	0.99	0.45	0.92	0.73
PA	0.21	0.14	0.82	0.28	1.00	1.00
RF	0.45	0.45	0.91	0.03	0.52	0.64
RI	0.14	0.21	0.82	0.28	1.00	1.00
RO	0.10	0.70	0.92	0.09	1.00	0.62
SL	0.10	0.09	1.00	0.70	0.92	0.62
SY	0.35	0.06	0.86	0.36	0.91	1.00
Xi	0.21	0.19	1.00	0.22	0.91	1.00

Table B. 25. P-values for Kruskal Wallis tests of significant difference between Senescence Phase derived GreenPixel integrals for the 2016 season. Test of significant differences are performed between all wheat varieties grown. Green shading indicates significant results, red shading indicates a nonsignificant result. N1 = 0 kg-N/ha, N2 = 100 kg-N/ha, N3 = 200 kg-N/ha, N4 = 350kg-N/ha.

Senescence Phase – GreenPixel – 2016						
Variety	**N1 × N2**	**N1 × N3**	**N1 × N4**	**N2 × N3**	**N2 × N4**	**N3 × N4**
AV	0.62	0.16	0.77	0.02	0.22	0.43
CA	0.92	0.21	0.62	0.01	0.17	0.31
CL	0.92	0.21	0.62	0.01	0.17	0.31
CN	0.62	0.12	0.64	0.03	0.28	0.57
CO	0.92	0.21	0.62	0.01	0.17	0.31
CR	0.62	0.16	0.77	0.02	0.22	0.43
EL	0.92	0.21	0.62	0.01	0.17	0.31
HE	0.92	0.21	0.62	0.01	0.17	0.31
HF	0.92	0.21	0.62	0.01	0.17	0.31
HL	0.92	0.21	0.62	0.01	0.17	0.31
HY	0.92	0.21	0.62	0.01	0.17	0.31
IL	0.92	0.21	0.62	0.01	0.17	0.31
IS	0.62	0.16	0.77	0.02	0.22	0.43
LE	0.62	0.06	0.45	0.06	0.42	0.91
LI	0.92	0.21	0.62	0.01	0.17	0.31
MA	0.92	0.21	0.62	0.01	0.17	0.31
ME	0.92	0.21	0.62	0.01	0.17	0.31
MW	0.62	0.06	0.45	0.06	0.42	0.91
PA	0.62	0.06	0.42	0.06	0.45	0.91
RF	0.62	0.16	0.77	0.02	0.22	0.43
RI	0.92	0.21	0.62	0.01	0.17	0.31
RO	0.62	0.09	0.52	0.04	0.36	0.73
SL	0.62	0.12	0.64	0.03	0.28	0.57
SY	0.92	0.21	0.62	0.01	0.17	0.31
Xi	0.92	0.21	0.62	0.01	0.17	0.31

Table B. 26. P-values for Kruskal Wallis tests of significant difference between Senescence Phase derived GreenPixel integrals for the 2017 season. Test of significant differences are performed between all wheat varieties grown. Green shading indicates significant results, red shading indicates a nonsignificant result. N1 = 0 kg-N/ha, N2 = 100 kg-N/ha, N3 = 200 kg-N/ha, N4 = 350kg-N/ha.

Senescence Phase – GreenPixel – 2017						
Variety	**N1 × N2**	**N1 × N3**	**N1 × N4**	**N2 × N3**	**N2 × N4**	**N3 × N4**
AV	0.92	0.21	0.62	0.01	0.17	0.31
CA	0.92	0.21	0.62	0.01	0.17	0.31
CL	0.62	0.06	0.45	0.06	0.42	0.91
CN	0.62	0.12	0.64	0.03	0.28	0.57
CO	0.92	0.21	0.62	0.01	0.17	0.31
CR	0.64	0.21	0.43	0.03	0.45	0.86
EL	0.92	0.21	0.62	0.01	0.17	0.31
HE	0.92	0.21	0.62	0.01	0.17	0.31
HF	0.62	0.03	0.28	0.12	0.64	0.57
HL	0.86	0.21	0.64	0.03	0.17	0.43
HY	0.62	0.16	0.77	0.02	0.22	0.43
IL	0.52	0.09	0.64	0.06	0.56	0.82
IS	0.62	0.04	0.36	0.09	0.52	0.73
LE	0.62	0.03	0.28	0.12	0.64	0.57
LI	0.62	0.06	0.45	0.06	0.42	0.91
MA	0.77	0.27	0.43	0.01	0.22	0.52
ME	0.77	0.27	0.43	0.01	0.22	0.52
MW	0.92	0.21	0.62	0.01	0.17	0.31
PA	0.62	0.12	0.64	0.03	0.28	0.57
RF	0.62	0.09	0.52	0.04	0.36	0.73
RI	0.62	0.12	0.64	0.03	0.28	0.57
RO	0.92	0.21	0.62	0.01	0.17	0.31
SL	0.56	0.42	0.91	0.01	0.28	0.45
SY	0.92	0.21	0.62	0.01	0.17	0.31
Xi	0.92	0.21	0.62	0.01	0.17	0.31

Table B. 27. P-values for Kruskal Wallis tests of significant difference between Senescence Phase derived GreenPixel integrals for the 2018 season. Test of significant differences are performed between all wheat varieties grown. Green shading indicates significant results, red shading indicates a nonsignificant result. N1 = 0 kg-N/ha, N2 = 100 kg-N/ha, N3 = 200 kg-N/ha, N4 = 350kg-N/ha.

Senescence Phase – GreenPixel – 2018						
Variety	**N1 × N2**	**N1 × N3**	**N1 × N4**	**N2 × N3**	**N2 × N4**	**N3 × N4**
AV	0.10	0.09	1.00	0.70	0.92	0.62
CA	0.36	0.16	1.00	0.14	1.00	0.91
CL	0.27	0.08	0.57	0.85	0.99	0.64
CN	0.27	0.14	1.00	0.22	1.00	1.00
CO	0.56	0.04	0.64	0.27	0.65	0.86
CR	0.14	0.21	0.82	0.70	1.00	0.99
EL	0.56	0.04	0.64	0.27	0.65	0.86
HE	0.14	0.21	0.82	0.28	1.00	1.00
HF	0.45	0.04	0.77	0.35	0.82	0.73
HL	0.10	0.09	1.00	0.70	0.92	0.62
HY	0.09	0.08	0.91	0.85	0.52	0.64
IL	0.56	0.70	1.00	0.42	0.82	1.00
IS	0.19	0.21	1.00	0.22	1.00	0.91
LE	0.16	0.08	0.73	0.62	0.77	0.56
LI	0.71	0.14	1.00	0.56	1.00	0.86
MA	0.27	0.14	1.00	0.22	1.00	1.00
ME	0.14	0.12	1.00	0.45	1.00	0.99
MW	0.19	0.28	1.00	0.16	1.00	1.00
PA	1.00	0.85	1.00	0.42	1.00	1.00
RF	0.52	0.45	0.73	0.01	0.36	0.35
RI	0.28	0.10	1.00	0.27	0.91	1.00
RO	0.27	0.22	1.00	0.14	1.00	1.00
SL	0.35	0.04	0.73	0.45	0.82	0.77
SY	0.85	0.08	0.64	0.09	0.52	0.91
Xi	0.70	0.16	0.86	0.06	0.64	0.65

Appendix D

Appendix B contains further details and explanation of custom image processing software developed for processing imagery, and extracting and analysing phenotypic results from plots. This software was developed for Rothamsted Research, who currently employ a UAV with RGB, Near Infrared (NIR) and thermal cameras to image field-based experiments totalling upwards of 10,000 plots. The collected images are calibrated and corrected as necessary before orthomosaics of each field are generated using Agisoft Photoscan (Agisoft, St Petersburg, Russia), a Structure from Motion photogrammetry software package. All calibration workflows for the RGB, NIR and thermal cameras have been developed in house and currently in a development stage. This makes processing of the high volumes of data collected tedious and inefficient, as the workflow lacks automation. Therefore, a set of graphical user interface (GUI) based 'tools' have been built to improve the efficiency and usability of past developed imaging processing python-based workflows. The objectives were to produce tools for the following three key processing steps involved with UAV-based phenotyping:

1. Calibration and correction of raw imagery to reflectance based on custom made calibration factors

2. Combining of datasets/orthomosaics from multiple sensors together in to single, multi-band image files for improved data storage and analysis.

3. Extraction of key statistics from multi-band image files based on user defined areas of interest.

The software tools were built using the Tkinter Python library and utilise several python libraries. DCRAW and ExifTool are two command line tools also utilised by the software. Currently the software requires python to be installed on the user's computer, as well as the non-standard python libraries.

The following sections outline the three tools contained within the software. More details on the required inputs, overall workflow, and design are provided below.

D2. Radiometric Calibration Tool.

This tool utilises a specific correction workflow developed for Rothamsted Research as part of the ongoing Studentship. The PhD work developed custom and novel image corrections and calibration factors to convert UAV imagery pixel values from digital numbers to calibrated reflectance. The tool takes a series of inputs, Table B. 28, required to in the radiometric calibration processing. The key steps of the image processing workflow, Figure B. 1, are as follows:

1. The raw images are converted to TIFF format using DCRAW. A linear conversion is used to ensure the raw data is maintained and any non-linear gamma corrections are not applied as is often the case with other consumer image processing software.

2. Exposure corrections are applied to normalise imagery to standard exposure settings. Novel exposure corrections have been developed and proven effective, allowing for imagery captured under different camera exposure settings to be normalised during post processing.

3. Vignetting filters are derived and applied through multiplication to each image to reduce the impact of vignetting (circular drop off in brightness) in the imagery.

4. Irradiance corrections are applied based on time matched readings from the Tec5 downwelling irradiance sensor. These corrections include a custom cross sensor calibration factor applied to the Tec5 measurement before being applied to the image.

5. The final images are saved as 16bit TIFF images ready for further processing, typically in photogrammetry software such as Agisoft Photoscan.

Table B. 28. Details of required inputs for the developed processing tools. The tools are designed to require minimal input, whilst also being designed to find required files based on expected inputs.

Input	Format	Description
Raw Imagery	Folder Path	Location of Raw imagery from cameras on UAV, unprocessed (.ARW for Sony Cameras).
Irradiance Data	Excel spreadsheet	Excel spreadsheet of raw data produced by the Tec5
Vignetting Folder	Folder Path	Path to folder in which generated vignetting filters will be saved
Output Folder	Folder Path	Path to folder in which final calibrated reflectance imagery will be saved.
Camera	Drop down menu selection	Defines whether the images are from the NIR or RGB camera.

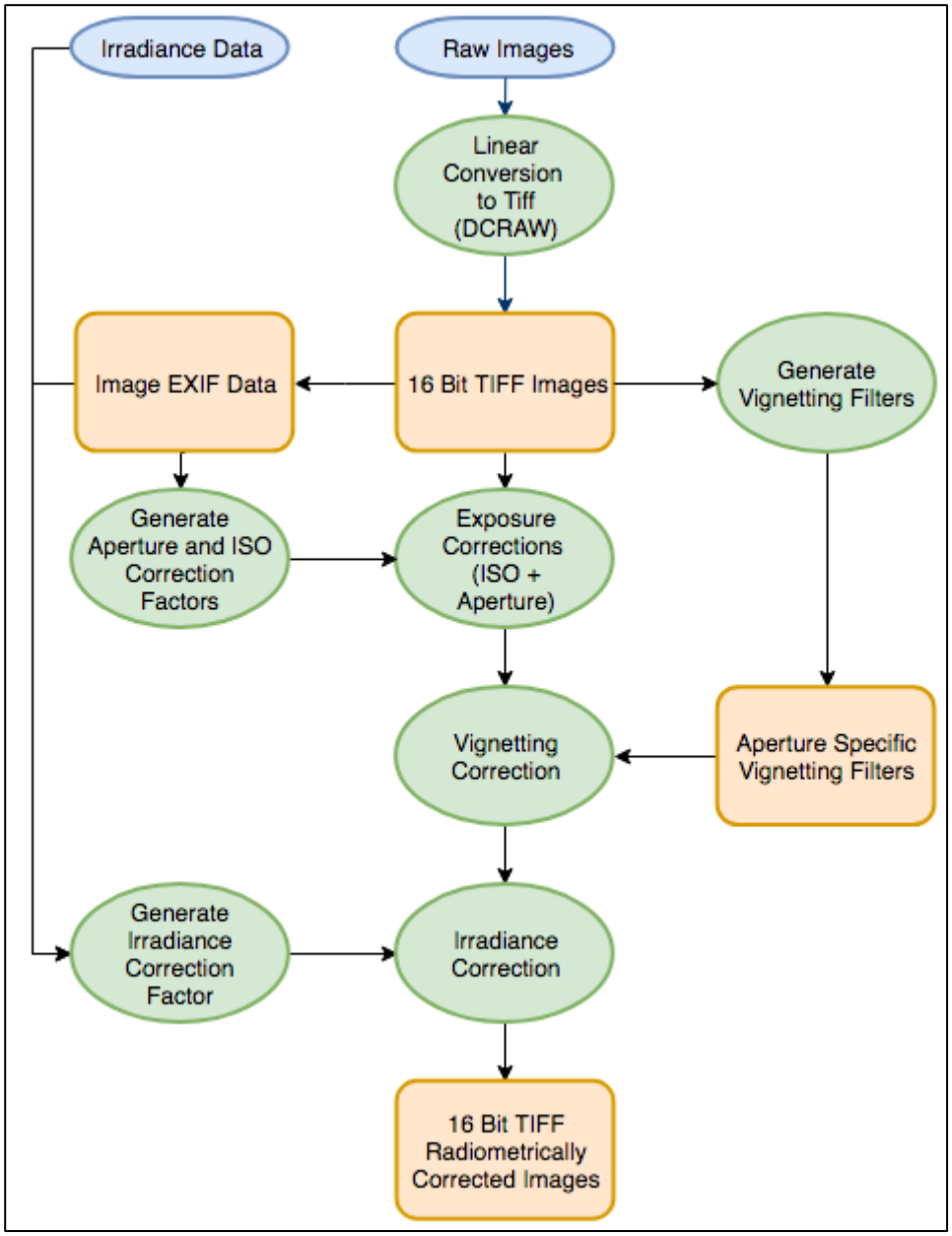

Figure B. 1. Workflow diagram outlining the key inputs, processing steps and outputs required and produced in the developed calibration tool. Blue shapes indicate inputs, Green shapes indicate processing, and Orange shapes indicate outputs.

After feedback from Rothasmted Research, several additional features were added to improve usability and automation of the tool. Firstly, the software was upgraded to autofill all file paths after the path to the folder containing RAW images was selected. This assumes the irradiance data file is in the same place, but helps to speed up input selection. The other significant improvement was the addition of a batch processing option. This feature allows the user to queue up multiple datasets for processing rather than having to each dataset individually.

D3. Data Merging Tool

This tool has been designed to merge the different orthomosaics/datasets produced by Rothamsted Research's drones for each experiment. This includes, RGB, NIR, Vegetation Indices, Digital Elevation Model and Thermal mosaics. By combining multiple layers, it improves data storage as well as analysis as all data is maintained within a single file.

The tool is designed to accept any combination of layers and will calculate an NDVI layer if RGB and NIR mosaics are provided. The key steps to the workflow, Figure B. 3, include:

1. Re-project layers to WGS84, if the layer is already in the correct projection system then this step is skipped.
2. Mask each layer to a common Area of Interest e.g. the field outline.
3. Merge layers together and output to single TIFF format file.

Importantly, no rescaling of resolution or compression is applied; ensuring that the original data of each layer is maintained; however, this does increase file size. An example of a typical output from this tool is provided in Figure B. 2.

As with the previous tool, feedback from Rothasmted Research, highlighted the preference for automation in selection of input and output files. This was added in subsequent versions and will automatically select the output file location and name based on input file parameters.

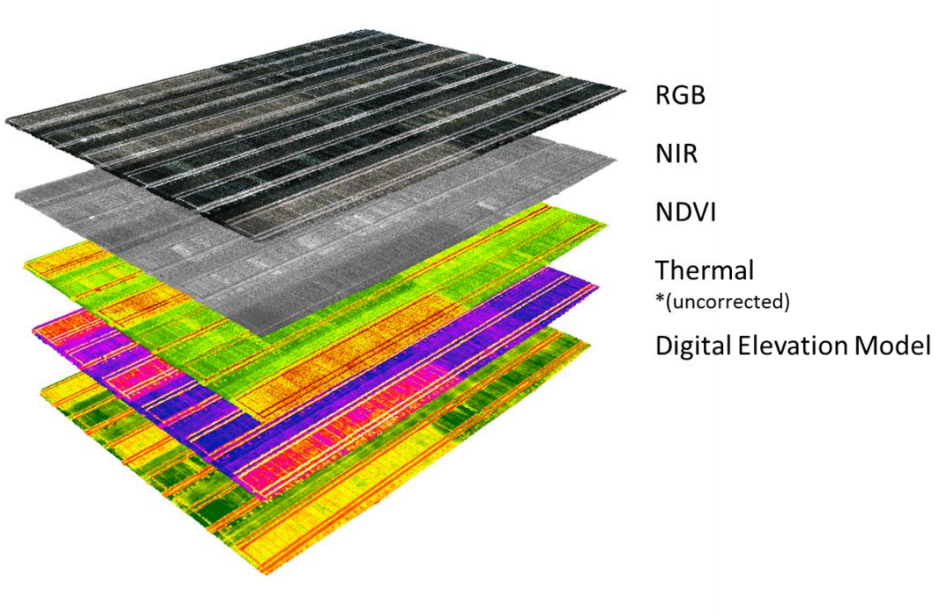

Figure B. 2. Example of a multi-layer stacked single image file generated from UAV derived spectral and thermal orthomosaics, and a normalised Digital Elevation Model.

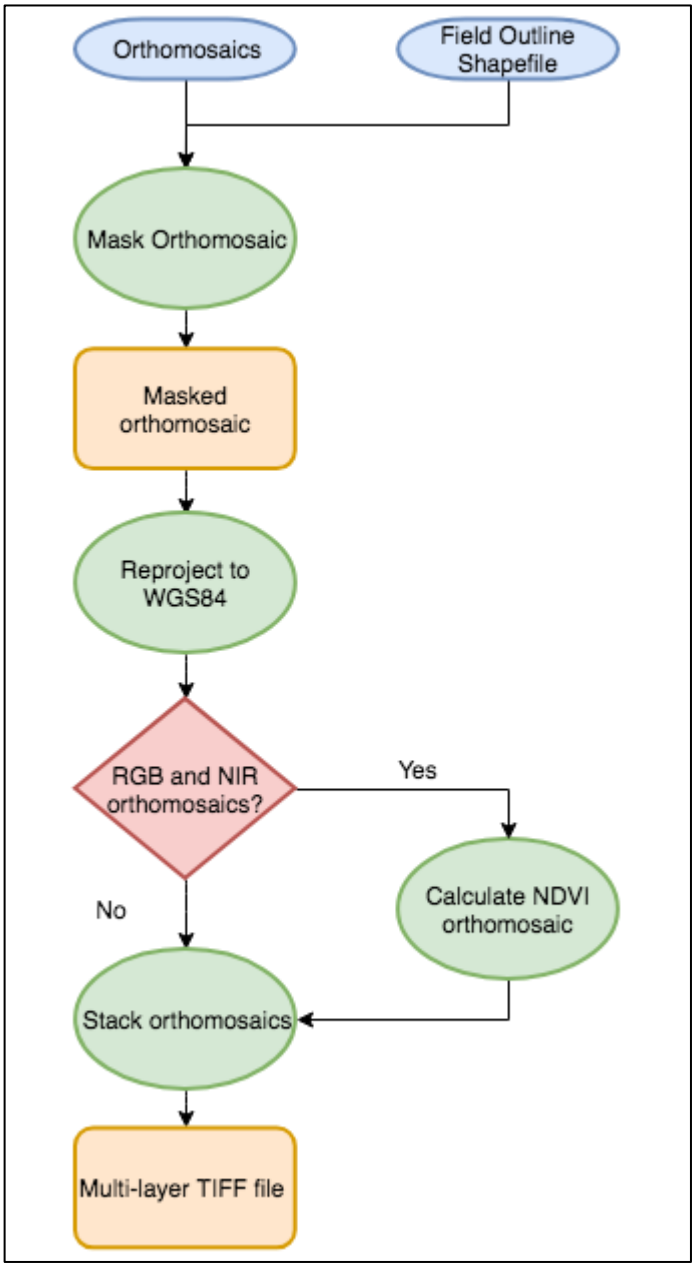

Figure B. 3. Flow diagram describing the key workflow steps used for the layer stacking of UAV derived orthomosaics and normalised Digital Elevation Models (nDEMs) into a single file. Blue shapes indicate inputs, Green shapes indicate processing, Red shapes indicate a condition, and Orange shapes indicate outputs.

D4. Data Extraction Tool

The Data Extraction Tool has been designed to simplify the extraction of key statistics for multiple plots. The tool provides an automated and quick way of extracting the same statistics for multiple plots over multiple experiments. This uses workflows developed previously in the PhD, using plot boundary shapefiles to isolate individual plots. From these, key statistics such as mean, median standard deviation and percentiles are extracted from the plot. The tool's workflow, Figure B. 4, uses pre-defined areas of interest to isolate and extract statistics for each plot. For each plot, the results are saved to an excel spreadsheet, where a separate sheet is produced for each band present in the input file.

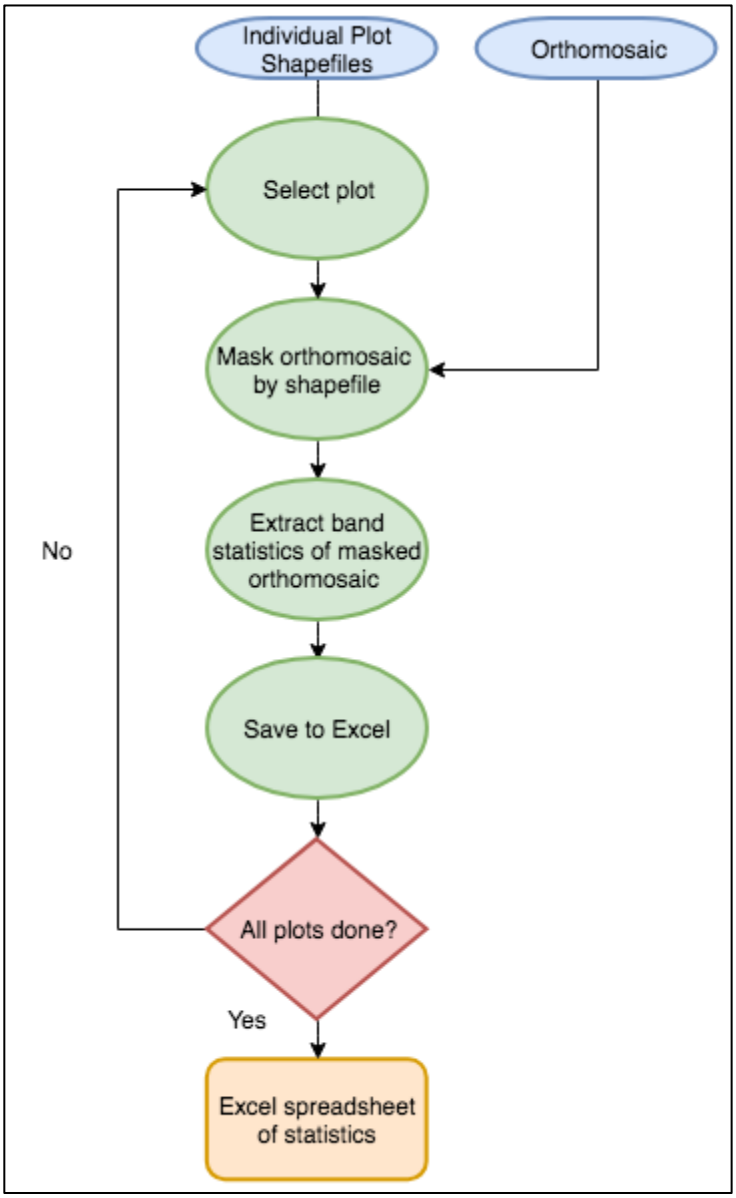

Figure B. 4. Flow diagram describing the key workflow steps used for the extraction of experimental plot statistics from UAV derived orthomosaics and normalised Digital Elevation Models (nDEMs). Blue shapes indicate inputs, Green shapes indicate processing, Red shapes indicate a condition, and Orange shapes indicate outputs.

D5. Future Development

The current suite of publicly available tools for processing, handling and extracting data are limited. The tools developed in this project have the potential to fill this gap, however further work is required to develop them in to general purpose software applicable to different sensors and field sites. A key area requiring further focus is the mapping of plots within the fields, currently done manually. This time-consuming step is the last section of data handling that has no automation available. The complexity of field plot layouts means any workflow developed will need to have enough flexibility to account for this. In addition, variations in plant type, image resolution and plant growth stage will all influence mapping of plots. Addition of this tool to software developed in this project would provide a full suite of tools able to process data from the raw image stage to statistical results with minimal user input.

The incorporation of thermal image calibration workflows is another area of future work with the software. Development of the calibration workflows for the thermal imagery is still on-going and as such will be incorporated as an additional tool in the software when complete.

End.